Draft:Monday 30th July, 2018-02:34

IHEP-CEPC-DR-2018-XX

IHEP-EP-2018-XX

IHEP-TH-2018-XX

CEPC

Conceptual Design Report

Volume II - Physics & Detector

The CEPC Study Group

Fall 2018

ACKNOWLEDGMENTS

The CEPC Physics and Detector Conceptual Design Report (CDR) was prepared and written by the CEPC Study Group. The study was organised and led by scientists from the Institute of High Energy Physics (IHEP) of the Chinese Academy of Sciences (CAS), and from many universities and other institutes in China and abroad. The study was partially supported ...

...

CONTENTS

CHAPTER 1

EXECUTIVE SUMMARY

This document is the second volume of the Conceptual Design Report (CDR) for the Circular Electron Positron Collider (CEPC) project. This volume summarizes the physics potential of the CEPC, possible detector concepts and the corresponding R&D program. The first volume [**?**], released in July 2018, describes the CEPC accelerator complex design, the associated civil engineering and strategic alternative scenarios. This CDR follows up on the preliminary Conceptual Design Report (preCDR) study [1], released in 2015, and culminates three years of work since then.

The main purpose of this document is to address the physics potential of a future circular electron positron collider. The CEPC operation will be staged in a few steps of center-of-mass energy to maximize its physics potential. It is expected the CEPC to start operations at 240 GeV, giving raise to a wealth of Higgs physics, and then move to lower center-of-mass energies and collect large samples of W and Z bosons. This complete program of precision standard-model physics will certainly place stringent constraints on new physics, and it has the potential for direct observation of new physics.

This CDR presents the essential features of the detectors that are required to extract the full physics potential of the CEPC. The experimental conditions at high-luminosity high-energy circular electron positron colliders are more challenging than those considered previously for electron-positron linear colliders due to the higher levels of beam-induced backgrounds, and the 25 ns bunch-spacing required to collect extremely large samples of Z boson events. A main goal of this report is to demonstrate that a wide range of high-precision physics measurements can be made at CEPC with detectors that are feasible expanding on the on-going realistic R&D program.

Consequently, part of this report is devoted to understanding the impact of the machine environment on the detector with the aim of demonstrating, with the example of a few

realistic detector concepts, that high-precision physics measurements can be made at the CEPC. This document concentrates on the detector requirements and physics measurements at the highest CEPC center-of-mass energy of 240 GeV, when the beam induced backgrounds are higher, but consideration is also given to the high-rate operation at the Z-boson mass energy.

A pre-release version of this Physics and Detector CDR was reviewed by an international review committee in September 2018. The comments from the reviewers have been taken into account in this final document, and details about it can be found in Appendix [**?**].

This section is just a placeholder for now. It will be a short introduction 2-4 pages with a very short motivation for the CEPC project [2] and the workings of the CDR. We will define here the goals of the CDR and will already mention the connection between the different detector concepts. We will mention quickly some of the challenges and the future R&D program. We can also provide the short descriptions to the chapters in the CDR. There will be no subsections sections in this text. Each part below will be a short executive summary of the corresponding sections in the text.

1.1 The Case for the CEPC-SppC in China

1.2 The Physics Potential

1.3 The Collider and the Experimental Environment

1.4 The Detector Concepts

1.5 The Performance and Physics Benchmarks

1.6 The Path to the TDR

References

[1] The CEPC-SPPC Study Group, *CEPC-SPPC Preliminary Conceptual Design Report, Volume II - Accelerator*, 2015. IHEP-CEPC-DR-2015-01, IHEP-AC-2015-01.

[2] CEPC project website. http://cepc.ihep.ac.cn.

CHAPTER 2

OVERVIEW OF THE PHYSICS CASE FOR CEPC

Lorem ipsum dolor sit amet, consectetuer adipiscing elit. Ut purus elit, vestibulum ut, placerat ac, adipiscing vitae, felis. Curabitur dictum gravida mauris. Nam arcu libero, nonummy eget, consectetuer id, vulputate a, magna. Donec vehicula augue eu neque. Pellentesque habitant morbi tristique senectus et netus et malesuada fames ac turpis egestas. Mauris ut leo. Cras viverra metus rhoncus sem. Nulla et lectus vestibulum urna fringilla ultrices. Phasellus eu tellus sit amet tortor gravida placerat. Integer sapien est, iaculis in, pretium quis, viverra ac, nunc. Praesent eget sem vel leo ultrices bibendum. Aenean faucibus. Morbi dolor nulla, malesuada eu, pulvinar at, mollis ac, nulla. Curabitur auctor semper nulla. Donec varius orci eget risus. Duis nibh mi, congue eu, accumsan eleifend, sagittis quis, diam. Duis eget orci sit amet orci dignissim rutrum.

Nam dui ligula, fringilla a, euismod sodales, sollicitudin vel, wisi. Morbi auctor lorem non justo. Nam lacus libero, pretium at, lobortis vitae, ultricies et, tellus. Donec aliquet, tortor sed accumsan bibendum, erat ligula aliquet magna, vitae ornare odio metus a mi. Morbi ac orci et nisl hendrerit mollis. Suspendisse ut massa. Cras nec ante. Pellentesque a nulla. Cum sociis natoque penatibus et magnis dis parturient montes, nascetur ridiculus mus. Aliquam tincidunt urna. Nulla ullamcorper vestibulum turpis. Pellentesque cursus luctus mauris.

This [1] is an example with plots, please edit ...

2.1 First theory subsection

Lorem ipsum dolor sit amet, consectetuer adipiscing elit. Ut purus elit, vestibulum ut, placerat ac, adipiscing vitae, felis. Curabitur dictum gravida mauris. Nam arcu libero, nonummy eget, consectetuer id, vulputate a, magna. Donec vehicula augue eu neque.

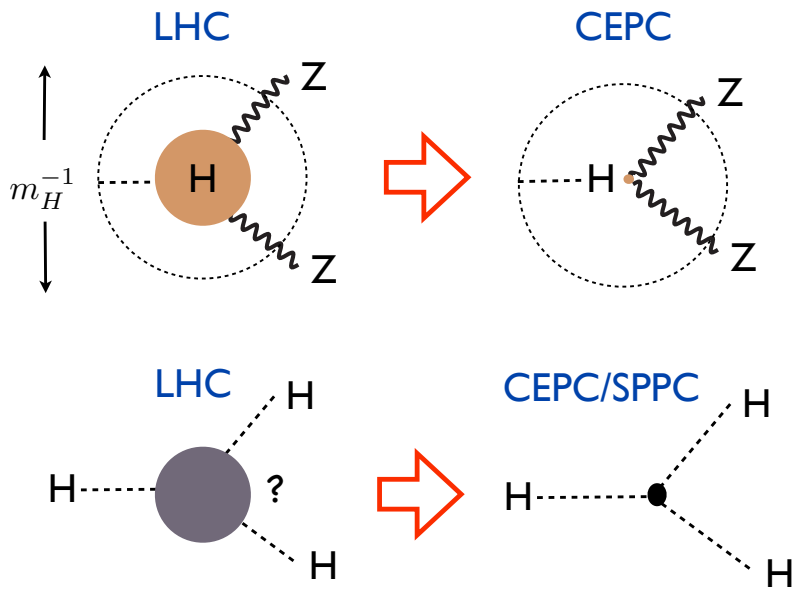

Figure 2.1: A sketch of two of the central goals of the CEPC and SPPC. The CEPC will probe whether the Higgs is truly "elementary", with a resolution up to a hundred times more powerful than the LHC. The SPPC will see, for the first time, a fundamentally new dynamical process — the self-interaction of an elementary particle — uniquely associated with the Higgs.

Pellentesque habitant morbi tristique senectus et netus et malesuada fames ac turpis egestas. Mauris ut leo. Cras viverra metus rhoncus sem. Nulla et lectus vestibulum urna fringilla ultrices. Phasellus eu tellus sit amet tortor gravida placerat. Integer sapien est, iaculis in, pretium quis, viverra ac, nunc. Praesent eget sem vel leo ultrices bibendum. Aenean faucibus. Morbi dolor nulla, malesuada eu, pulvinar at, mollis ac, nulla. Curabitur auctor semper nulla. Donec varius orci eget risus. Duis nibh mi, congue eu, accumsan eleifend, sagittis quis, diam. Duis eget orci sit amet orci dignissim rutrum.

Nam dui ligula, fringilla a, euismod sodales, sollicitudin vel, wisi. Morbi auctor lorem non justo. Nam lacus libero, pretium at, lobortis vitae, ultricies et, tellus. Donec aliquet, tortor sed accumsan bibendum, erat ligula aliquet magna, vitae ornare odio metus a mi. Morbi ac orci et nisl hendrerit mollis. Suspendisse ut massa. Cras nec ante. Pellentesque a nulla. Cum sociis natoque penatibus et magnis dis parturient montes, nascetur ridiculus mus. Aliquam tincidunt urna. Nulla ullamcorper vestibulum turpis. Pellentesque cursus luctus mauris.

References

[1] CEPC project website. http://cepc.ihep.ac.cn.

CHAPTER 3

TRACKING SYSTEM

3.1 Vertex tracker detector

The identification of heavy-flavor (b- and c-) quarks and τ leptons is essential for the CEPC physics program. It requires precise determination of the track parameters of charged particles in the vicinity of the interaction point (IP), permitting reconstruction of the displaced decay vertices of short-lived particles. This drives the need for a vertex detector with low material budget and high spatial resolution. The baseline design of CEPC vertex detector is a cylindrical barrel with six silicon pixel layers and optimized for the energy regime and utilizes modern sensors.

3.1.1 Performance Requirements and Detector Challenges

As required for the precision physics program, the CEPC vertex detector is designed to achieve excellent impact parameter resolution, which in the $r\phi$ plane can be parameterized by:

$$\sigma_{r\phi} = a \oplus \frac{b}{p(GeV)sin^{3/2}\theta} \tag{3.1}$$

where $\sigma_{r\phi}$ denotes the impact parameter resolution, p the track momentum, and θ the polar track angle. The first term describes the intrinsic resolution of the vertex detector in the absence of multiple scattering and is independent of the track parameters, while the second term reflects the effects of multiple scattering. a=5 μm and b=10 $\mu\mathrm{m} \cdot \mathrm{GeV}$ are taken as the design values for the CEPC vertex detector. The main physics performance goals can be achieved with a three-layer pixellated vertex detector with the following characteristics:

- Single-point resolution near the IP better than 3 μm;

- Material budget below 0.15% X_0/layer;
- First layer located close to the beam pipe at a radius of 16 mm, with a material budget of 0.15% X_0 for the beam pipe;
- Detector occupancy not exceeding 1%.

The power consumption of the sensors and readout electronics should be kept below 50 $\mathrm{mW/cm^2}$, if the detector is air cooled. The readout time of the pixel sensor needs to be shorter than 20 μs, to minimize event accumulation from consecutive bunch crossings. The radiation tolerance requirements, which are critical for the innermost detector layer, are driven by the beam related backgrounds as described in Chapter 9.

3.1.2 Baseline design

The baseline layout of the CEPC vertex detector consists of three concentric cylindrical layers of double-sided pixellated silicon detector located between 16 and 60 mm from the beam line. The ladders, which are the main mechanical structure, support high spatial resolution silicon pixel sensors on both sides. The CEPC vertex detector is designed to deliver six precise space-points for charged particle traversing the detector. The material budget of each detector layer amounts to ~0.15% X_0. Extensive simulation studies (see Section 3.1.3) show that the chosen configuration with the single-point resolutions listed in table 3.1 achieves the required impact parameter resolution.

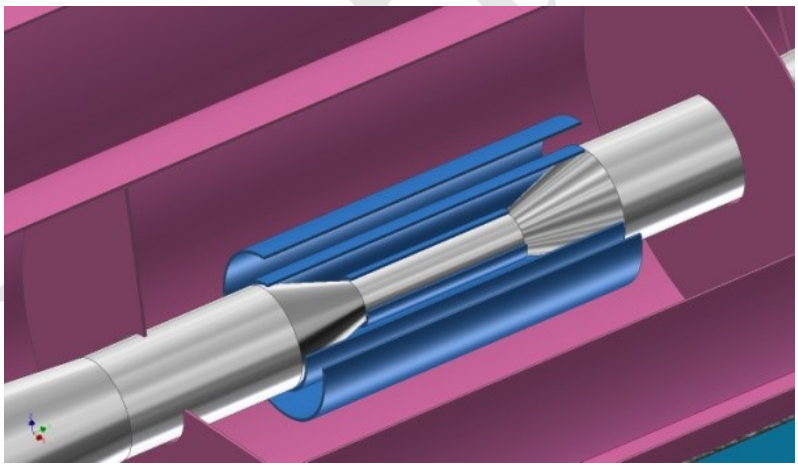

Figure 3.1: Schematic view of pixel detector (blue)

3.1.3 Detector performance studies

The identification of b/c-quark jets (called "flavor-tagging") is essential in physics analysis where signal events with b/c-quark jets in the final state have to be separated. Flavor tagging requires the precise determination of the impact parameter of charged tracks embedded in the jets. For CEPC operation at the center-of mass energy of 240 GeV, those tracks are often of low momentum, for which the multiple scattering effect dominates the tracking performance as illustrated by Eq. 3.1.

The CEPC vertex detector layout has been fully implemented in the GEANT4-based simulations framework MOKKA [1]. In addition, the LiC Detector TOY fast simulation

	$R(mm)$	$\|z\|(mm)$	$\|cos\theta\|$	$\sigma(\mu m)$	$Readout\ time(us)$
Layer 1	16	62.5	0.97	2.8	20
Layer 2	18	62.5	0.96	6	1-10
Layer 3	37	125.0	0.96	4	20
Layer 4	39	125.0	0.95	4	20
Layer 5	58	125.0	0.91	4	20
Layer 6	60	125.0	0.90	4	20

Table 3.1: Vertex detector parameters

and reconstruction framework (LDT) [2] have been used for detector performance evaluation and layout optimization. The preliminary studies for optimization to evaluate the sensitivity of the results on the chosen parameters have been done, for the purpose of assessing the impact of the detector geometries and material budgets on required flavor-tagging performance. However, beam-induced background was not included at the moment.

3.1.3.1 Performance of the Baseline Configurations

The impact parameter resolution following from the single-point resolutions provided in the table 3.1 is displayed in figure 3.2 as a function of the particle momentum, showing that the ambitious impact parameter resolution is achievable.

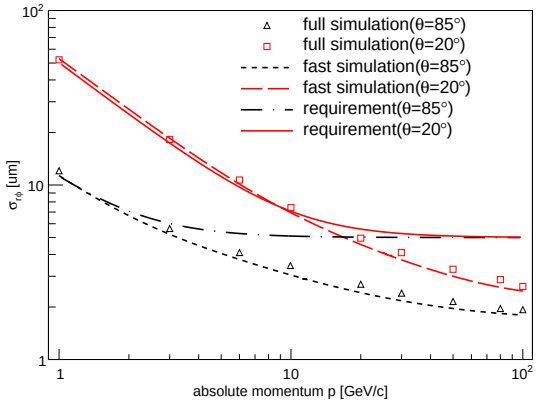

Figure 3.2: Transverse impact-parameter resolutions for single muon events as a function of the momentum for different polar angles.

3.1.3.2 Material Budget

The baseline design includes very small material budget for the beam pipe as well as for the sensor layers and their support. To assess the sensitivity of the performance on the amount of material, the material budget of the beam pipe and the vertex detector layers has been varied. The resulting transverse impact-parameter resolutions for low-momentum tracks are shown in Figure 3.3. When increasing the material of the detector layers by a factor of two, the resolution degrades by approximately 20%.

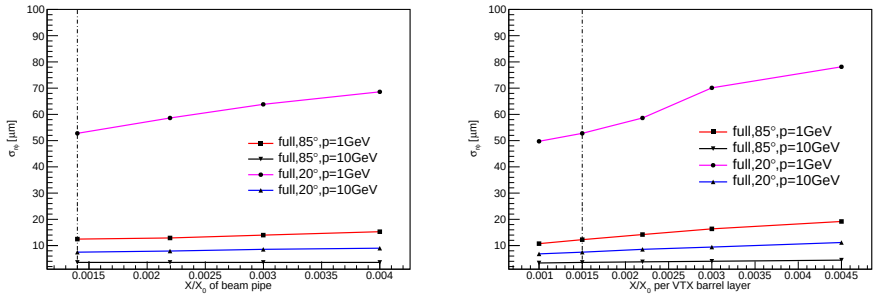

Figure 3.3: Transverse impact-parameter resolution as function of the amount of material inside the beam pipe (left) and inside the vertex barrel double layers (right), as obtained from the simulation. The results are shown for 1 GeV and 10 GeV tracks and for polar angles of θ=20 degrees and of θ=85 degrees. The material budget corresponding to the baseline configuration is indicated by dashed lines.

3.1.3.3 Dependence on Single-Point Resolution

The dependence of the transverse impact-parameter resolution on the pixel size was studied by worsening the single-point resolution of the vertex layers by 50% w.r.t. the baseline values. The resulting impact parameter resolution for high and low momentum track as function of the polar angle θ is shown in Figure 3.4. The resolution for track momenta of 100 GeV is found to change by approximately 50% in the barrel region, which is totally expected. Here they are better than the target value for the high-momentum limit of a$\approx$5 μm in both cases, as expected from the corresponding single-point resolutions. For 1GeV, where multiple-scattering effects dominate and the corresponding variation of the transverse impact-parameter resolution is only 10% larger. The target value for the multiple-scattering term of b$\approx$10 $\mu\mathrm{m}\cdot\mathrm{GeV}$ is approximately reached in both cases. It should be noted, however, that the pixel size is also constrained by the background occupancies (see Section 3.1.4) and the ability to separate adjacent tracks in very dense jets in the presence of such backgrounds.

3.1.3.4 Distance to IP

The distance of the first double vertex layer from the IP was varied by $\pm$4 mm relative to baseline geometry of the CEPC vertex detector. Figure 3.5 shows the resulting transverse impact parameter resolution at θ=85 degrees as function of the momentum and for different radial distance of the innermost barrel vertex layer from the IP. For low momentum tracks, the transverse impact-parameter resolution is proportional to the inner radius, as expected from the parameter formula.

3.1.4 Beam-induced Background in the Vertex Detector

The pair-production and off-energy particles are expected to be the dominating source of detector backgrounds originating from the interaction region. These processes have been studied with detailed Monte Carlo simulation in Chapter 9. For the first vertex detector layer, the maximum annual values of the Total Ionising Dose (TID) and Non-Ionising Energy Loss (NIEL) are estimated to be 3.4 MRad and 6.2×10^{12} 1 MeV $\mathrm{n_{eq}/cm^2}$ respectively, with a safety factor of 10 included (see Table 8.4 in Chapter 9). This happens

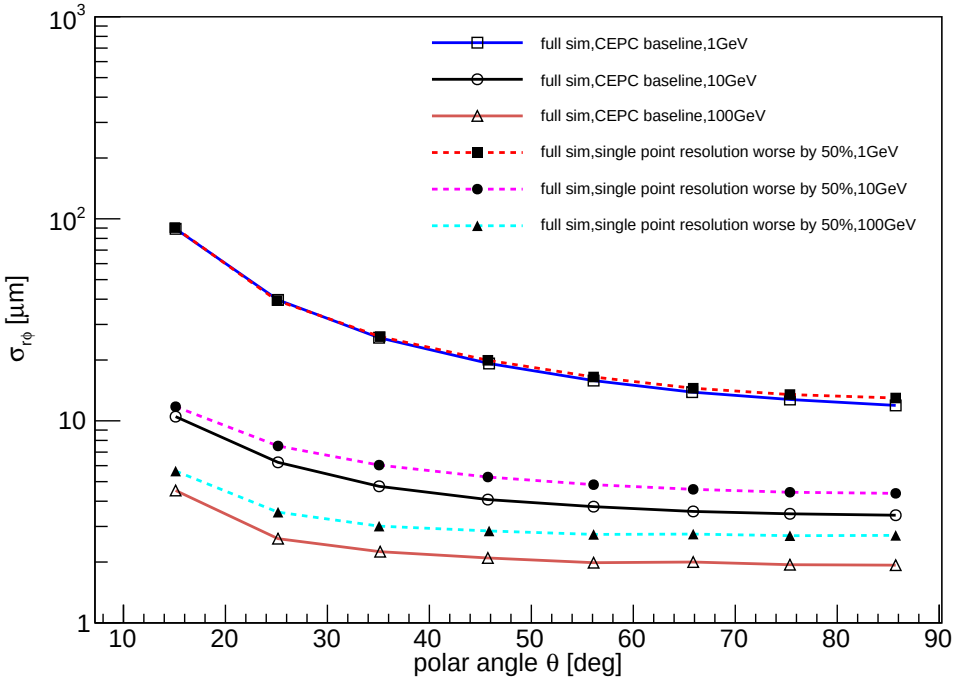

Figure 3.4: Transverse impact-parameter resolutions as function of the polar angle theta for different values of the single-point resolution of the CEPC barrel vertex detector. Shown are the resolutions for 1 GeV, 10 GeV and 100 GeV tracks.

when the machine operating in Z-pole energy, and imposes radiation tolerance as the requirement of silicon pixel sensor and associated readout electronics.

	H(240)	W(160)	Z(91)
Hit density ($\mathrm{hits}\cdot\mathrm{cm}^{-2}\cdot\mathrm{BX}^{-1}$)	2.4	2.3	0.25
Bunching spacing (μs)	0.68	0.21	0.025
Occupancy (%)	0.16	0.50	0.46

Table 3.2: Occupancies of the first vertex detector layer at different machine operation energies

The beam-induced background will have impacts on vertex detector occupancy, which is critical for the innermost detector layer. Table 3.2 shows the expected hit density and occupancies of the first vertex detector layer at different machine operation energies. The result of occupancies depends on assumptions of detector readout time and average cluster size. Here we assume a 20 μs of readout time for silicon pixel sensor and an average cluster size of 9 pixels per hit, where a pixel is taken to be 16×16 $\mu\mathrm{m}^2$. The resulting maximal occupancy at each machine operation mode is below 1%.

3.1.5 Sensor Technology Options

Significant progress has been made over the 20 years since the first silicon pixel detector was introduced in the DELPHI detector [3] at LEP in 1995. Considerable R&D efforts

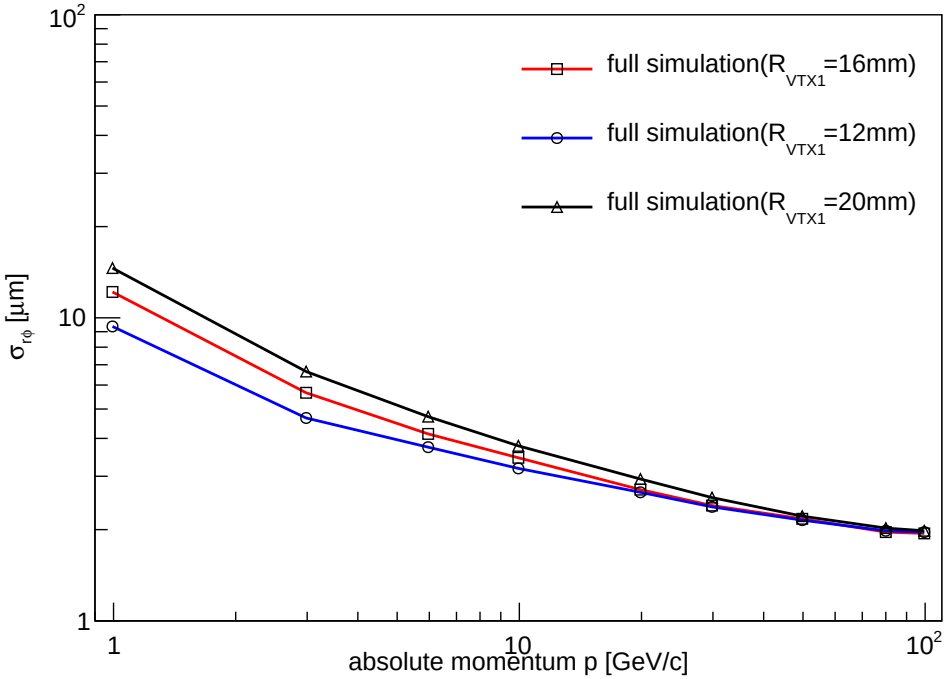

Figure 3.5: Transverse impact-parameter resolution at θ=85 degrees as function of the momentum for different values of inner most layer radius R_{min}. The red curve indicates the baseline configuration of R_{min}=16 mm.

have taken place to develop pixel sensors for vertex tracking at future particle physics experiments [4], driven by track density, single-point resolution and radiation level.

As outlined in Section 3.1.1, the detector challenges for the CEPC include high impact-parameter resolution, low material budget, low occupancy and sufficient radiation tolerance (mild comparing to LHC but not necessarily easy to achieve). To fulfill these requirements at system level, sensor technologies which achieve fine pitch, low power and fast readout must be selected. In fact the CEPC vertex detector is more demanding than previous applications. CEPC is continuous, and power pulsing cannot be utilized to reduce average power. Other experiments such as the STAR[5], BELLEII[6] and ALICE upgrade[7] readout continuously as the CEPC. However, they have less stringent requirements in terms of impact-parameter resolution and material budget.

The monolithic pixel sensor has the potential to satisfy the low-material and high-resolution requirements of the CEPC vertex detector. This technology has been developing fast. The 1st generation MAPS-based vertex detector for STAR HFT upgrade [5, 8] just completed 3-year physics run successfully, while the new generation HR CMOS Pixel Sensor for ALICE-ITS upgrade [7] is in mass production. In the previous 0.35 μm double-well process, only N-MOS transistors can be used in the pixel design. This constraint is removed in the new 0.18 μm quadruple-well process. Both N and P-MOS transistors can be used in the pixel design. Combining with the smaller feature size, it becomes a very appealing technology. A good start point for the CEPC vertex would be the ALPIDE design [9], which is developed for the aforementioned ALICE-ITS upgrade and has achieved performances very close to the requirements of the CEPC. Further R&Ds are needed to

shrink the pixel pitch to 16 μm (binary readout) in order to accomplish the required 2.8 μm single-point resolution. Another monolithic option is the Silicon On Insulator (SOI) pixel sensor. After more than 10 years evolution, SOI has entered a new stage of maturity. Fundamental issues, including the transistor shielding [10] and the TID tolerance [11], have been addressed and wafer thinning [12] has been demonstrated. In the meanwhile, R&Ds for the ILC and the CLIC [13, 14] are exploring time stamping and analog readout scheme. The SOI has a unique feature of fully-depleted substrate as the active silicon. And its 0.2 μm CMOS process provides the necessary density of transistors as the 0.18 μm CMOS in HR CMOS does. Therefore it is envisaged that the readout design for the CEPC vertex may be adapted for both processes and to exploit each one's potentials.

Depleted P-channel Field Effect Transistor (DEPFET) is referred to as semi-monolithic because it allows to integrate the first amplification stage into the pixel combined with subsequent processing circuit in separate readout ASICs. The BELLE II is anticipating its full detector operation with the DEPFET-based vertex [6] installed at the end of 2018. It is very helpful to have the readout ASICs located outside the detector acceptance area as the major heat sources, while keeping the sensors exceptionally low power and low material. The challenge is to periodically sample the modulated current over a large pixel array within required intervals, 20 μs/frame or even less.

Hybrid pixel has been used at hadron colliders for the past decades, and now CLIC R&D is pushing for 50 μm thinned sensors bump bonded on 25 μm pitch to 50 μm thinned ASICs [15]. The hybrid approach evolves constantly and profits from industrial technology developments. Apart from the Very Deep Sub-Micron (VDSM) ASIC technology that enables complex functionalities and superior performances, a close watch on industrial developments of the vertical and lateral inter-connection technologies will also be very helpful to meet the material budget.

3.1.6 Mechanics and Integration

The design of the vertex detector is conceived as a barrel structure with three concentric cylinders of double-sided layers. Each double-sided layer is equipped with pixel sensors on both sides, and has a common support frame. In the azimuthal direction, each layer is segmented in elements called ladders. The ladder, which extends over the whole length of the layer, is the basic building block of the detector. It contains all structural and functional components, such as chips, flex cable, support frame and cold plate if it is necessary. Pixel chips in a row are connected to flex cable by wire bonding or other bonding techniques, and then glued to the support frame, which is composed of low Z materials, such as carbon fiber and silicon carbide, providing stable mechanical support. The other side of the support frame is equipped with another layer of pixel sensors.

The design of the ladders should take into account the specifications of the vertex detector. In order to reduce a small multiple Coulomb scattering contribution to the charged-track vertex resolution and control deformations from gravity and cooling forces for the sensors position stability, the ladder mechanical support must fulfill stringent requirements in terms of minimum material budget and highest stiffness. Ladder designs similar to the STAR pixel detector, the ALICE ITS, the BELLE II PXD, and the ILD double-sided ladder are under consideration.

The ladder mechanical support is inherently linked to the layout of the cooling system that will be adopted to remove the heat dissipated by the pixel sensors since the cooling

system is integrated in the mechanical structure. The cooling system of the CEPC vertex detector must balance the conflicting demands of efficient heat dissipation with a minimal material budget. Therefore a suitable, high thermal conductivity and low material budget, cold plate coupled with pixel sensors should be implemented in the ladder design. There are two main types of cooling methods in particle physics experiments, air cooling and active cooling. Table 3.3 gives a list of cooling methods and the corresponding material of each layer of the aforementioned experiments. The upgrade of ALICE ITS [7] adopts water cooling with respect to a chips power dissipation value of 300 $\mathrm{mW/cm^2}$. Polyimide cooling pipes fully filled with water are embedded in the cold plate. STAR- PXL [16] uses air cooling according to its chips power consumption of 170 $\mathrm{mW/cm^2}$. For ILD [17] vertex system, two different cooling options are considered, depending on the sensor technology. The sensors and SWITCHER chips of BELLE II PXD [18] require air cooling, while active cooling will be used for readout chips on each end of the detector, which is out of the sensitive region of the detector. So for CEPC vertex detector, the suitable cooling method will be determined according to the sensor option and the power consumption.

Vertex detector	Power dissipation	Cooling method	Material budget requirement/layer
Alice ITS	300 mW/cm^2	water	0.3%
STAR PXL	170 mW/cm^2	air	0.39%
ILD vertex	<120mW/cm^2 (CPS and DEPFET)	air or N_2	0.15%
	35W inside cryostat (FPCCD)	two-phase CO_2	
BELLEII PXD	20W for sensor and SWITCHER	Air	0.2%
	180W on each end	CO_2	

Table 3.3: Cooling method of the vertex detector in each experiment

Simulation and module prototype studies should be carried out to find suitable designs that can meet requirements of stability, cooling and the performance of the vertex detector.

For the design of the whole mechanical structure of the vertex detector, some criteria must be taken into account. Firstly, minimum material has to be used in the sensitive region to reduce multiple Coulomb scattering. Secondly, to ensure high accuracy in the relative position of the detector sensors and provide an accurate position of the detector with respect to the central tracker of TPC and the beam pipe, a mechanical connector or locating pin at each end of the ladder should be considered to allow the fixation and alignment of the ladder itself on the end rings. Thirdly, cooling system should be arranged reasonably to ensure stable heat dissipation. At last, to reduce the dead region caused by the boundary of each ladder, neighboring ladders should be partially superimposed.

In addition, the main mechanical support structures of the vertex should also meet the requirements of the integration with the other detectors, such as time projection chamber (TPC) and forward tracking disks.

3.1.7 Critical R&D

The inner most layers have to fulfill the most demanding requirements imposed by the physics program. In addition, the system is bounded by stringent running constraints. The technology options in Section 3.1.5 are able to meet each individual requirement, including single-point resolution, low material budget, fast readout, low power consumption and radiation tolerance, but R&D is needed to select the specific design which can achieve the combination of all these criteria. Due to the limited manpower and availability of process, presently R&D efforts have been put into CMOS and SOI pixel sensor development to address the challenges concerning single-point resolution and low power consumption. Further developments are foreseen to follow in the future, including enhancement of density, radiation hardness and ultra-light module assembling.

The current R&D activities have access to two advanced processes. The TowerJazz 0.18 μm quadruple-well process enables the full CMOS pixel circuit, while LAPIS 0.2 μm double-SOI process has properly solved the crosstalk between sensor and digital part, and improved TID tolerance significantly.

In order to exploit the potential of these new developments, two design teams have started chip designs using HR CMOS and SOI technologies respectively. Two designs have been submitted to the TowerJazz foundry. The first one uses simple three transistor (3T) analog amplification circuit to carry out the optimization of sensing diode and evaluate the influence of radiation damage [19]. The second one implements a well-proved rolling shutter readout as well as an innovative data-driven readout [20, 21]. Another two designs that adopt the SOI technology have also been submitted [22]. With the amplifier and discriminator integrated into each pixel, the pixel size has been shrunk to 16μm pitch. The chip has been thinned to 75 μm successfully and an infrared laser test has shown that a single-point resolution of 2.8 μm is achievable with that pitch [12]. All the designs for current R&D are in line with the same principle of in-pixel discrimination even though each one has its own implementation. An in-pixel discriminator can reduce analog current therefore lead to reduced power consumption.

Enhancements of the TowerJazz 0.18 μm process or Lapis 0.2 μm process are possible by migrating to a smaller feature size, 0.13 μm for example, or combining with a micro-bump 3D integration process. The latter is able to attach a second layer of pixel circuit on top of the existing layer of the sensing diode and front-end circuit. The upper tier can be fully digital part that implements data-driven readout architecture, while the lower tier can be HR CMOS or SOI pixel matrix. A promising result has been demonstrated by the successful formation of 2.5 μm Au cone bump with NpD (Nano-particle deposition) technique [23]. However, the throughput needs further improvement and the thinning of sensors has to be compatible with micro-bump 3D integration.

The TowerJazz process is expected to be sufficiently radiation hard for the expected TID. An N-type plain implant has recently been added to improve the charge collection efficiency [24], which therefore will benefit the non-ionization radiation damage. In terms of SOI process, the weak point is the BOX layer of SiO_2. Although the TID tolerance of the SOI process has been improved dramatically by the introduction of Double-SOI and

the optimization of transistor doping recipe (LDD, lightly doped drain) [11], SOI needs carefully study on the irradiation of large scale chip and of low power designs.

Sensor thinning and ultra-low material construction of modules are subject to the constraint of 0.15% X_0/layer. HR CMOS wafer thinned to 50 μm is routine in semiconductor industry nowadays. SOI wafers thinned to 75 μm with backside implant have also been demonstrated by current R&D. However, low material detector modules need to integrate mechanical support, power and signal connection, and sufficient stiffness to avoid vibration.

3.1.8 Summary

The basic concepts of the CEPC Vertex detector, including the pixel sensors specifications required by the impact parameter resolution and radiation tolerance, the low-mass mechanical design, and the detector layout, are implemented in the baseline design. It will be crucial to develop pixel sensors with lower power consumption and fast readout electronics because of continuous colliding mode and strong beam-related background. Detailed designs for mechanical supports and cooling, cabling, and power conversion are also necessary. Most of these issues will be addressed by R&D for the CEPC and by exploring synergies with experiments which have similar requirements.

3.2 Silicon tracker detector

As described in the PreCDR [25], the silicon tracker, together with the vertex detector and the TPC (Time Projection Chamber, see Section 3.3), forms the complete tracking system of CEPC. With sufficiently low material budget to minimize the multi-scattering effect, the silicon tracker provides additional high-precision hit points along trajectories of charged particles, improving tracking efficiency and precision significantly. In addition to complementary tracking, it also provides the following functionalities:

- monitoring possible field distortion in the TPC,
- contributing detector alignment,
- separating events between bunch crossings with relative time-stamping,
- potentially dE/dx measurement.

The transverse momentum resolution can be parameterized as [26]

$$\sigma_{1/p_{\mathrm{T}}} = a \oplus \frac{b}{p \sin^{3/2}\theta} \quad [\mathrm{GeV}^{-1}] \tag{3.2}$$

with p and p_{T} in GeV, θ the polar angle, a in GeV^{-1} and b a dimensionless number. The two terms characterize tracking resolution and multiple scattering effect separately. If a track is measured at N points equally distributed along the trajectory, we have

$$a = \frac{\sigma_{\mathrm{SP}}}{0.3BL'^2}\sqrt{\frac{720}{N+4}}$$

where B is in tesla, σ_{SP} in meter is the measurement resolution of each point and L' in meter is the projected length of the track onto the transverse plane. For multiple scattering

and for relativistic particles, namely $\beta = 1$, there is

$$b = 0.053 \frac{1}{BL'} \sqrt{\frac{L'}{X_0}}$$

where X_0 is radiation length in units of length.

The CEPC physics requirements put required performance on a tracker as

$$a \sim 2 \times 10^{-5}\,\mathrm{GeV}^{-1} \quad \text{and} \quad b \sim 1 \times 10^{-3}. \tag{3.3}$$

At low momenta, less than $50\,\mathrm{GeV}$ for perpendicular tracks, the resolution is dominant with the multiple scattering effect, and at high momenta, the resolution approaches to the tracking resolution, in turn determined by the single-point resolution. Hence, stringent constrain has to be put on material budget.

3.2.1 Baseline design

The main characteristic of the baseline design for the CEPC silicon tracker is a silicon envelope [27] around the TPC. It consists of four components: the Silicon Inner Tracker (SIT), the Silicon External Tracker (SET), the End-cap Tracking Detector (ETD) and the Forward Tracking Detector (FTD). The overall layout is shown in Figure 3.6, and the main parameters are summarized in Table 3.4.

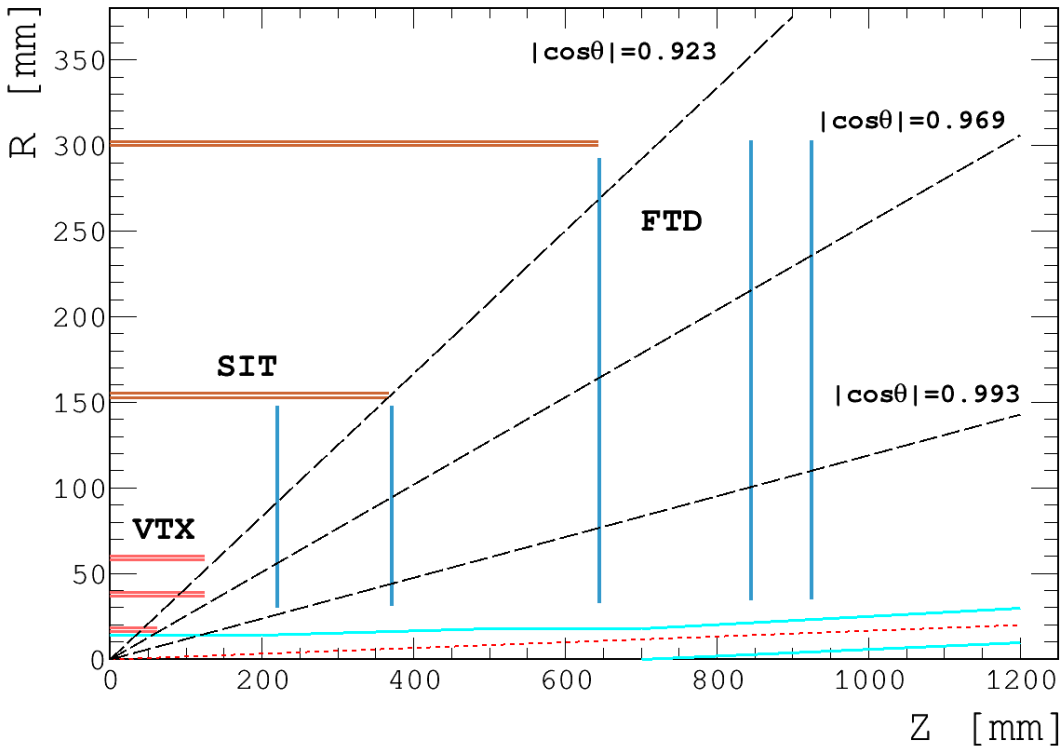

Figure 3.6: Preliminary layout of the CEPC silicon tracker. The red lines indicate the positions of the vertex detector layers and the blue lines the SIT and FTD for the silicon tracker. The SET and ETD, which sit outside the TPC, are not displayed.

Detector		Geometric dimensions			Material budget $[X/X_0]$
SIT	Layer 1:	$r = 153$ mm,		$z = 371.3$ mm	0.65%
	Layer 2:	$r = 300$ mm,		$z = 664.9$ mm	0.65%
SET	Layer 3:	$r = 1811$ mm,		$z = 2350$ mm	0.65%
FTD	Disk 1:	$r_{in} = 39$ mm,	$r_{out} = 151.9$ mm,	$z = 220$ mm	0.50%
	Disk 2:	$r_{in} = 49.6$ mm,	$r_{out} = 151.9$ mm,	$z = 371.3$ mm	0.50%
	Disk 3:	$r_{in} = 70.1$ mm,	$r_{out} = 298.9$ mm,	$z = 644.9$ mm	0.65%
	Disk 4:	$r_{in} = 79.3$ mm,	$r_{out} = 309$ mm,	$z = 846$ mm	0.65%
	Disk 5:	$r_{in} = 92.7$ mm,	$r_{out} = 309$ mm,	$z = 1057.5$ mm	0.65%
ETD	Disk:	$r_{in} = 419.3$ mm,	$r_{out} = 1822.7$ mm,	$z = 2420$ mm	0.65%

Table 3.4: Main parameters of the CEPC silicon tracker.

The barrel components SIT and SET provide precise hit points before and after the TPC, improving the overall tracking performance in the central region. The SIT helps the link between the vertex detector and the TPC, enhancing the reconstruction efficiency, particularly for low-momentum charged particles. The SET sits between the TPC and the calorimeter and helps in extrapolating from the TPC to the calorimeter. In addition, the good timing resolution of silicon sensors provides time-stamping for bunch separation.

The ETD is positioned in the gap between the endplate of the TPC and the end-cap calorimeter. It helps to reconstruct charged particles with a reduced path in the TPC. The SIT, SET and ETD covers the central tracking region. They form the complete silicon envelope and help in calibrating the tracking system.

The FTD is installed between the beam pipe and the inner cage of the TPC, covering the very forward region. It consists of five silicon disks on each side. The FTD is essential for precise and efficient tracking down to very small (or large) solid angles, where a number of challenges exist: the magnetic field approaching zero along the beam pipe, significantly larger occupancies due to forward going jets and high backgrounds from the interaction region. To achieve the best tracking performance, the FTD needs precise space points, a large lever arm, but low material budget. The baseline design would be a compromise among the constraints. Using highly granular pixel sensors for the first two disks can be foreseen to lower the occupancy and improve the $r\phi$ resolution.

3.2.2 Sensor technologies

The basic sensor technology is silicon microstrips for all tracker components except the two innermost FTD disks where silicon pixels are foreseen. Requirements of the single point resolution vary with positions of tracker components, but a general condition of $\sigma_{\mathrm{SP}} < 7\,\mu\mathrm{m}$ is required for high precision tracking. The microstrip sensors have proven to be capable of the resolution, taking into account material budget and power consumption. The baseline features of microstrip sensors will be a large detection area of $10 \times 10\ \mathrm{cm}^2$, a fine pitch of $50\,\mu\mathrm{m}$ and the thickness $< 200\,\mu\mathrm{m}$ to minimize the multi-scattering effect.

The alternative is a fully, or at least for inner components, pixelated silicon tracker. Although the choice of pixel technologies is open, the CMOS pixel sensors (CPS) have

gained particular interest. The main advantages of the CPS comparing to the microstrip sensors are two folds:

- Granularity. The CPS provides better single-point spatial resolution and significantly reduces the ambiguity caused by multiple hits in a single strip.
- Material budget. The CPS can be thinned to less than $50\,\mu\mathrm{m}$, whereas the strip sensor is usually a few hundred microns.

As for the cost, because the CPS is based on the standard CMOS procedure in industry, production cost could be significantly reduced for fabricating large area sensors. In addition, the size of pixels used for the tracker can be comparatively large, hence it's possible to embed complicated circuits in the pixel to simplify the tracker readout circuitry. Initial R&D on large area CPS has been carried out.

Table 3.5 estimates the pixel occupancy of SIT-L1 and FTD-D1. There are a few assumptions in the estimation.

1. The pixel dimension is assumed to be $50\,\mu\mathrm{m} \times 350\,\mu\mathrm{m}$, with which at least in one dimension spatial resolution can reach $7\,\mu\mathrm{m}$ by implementing in-pixel ADC with multiple bits.
2. The track multiplicities in different operation modes are inferred from hit densities in Table 8.4.
3. Readout time of pixel sensors is set as $20\,\mu\mathrm{s}$, the same as that of VTX.
4. Cluster size is set as 9 hits per track.

Table 3.5: Pixel occupancy of SIT-L1 and FTD-D1. See context for explanations.

operation mode	H (240)	W (160)	Z (91)
track multiplicity (BX^{-1})	310	300	32
bunching spacing (ns)	680	210	25
SIT-L1 occupancy (%)	0.19	0.58	0.52
FTD-D1 occupancy (%)	0.17	0.54	0.48

3.2.3 Front-End electronics

The Front-End (FE) electronics will depend on the choice of sensor, namely microstrips or pixels.

For the microstrips, custom designed ASICs with deep sub-micron CMOS technology will be used. The chips will provide functions of the analogue to digital conversion (ADC), zero suppression, sparcification and possibly time stamping, together with necessary control circuitry. The high degree digitization is for relaxing the data processing pressure on downstream electronics.

As for the pixels, all FE functions can be realized in a pixel chip, even with some functions, e.g., ADC on pixels themselves. Particular concerns are readout time and electronic channels.

Commonly, the FE chip will be developed in mind with low noise, low power consumption and high radiation tolerance. New developments, such as in the SiLC collaboration and the LHC experiment upgrades, will be good references.

3.2.4 Powering and cooling

Powering and cooling are a challenge for the CEPC silicon tracker. It is important to investigate the novel powering scheme based on DC-DC converters, which has been already actively pursued by the ATLAS and CMS experiments for silicon detector upgrades [28–30]. It allows significant reduction in material budget for the low-voltage power cables and gives less power dissipation in the delivery system. Cooling is another critical issue. Although cooling based on forced cooled gas flow might be still feasible to efficiently conduct away the heat generated by the sensors, ASICs and other electronics, it is important to look into other cooling techniques, such as silicon micro-channel cooling [31], which are being investigated by several other experiments. The technique chosen will have to provide sufficient cooling without compromising the detector performance.

3.2.5 Mechanics and integration

There will always be additional challenging aspects of the mechanical design for a large area silicon tracker. A lightweight but stiff support structure can be built based on Carbon fibre Reinforced Plastic material [32]. The support structure, cable routing and electronics common to other sub-detectors need to be carefully designed to minimize the overall quantity of material and make easy construction and integration possible. Precise and quick system alignment might be achieved with dedicated laser monitoring systems, while the final alignment will be accomplished using tracks from well-understood physics events [33].

3.2.6 Silicon tracker performance

The performance study described in the section is based on the vertex detector and the silicon tracker.

While the tracking performance in the central region has been extensively studied, the performance in the forward region, which has been designed to cope with the rather short L^*, requires additional careful evaluation. Figure 3.7 shows the estimated transverse momentum resolution for single muon tracks for two polar angles $\theta = 20^\circ$ and 85°, and the analytical results from Eq. (3.2) and Eq. (3.3). Due the reduced lever arm of the tracks and fewer FTD disks in the forward region ($\theta = 20^\circ$), the resolution is worse than the required performance.

Tracking performance of the alternative pixelated silicon tracker has been studied with fast simulation, in which the microstrips are replaced with double-sided pixels with certain single point resolution and material budget reduced to $0.3\%X_0$, the same as VTX. Figure 3.8 shows the transverse momentum resolution for single muons with fixed momentum as a function of polar angle, comparing the pixelated tracker with various single point resolutions to the baseline microstrip tracker. Significant improvement can be observed when the polar angle is below about 20°, in the tracking region of FTD. There is no, however, obvious difference for chosen pixel resolutions, all less than $10\,\mu\mathrm{m}$.

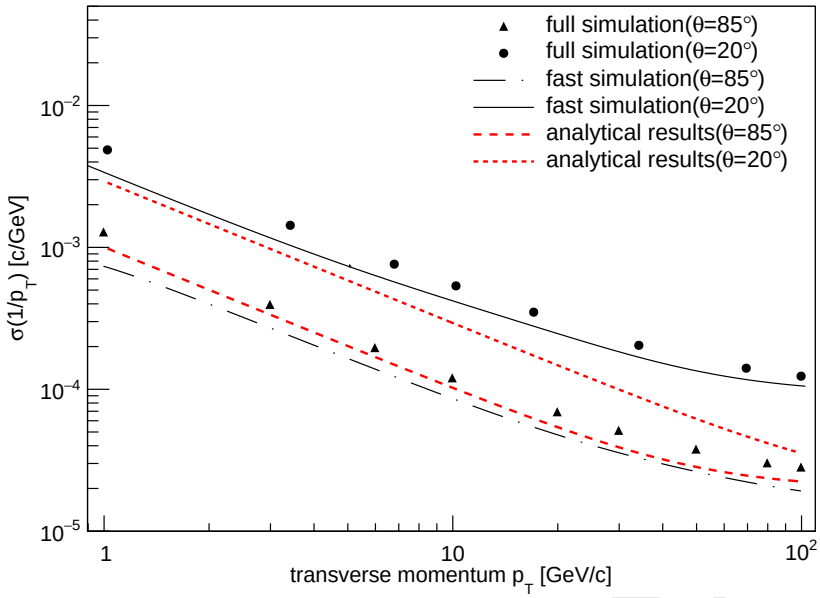

Figure 3.7: Transverse momentum resolution for single muon tracks as a function of the track momentum estimated for the CEPC baseline design with full simulation (dots) and fast simulation (black lines) compared to the analytical results obtained with Eq. 3.2 (red lines).

Given the importance for heavy-flavor tagging, the impact parameter resolution, both transverse and longitudinal, is assessed, as shown in Figure 3.9 with muon momentum of 10 GeV. Similar improvements can be observed, even in the high momentum range for the longitudinal impact parameter.

Further comparison is made for tracks at a fixed forward polar angle, 10°, which pass all five FTD disks, as shown in Figure 3.10. Significant improvements can be observed in the whole momentum range for resolutions of transverse momentum and transverse impact parameter. As for longitudinal impact parameter, there is only slight improvement for high momenta, that is understandable because the z-resolution mainly depends on disk positions.

The studies are quite preliminary. There are spaces to optimize the performance of the pixelated tracker, particularly the pixel layout of FTD disks. Some other preliminary studies on the resolution of transverse impact parameter can be found in PreCDR [25].

3.2.7 Critical R&D

Silicon technology for large-area tracking detectors will continue to evolve over the next few years [34]. There are ongoing R&D activities conducted by the ATLAS and CMS experiments to develop advanced silicon detectors for the High Luminosity LHC as well as several pioneering R&D projects by the SiLC (Silicon tracking for the Linear Collider) collaboration. Despite the rather different operation conditions and requirements, it is always important to exploit synergies with existing R&D from other experiments to share expertise. During the preliminary studies, several critical R&D items have been identified for the CEPC silicon tracker. All of them, as listed below, will be pursued in the R&D phase of the CEPC project and made available for engineering construction.

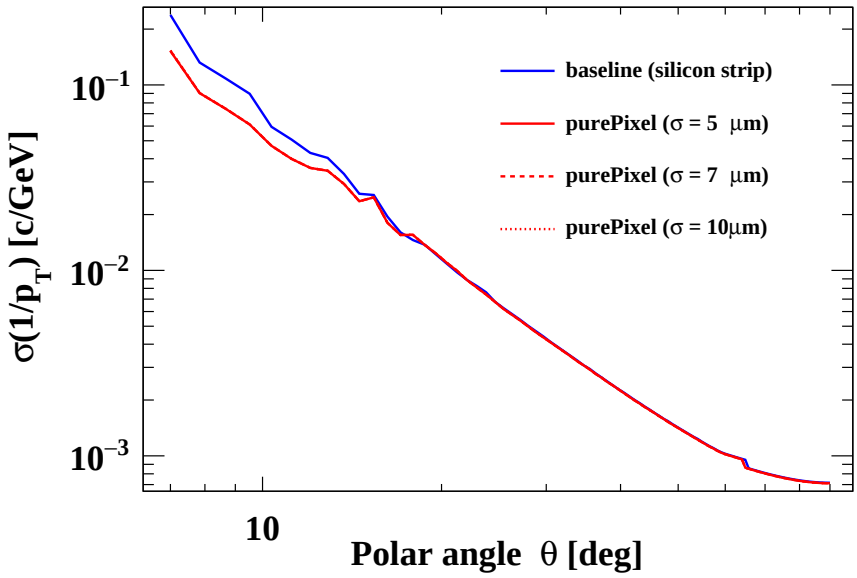

(a) $p = 1\,\mathrm{GeV}$

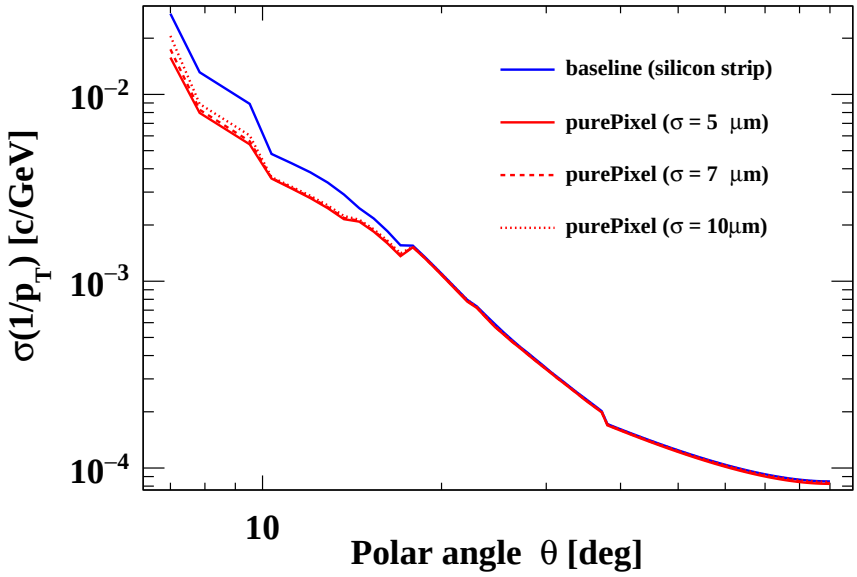

(b) $p = 10\,\mathrm{GeV}$

Figure 3.8: Transverse momentum resolution for single muons with momentum of $p = 1\,\mathrm{GeV}$ (a) and $p = 10\,\mathrm{GeV}$ (b) as a function of polar angle, obtained for the baseline CEPC silicon tracker with microstrips (in blue) and for pixelated tracker (purePixel) with various single point resolutions (in red).

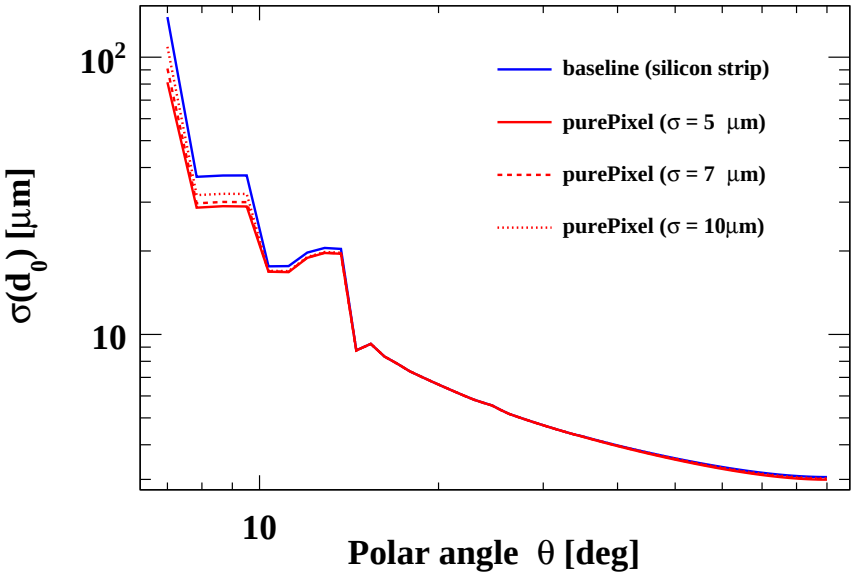

(a) σ_{d_0}

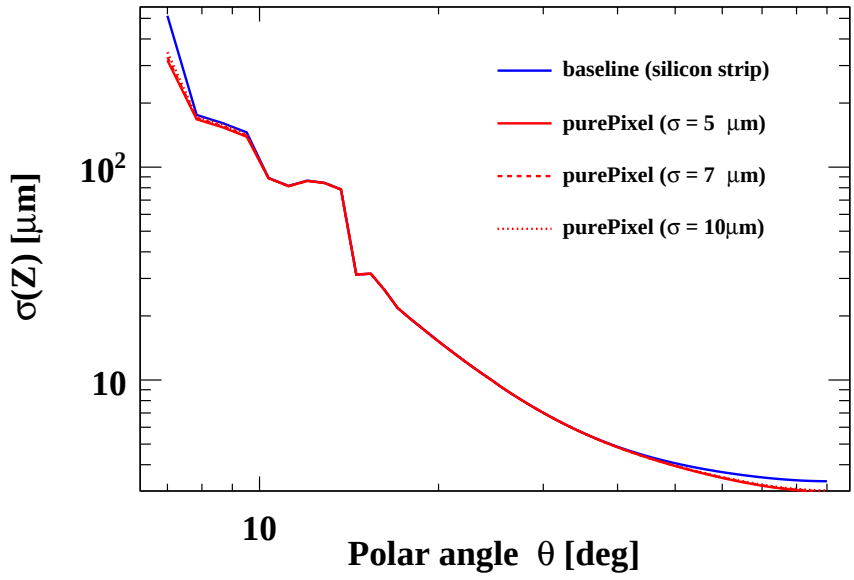

(b) σ_z

Figure 3.9: Transverse (a) and longitudinal (b) impact-parameter resolution for single muons with momentum of $p = 10\,\mathrm{GeV}$ as a function of polar angle, obtained for the baseline CEPC silicon tracker with microstrips (in blue) and for pixelated tracker (purePixel) with various single point resolutions (in red).

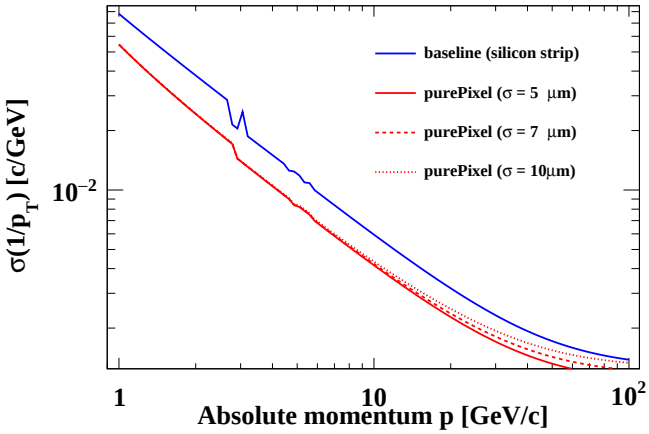

(a) σ_{1/p_T}

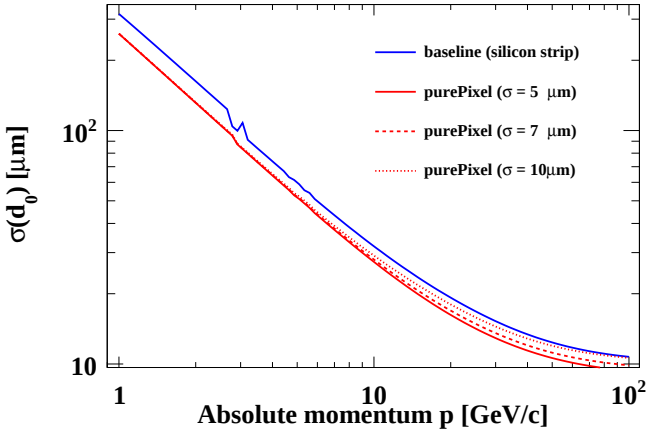

(b) σ_{d_0}

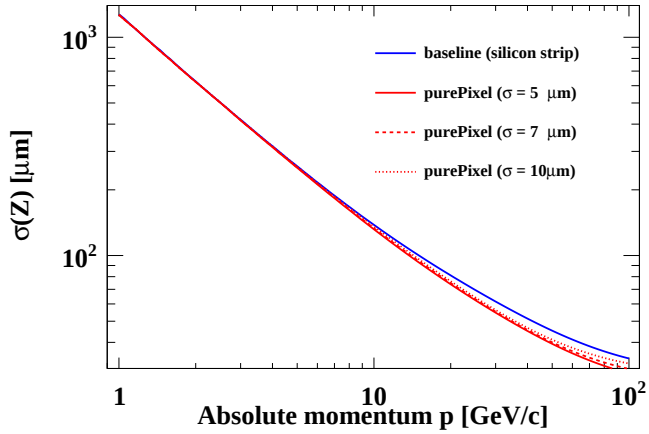

(c) σ_z

Figure 3.10: Transverse momentum (a) and transverse (b) and longitudinal (c) impact-parameter resolution for single muons with the polar angle of 10° as a function of the track momentum, obtained for the baseline CEPC silicon tracker with microstrips (in blue) and for pixelated tracker (purePixel) with various single point resolutions (in red).

- Alternative pixelated strip sensors with CMOS technologies;
- p^+-on-n silicon microstrip sensors with slim-edge structure;
- Front-end electronics with low power consumption and low noise, fabricated with CMOS technologies of small feature size;
- Efficient powering with low material budget and CO_2 cooling techniques;
- Lightweight but robust support structure and related mechanics;
- Detector layout optimization, in particular in the forward region.

It will be vital to develop necessary instrumentation for the module assembly and to verify the detector module performance with beam tests. Prototypes of support structures, including cooling solutions, shall be also built for mechanical and thermal tests.

3.3 TPC tracker detector

Time Projection Chambers (TPCs) have been extensively studied and used in many fields, especially in particle physics experiments, including STAR [35] and ALICE [36]. Since the tracking system are expected to affect the translation of the trackers as less as possible, which require it to be as light as possible. The particle ID ability is one of the feasibility of the tracking system, however for such energetic tracks, the classic method, such as dE/dx, TOF are not reliable, so that the TPC could be used as a primary central tracker [37] [38], In CEPC, the inner tracking system should be sensitive in momentum measurement to charged particles, which transverse momentum ranged from 0 to 80GeV, furthermore, the accelerator with precision appropriate to the energy uncertainty of a beam[39].Their inexpensive material budget and excellent pattern recognition capability make them ideal for three-dimensional tracking and identification of charged particles. They are also the exclusive type of electronically read gaseous detector delivering direct three-dimensional track information. Nevertheless, there has always been a critical problem with TPCs, especially in high background conditions, the space charge distortion due to the accumulation of positive ions in the drift volume [40].

TPC will be as a part of the detector concepts for the CEPC, and it can measure the momentum of tracks of charged particles in the magnetic field. Micro Pattern Gas Detector (MPGD) such as Gas Electron Multiplier (GEM) and Micro-MEsh GAseous Structure (Micro MEGAS) or the Timepix chip is a candidate for the readout technology [37]. Used the MPGD as readout, the $r\phi$ position resolution could be reach to 100 μm, even it is better in the vast magnetic field(3.0T) [41]. Also, the TPC can reconstruct and identify particle species using energy loss (dE/dx) measured by the readout pad rows. In the reaction event of the electron-positron annihilation in the CEPC experiment, it is required to identify charged particle species such as pion, kaon, electron, etc. and to reconstruct the events. For the CEPC-TPC, expected dE/dx resolution is less than 5% for clear identification.

Understanding the properties and achieving the best possible point resolution have been the object of $R\&D$ studies of Micro-Pattern Gas Detectors, GEM, MicroMEGAS, and pixel, and results from many years work in LC-TPC international collaboration group [42].

For improving on the performance, optimising readout module and controlling ion back-flow effectively in the circular machine (CEPC), these studies will continue for the next few years in order to understand and solve several critical technology challenges.

3.3.1 Principle of Time Projection Chamber

A TPC customarily consists of a cylindrical drift volume with a central cathode and an anode at the two endplates. In the case of a colliding experiment, the TPC contains an inner radius in which the beam pipe and inner detectors are placed.

The anodes are at ground, while the cathode is at a potential high voltage to keep the rang of from 100V/cm to 1000V/cm in drift length. The walls of the volume are the field cage, which ensures a highly homogeneous electrical field between the electrodes. The magnetic field is parallel to the electric field to suppress transverse diffusion. The reason for the magnetic field is that if there is no magnetic field, diffusion will dominate, degrading the track and momentum reconstruction. The electrons are released after the ionisation of the sensitive gas volume and drift along the electric field to the anodes, while the ions drift toward the cathode. An amplification device is placed in front of the anodes and creates an electron avalanche as the readout(GEM, MicroMEGAS or others).

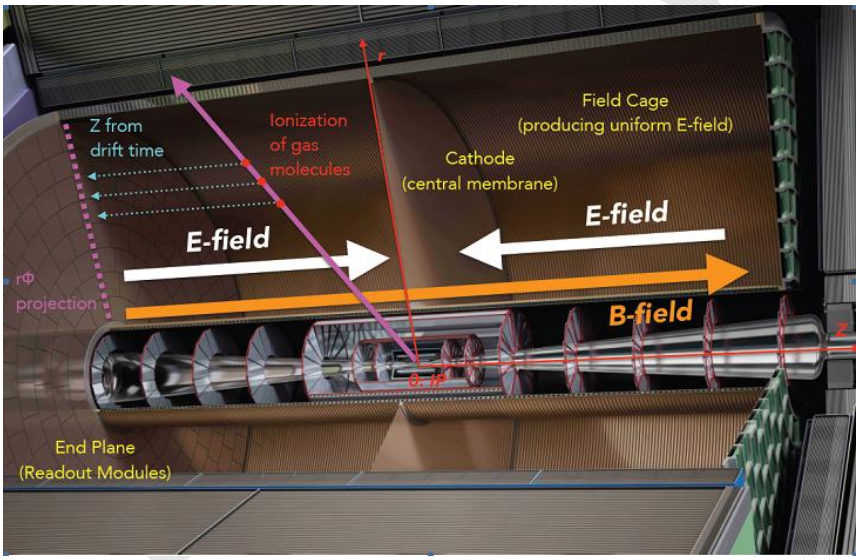

Figure 3.11: Sketch of the TPC structure.

All of TPC will be included some parts:

1. Chamber TPC chambers are typically cylindrical and operate under the atmospheric pressure with the working gas filled inside. Chambers in high magnetic field close to the centre of the magnet, usually have a higher occupancy due to the curling low-energy tracks. Hence the material budget of stations inside the magnet is kept as inexpensive as possible. In the active area, the added the material due to the filled gas should be less than $1\%X_0$. The chambers are attached to the end-plate from the inside to minimise the dead area between adjacent chambers. Thus, a particular mounting technique is required to enable rotation and tilting of the chambers.

2. Field cage The cylindrical chamber's inner and outer composite walls hold the field and forming strips, which are attached to a resistor divider chain network. The resis-

tors must be non-magnetic. A central cathode will be held at approximately 50 kV when the drift field is 300 V/cm, with the end-plates and the other outer surfaces of the TPC at ground potential. Therefore the composite walls must self-stand the enormous potential of the central cathode. The narrow mirror strips will be arranged between the inner and outer walls to maintain the electron field uniform in over the whole active TPC volume.

3. End-plate To obtain high position resolution, every end-plate is subdivided into many independent MPGD detector modules (GEM or Resistive/no Micromegas detector, so on), which can provide nearly full coverage of the end-plate. Power cables, electronic connectors, cooling pipes, PCB boards and support brackets wall are also mounted on the end-plate. In case the detector modules are damaged by the discharge or spark, they can be replaced, and the end-plate should be kept stable during the replacement. Besides, the end-plate needs to constructed from a lightweight material, not only compromise the jet energy resolution in the forward region but also should be still sufficiently rigid to achieve stable positioning of the detector modules with a position accuracy better than 50 μm.The material budget of the mechanical structure accounts for $8\%X_0$. Additional materials for the readout planes, front-end electronics and cooling are estimated to be $7\%X_0$, and power cables and the connector up to $10\%X_0$.

The TPC could provide some physics information: Firstly, the function is 3-dimensional track reconstruction, by getting the XY information from the anode segmented in pads and the Z coordinate delivered by the drift time. To obtain the Z coordinate from the drift time, the drift field has to be very homogeneous. Because this coordinate is obtained via the drift velocity of the electron, it should have a moderate dependence on the drift field for a given gas mixture. Secondly, a parameter is the total momentum of a charged particle, by measuring the radius, ρ, of the electron trajectory to get the transverse momentum, and adding this information to the knowledge of the trajectory in the Z plane. The final function is the particle identification. The energy loss can be extracted by measuring the charge deposited on the readout pads. The energy loss combined with the measurement of momentum in the magnetic field provides then the particle identification.

3.3.2 Baseline design and technology challenges

3.3.2.1 Main parameters of the detector geometry

In TPC parameters, the geometry will be limited with an inner diameter, outer diameter, drift length, electric field, and the magnetic field. The transverse momentum resolution Δp_t of a tracking device - one of the basic figures of merit - is described by the Gluckstern formula

$$\frac{\Delta p_t}{p_t^2} \propto \frac{\sigma_{r\phi}}{BL^2}\sqrt{\frac{720}{n+4}} \tag{3.4}$$

where $\sigma r\phi$ denotes the spatial single-point resolution in the $r\phi$-plane, B is the magnetic field strength, L is the length over which the measuring points are distributed, and n is the number of single-point measurements that are used in the overall track fit.

From that formula [43], there is strong confidence that a TPC will be able to meet the performance goals of the CEPC tracker detector since it has corresponding advantages:

with a single-point resolution of $r\phi$=100μm, with a magnetic field of 3T, with an inner radius of 0.3m and an outer radius of 1.5-1.8m, and with approximately 200 pad rows.

The resolution of the TPC is limited by the diffusion of the drifting electrons. An upper bound on the diffusion is calculated using the standard Gluckstern parameterization, assuming a large number of measurements along the length of the track

$$D < \frac{\sigma_p t}{p_t}\sqrt{\frac{n_T L}{720}}(L[m]^2)\frac{0.3B[T]}{p_t[GeV/c]}\frac{1}{\sqrt{L_{drift}}} = 100\frac{\mu m}{\sqrt{cm}} \tag{3.5}$$

where the diffusion component of the momentum resolution (σ_{pt}/p_t) is required to be less than 10^{-4} at p_t=1GeV/c, n_T=30 ionization electrons per cm of gas (mainly argon) for a track measured over L=1.8m and for a drift distance of L_{drift}=2.0m in the magnetic field of 3.0T [44].

A large volume TPC with about 200 points per track provides continuous tracking for a large volume (several meters level). The TPC is optimised for superb three-dimensional point resolution and minimum material in the field cage and the end plate. It also provides particle identification capabilities based on the energy loss of particles per unit of distance (dE/dx). The geometry baseline should be considered the following reasons: Sensitive to the track segment as long as possible, stronger enough magnetic field for track bending and as good as possible and position resolution of the track measurement.

3.3.2.2 Modularization design

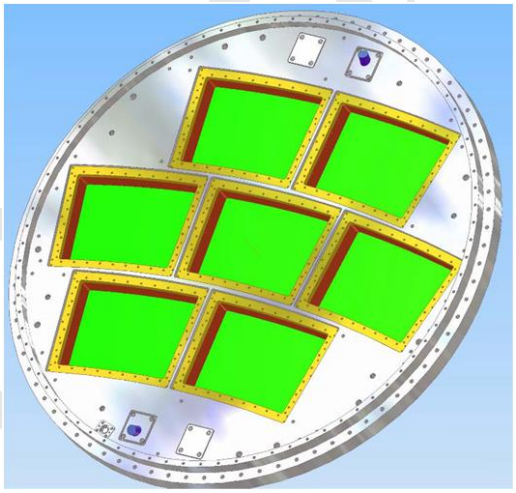

Figure 3.12: The diagram of large prototype module design.

In the large collider machine, the readout structure is designed to be modularised to change and maintain readily. Each module will consist of gas amplification system, readout pad plane and following electronics. High-density electronics make it possible to integrate the electronics directly on the back of the readout pad plane. The readout module will then have to provide all necessary high and low voltages and cooling for heat dissipation, notwithstanding, mainly because power-pulsing will not be available at the CEPC. To achieve the required performance, an MPGD-based gas amplification system will be developed. The charge from the amplification system will be collected on a pad board. Each module size will be about 160mm-180mm of width and 190mm-210mm of height.

The figure3.12 shows that the diagram of large prototype module design in LC-TPC international collaboration group $R\&D$.

To satisfy the physics performance basing on the modularisation design, tt has been demonstrated that any amplification technologies combined with pad readout can be built as modules which cover large areas with little dead space.

3.3.2.3 Gas amplification detector module

Typically gains of $10^3 - 10^4$ are achieved with many gases under standard conditions. Gas Electron Multipliers[45] and MICRO-Mesh device[46] of the (MPGDs) detectors[47] have been developed for the high energy physics experiments. For the detector modules, the electron gas amplification is obtained in very high fields generated by modest voltages (300-400V) across $50 - 100\mu m$ structures suitable for large-area applications. GAseous structure are two example of MPGDs.

This gas amplification detector module for a pad-based TPC will be either GEM, MicroMEGAS or others structure since single of them do not satisfy the ambitious performance purposes. Two or three GEMs are stacked together to achieve sufficient charge amplification resistive MicroMEGAS have enough amplification in a single structure.

Micro-pattern devices for TPC provide in the e^+e^- collider machine:

1. Higher rate capability: MPGDs provide a rate capability over $10^5 Hz/mm^2$ without the discharge to protect the electronics.
2. Intrinsic ion feedback suppression: The ions produced on these field lines do not go back to the drift volume and most of them will be neutralised on the mesh or GEM foil.
3. A direct electron signal, which gives a better time resolution($-100\mu m$).
4. A larger gain, by the specific operation high voltage.
5. Much smaller $E \times B$ effects than wires chamber for which the spacing of the wires is about a few mm.

3.3.2.4 Optimization readout pad size

Design of readout pad size is a vital parameter for the TPC detector module whether using GEM, MicroMEGAS or combination structure as the readout detector. Accurate position information requires to process the adjacent pad's signal with the Center-of-Gravity Method(CGM).

The design of the two-dimensional readout strips has been developed with the triple GEMs of $100mm^2$ in IHEP. The readout strips in the X direction are $193\mu m$ wide at $752\mu m$ intervals. There are pads with a size of 356 $\mu m \times 356\mu m$ connected with each other in the Y direction, and their strip pitch is $457\mu m$. The difference in strip widths is to improve signal sharing between X-axis and Y-axis strips, to ensure a homogeneous charge distribution between adjacent strips. The total number of strips in X and Y directions are 267 channels and 437 channels respectively. Each strip is connected to one electronic channel to process the signal.

In the figure3.13 of the typical profile of the electrons cluster in readout strips, the pink circle could be move to the blue circle and the profile is the Gaussian distribution. If there is a enough number pads to use Center-of-Gravity Method, the pad width should

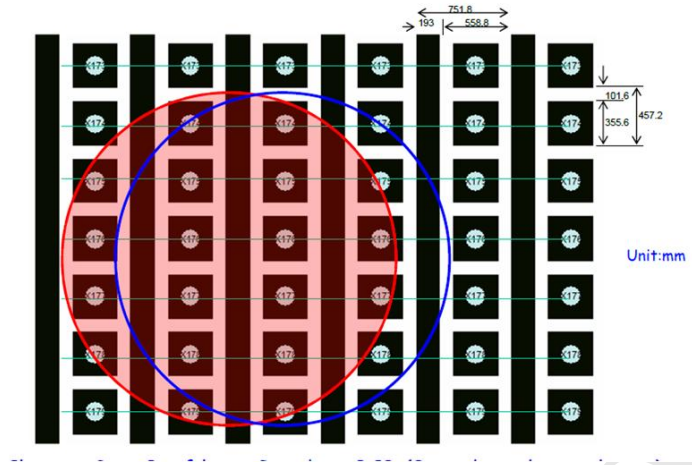

Figure 3.13: The profile of the electrons cluster in Triple GEMs.

be designed to 1.0mm and the length of pad should be designed to 6.0mm to obtain the sufficient charge information when the amplifier gain is 10mV/fC.

3.3.2.5 Operation gas for the long drift

As with any gaseous detector, the choice of the chamber gas strongly affects the properties and eventually the performance of a TPC. Desirable characteristics are:

1. Higher drift velocity (to avoid accumulation of too many events inside the chamber)
2. A very low transverse and a low longitudinal diffu0sion coefficient (to prevent deterioration of the spatial resolution)
3. A sufficiently large specific energy loss dE/dx
4. A high enough stability against electrical breakthroughs (to allow reliable operation of the amplification device)
5. Nonhazardous chemical properties (to address safety concerns like in-flammability and damages to the hardware)

The gas mixture should be chosen to minimize the capture of electrons by the molecules of electronegative impurities. Due to the long drift distance of the several meters(3.0m), and the fact that ions are more massive and much slower than electrons, ions can accumulate in the chamber. This effect can lead to electric field distortions and should be avoided. To decrease this effect, the structure of the readout chambers is generally designed to avoid ions from escaping into the gas volume. A gas with a large drift velocity is also chosen in experiments with large interaction rate.

In given the working gas and the electric field, the drift velocity of electron could be determined with Eq. 3.6

$$\mu_e = f(\frac{E}{P}) \tag{3.6}$$

where E denotes the electric field vector, P the gas pressure and μ_e the electron drift velocity. After reaching the maximum value of the drift velocity, the electron drift velocity depends slightly on the electric field. Fig. 3.14 shows that the drift velocity obtained in

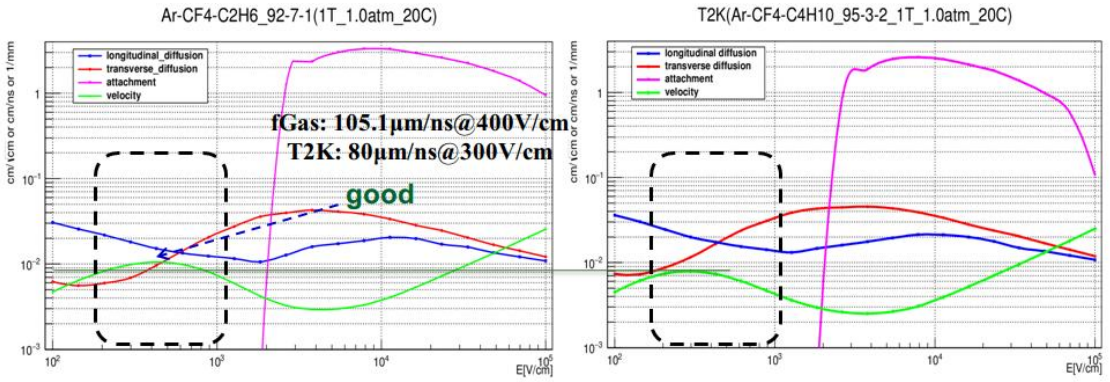

Figure 3.14: The drift velocity in different gas mixture.

different mixture gases. For the CEPC TPC detector, it is required to be sensitive to as long as possible track segment. The working gas should be selected in such way to achieve high velocity in low drift field to lower the high voltage in all of the drift length, and small transverse diffusion in the magnetic field to decrease the electron cluster size on the readout pads.

The gas mixture of Ar/CF_4/iC_4H_{10} (95%/3%/2%) have been used for the Large Prototype of TPC Detector for the ILD TPC and the TPC chamber for the T2K experiment. The saturated drift velocity of the mixed gas reaches approximately 8 cm/μs in a drift field of 300 V/cm. In addition, the gas has a large parameter of $\omega\tau$ (same as the Eq. 3.6) and transverse diffusion coefficient of 30 μm/$\sqrt{\text{cm}}$ in the drift field of 300 V/cm. In the B-field, a reasonable transverse diffusion coefficient could be realized at 100 V/cm of the drift field. The bunch spacing at the CEPC is ~ 3.6 μs(the preliminary example beam structure parameter). The working gas has a higher saturated drift velocity than the T2K mixed gas should be considered. Besides, the gas amplification requires to achieve approximately 6000 and the signal attenuation of the electron attachment should be kept below $1\%/m$.

3.3.2.6 Low power consumption electronics readout

Small readout pads of a few square millimeters (e.g. $1mm \times 6mm$)are needed to achieve high spatial and momentum resolution in TPC, demanding about 1 million channels of readout electronics per endcap. The total power consumption of the front-end electronics is limited by the cooling system to be several kilo-watts in practice, and they have to work continuously in CEPC. Hence the technique of so-called power pulsing cannot be applied. The architecture of the TPC readout electronics is shown in Fig.1, selected from a broad range of survey on current electronics installed or under development during past decades, including ALTRO/S-ALTRO and more recently SAMPA for ALICE,AFTER/GET for T2K and Timepix for ILC. It consists of the front-end electronics on the detector panel and the data acquisition system several meters away from the detector.

The waveform sampling front end is preferable, including a preamplifier and a shaper as the analog front-end (AFE), a waveform sampling ADC in 10MSPS, a dedicated digital signal processing (DSP) and zero-suppression unit and a de-randomize event buffer for each channel. To satisfy the stringent requirements on the integration and the power consumption, a front-end ASIC will be developed in advanced 65nm CMOS process. The key specifications of the front-end ASIC are summarized in Table as follow.

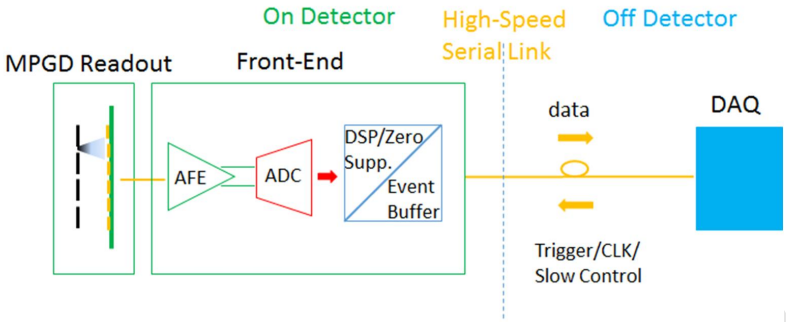

Figure 3.15: The architecture of the TPC readout electronics.

Total number of channels		1 million per endcap
APE	ENC	500e@10pF input cap
	Gain	$10mV/fC$
	Shaper	CR-RC
	Peaking time	100ns
ADC	Sampling rate	$\geq 20MSPS$
	Resolution	10 bit
Power consumption		$\leq 5mW$ per channel
Output data bandwidth		300MB-500MB
Channel number		32
Process		TSMC 65nm LP

Table 3.6: TPC readout electronics.

CMOS scales down in favor of digital circuits regarding power and density. The power consumption of the DSP circuits reported in $Ref.[3]$ was $4mW/ch$ in a 130nm process and could be reduced by a factor of at least two by migrating the same design to 65nm. However, this is not the equivalent of the analog circuits. The design strategy for the front-end ASIC is to keep the analog part as simple as possible. The block diagram of the analog front-end and the successive approximation (SAR) ADCare shown in Fig.2 and Fig.3 respectively. The CR-RC shaper and the SAR ADC instead of pipeline ADC will be used for their simplicity in analog circuits and hence the higher power efficiency, hence the development of the low power front-end ASIC is essential.

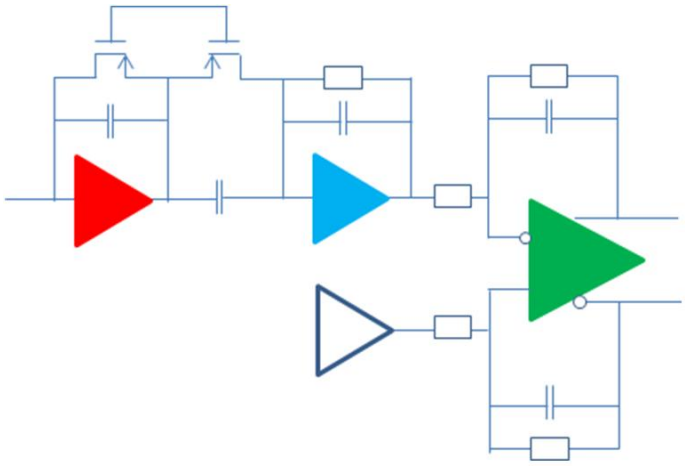

Figure 3.16: The block diagram of the analog front-end.

Dedicated digital filters will be applied to the continuously digitized input signals to suppress the pedestal perturbations caused by the non-ideal effects such as temperature variation and environmental disturbance. Then the data will be compressed by only storing the data packets above a programmable threshold with a specified number of pre- and post-samples. A data head will be added to each packet with its timestamp and other information for reconstruction afterward. The buffered data are readout through high-speed serial links to the DAQ system. The front-end electronics can support both external trigger and self-trigger mode.

Even with the state of the art technology, the TPC front-end electronics on the endplate needs cooling system to keep the temperature stable. Two-phase CO_2 cooling[7] is a well-developed technology and can be used as a baseline solution to bring out the heat generated by the front-end electronics and to keep the temperature of the TPC chamber stable at 20°C. Micro-channel CO_2 cooling has lower mass and may be studied further and can be an alternative technique to copper pipes [8].

The TPC readout electronics are meters away from the collision point, and the radiation dose is rather low ($< 1krad$) at CEPC, which allows us to use standard, radiation soft technologies. On the other hand, energetic particles can always produce instantaneous failure (SEU or SEL) from time to time. Hence radiation sophisticated design needs to be considered that the overall system performance will not be affected or even irreversibly damaged by the rare events.

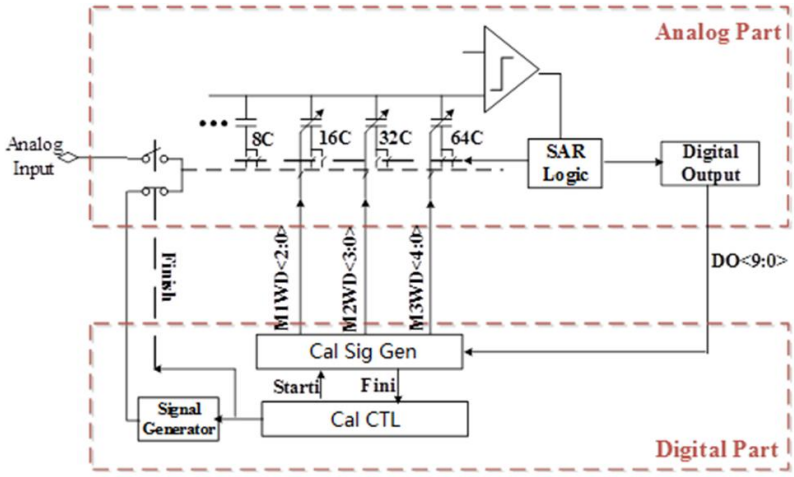

Figure 3.17: The block diagram of the SAR-ADC.

3.3.2.7 Critical technology challenges of TPC detector

The mechanical structure of the TPC consists of a field cage, which is made with advanced composite materials, and two readout end-plates that are self-contained including the gas amplification, readout electronics, supply voltage, and cooling. It will be challenging to design and manufacture the TPC support structure with a relatively light material, and at the same time very rigid. It is required to maintain accuracy, robustness in all directions, and stability over long time periods. As the field cage is not strong enough due to the limited material budget, the end-plates become the only choice, where the support structure connects to. In the current stage of design, how the TPC end-plate should be supported is not fixed yet. A promising solution is to suspend from the solenoid, in which a number of spokes run radically along the faces of the calorimeter to the TPC end-plates. A bearing is not the most challenging issue.

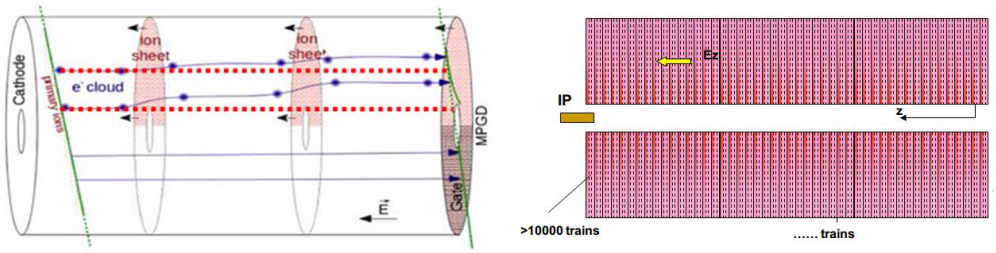

Figure 3.18: The diagram of distortion and ion disks in CEPC.

Gas amplification device creates not only secondary electrons but also the same amount of ions. These ions move in the opposite direction away from the anode region into the primary chamber volume - and furthermore have a much lower drift velocity, meaning that they could accumulate in the chamber gas and build up a significant space charge in the form of 'ion discs.' In CEPC, the majority of ions inside the drift volume are backflowing ions from the amplification region of the TPC readout devices. It is thus of

great importance to limit ion backflow (IBF) from the amplification region. This influence might affect the drifting electron tracks through electrostatic attraction as well as inhomogeneities of the drift velocity (which depends on the electric field strength). To minimize this deteriorating influence on the spatial resolution of the chamber, the backflow of ions should be suppressed.

One possible mechanism of backflow suppression frequently used together with a wire mesh device, is a so-called gating grid. The critical problem with this relatively simple yet effective scheme is that it cannot be immediately applied to the timing structure of the CEPC: the bunch spacing of the machine is so miniature ($3.6\mu s$ or less, compared to the readout time) that tracks from many events are drifting through the chamber. It indicates in the figure3.18 of the diagram of distortion and ion disks in CEPC. Another promising option is to exploit the 'built-in' ion backflow suppression of GEMs or MicroMEGAS. In next section, the $R\&D$ study of the hybrid detector module has been promoted to control ions continuously, and the updated results will be described.

3.3.3 Simulation and estimation for the key issues

3.3.3.1 Occupancy requirement of Higgs and Z pole run

The CEPC is a proposed electron positron collider after the Higgs discovery. It will be applied as a Higgs factory and Z factory. As a Higgs factory, it will be operated at $240GeV$ center of mass energy, produce 1 million Higgs bosons in 10 years and measure the Higgs couplings to 0.1% - 1% level accuracy[48]. It will also be operated at the Z pole and produce approximately 10 billion Z bosons each year. The typical cross-sections and event rates for nominal CEPC accelerator parameters are given(Higgs runs: $2 \times 10^{34} cm^2 s^{-1}$ of the instant luminosity and signal cross-section of $200fb$, Z pole runs: $2 \times 10^{34} cm^2 s^{-1}$ of the instant luminosity and signal cross-section of $300nb for Z \to q\overline{q}$).

Using an sample of 9 thousand fully simulated $Z \to q\overline{q}$ events at center of mass energy of 91.2 GeV[49], we studied the voxel occupancy and the local charge density of the CEPC TPC at Z pole operation for future circular electron positron colliders, with the value of an instant luminosity from $2 \times 10^{34} cm^2 s^{-1}$ to $2 \times 10^{36} cm^2 s^{-1}$.

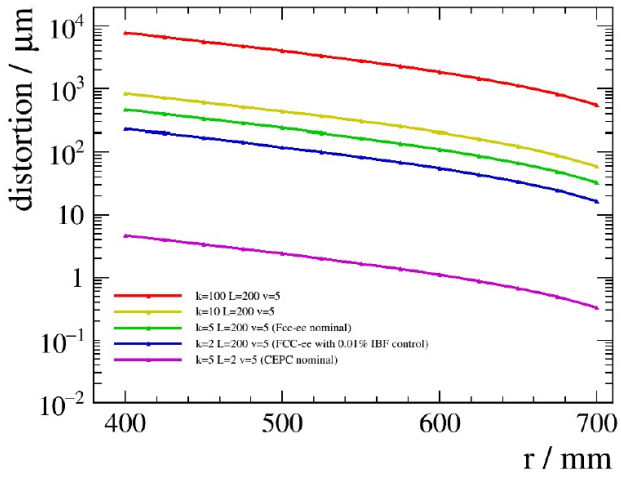

Figure 3.19: Distortion as a function of electron initial r position with different parameters.

Given the fact that the beam bunch is evenly distributed along the accelerator circumference, the voxel occupancy is extremely low ($1.4 \times 10^{-5}/1.4 \times 10^{-7}$ for the innermost layer and $3.4 \times 10^{-6}/3.4 \times 10^{-8}$ for average) and poses no pressure for the TPC usage. The distortion on TPC hit positions induced by the ion charges is estimated with dedicated program and calculation. At instant luminosity of 1×10^{36} and an ion backflow control of percent level, the distortion can be as significant as 10 mm at the innermost TPC layer at the CEPC conceptual detector geometry, which is two orders of magnitude larger than the intrinsic TPC spatial resolution.

A few approaches are proposed to reduce the effects caused by distortion:

1. Ion backflow control technology; the ion backflow should be controlled to per mille level, in other words, only $1 - 10$ backflow ions are allowed for each primary ionization.

2. Dedicated distortion correction algorithm, for the innermost layers, which should result in a mitigation of the hit position distortion by one order of magnitude.

3. Adequate track finding algorithm that could link the TPC track fragments to vertex tracks at high efficiency and purity.

Taking all of these approaches account, the distortion can be mitigated by approximately the safe factors of magnitude. To conclude, the pad occupancy and distortion stress no pressure to CEPC and if the above items can be achieved.

3.3.3.2 Distortion of Ions backflow in drift length

Early TPCs were equipped with multi-wire positional chambers (MWPCs) as gas amplification devices. The IBF ratio in a standard MWPC is $30 - 40\%$, so a gating grid is essential to prevent ions from reaching the drift volume. In the presence of a trigger, the gating grid switches to the open state to allow ionization electrons to travel into the gas amplification region. After a maximum drift time of about 100 μs (depending on the drift length, electric field and gas mixture), the gating grid is closed to prevent positive ions from drifting back into the drift volume. Since it must remain closed until the ions have been collected on the grid wires, the ionization electrons are also blocked during this time and the dead time consequently increases.

Triggered operation of a gating grid will, therefore, lead to loss of data. Thus, the TPC at the proposed circular collider will have to be operated continuously, and the backflow of ions must be minimized without the use of a gating grid.

The ions generated from the ionisation in the drift volume or from the avalanche multiplication and have found their way into the drift region will not only introduce field distortion, but also reduce the TPC counting rate capability. This effect is called ion backflow, and should be fully suppressed in the TPC drift volume. With an averaged 300 eV required by per ion-electron ionisation and 2 keV energy loss per mili-meter, there will be roughly $12,000$ primary electrons generated by a track with a typical length of 1.8 m in the TPC and there will be in total 240 k electrons in one event. With the electron drift velocity of 5 cm/μs, it takes ~ 40 μs for all the electrons to drift 2 m to reach the end-plate. With the expected bunch spacing of 3.6 μs at the CEPC, there will be about 11 events overlapping in the TPC volume. Therefore there will be 240k$\times 11/2 = 1.32$ M electrons continuously drifting toward the end-plate. On the other hand, ions drift much slower than electrons, with a velocity of only 500 cm/s in an electric field of 500 V/cm. This leads

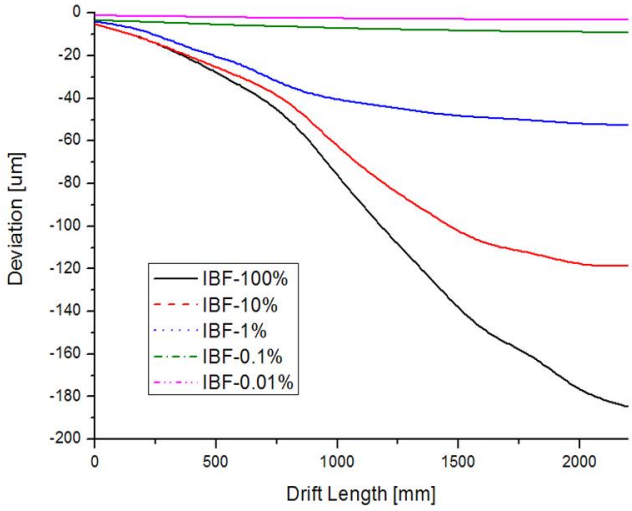

Figure 3.20: Evaluation of track distortions due to space charge effects of positive ions.

to ions from 110,000 events overlapping in the TPC volume. All of the ions should be reduce continuously.

3.3.4 Feasibility study of TPC detector module and future work

3.3.4.1 Hybrid structure TPC detector module

TPC readout with micro-pattern gaseous detectors (MPGDs), especially Gas Electron Multipliers (GEM)and micro-mesh gaseous structures (Micromegas), is very attractive, because the IBF of those detectors is intrinsically low, usually around a few percents. GEM detectors have been extensively proved in the last decade to be the prime candidate, as they offer excellent results for spatial resolution and low IBF. Numerous GEM foils can be cascaded, allowing multilayer GEM detectors to be operated at an overall gas gain above 10^4 in the presence of highly ionized particles. Micromegas is another kind of MPGD that is likely to be used as endcap detectors for the TPC readout. It is a parallel plate device, composed of a very thin metallic micromesh which separates the detector region into a drift and amplification volumes. The IBF of this detector is equal to the inverse of the field ratio between the amplification and the drift electric fields. Low IBF, therefore, favors high gain. However, the high gain will make it particularly vulnerable to sparking. The idea of combining GEM with Micromegas was first proposed with the goal of reducing the spark rate of Micromegas detectors. Pre-amplification using GEMs also extends the maximum achievable gain, so there have also been studies on gaseous photomultipliers with this hybrid configuration.

The TPC detector at the proposed circular collider will have to be operated continuously and the IBF of ions must be minimized without the open/close time of a gating device technology. The gain of the selection detector module can be achieved up to about 5000 without any obvious discharge behaviour. The currents on the anode and drift cathode were measured precisely with an electrometer. The experimental results showed that IBF can be reduced to -0.1% at the gain of about 5000.

To accomplish the physics purposes of the future circular collider, a TPC with superior performance is required. MPGDs with outstanding single-point accuracy and excellent

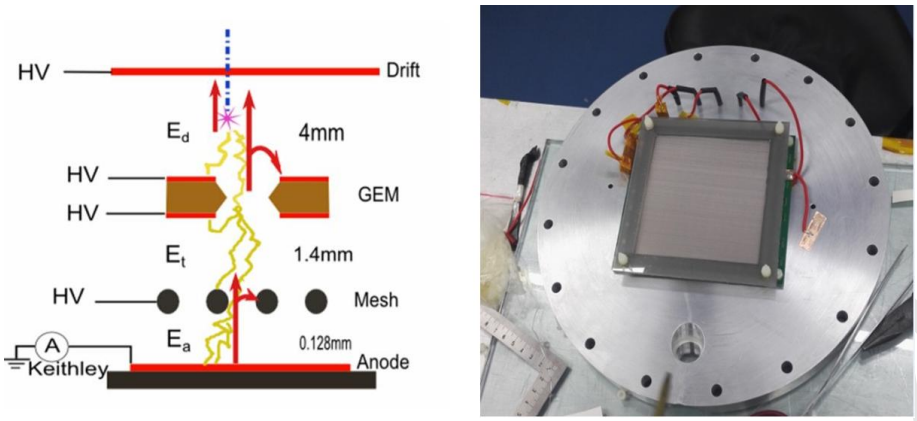

Figure 3.21: Schematic diagram of the detector module.

multi-track resolution are needed. We have proposed and investigated the performance of a novel configuration detector module: a combination of GEM and a Micromegas. The detector will be called GEM-MM for short throughout this paper. This study aims to suppress IBF continually by eliminating the gating grid. The design concept and some preliminary results of the detector module are described as following.

^{55}Fe X-ray source with a characteristic energy of 5.9 keV was used in the test. In the argon-based working gas mixture, a typically pulse height spectrum for a GEM or Micromegas detector contains one major peak corresponding to the 5.9 keV X-rays and an escape peak at lower pulse heights corresponds to the ionization energy of an electron from the argon K-shell.

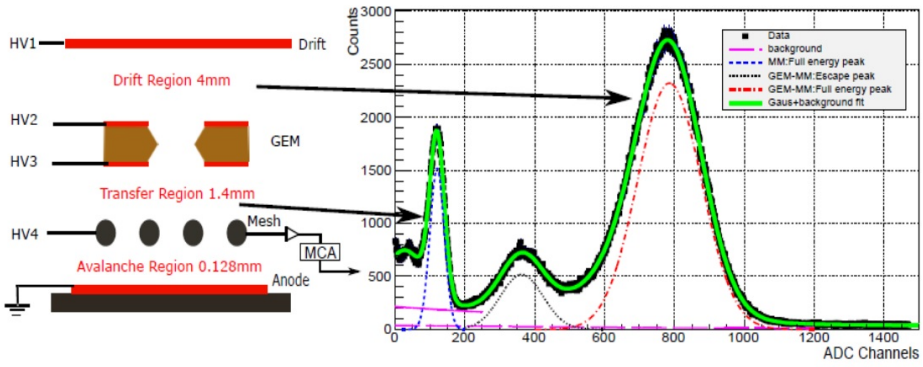

Figure 3.22: Result of the IBF TPC detector module.

In the GEM-MM detector, the situation is different. There are two amplification stages inside this detector. The primary ionization created by photon absorption can be in the drift region or in the transfer region (Figure3.22). Photoelectrons starting from the drift region get amplified by both the GEM detector and the Micromegas detector before they are collected on the anode. If the photons are absorbed in the transfer region, the primary electrons will be amplified only once (by Micromegas).

Figure3.22 depicts a typical ^{55}Fe pulse height spectrum obtained by the GEM-MM detector. Four peaks are seen in the pulse height spectrum. From left, the first peak and the

second peak are the escape peak and the full energy peak of the stand alone Micromegas. The last two peaks are created by photons with their energy deposited in the drift region. These primary electrons show combination amplification. The principle of the GEM-MM detector is fully verified.

Another issue should be considered that is the spacee charge effect to reduce the IBF value. To quantify the effect of IBF in terms of resulting space-charge distortions one can study the gas-dependent parameters as a function of the space-charge density. We make the experiment to confirm the IBF value according to the different X-ray's voltage and current.

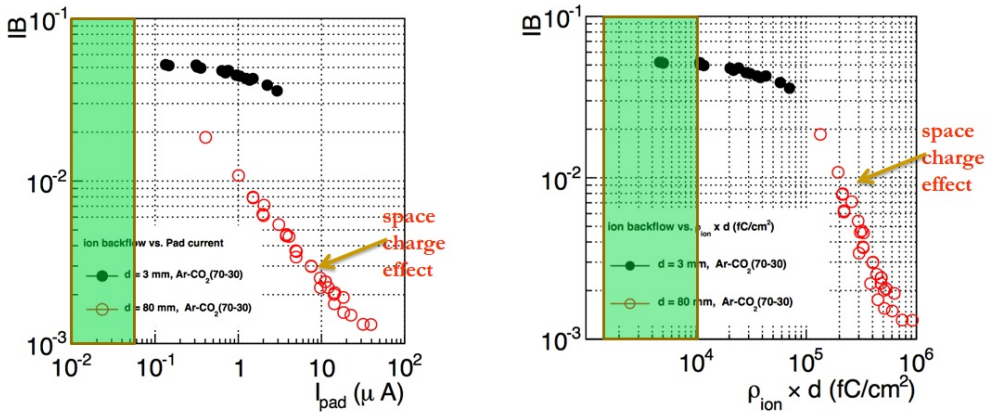

Figure 3.23: Comparison of the IBF with the different X-ray's voltage and current.

Our IBF results just obtained in the green rectangle area, there is no any obvious discharge or spark, and there is no high electrons to led the high space charge to reduce the value of IBF.

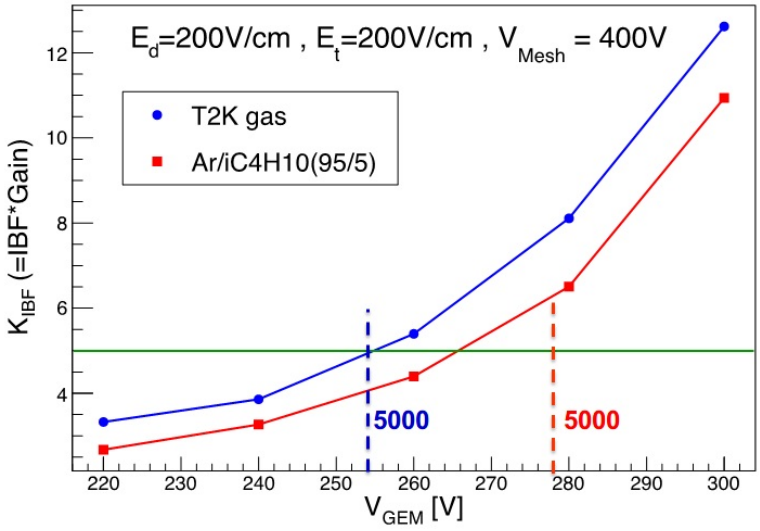

Figure 3.24: Result of the IBF TPC detector module.

A new concept in IBF reduction uses a hybrid structure with one GEM foil above a MicroMega detector. A prototype has been built, and tests have been carried out in Ar/CO_2

(90/10) gas mixture with a 55Fe X-ray source. The pre-amplification effect of GEM foil has been demonstrated in the energy spectrum measurement. With the novel hybrid structure, the effective gain of the GEM can be measured even when it is relatively low. The energy resolution of this hybrid structure gaseous detector is measured to be 27%(FWHM). The gain properties of this device were measured. A gain up to about 5000 can be achieved without any apparent discharge behavior. The currents on the anode and drift cathode were measured precisely with an electrometer. Out experimental measurements show that IBF can be reduced down to 0.19% at a gain of about 5000.

In 2018, the parameters of the electric field of drift, transfer, GEM detector and Micromegas detector have been optimized testing. The key factor of the gas gain times IBF obtained at the mixtures gases of T2K and Ar/iC_4H_{10} separately. The new results has been shown in the Figure3.24.

3.3.4.2 Laser calibration and alignment system

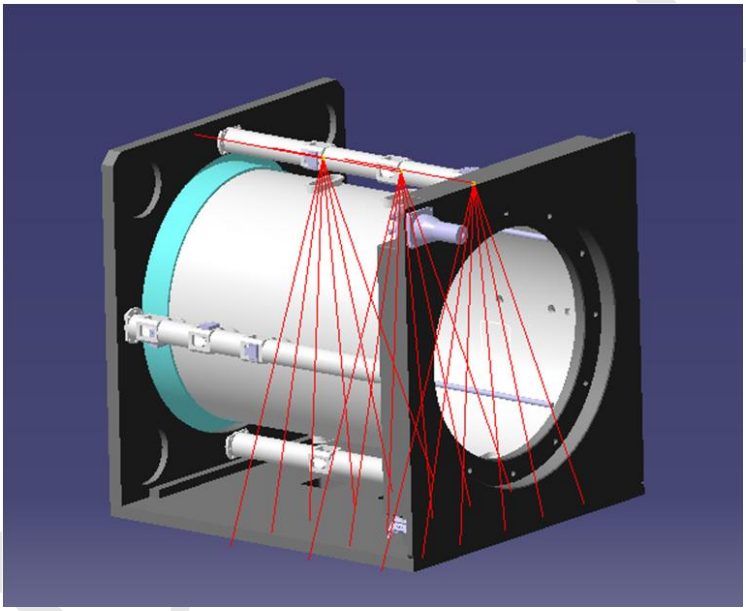

Figure 3.25: Schematic diagram of the detector module with the laser system.

The laser calibration system could be used for the TPC detector, the narrow laser beams inside the drift volume of the TPC simulate ionizing tracks at predefined locations. The goal is to obtain a uniformity of the TPC drift field within a reasonable relative error corresponding to a spacial resolution of $\sigma_{r\phi} = 100\mu m$. The system can be used for tests and calibration either outside or during normal data taking with the aim of understanding the chamber performance. Of particular interest is the testing of electronics, alignment of the read-out chambers, and measurements of variations of the drift velocity due to mechanical imperfections and non-uniformities in the gas, temperature and the electric and magnetic fields.

The laser system would be used for calibration and distortion measurement in the prototype with one module as a readout or large, A Nd:YAG laser with a wavelength of 266nm shall be used to study the track distortions. An additional UV-lamp could generate additional ions. The complete optical path and the laser power will be split into $6-7$ laser tracks. The laser map coupling into the chamber and the planned laser tracks

could be designed. The UV laser beam for calibration and alignment purposes to monitor the drift velocity, operation gas, gain uniformity and electric field. Nd:YAG laser device with 266nm wavelength could make the ionization in the gas volume along the laser path occurs via two-photon absorption by organic impurities. The laser power should reach $10J/mm^2$ to equal $10MIP$.

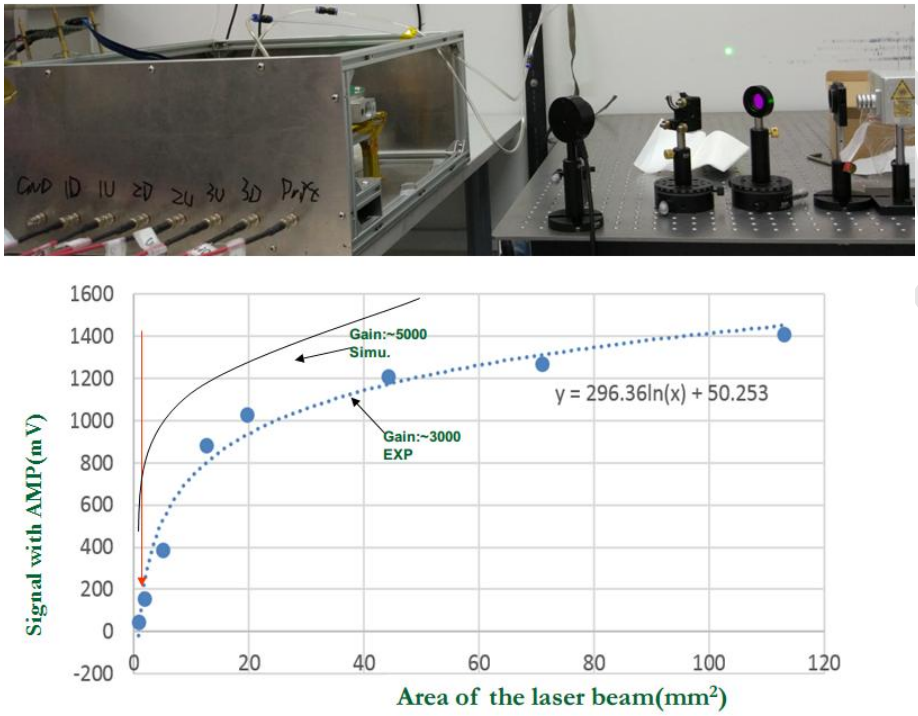

Figure 3.26: Signal with the different size of laser beam.

- Photoelectric laser source with UV light source: Enlights the cathode with UVs could produce photoelectrons to study and monitor distortions, the cathode with UVs to produce photoelectrons to study and monitor distortions, Deuterium lamp with $160nm - 400nm$ of the wavelength as UV light source and smooth Aluminum film as a cathode. To mimic the bunch structure and the ions distortion with UV light lamp by the specific time structure shine controller, UV could create more than about 10000 $electrons/s.mm^2$.

- Calibration laser beam size: The shine and entrance window could use the fused silica as of $99\%\ trans.@266nm$. Provides a UV laser beam for calibration and alignment purposes to monitor the drift velocity, operation gas, gain uniformity and electric field. The ionization in the gas volume along the laser path occurs via two-photon absorption by organic impurities. The study has been done using Nd:YAG laser device has the 266nm of wavelength(4.68eV). The optimization laser beam area of the laser device will be the range from $0.8mm^2$ to $1.0mm^2$ in the figure3.26.

To solve the critical technology problems in CEPC, the hybrid structure MPGD detector module has been developed, and some preliminary results have been obtained and analyzed, the further study will be done from this combination detector module. Another small TPC prototype with 266nm laser calibration system and UV photoelectric func-

tion has been designed and would be assembled, and the calibration experiment would be further studied for CEPC.

3.3.5 Conclusion

The TPC designed following the CEPC CDR concept provides an excellent starting point for the CEPC TPC R&D, but numerous modifications are foreseen due to the different performance requirements and experimental conditions. Several critical R&D issues have been identified in pre-studies. Possible solutions to those issues have been suggested and will have to be verified with a prototype TPC in future.

Aiming for the CDR and next steps of the CEPC project, two-phase funding scheme is proposed by the funding agency, the Ministry of Science and Technology (MOST) of China. To launch the project, the MOST funded the CEPC accelerator and detector R&D project for phase-I period of $2016 - 2021$. Among sub-detectors, the feasibility study of the TPC tracker detector was initiated for the purpose to identify feasible technology options and to gain expertise to build the detector units which meet the basic requirements of the CEPC detector design.

3.4 Full-silicon tracker detector

3.4.1 Introduction

The tracking system at CEPC are required to provide excellent tracking efficiency and precision over a wide range of momenta for charged particles from the interaction point as well as from the decay of secondary particles. The tracking system must be built with minimal material to preserve the momentum resolution and being covered hermetically down to the dip angle of $|cos\theta| < 0.992$ from the beam pipe.

The full-silicon tracker offers a well known technology that provides excellent space point resolution and granularity to cope track separation in dense jets and hits from the high luminosity beam related background, which is an ideal tracker running at the Z-pole. The drawbacks include the relative high materia density within the tracking system, less redundancy, and limited dE/dx measurements. The purpose of this study is to demonstrate that the full-silicon tracking concept is a viable option for CEPC under the same detector boundary conditions used by the CEPC baseline detectors as summaried in the following:

- the solenoid B field is set to 3 Tesla,
- the tracking envolope consists of a cylinder with a radius of 1.83 m and a length of 4.6 m,
- the tracker covers down to 7.25 degree from the beam pipe,
- the Be beam pipe has a radius of 1.45 cm and 14 cm long.

There are two detailed design options for ILC detectors [50, 51], the large TPC+Silicon detector (ILD) and the compact full-silicon detector (SID), with very different detector configurations to achieve the same performances. Given the fact that the ILD and SID detectors costs very similar with very different sizes, we did not try to change the detector boundary conditions such as, the B field, the track volume given by the CEPC baseline detectors in order to achieve the optimal performances. However, within these boundary

conditions, we have optimized the layout with the number of silicon layers, single vs double sized, and support materials using a toy simulation described below.

3.4.2 Full silicon tracker layout

The CEPC baseline detector relies on a mixture of Time Projection Chamber (TPC) and silicon tracking system. However, the tracker could be converted using full silicon if the TPC is replaced with additional silicon stereo-strip layers (SIT) in the central region with disks of silicon stereo-strip detectors (FTD) on each side. In this design, the outer tracking system consists of a full-silicon tracker arranged as a set of six nested SIT layers in the central region with five FTD strip endcap disks on each side as shown in Fig. 3.27. Details for design of SIT and FTD detectors can be found in the discussion of CEPC baseline design [**?**] and we will use the same module design to build a full silicon detector as CEPC-FST. The pixel vertex detector (VTX) is kept the same as in CEPC v_4.

This new proposed tracking system provides at least 11 precisely measured points for all tracks down to a polar angle of about 15 degree and at least 7 measured points down to a polar angle of about 7.25 degree, as shown in Fig. 3.28. With three double pixel layers and forward disks covering a wide of polar angle, they are capable of providing excellent tracking on their own. The outer tracker adds additional track-finding constrains at large radii where hit density is low while improving the momentum measurement over a large level arm with excellent hit resolution in the transverse plane.

Alternatively, we start with the design of ILC-SID detector for CEPC by enlarging the outer silicon strip layers to fulfil the space up to a radius of 1.83 m and z at $\pm$ 2.3 m in order to achieve comparable momentum resolution using a lower solenoid B filed of 3 Tesla as shown in Fig 3.27. The pixel detectors again are kept the same as in the ILC-SID design. We will label this option as CEPC-FST2, which provides an independent cross check on the tracking performance for a full-silicon tracker. The number of expected hits on the track from CEPC-FST2 is also shown in Fig. 3.28.

Table 3.7 summarizes the geometry parameters of the proposed outer strip silicon trackers for CEPC between two full silicon options.

3.4.3 Toy simulation

For each layout, we use a toy simulation (Idres) to calculate the expected tracking resolution as function of track momentum for a given incident angle θ, in which the effect of multiple scattering due to the materia are taken into account correctly. Idres was developed by the ATLAS experiment [52]. The results are also cross checked using LDT program [53], which gives a consistent result.

The coverage of the full-silicon tracking system is shown in Fig. 3.28 as function of track pesudo-rapidity. At least 7 hits are measured for all tracks with a polar angle down to about 7.25 degree. The total radiation length for all-silicon tracking systems, including dead material such as readout, cables and supports, is about 5-7% for CEPC-FST and 7-10% for CEPC-FST2, respectively.

The expected momentum (p_T) and impact parameters (d0, and z0) resolutions are compared as function of track p_T in GeV/c for tracks with $\theta = 85$ and 20 degree, respectively, as shown in Fig. 3.29. The z0 resolution is better for CEPC-FST than for CEPC-FST2 due to extra stereo-strip layers while the p_T and d0 resolutions are similar.

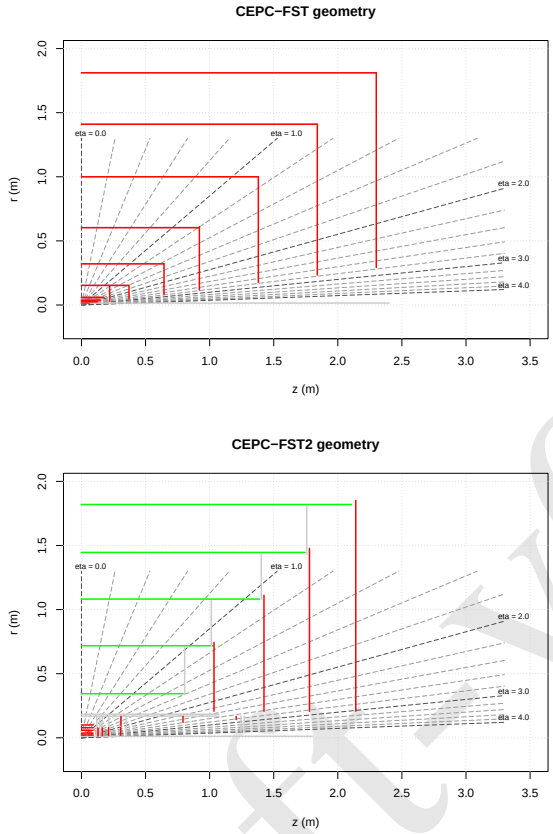

Figure 3.27: The R-Z view of the full silicon tracker proposed for CEPC-FST (left) and CEPC-FST2(right).

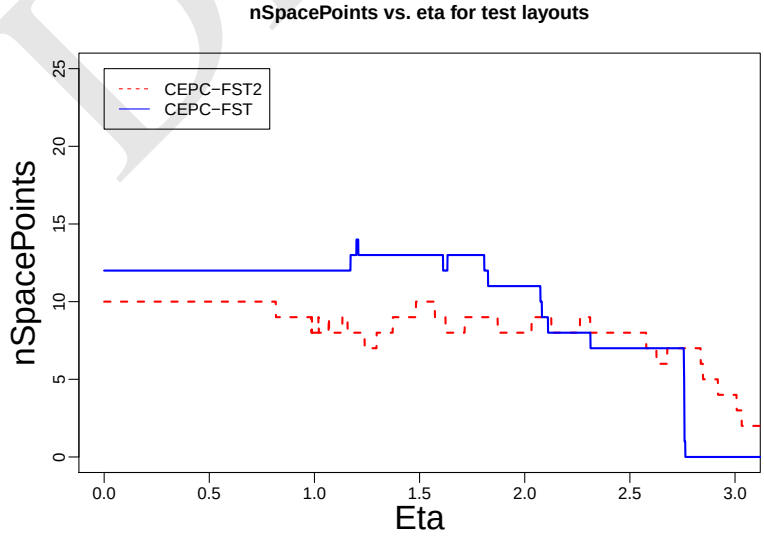

Figure 3.28: The number of expected hits are shown as function of track pesuro-rapadity.

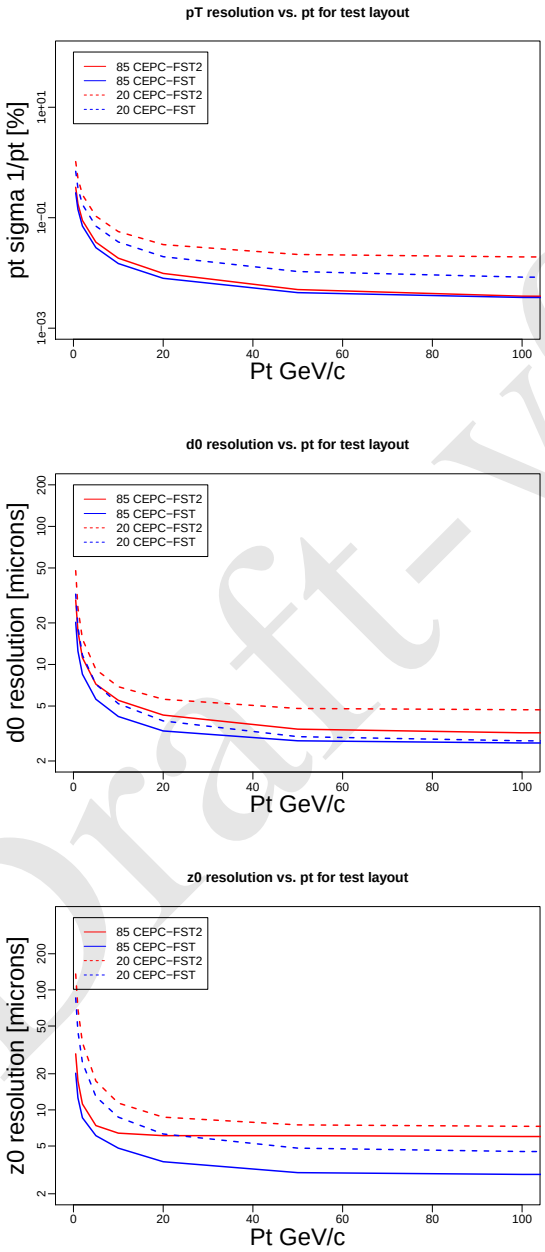

Figure 3.29: The expected p_T, d0, and z0 resolutions from the toy simulation (Idres) are compared as function of track p_T in GeV/c for tracks with $\theta = 85$ and 20 degree, respectively.

Table 3.7: The proposed geometry parameters for the outer strip barrel layers and disks, where D and S stand for double and single-strip layer.

	CEPC-FST				CEPC-FST2			
Barrel	R (m)		±z (m)	Type	R (m)		±z (m)	Type
layer 0	0.153		0.368	D	0.344		0.793	S
layer 1	0.321		0.644	D	0.718		1.029	S
layer 2	0.603		0.920	D	1.082		1.391	S
layer 3	1.000		1.380	D	1.446		1.746	S
layer 4	1.410		1.840	D	1.820		2.107	S
layer 5	1.811		2.300	D				
Endcap	R_{in} (m)	R_{out} (m)	±z (m)	Type	R_{in} (m)	R_{out} (m)	±z (m)	Type
Disk 0	0.082	0.321	0.644	D	0.207	0.744	1.034	D
Disk 1	0.117	0.610	0.920	D	0.207	1.111	1.424	D
Disk 2	0.176	1.000	1.380	D	0.207	1.477	1.779	D
Disk 3	0.234	1.410	1.840	D	0.207	1.852	2.140	D
Disk 4	0.293	1.811	2.300	D				

3.4.4 Detector simulation and reconstruction

In order to optimize the full silicon tracker detector for CEPC, we generate several benchmark processes that include single muon events, $e^+e^- \to ZH \to \nu\nu\mu\mu$, and $e^+e^- \to ZH \to \nu\nu GG$ (two gluon jets). The events are then simulated and reconstructed using different detector geometries, which are then used for the tracking performance studies.

3.4.4.1 CEPC-FST detector

The implement of geometry for the CEPC-FST detector is based on a simulation tool Mokka[54]. The CEPC baseline detector is based on a version of database cepc_v4 [**?**], in which the tracker is composed of VXD, SIT, TPC, SET and FTD. In order to implement a full-silicon-tracker, the TPC and SET are considered to be replaced with a new silicon-based strip tracker based on the design of SIT layers and disks while keeping the rest of detectors same as in cepc_v4.

In order to improve the flexibility of design, a new package of SiTracker is implemented in Mokka which represents the silicon tracker by planar structure, which consists of a thin layer of silicon with 150 μm thickness and 50 μm pitch size. For VXD and SIT, they are composed by several layers, and each layer is composed by several ladders, and each ladder is divided to several sensors. The SIT layer consist of double silicon layers mounted back to back with a stereo-angle of 7 degree. For FTD, it is composed by several pixel disks FTD_PIXEL and several double-side strip disks FTD_STRIP that are composed by petals. The strip FTD disk has two sensitive silicon sub-layers on each side with a stereo-angle of 5 degree. The number of ladders/petals, the size and position of layers, and the

sub-structure of layers can be modified easily in input file as globalModelParameter. In future, a XML structure is considered as the method to input parameters.

The lcio format is used to output the simulated signals from the full-silicon-tracker, same as other sub-detector system [55]. The digitization and clustering are done in reconstruction process. In the default version, a smearing technology based on truth information is used as a simple digitization and clustering, which is used for this study. Recently, a new digitization for silicon-based detector has been developed. It first finds out the pixel which the hit is located, and uses the center of the pixel or strip as the new position for the hit. And then those hits in same pixel or neighnoring will be merged into single hit.

A new conformal tracking algorithm has been adapted for the full silicon tracker, which is developed as the main track pattern recognition algorithm at CLIC [55] at FCC-ee. Through the conformal transform $u = \frac{x}{x^2+y^2}$ and $v = \frac{y}{x^2+y^2}$, where x and y are the positions of the track hits in the detector space, the positions of the track hits in the conformal space lie at a straight line for the track in a magnetic field. Therefor, track finding becomes straight line searching in the pattern recognition. Currently, a cellular automaton is used as pattern recognition for the straight line searching.

3.4.4.2 CEPC-FST2 detector

For CEPC-FST2, events were simulated and reconstructed using a software developed for the International Linear Collider (ILC) [50, 51], but re-worked for the HepSim project [56, 57]. The response of the CEPC-FST2 detector to physics events is simulated using the "Simulator for the Linear Collider" (SLIC) 5.0 software [58] interfaced with the GEANT4 10.3p1 program [59]. The track reconstruction was performed with the LCSIM 4.0 package [55] using the "seed tracker" algorithm as for the SiD detector simulation. Track candidates with at least six hits in the silicon pixel and microstrip layers were considered. Only tracks with a minimum transverse momentum (p_T) of 100 MeV were accepted. The track-fitting was performed with the following requirements; maximum distance of closest approach (DCA) is $|DCA| < 6$ mm, $|z_0| < 10$ mm, and fit $\chi^2 < 10$. The reconstruction includes particle-flow algorithms (PFA) which enable identification and reconstruction of individual particles. The PFA objects can be reconstructed using the software algorithms implemented in the PANDORA package [60, 61].

The geometry of CEPC-FST2 detector is implemented using the compact XML geometry description, which can load and built at runtime. The main changes over the ILC-SID detector include the reduced B-field from 5 Tesla to 3 Tesla. The outer tracker is scaled up by a factor of about 1.44 to the radius of 1.83 m and z of $\pm$ 2.3 m. The silicon module sizes were appropriately scaled. The first inner layer of the barrel vertex detector was positioned at 15 mm, just outside of the beam pipe. The outer barrel layer of the silicon vertex detector was moved to 100.3 mm (vs 59 mm for the SiD detector), while other barrel layers are equally spaced. The forward disks, together with the support structures, were appropriately scaled in z by a factor 1.37.

As for the SiD detector, the barrel tracker consists of five layers of silicon sensors with 50 μm pitch. The forward tracker has four disks of silicon sensors. The silicon pixel detector had 20 μm pitch, consisting of five layers in the barrel and six disks in the forward region. The hadronic and electromagnetic calorimeters, as well as the muon detector, were optimized for CEPC physics as described in [62].

3.4.5 Tracking performance

After the detector simulation and reconstruction, the tracking performances are measured in terms of efficiencies, fake rates, momentum resolution, and the impact parameter resolutions using single muons or $e^+e^- \rightarrow ZH$ events. The tracking efficiency is defined as a fraction of stable charged particles that can be matched to well reconstructed tracks. The stable particles are defined as those charged particles with p_T >1 GeV/c in the detector fiducial region ($9 < \theta < 170$ degree), originated from the interaction point, and lived long enough to reach the calorimeter. A well reconstructed track is defined as sharing more than 50% of its assigned silicon hits originating from a single particle (truth hits). We define a truth hit fraction as ratio of truth hits over total assigned hits of the track using silicon hits only. A poorly reconstructed track is defined to have the truth hit fraction less than 50%. The fake rate is defined as the fraction of poorly reconstructed tracks out of total reconstructed tracks, but this requires a realistic detector simulation, which we are not there yet. Since the CEPC baseline and the CEPC-FST detectors are sharing the common software and design, we will focus on their tracking performance comparisons to demonstrate that the full-silicon tracking concept is a viable option for CEPC.

3.4.5.1 Single muon particle

Figure 3.30 shows the tracking efficiency for single muons in CEPC-FST as function of p_T. The tracking efficiency is close to 100% at high p_T and slightly lower at small p_T. The trend is the same for CEPC baseline (v_4) , which indicate both trackers are capable of finding tracks efficiently in the detector fiducial region.

The number of silicon hits found on the track are shown in Fig. 3.31 where the hit purity is reached close to 100% for both detectors.

Since the track resolution depends on the track angle θ, we divide the tracks in the barrel region with $40 < \theta < 140$ degree and in the endcap region with $7.25 < \theta < 40$ degree or $140 < \theta < 172.75$ degree. Figure 3.32 shows the track resolutions of p_T, d0, and z0 as function of track p_T in the barrel and endcap region. The resolutions seem comparable to each other, but they seem slightly better for the low momentum tracks in the CEPC v_4 detector (TPC+Silicon) than CEPC-FST due to extra materia in the detector while they are compatible at the high p_T.

3.4.5.2 Di-muon mass resolution

Figure 3.33 shows the di-muon invariant mass distributions from $ZH \rightarrow \nu\nu\mu\mu$ decay between different detector configurations. The higgs mass used in the simulation is 125 GeV/c^2. The di-mass from CEPC baseline detector seems shifted by 0.2 GeV from the input Higgs mass while the mass from CEPC-FST agrees with the expectation. The di-muon mass resolution from CEPC-FST has $\sigma = 0.21$ GeV/c^2 and seems 14% better than ones obtained from CEPC baseline detector.

3.4.5.3 Tracking inside the jets

In order to study the tracking performance inside the jets, we generated and simulated some Higgs decaying into two gluon jets (GG) in $zH \rightarrow \nu\nu GG$ events. Figure 3.34 shows the tracking efficiency inside the jets as function of track momentum. The efficiency of finding tracks inside the jets is very similar between the CEPC baseline and the CEPC-FST detectors, which is close to 97%.

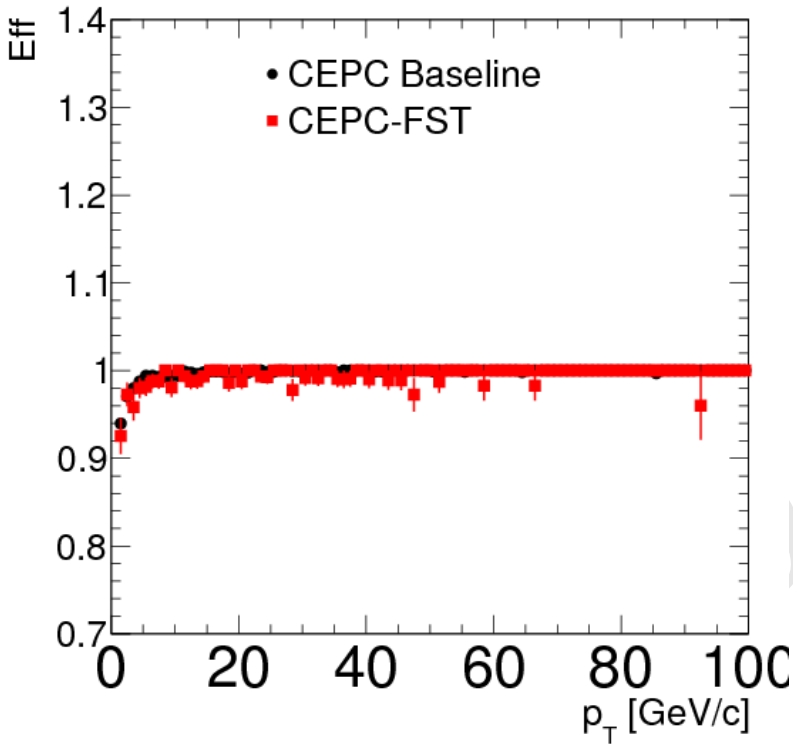

Figure 3.30: The tracking efficiencies are measured as function of p_T for single muons using CEPC baseline (v_4) and CEPC-FST detetcors.

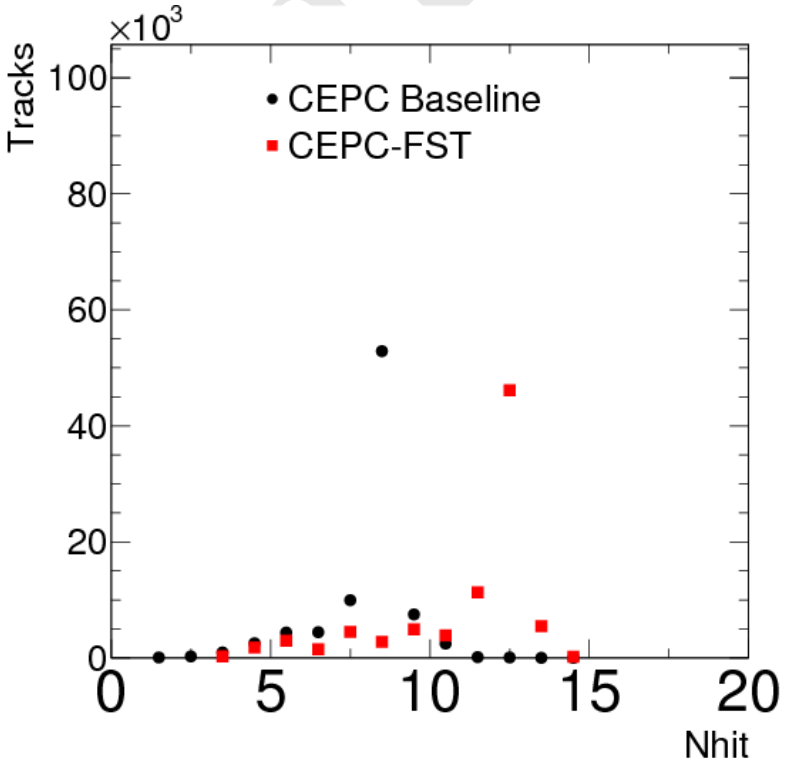

Figure 3.31: The distributions are shown for the number of silicon hits on the track.

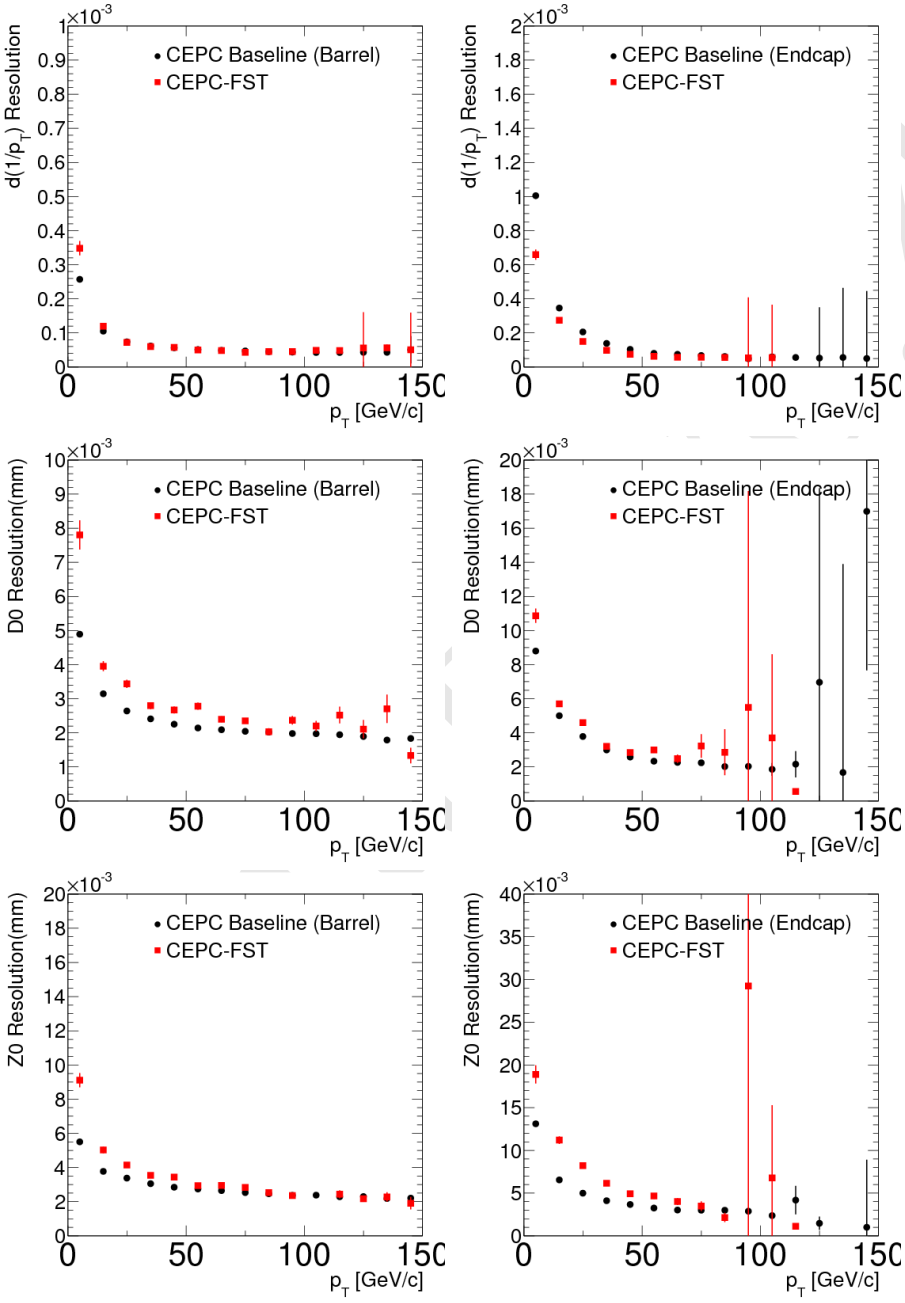

Figure 3.32: The tracking p_T, d0, and z0 resolutions are measured as function of p_T, ϕ, and θ using single muons, left in the barrel region and right in the endcap region. They are compared between CEPC v_4 and CEPC-FST detectors.

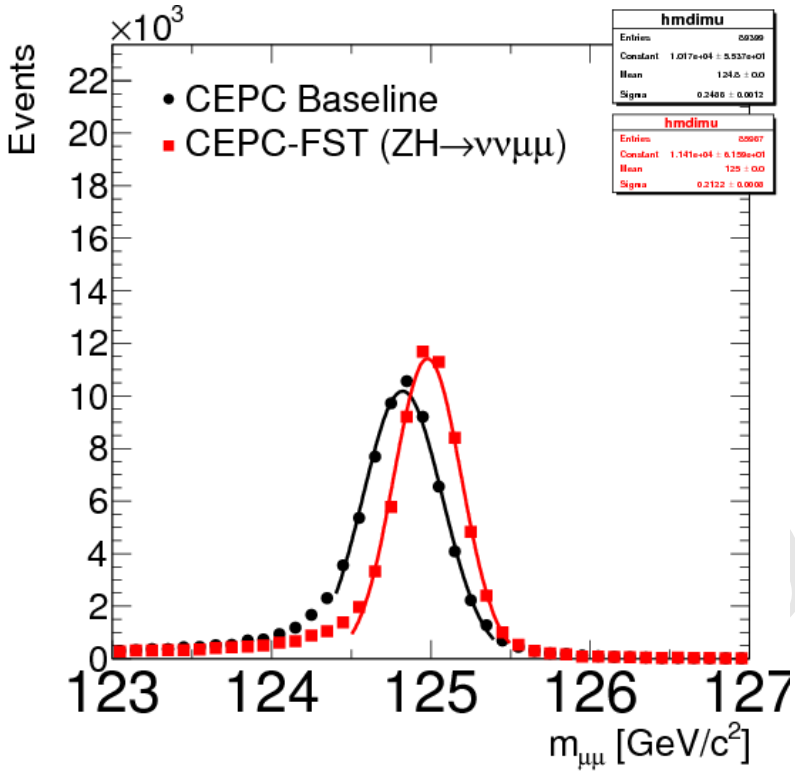

Figure 3.33: The di-muon mass distribution is compared from CEPC baseline and CEPC-FST detectors.

3.4.6 Conclusion

We present a preliminary study of full silicon tracker option as an alternative design for CEPC tracker. Two approaches are considered for the design: the first is to keep the silicon detectors (VXD, SIT, FTD) in the CEPC baseline detector and replacing TPC with additional silicon detectors, the second is to optimize the ILC-SID tracker to fulfil the CEPC tracking volume in order to achive the excellent momentum resolution using 3 Tesla B field. The new detector geometry has been implemented in the simulation and the track reconstruction has also been adoped for the full silicon tracker. The initial study of the tracking performance looks promising. There are still many improvements needed in the simulation and reconstruction in order to explore the full potential of the full-silicon tracker.

3.5 Drift chamber tracker detector

3.5.1 Introduction

The drift chamber (DCH) is designed to provide good tracking, high precision momentum measurement and excellent particle identification by cluster counting.

Main peculiarity of this drift chamber is its high transparency, in terms of radiation lengths, obtained thanks to the novel approach adopted for the wiring and assembly procedures. The total amount of material in radial direction, towards the barrel calorimeter, is of the order of $1.6\%\ X_0$, whereas, in the forward and backward directions, this is equiv-

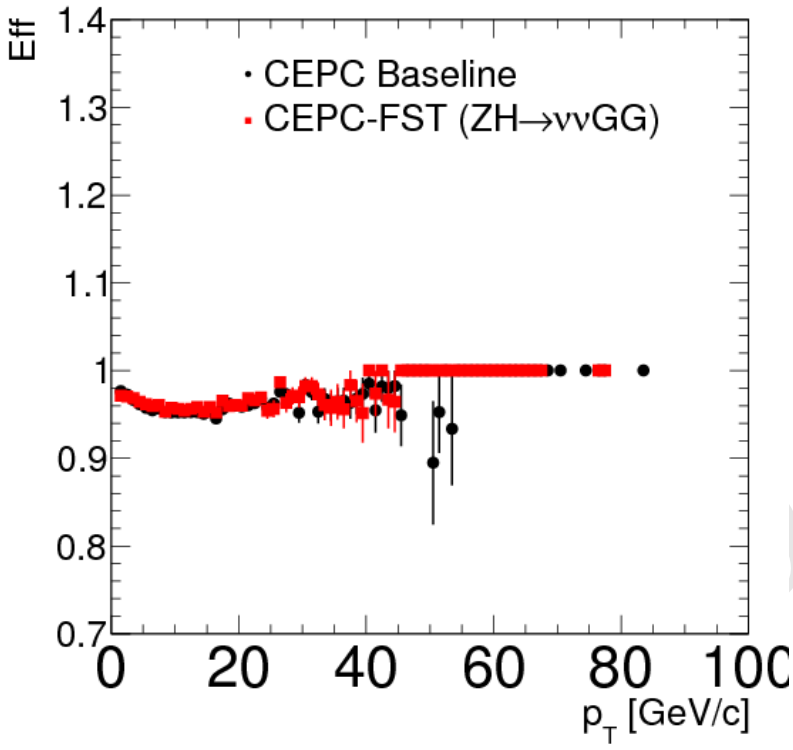

Figure 3.34: The tracking efficiencies for the stable particles inside the gluon jets as function of track p_T with CEPC v_4 and CEPCSID.

alent to about $5.0\%\ X_0$, including the endplates instrumented with front end electronics. The high transparency is particularly relevant for precision electroweak physics at the Z pole and for flavour physics, where the average charged particles momenta are in a range over which the multiple scattering contribution to the momentum measurement is significant.

Original ancestor of the DCH design is the drift chamber of the KLOE experiment[63], more recently culminated in the realisation of the MEG2[64] drift chamber.

3.5.2 Overview

The DCH is a unique volume, high granularity, all stereo, low mass cylindrical drift chamber, co-axial to the 2 T solenoid field. It extends from an inner radius R_{in} = 0.35 m to an outer radius R_{out} = 2 m, for a length L = 4 m and consists of 112 co-axial layers, at alternating sign stereo angles (in the range from $50\,mrad$ to $250\,mrad$), arranged in 24 identical azimuthal sectors. The square cell size (5 field wires per sense wire) varies between 12.0 and 14.5 mm for a total of 56,448 drift cells. Thanks to the peculiar design of the wiring procedures, successfully applied to the recent construction of the MEG2 drift chamber, such a large number of wires poses no particular concern.

A system of tie-rods directs the wire tension stress to the outer endplate rim, where a cylindrical carbon fibre support structure bearing the total load is attached. Two thin carbon fibre domes, suitably shaped to minimise the stress on the inner cylinder and free to deform under the gas pressure without affecting the wire tension, enclose the gas volume.

The angular coverage, for infinite momentum tracks originated at the interaction point and efficiently reconstructed in space, extends down to approximately $13°$.

In order to facilitate track finding, the sense wires are read out from both ends to allow for charge division and time propagation difference measurements.

The chamber is operated with a very light gas mixture, $90\%He - 10\%iC_4H_{10}$, corresponding to about $400\,ns$ maximum drift time for the largest cell size. The number of ionisation clusters generated by a $m.i.p.$ in this gas mixture is about $12.5\,cm^{-1}$, allowing for the exploitation of the cluster counting/timing techniques for improving both spatial resolution ($\sigma_x < 100\,\mu m$) and particle identification ($\sigma(dN_{cluster}/dx)/(dN_{cluster}/dx) \approx 2\%$).

3.5.3 Expected performance

Figure 3.35 indicates a $100\,\mu m$ drift distance resolution, averaged over all drift times, measured in a MEG2 drift chamber prototype[65] ($7\,mm$ cell size), with very similar electrostatic configuration and gas mixture. A better resolution is expected for DCH, because of the longer drift distances. Cluster timing technique may further improve it. Analytical calculations for the expected transverse momentum and angular resolutions are plotted in Figure 3.36.

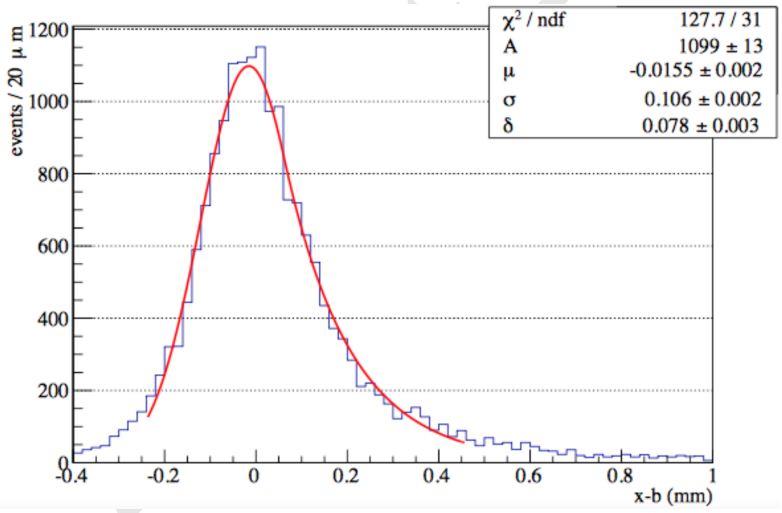

Figure 3.35: Measured drift distance residue distribution in the MEG2 drift chamber prototype under cosmic rays, indicating a resolution of less than 110μm, averaged over all drift times and in a wide range of track angles. $85\%\,He - 15\%\,iC_4H_{10}$ gas mixture.

Based on the assumption that one can, in principle, reach a relative resolution on the measurement of the number of primary ionisation clusters, N_{cl}, equal to $1/\sqrt{N_{cl}}$, the expected performance relative to particle separation in number of units of standard deviations is presented in Figure 3.37 as a function of the particle momentum. Solid curves refer to cluster counting technique applied to a $2\,m$ track length with 80% cluster identification efficiency and negligible (a few percent) fake clusters contamination. Dashed curves refer to the best theoretical prediction attainable with the dE/dx technique for the same track length and same number of samples. For the whole range of momenta, particle separation with cluster counting outperforms dE/dx technique by more than a factor of

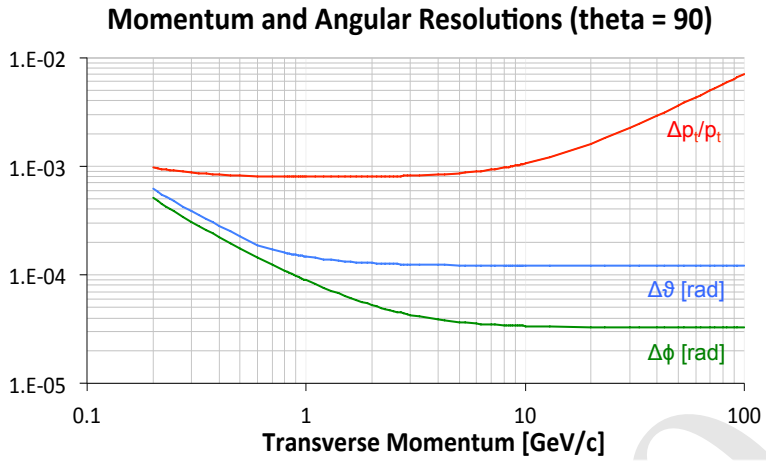

Figure 3.36: Momenta and angular resolutions as a function of the particle momentum for $\theta = 90°$ (left) and of the polar angle for $p = 10\,GeV/c$ (right)

two, estimating an expected pion/kaon separation better than three standard deviations for all momenta below $850\,MeV/c$ and slightly above $1.0\,GeV/c$.

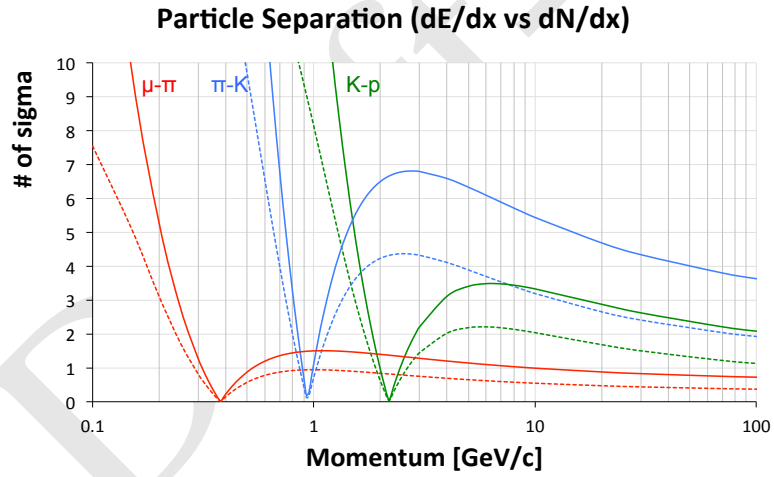

Figure 3.37: Particle type separation in units of standard deviations, with cluster counting (solid lines) and with dE/dx (broken lines) as a function of the particle momentum. A cluster counting efficiency of 80% and a dE/dx resolution of 4.2% have been assumed.

3.5.4 Tracking system simulation results

For the purpose of optimising the track reconstruction performance, a vertex detector (different from the baseline choice) made of seven cylindrical layers, inside the drift chamber inner radius, and of five forward disks, has been simulated together with a layer of silicon microstrip detectors surrounding the drift chamber both in the barrel and in the forward regions, followed by a pre-shower detector system within a homogeneous $2\,T$ longitudinal magnetic field. Details of ionisation clustering for cluster counting/timing analysis have not been included in the simulations, limiting the drift chamber performance both in spatial resolution (a $100\,\mu m$ gaussian smeared point resolution has been assumed) and in

particle separation (no dN_{cl}/dx analysis has been simulated). A simplified track finding algorithm at its preliminary stage of development has been used to feed the space points to the GenFit2 interface for the ultimate track fit. Figure 3.38 shows the momentum, angle and impact parameter resolutions obtained by the tracking system simulation. No optimisation has been tried yet. Momentum resolutions $\Delta p/p = 4 \times 10^{-3}$ at $p = 100\,GeV/c$, for $\theta = 65°$, and angular resolutions $\leq 0.1\,mrad$ for $p \geq 10\,GeV/c$, are within reach. Lastly, a fit to the bottom right plot in Figure 3.38 gives a d_0 impact parameter resolution:

$$\sigma_{d_0} = a \oplus \frac{b}{p \sin^{3/2}\theta}$$

with $a = 3\mu m$ and $b = 15\mu m \cdot GeV/c$.

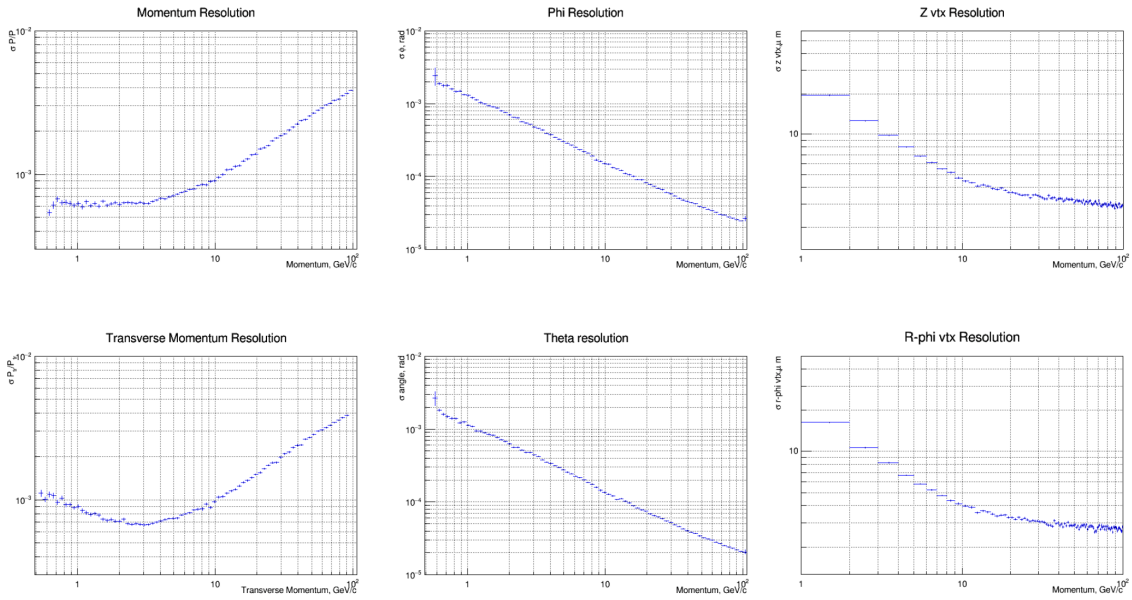

Figure 3.38: Momentum resolutions (top and bottom left), angle resolutions (top and bottom center) and impact parameter resolutions (top and bottom right) from simulation of isolated tracks.

3.5.5 Backgrounds in the tracking system

Of the main sources of backgrounds in the tracking system: incoherent pair production (IPC), synchrotron radiation and $\gamma\gamma$ to hadrons, IPC is the dominant one. However, only very few of the primary $e^{\pm}$ particles will have a transverse momentum large enough to reach the inner radius of the drift chamber and the majority of the hits will be generated by secondary particles (mainly photons of energy below 1 MeV) produced by scattering off the material at low radii. Based on experience from the very similar MEG2 drift chamber, which has a smaller number of hits per track and a much more complicated event topology, occupancies of up to several percent will not affect tracking efficiency and single track momentum resolution. The level of occupancy here is expected to be even smaller with the use of the drift chamber timing measurement. As opposed to charged particles, indeed, that leave a string of ionisation in the drift cells they traverse, photons are characterised by a localised energy deposition. Signals from photons can therefore be

effectively suppressed at the data acquisition level by requiring that a threshold be reached by the number of ionisation clusters within a reasonable time window. In addition, charge strings with holes longer than the average cluster separation can be interpreted as due to separate signals, thus avoiding pilling up of any remaining photon induced background. With this effective suppression of photon induced signals, the background from IPC is expected to remain low and is unlikely to cause adverse issues for the track reconstruction.

3.5.6 Constraints on the readout system

With a drift chamber, all digitised hits generated at the occurrence of a trigger are usually transferred to data storage. The IDEA drift chamber transfers 2 B/ns from both ends of all wires hit, over a maximum drift time of 400 ns. With 20 tracks/event and 130 cells hit for each track, the size of a hadronic Z decay in the DCH is therefore about 4 MB, corresponding to a bandwidth of 40 GB/s at the Z pole (at a trigger rate of approximately 10 KHz). The contribution from $\gamma\gamma$ to hadrons amounts to 6 GB/s. As mentioned in the previous paragraph, the IPC background causes the read-out of additional 1400 wires on average for every trigger, which translates into a bandwidth of 25 GB/s. A similar bandwidth is taken by the noise induced by the low single electron detection threshold necessary for an efficient cluster counting. Altogether, the various contributions sum up to a data rate of about 0.1 TB/s. Reading out these data and sending them into an "event builder" would not be a challenge, but the data storage requires a large reduction. Such a reduction can be achieved by transferring, for each hit drift cell, the minimal information needed by the cluster timing/counting, i.e., the amplitude and the arrival time of each peak associated with each individual ionisation electron, each encoded in 1 Byte, instead of the full signal spectrum. The data generated by the drift chamber, subsequently digitised by an ADC, can be analysed in real time by a fast read-out algorithm implemented in a FPGA[66]. This algorithm identifies, in the digitised signal, the peaks corresponding to the different ionisation electrons, stores the amplitude and the time for each peak in an internal memory, filters out spurious and isolated hits and sends these reduced data to the acquisition system at the occurrence of a trigger. Each hit cell integrates the signal of up to 30 ionisation electrons, which can thus be encoded within 60 B per wire end instead of the aforementioned 800 B. Because the noise and background hits are filtered out by the FPGA algorithm, the data rate induced by Z hadronic decays is reduced to 3 GB/s, for a total bandwidth of about 3.6 GB/s, roughly a factor 30 reduction.

References

[1] P. M. De Freitas and H. Videau, *Detector simulation with MOKKA/GEANT4: Present and future*, in *International Workshop on Linear Colliders (LCWS 2002), Jeju Island, Korea*, pp. 26–30. 2002.

[2] M. Regler, M. Valentan, and R. Frühwirth, *The LiC detector toy program*, Nuclear Instruments and Methods in Physics Research Section A:Accelerators,Spectrometers,Detectors and Associated Equipment **581** (2007) no. 1, 553–556.

[3] A. Andreazza, G. Barker, V. Chabaud, P. Collins, H. Dijkstra, Y. Dufour, M. Elsing, F. Ledroit, C. Eklund, R. Orava, et al., *The DELPHI Silicon Tracker at LEP2*, .

[4] M. Battaglia, C. Da Viá, D. Bortoletto, R. Brenner, M. Campbell, P. Collins, G. Dalla Betta, M. Demarteau, P. Denes, H. Graafsma, et al., *R&D paths of pixel detectors for vertex tracking and radiation imaging*, Nuclear Instruments and Methods in Physics Research Section A:Accelerators,Spectrometers,Detectors and Associated Equipment **716** (2013) 29–45.

[5] G. Contin, E. Anderssen, L. Greiner, J. Schambach, J. Silber, T. Stezelberger, X. Sun, M. Szelezniak, C. Vu, H. Wieman, et al., *The MAPS based PXL vertex detector for the STAR experiment*, Journal of Instrumentation **10** (2015) no. 03, C03026.

[6] C. Lacasta, *The DEPFET pixel detector for the Belle II experiment at SuperKEKB*, PoS (2014) 005.

[7] B. Abelev, J. Adam, D. Adamova, M. Aggarwal, G. A. Rinella, M. Agnello, A. Agostinelli, N. Agrawal, Z. Ahammed, N. Ahmad, et al., *Technical design report for the upgrade of the ALICE inner tracking system*, Journal of Physics G: Nuclear and Particle Physics **41** (2014) no. 8, .

[8] I. Valin, C. Hu-Guo, J. Baudot, G. Bertolone, A. Besson, C. Colledani, G. Claus, A. Dorokhov, G. DoziÃšre, W. Dulinski, M. Gelin, M. Goffe, A. Himmi, K. Jaaskelainen, F. Morel, H. Pham, C. Santos, S. Senyukov, M. Specht, G. Voutsinas, J. Wang, and M. Winter, *A reticle size CMOS pixel sensor dedicated to the STAR HFT*, Journal of Instrumentation **7** (2012) no. 01, C01102. http://stacks.iop.org/1748-0221/7/i=01/a=C01102.

[9] G. A. Rinella, *The ALPIDE pixel sensor chip for the upgrade of the ALICE Inner Tracking System*, Nuclear Instruments and Methods in Physics Research Section A: Accelerators, Spectrometers, Detectors and Associated Equipment **845** (2017) 583 – 587. http://www.sciencedirect.com/science/article/pii/S0168900216303825. Proceedings of the Vienna Conference on Instrumentation 2016.

[10] Y. Lu, Q. Ouyang, Y. Arai, Y. Liu, Z. Wu, and Y. Zhou, *First results of a Double-SOI pixel chip for X-ray imaging*, Nuclear Instruments and Methods in Physics Research Section A: Accelerators, Spectrometers, Detectors and Associated Equipment **831** (2016) 44 – 48. http://www.sciencedirect.com/science/article/pii/S0168900216301851. Proceedings of the 10th International Hiroshima Symposium on the Development and Application of Semiconductor Tracking Detectors.

[11] I. Kurachi, K. Kobayashi, M. Mochizuki, M. Okihara, H. Kasai, T. Hatsui, K. Hara, T. Miyoshi, and Y. Arai, *Tradeoff Between Low-Power Operation and Radiation Hardness of Fully Depleted SOI pMOSFET by Changing LDD Conditions*, IEEE Transactions on Electron Devices **63** (2016) no. 6, 2293–2298.

[12] Z. Wu, *A prototype SOI pixel sensor for CEPC vertex*, https://indico.cern.ch/event/577879/contributions/2741627/attachments/1575067/2486910/A_prototype_SOI_pixel_sensor_for_CEPC_vertex.pdf.

[13] S. Ono, M. Togawa, R. Tsuji, T. Mori, M. Yamada, Y. Arai, T. Tsuboyama, and K. Hanagaki, *Development of a pixel sensor with fine space-time resolution based on SOI technology for the ILC vertex detector*, Nuclear Instruments and Methods in Physics Research Section A: Accelerators, Spectrometers, Detectors and Associated Equipment **845** (2017) 139 – 142. http://www.sciencedirect.com/science/article/pii/S0168900216303783. Proceedings of the Vienna Conference on Instrumentation 2016.

[14] M. Idzik, *SOI-Cracow*, https://agenda.linearcollider.org/event/7450/contributions/38595/attachments/31561/47538/2017_LCVertex_Idzik.pdf.

[15] S. Spannagel, *Silicon technologies for the CLIC vertex detector*, Journal of Instrumentation **12** (2017) no. 06, C06006. http://stacks.iop.org/1748-0221/12/i=06/a=C06006.

[16] H. Wieman, E. Anderssen, L. Greiner, H. Matis, H. Ritter, X. Sun, and M. Szelezniak, *STAR PIXEL detector mechanical design*, Journal of Instrumentation **4** (2009) no. 05, P05015.

[17] H. Abramowicz et al., *The International Linear Collider Technical Design Report - Volume 4: Detectors*, arXiv:1306.6329 [physics.ins-det].

[18] Belle-II Collaboration, T. Abe et al., *Belle II Technical Design Report*, arXiv:1011.0352 [physics.ins-det].

[19] Y. Zhang, H. Zhu, L. Zhang, and M. Fu, *Charge collection and non-ionizing radiation tolerance of CMOS pixel sensors using a 0.18* µm *CMOS process*, Nuclear Instruments and Methods in Physics Research Section A: Accelerators, Spectrometers, Detectors and Associated Equipment **831** (2016) 99 – 104. http://www.sciencedirect.com/science/article/pii/S0168900216300481. Proceedings of the 10th International Hiroshima Symposium on the Development and Application of Semiconductor Tracking Detectors.

[20] Y. Zhou, *Development of highly compact digital pixels for the vertex detector of the future e+e- collider*, https://indico.cern.ch/event/577879/contributions/2740073/.

[21] Y. Zhang, *A Monolithic Active Pixel Sensor prototype for the CEPC vertex detector*, https://indico.cern.ch/event/577879/contributions/2740125/attachments/1574470/2485730/P15_ZY_POSTER_Final.pdf.

[22] Y. Lu, *Study of SOI Pixel for the Vertex*, http://indico.ihep.ac.cn/event/6433/.

[23] M. Motoyoshi, T. Miyoshi, M. Ikebec, and Y. Arai, *3D integration technology for sensor application using less than 5ÎŒm-pitch gold cone-bump connpdfection*, Journal of Instrumentation **10** (2015) no. 03, C03004. http://stacks.iop.org/1748-0221/10/i=03/a=C03004.

[24] W. Snoeys, G. A. Rinella, H. Hillemanns, T. Kugathasan, M. Mager, L. Musa, P. Riedler, F. Reidt, J. V. Hoorne, A. Fenigstein, and T. Leitner, *A process modification for CMOS monolithic active pixel sensors for enhanced depletion, timing performance and radiation tolerance*, Nuclear Instruments and Methods in Physics Research Section A: Accelerators, Spectrometers, Detectors and Associated Equipment **871** (2017) 90 – 96. http://www.sciencedirect.com/science/article/pii/S016890021730791X.

[25] CEPC-SPPC Study Group, *CEPC-SPPC Preliminary Conceptual Design Report. Volume I - Physics & Detector*, .

[26] Particle Data Group Collaboration, C. Patrignani et al., *Review of Particle Physics*, Chin. Phys. **C40** (2016) no. 10, 100001.

[27] J. E. Augustin et al., *A silicon envelope for the TPC*, .

[28] A. Affolder et al., *DC-DC converters with reduced mass for trackers at the HL-LHC*, JINST **6** (2011) C11035.

[29] S. Diez, *System Implications of the Different Powering Distributions for the ATLAS Upgrade Strips Tracker*, Phys.Procedia **37** (2012) 960–969.

[30] K. Klein et al., *DC-DC conversion powering schemes for the CMS tracker at Super-LHC*, JINST **5** (2010) C07009.

[31] A. Nomerotski et al., *Evaporative CO2 cooling using microchannels etched in silicon for the future LHCb vertex detector*, JINST **8** (2013) P04004, arXiv:1211.1176 [physics.ins-det].

[32] The ATLAS Collaboration, A. Affolder, *Silicon Strip Detectors for the ATLAS HL-LHC Upgrade*, Phys.Procedia **37** (2012) 915–922.

[33] V. Blobel, *Software alignment for tracking detectors*, Nucl.Instrum.Meth. **A566** (2006) 5–13.

[34] A. Savoy-Navarro, *Large Area Silicon Tracking: New Perspectives*, arXiv:1203.0736 [physics.ins-det].

[35] F. Shen, S. Wang, C. Yang, and Q. Xu, *MWPC prototyping and testing for STAR inner TPC upgrade*, JINST **12** (2017) no. 06, C06008.

[36] ALICE Collaboration, D. Rohr, *Tracking performance in high multiplicities environment at ALICE*, in *5th Large Hadron Collider Physics Conference (LHCP 2017) Shanghai, China, May 15-20, 2017*. 2017. arXiv:1709.00618 [physics.ins-det]. https://inspirehep.net/record/1621494/files/arXiv:1709.00618.pdf.

[37] I. Garzia et al., *GEM detector performance with innovative micro-TPC readout in high magnetic field*, EPJ Web Conf. **170** (2018) 01009.

[38] B. Mauss, T. Roger, J. Pancin, S. Damoy, and G. F. Grinyer, *MICROMEGAS calibration for ACTAR TPC*, EPJ Web Conf. **174** (2018) 01010.

[39] *CEPC project website*, http://cepc.ihep.ac.cn.

[40] P. Bhattacharya, S. S. Sahoo, S. Biswas, B. Mohanty, N. Majumdar, and S. Mukhopadhyay, *Numerical Investigation on Electron and Ion Transmission of GEM-based Detectors*, EPJ Web Conf. **174** (2018) 06001.

[41] ALICE Collaboration, S. Biswas, *ALICE TPC upgrade for High-Rate operations*, PoS **ICPAQGP2015** (2017) 094, arXiv:1511.04988 [physics.ins-det].

[42] LCTPC Collaboration, D. Tsionou, *Studies on GEM modules for a Large Prototype TPC for the ILC*, Nucl. Instrum. Meth. **A845** (2017) 309–312.

[43] J. Huth and D. Nygren, *Feasibility Tests of a High Resolution Sampling Radial Drift Chamber*, Nucl. Instrum. Meth. **A241** (1985) 375.

[44] DarkSide Collaboration, P. Agnes et al., *Electroluminescence pulse shape and electron diffusion in liquid argon measured in a dual-phase TPC*, Submitted to: Nucl. Instrum. Meth. A (2018) , arXiv:1802.01427 [physics.ins-det].

[45] M. Posik and B. Surrow, *Construction of a Triple-GEM Detector Using Commercially Manufactured Large GEM Foils*, 2018. arXiv:1806.01892 [physics.ins-det].

[46] ATLAS Muon Collaboration, D. Sampsonidis, *Study of the performance of Micromegas detectors in magnetic field*, EPJ Web Conf. **174** (2018) 05003.

[47] S. Dalla Torre, E. Oliveri, L. Ropelewski, and M. Titov, *R&D Proposal: RD51 Extension Beyond 2018*, arXiv:1806.09955 [physics.ins-det].

[48] C.-S. S. Group, *CEPC-SPPC Preliminary Conceptual Design Report. 1. Physics and Detector*, .

[49] M. Zhao, M. Ruan, H. Qi, and Y. Gao, *Feasibility study of TPC at electron positron colliders at Z pole operation*, JINST **12** (2017) no. 07, P07005, arXiv:1704.04401 [physics.ins-det].

[50] C. Adolphsen et al., *The International Linear Collider Technical Design Report - Volume 3. II: Accelerator Baseline Design* , 2013. arXiv:1306.6328 [physics.acc-ph].

[51] H. Abramowicz et al., *The International Linear Collider Technical Design Report - Volume 4: Detectors* , 2013. arXiv:1306.6329 [physics.ins-det].

[52] N. Calace and A. Salzburger, *ATLAS Tracking Detector Upgrade studies using the Fast Simulation Engine*, J. Phys.:Conf. Ser. **664** (2015) 072005.

[53] M. Regler et al., *The LiC Detector Toy program*, J. Phys.:Conf. Ser. **119** (2008) 032034.

[54] P. Mora de Freitas and H. Videau, *Detector simulation with Mokka/GEANT4: Present and future, LC-TOOL-2003-010, 623-627 (2002).*, (2002) .

[55] N. Graf and J. McCormick, *LCSIM: A detector response simulation toolkit*, in *2012 IEEE Nuclear Science Symposium and Medical Imaging Conference Record (NSS/MIC)*, p. 1016. Oct, 2012.

[56] S. V. Chekanov, *Public repository with Monte Carlo simulations for high-energy particle collision experiments*, PoS **ICHEP2016** (2016) 229, arXiv:1609.04455 [hep-ex].

[57] S. V. Chekanov, M. Beydler, A. V. Kotwal, L. Gray, S. Sen, N. V. Tran, S. S. Yu, and J. Zuzelski, *Initial performance studies of a general-purpose detector for multi-TeV physics at a 100 TeV pp collider*, JINST **12** (2017) no. 06, P06009, arXiv:1612.07291 [hep-ex].

[58] N. Graf and J. McCormick, *Simulator for the linear collider (SLIC): A tool for ILC detector simulations*, AIP Conf. Proc. **867** (2006) 503–512.

[59] J. Allison et al., *Recent developments in Geant4*, Nuclear Instruments and Methods in Physics Research A **835** (2016) 186.

[60] M. J. Charles, *PFA Performance for SiD*, in *Linear colliders. Proceedings, International Linear Collider Workshop, LCWS08, and International Linear Collider Meeting, ILC08, Chicago, USA, Novermber 16-20, 2008* . 2009. arXiv:0901.4670 [physics.data-an].

[61] J. S. Marshall and M. A. Thomson, *Pandora Particle Flow Algorithm*, in *Proceedings, International Conference on Calorimetry for the High Energy Frontier (CHEF 2013)*, pp. 305–315. 2013. arXiv:1308.4537 [physics.ins-det].

[62] S. V. Chekanov and M. Demarteau, *Conceptual Design Studies for a CEPC Detector*, Int. J. Mod. Phys. **A31** (2016) no. 33, 1644021, arXiv:1604.01994 [physics.ins-det].

[63] M. Adinolfi et al., *The tracking detector of the KLOE experiment*, Nucl. Instrum. Meth. **A488** (2002) 51–73.

[64] A. M. Baldini et al., *MEG Upgrade Proposal*, arXiv:1301.7225 [physics.ins-det].

[65] A. M. Baldini et al., *Single-hit resolution measurement with MEG II drift chamber prototypes*, arXiv:1605.07970 [physics.ins-det].

[66] G. Chiarello, C. Chiri, G. Cocciolo, A. Corvaglia, F. Grancagnolo, M. Panareo, A. Pepino, and G. F. Tassielli, *The Use of FPGA in Drift Chambers for High Energy Physics Experiments*, 2017. http://inspirehep.net/record/1663851/files/53616.pdf.

CHAPTER 4

CALORIMETRY

4.1 Introduction to calorimeters

In order to fully exploit the CEPC physics potential for Higgs, W, Z and related SM processes, the detector resolution in the measurements of the energy of electrons, photons, taus and hadronic jets, needs to be pushed quite beyond today's limits. For example, the jet energy resolution σ_E/E is required to reach 3%-4%, or $30\%/\sqrt{E}$, at energies below about 100 GeV. This resolution is about a factor of two better than the performance provided by the LEP detectors and the currently operating calorimeters at the LHC and it would significantly improve the separation of the W and Z bosons which decay into two jets, as shown in Figure 4.1. The basic requirements for standalone electromagnetic and hadronic shower energy resolution are $\sim 16\%/\sqrt{E}$ and $\sim 50\%/\sqrt{E}$, respectively. Two different approaches are being followed, the first one for the design of independent, separate electromagnetic (ECAL) and hadronic (HCAL) sections based on high-granularity imaging, the second aiming at a homogeneous, integrated solution based on the dual-readout approach. Both options will be described in the following.

To achieve the required jet energy resolution, many R&D researches are carried out within the CALICE collaboration since 2000 [1]. The majority of these studies aim to develop extremely fine granularity and compact imaging calorimeters with several technology options, as shown in Figure 4.2. Imaging calorimeter is a rapidly developing novel particle detection tecnique based on an excellent spatial resolution. It is capable to provide enormous position information of incident and showering particles, which makes it possible to reconstruct every single particle cluster. This is vital for Particle Flow Algorithm (PFA [2]) in order to significantly improve the energy resolution of hadrons. The basic

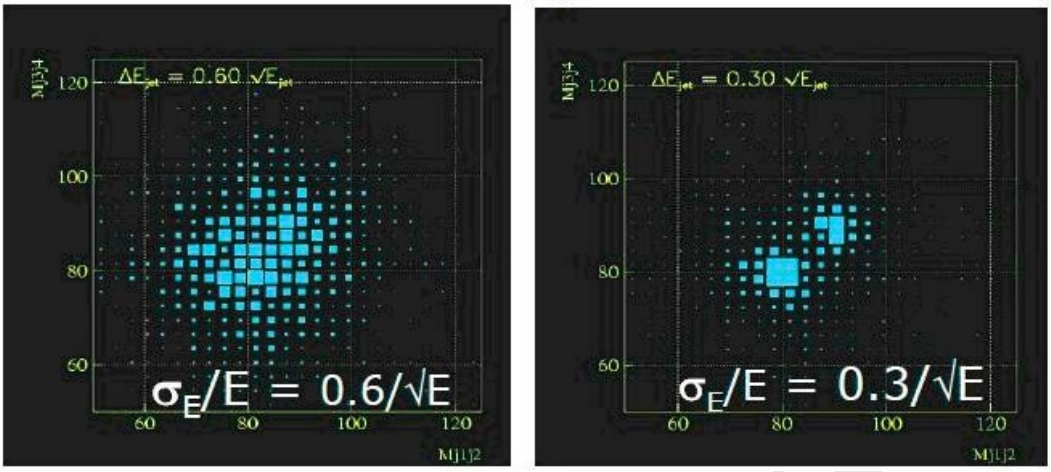

Figure 4.1: Separation of W and Z bosons with different jet energy resolutions.

idea of PFA is to distinguish energy depositions inside the calorimeter coming from incident charged particles and incident neutral particles. In average, the jet energy is shared among the two categories in the ratio $\sim 65\%$ (charged) and $\sim 35\%$ (neutral). Charged particles are measured in the inner tracker with high momentum resolution and matched to their energy depositions in the calorimeters. Energy depositions without matched inner tracks are considered to originate from neutral particles inside jets. Among these neutral particles, about 25% of the jet energy is carried by photons and is measured in the ECAL with good energy resolution. The residual 10% jet energy fraction is distributed among neutral hadrons and is measured in both calorimeters, with a worse energy resolution dominated by the HCAL performance. Hence, the jet energy is determined with the track momenta of charged particles measured in the inner tracker and the energy depositions of neutral particles in the calorimeters. It has been demonstrated, through both MC simulations and test beam measurements, that significant improvements of the jet energy resolution are achievable with this approach. However, more efforts are needed to optimize the calorimeter design, improve the PFA, and develop the technologies for high-granularity imaging calorimeters.

In the most general case, the calorimeter system includes two sub-detectors, an electromagnetic calorimeter (ECAL), optimized for the measurement of photons and electrons, and a hadronic calorimeter (HCAL), employed to measure the energy deposit of hadronic showers. The two sub-detectors should be installed inside the solenoid coils in order to minimize the inactive material in front of the calorimeters and to reliably associate tracks to energy deposits. Along the beam direction, the calorimeter system is divided into three regions, one cylindrical barrel and two end-caps.

ECAL consists of layers of active sensors (such as silicon pads or pixels, or scintillator detector) interleaved with absorber tungsten plates. For HCAL, both digital (DHCAL) and analog (AHCAL) solutions are presently under study. DHCAL is expected to have stainless steel absorber plates with gaseous detectors, such as glass Resistive Plate Chambers (gRPC) or GEM, while the AHCAL design is based with scintillators with SiPM readout as sensor. Both ECAL and HCAL are sampling detectors with very fine granularity and readout segmentation, driven by the requirement of an excellent performance in

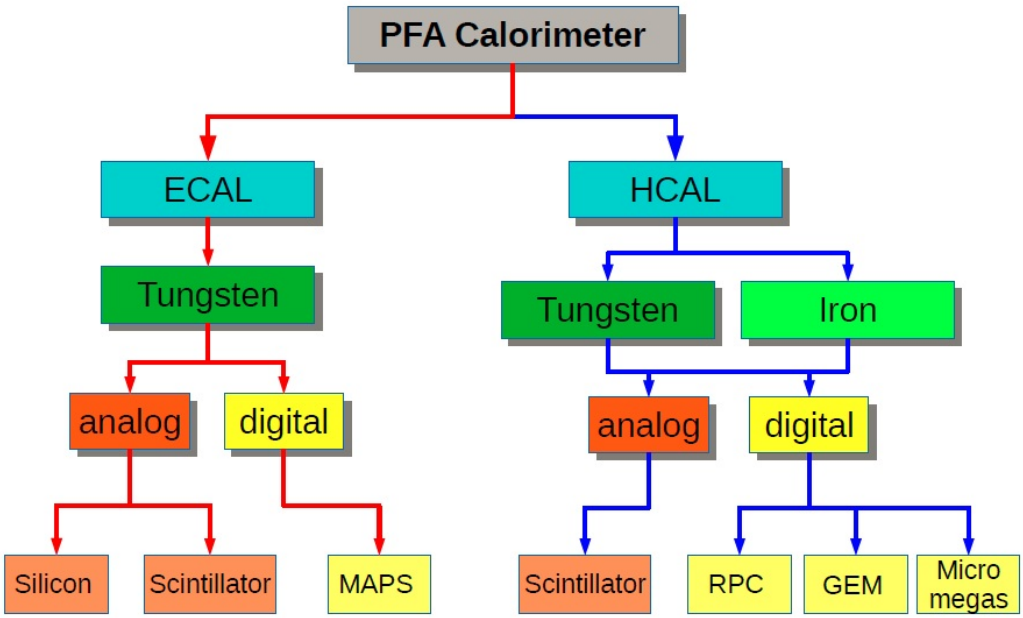

Figure 4.2: PFA: Imaging calorimeters being developed by the CALICE collaboration since 2000.

the separation capability of charged and neutral particles for the particle flow algorithms. The baseline design of the calorimeters for MC simulations includes a silicon ECAL with cell size of $5 \times 5\ mm^2$ and a semi-digital hadronic calorimeter (SDHCAL) based on RPC with cell size of $10 \times 10\ mm^2$. Further optimization of cell sizes for both ECAL and HCAL based on benchmark physics processes are underway.

As shown in Figure 4.2, enormous worldwide R&D efforts are ongoing, within the CALICE collaboration, on more detector options.

An alternative approach for a combined, high-performance, electromagnetic and hadronic calorimeter aims at reaching an even better (standalone) hadronic resolution, without spoiling the electromagnetic one, by exploiting the dual-readout (DR) technique. Indeed the main limiting factor to the energy resolution in hadron calorimetry arises from the fluctuations of the electromagnetic component (f_{em}) that each hadronic shower develops as consequence of π^0 and η production. Since typically the detector response to the hadronic and em components is very different ($h/e \neq 1$), the reconstructed signal heavily depends on the actual value of f_{em}. By using two independent processes (namely scintillation and Čerenkov light production) that have a very different sensitivity to the hadronic and em components, it is possible to reconstruct f_{em}, event by event, and eliminate the effects of its fluctuations.

Among the possible DR implementations, a fibre-sampling DR calorimeter, based on either copper or lead as absorber material, looks the most suitable to provide the required performance in a cost-effective way. Preliminary results of Geant4 simulations point to possible resolutions better than 15% and around $30\% - 40\%$ (over $\sqrt{E}$), for electromagnetic and hadronic showers, respectively (see section 4.4.6).

Moreover, if the fibres are readout with SiPM, the high detector granularity and the possibility of longitudinal segmentation will make this solution easily compatible with Particle Flow Algorithms.

4.2 Electromagnetic Calorimeter for Particle Flow Approach

The particle flow paradigm has tremendous impact on the design of the electromagnetic calorimeter detector. Separating overlap showers from each other is principal requirement of the detector. A calorimeter used for particle flow thus needs to be able to do pattern recognition in the shower. The electromagnetic section has lots of tasks to fulfill. It should be able to select photons from close-by particles. It should be able to reconstruct the detailed properties of the shower, such as shower shape, starting point and energy distribution. It should be able to distinguish early starting electromagnetic showers from hadronic ones. The imaging capabilities of the calorimeter are more important than the intrinsic single particle energy resolution, although the latter is still important to the particle flow performance for electron, photons and jets. Due to the reason that about half of the hadronic showers will start development inside the electromagnetic calorimeter, a calorimeter with excellent three dimensional granularity is of utmost importance. In order to have the ability of separate close-by showers in the calorimeter, the detector with small Molière radius is required. A large ratio between interaction length and radiation length of the detector is advantageous to the separation between electromagnetic and hadronic showers. A small radiation length will make the start of the electromagnetic shower earlier in the calorimeter, while a large interaction length will reduce the fraction of hadronic showers starting in the calorimeter. At the same time, the calorimeter with a compact structure is favorable.

In this section, we focus on two detector options for the ECAL, which consist of layers of active sensors (silicon pads or pixels, or scintillator detector) interleaved with absorber tungsten plates.

4.2.1 Silicon-Tungsten Sandwich Electromagnetic Calorimeter

4.2.1.1 Introduction

The study of the Higgs is not the only goal of a machine at 250 centre-of-mass energy. It can be generalised to the multi boson physics (Z, W and H). The best way to use the excellent luminosity foreseen at CEPC, consist to tag the boson through their mass in their decays into $q\bar{q}$ (2 jets). Taking into account the natural width of the Z and W, it has been shown that this goal required to achieve a jet energy resolution of $30\%/\sqrt{E_{\mathrm{Jet}}}$, thus a factor two better than the energy resolution achieved for a typical detector at LEP.

It has been shown [3] that a method consisting to fully reconstruct every single particle could reach this goal (Particle Flow Algorithm); it requires both a high performance tracker, typically achieving $\delta p/p$ of $10^5 p/GeV$ associated with high granularity calorimeters able to separate the contribution from individual particles down to the MIP level. As a typical jet is contains fractions in energy of 65%, 25% and 10% of charged particles, photons and neutral hadrons respectively, a moderate calorimetric resolution is then sufficient to achieve the goal. In this framework, the electromagnetic calorimeter (ECal), is first devoted to measure photon(s) and to a lesser extent electron(s) and to make a full pattern of the deposited energy of the hadron, i.e. shower of hadron interacting in the ECAL. To avoid "blind region", the entire calorimeter has to be put inside the super-conductive solenoid. The compactness is therefore an important criterion.

The design of the calorimeters have to take the following guidelines into account [4]:

- Optimisation of the number of calorimeter cells (cell size and number of layers)
- Choice of the absorber material in order to insure a high level of compactness and the infra-structural components such as cooling, power supplies, readout cables and the very front end electronics.

For the electromagnetic calorimeter these criteria has led to the choice of Tungsten with a radiation length of Xo=3.5mm, a Molière radius of RM=9mm and an interaction length of $\lambda_{\mathrm{I}} = 96mm$.

4.2.1.2 Silicon sensors

Among several sensor techniques, high resistivity silicon pin diodes offer several unique intrinsic advantages:

- stability: under a reasonable bias voltage, completely depleted pin-diode have a gain of one, and a signal response to MIP mostly defined by the thickness of the sensor, with a very low dependence on temperature, radiation, humidity, ...
- uniformity: for the same reason, the control of the thickness over large batches (typically to less than a percent) ensures a uniformity of response within a wafer and between them. The nonsensitive area between wafers has recently been reduced by the use of laser cutting, thinned guard-ring design [5], and would benefit from the use of larger ingot size (8" becoming the standard).
- flexibility: the dimension and geometry of the cells are defined by the readout pad on the PCB.
- High Signal-to-Noise ratio: with $\simeq 80$ electron-hole pairs created by linear mm of MIP track, MIPs tracks can easily be traced in the calorimeters, which is critical for the god performance of

The only real drawback of Silicon sensors remaining is their price, to be expected around $2 - 3\$/cm^2$.

By associating of Silicon sensors with Tungsten absorbers and Carbon Fibre structures, the SiW-ECAL offers an excellent option for PFA optimised calorimetry.

4.2.1.3 Constraints

High granularity calorimetry, and ECal especially, is technically challenging: the very number of channels calls for an embedded readout and zero suppression, to limits the amount of connections; in turn embedded readout power consumption should be as limited as possible to avoid large cooling systems which would degrade the capacity of the calorimeter. In the best case the cooling should stay passive at the heart of the calorimeters.

The design proposed for the CEPC SiW-ECal is very largely inspired by the one of the ILD detector for ILC as described in the Detector baseline Document [6]; it is influenced by the options studied for the CMS High-Luminosity upgrade endcap replacement HGCAL [7, 8], concerning cooling and electronics. In terms of luminosity and collision rates, the CEPC lies between the 2 options.

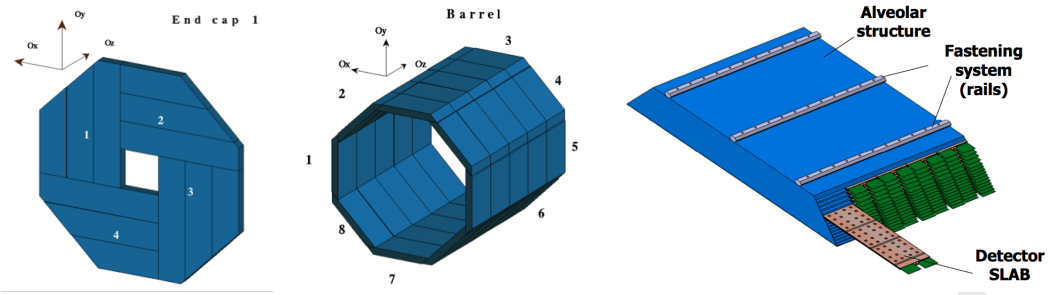

Figure 4.3: Left: Geometry of the SiW-ECAL Endcaps. Middle: Barrel Right: Geometry of the barrel modules.

4.2.1.4 Mechanics & design

The geometry presented here reflects the current (october 2017) status on the realistic models developed for ILD. It differs slightly form the CEPC_v1 and CEPC_v4 models [9], mainly on ECAL thickness ($223mm$ vs $185mm$), and inner radius of the endcaps (226.8 and $245mm$ vs $400mm$).

4.2.1.5 Geometry

The geometry of the detector is based on ILD detector, where there is no blind zone between modules, but only "special zone", where it has been shown that performance of the reconstruction of jets or photon(s) is not downgraded significantly [10].
The figure below shows this octagonal geometry and the possible way to build the detector:

ECal thickness For a baseline design featuring 30 layers – split in 2 sections of 20 and 10 layers, holding each an equal amount of $12Xo$ of W – $525microns$ thick wafers, and a base plate of $20mm$ of carbon, the ECal thickness is estimated at $223mm$.

For a reduced number of layers, at 22 (with section of 14 and 8), but thicker wafers ($725microns$), the thickness becomes $191mm$.

ECal dimensions The Barrel consist of 8 staves of 5 trapezoidal modules. Each barrel module contains 5 columns of alveoli. The number of modules and alveoli is even in order to avoid any special region at the azimuthal angle $theta = 0$. The alveolus size is fixed to $186mm$ by mechanical limits and by cost optimisation considerations, to contain exactly two 6-inch wafers or one-and-a-half 8-inch wafer. Integrating the alveolus size, walls of modules and contingencies, the barrel length amount to $4700mm$. ($4900mm$ in CEPC simulations). A gap of typically $70mm$ ($100mm$ in simulation) is left between the barrel sides and end-cap front parts, whose precise dimension will depend on the amount of ancillaries needed to service the ECAL and trackers (power and DAQ cables, cooling pipes, patch panels).

The end-caps are made of quadrants of 2 modules of 4 and 3 alveoli columns. Their inner radius is fixed by the ECal ring at $400mm$. With 7 alveoli columns, the end-cap outer radius is $1755mm$. An overshoot of $32mm$ is left between the outer radius of the barrel and of the end-caps, in order to contain the EM shower impinging the region of overlap. see figure 4.4. This fixes the inner radius size of the ECal barrel at $1498mm$ or $1530mm$.

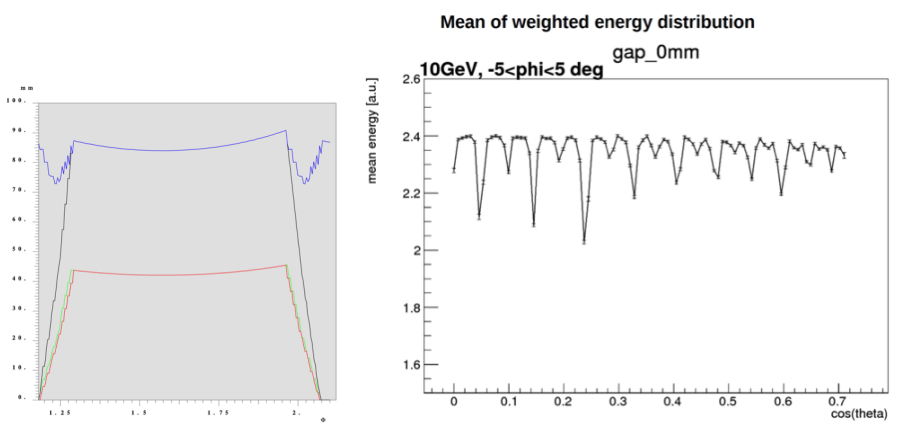

Figure 4.4: Left: Thickness of Tungsten seen as function of the polar azimuthal angle scan of one octant of the barrel. Right: Mean Theta angle scan

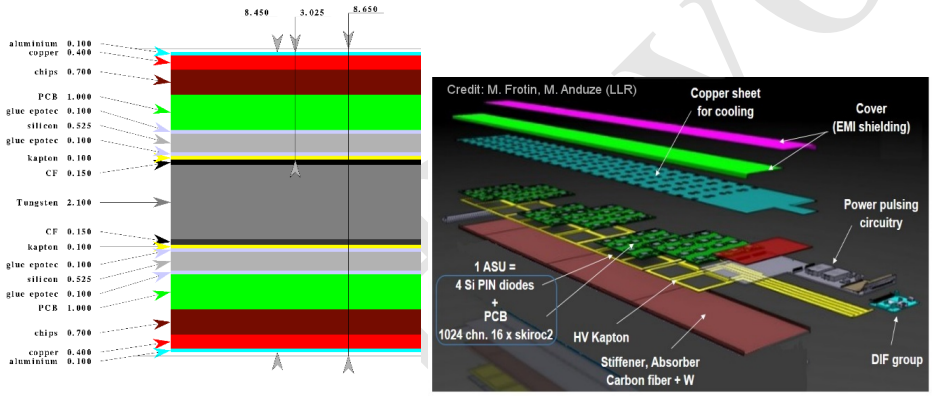

Figure 4.5: Left: Transverse cut through of a thin layer of the SLAB. Right: Exploded view of the top layer of a slab of the SiW-ECAL. The same structure is mirrored below the slab.

For such a geometry, summing the barrel (200) and end-caps (56), 256 alveoli columns are needed. For 22 (resp. 30) layers, and this yields 5632 (7680) alveoli, and as many detector slabs.

Slab geometry In each alveola of the modules, a slab is inserted. Slabs contains 2 symmetric layers of Silicon sensors glued on PCB, equipped with readout ASICs, high voltage distribution by a Capton foil and copper layers for passive cooling. The elements are chained on both sides of a Carbon fibre cradle taking the shape of an H, with a core of Tungsten, and shielded by an aluminium cover. This so-called H-Structure is illustrated below.

To insure scalability and industrial production, the design has been made as modular as possible: the basic unit is the ASU (Assembly Single Unit), made of a $18x18mm^2$ PCB onto which 4 wafers of $90x90mm^2$ wafers are glued. Each ASU would handle 256 cells with 4 ASICs, for cell surfaces of $11.25x11.25mm^2$.

The ASUs are chained together for the clock and configuration distribution and data collection. For a radius of $1498mm$ the longest (shortest) barrel slabs measure $1146mm$ ($955mm$).

4.2.1.6 Electronics

One of the most critical element of the CEPC calorimeters is the readout electronics which is defined by the dynamic range, the effective digitisation, mode of trigger, the rate of working and power consumption per channel.

Dynamic range: A MIP going through a $725 microns$ diode would produce $\simeq 60000$ electron-pairs holes or a charge of $9.6fC$ as the most probable value (MPV). To record MIPs with an efficiency higher than 95% this ports the low-end of the dynamic range to a 1/3 of the MPV. The high-end is determined by the number of MIP equivalent at the core of the high-energy EM showers, which can reach up-to 10000 MPV or $96pC$ for $11x11mm^2$ cells.

Timing: Time measurement of deposits in the calorimeters can be useful to Particle Flow algorithms to help disambiguate particle contributions. For the CMS HGCAL it is planned to distinguish particle stemming from different interactions [7], by achieving a timing of $50 - 20ps$ on EM showers. For e^+e^- colliders, with a single primary vertex, precision timing of individual cells – or group of cells – could still be useful to reduced the confusion and improve the resolution. The required precision is uncertain and should be studied further. Recent version of the SKYROC2a ASIC, could be operated [11] on test board with a measure of time close to 1.4ns. The performance has to be measured in an integrated design.

Rates: The running conditions a circular collider preclude any pulsed operation as is planned for the linear ones, where clocks, pre-amps, digital conversion are powered sequentially at a few Hz. A partial in-time shut-off or local on-demand switch-on of the ADC and TDC parts can be envisaged, leaving the pre-amp as the single major power consumer. As a point of reference, the current power consumption for SKIROC2 chips designed for the SiW-ECAL of ILD is of $5mW$ per channel in continuous mode.

Occupancy: The occupancy of the calorimeters should be very low. This pushes in the the direction of designing pre-amps with a very small consumption when there is no signal.

4.2.1.7 Power & Cooling

To the first order, the amount of power dissipates scales with the number of electronics channels. One important issue is to decide on the power scheme:

- a reduced number of channels using only passive cooling at the heart of the detector, such as planned at the ILD; a $400 microns$-thick copper sheet will drain the heat to the end of the slab, where it is removed by a cooling system.

- keep a high granularity but include CO_2 cooling in the absorbers such as envisaged for the HGCAL.

The CEPC ECAL is at edge of both options, with a limit for the purely passive option of the order of $2x2cm^2$ cells for a increase of temperature limited to $\Delta T \sim 10°C$ at the remote-end of the slab.

Water cooling Current plans for the ILD SiW-ECAL is to use a leak-less water cooling system to extract the heat at the end of each slab from the copper. Details of implementation can be found in [12**?**].

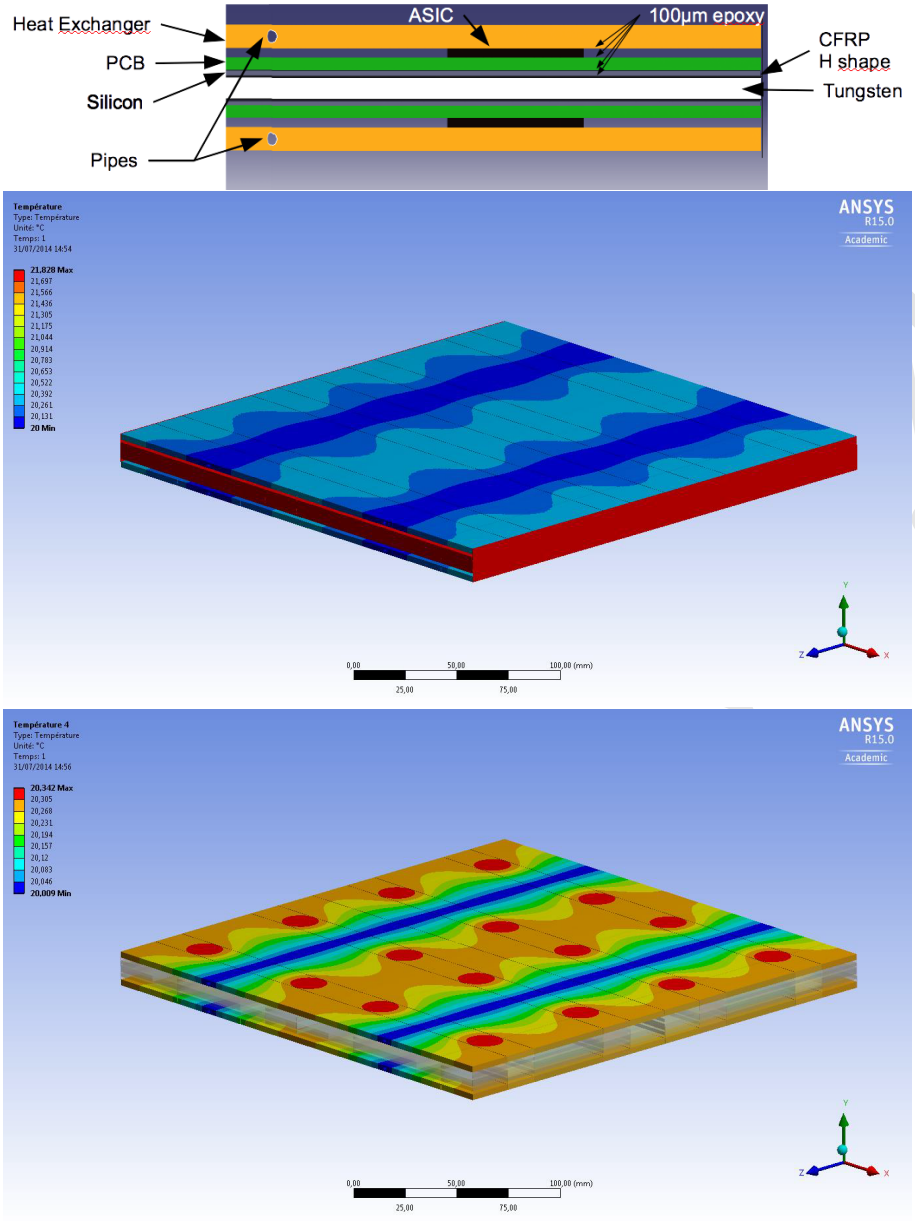

Figure 4.6: Top: Transverse section of slab equipped with CO_2 cooling pipes embedded in the cooling plates Left: Heat map over the full module. Right: heat map in the heat exchanger

CO_2 cooling HGCAL is preparing a biphasic CO_2 cooling system, with pipes circulating inside the absorber planes, made of an alloy of Tungsten and Copper.

A similar system adapted to the SiW-ECAL has been simulated [13]. The ILD $400microns$ passive colling are replaced by plates of $3mm$ of Copper, equipped with $1.6mm$ inner-diameter pipes for CO_2 circulation, glued on the ASICs, on both side of the slab. Assuming a fully transversally isolated system, with ASICs a sole heat source at equilibrium dissipating $0.64W$ ($10mW$ per channel times 64 channels), and a fixed working point of $20°C$ for CO_2 (i.e assuming perfect heat absorption), a doubled sided module of $252x252mm^2$ holding 32 chips cooled by $2x2$ pipes was simulated.

Very preliminary simulations in "ideal conditions" show a difference of $\Delta T \sim 2°C$ mostly centered on ASIC's ($0.3°C$ in the exchanger itself only).

4.2.1.8 Status of R&D

The performances of a Silicon-Tungsten ECAL have beed explored using the "physical prototype" of the CALICE collaboration, on numerous beam tests during the years 2005-2011 [14–16].

Some ASU, similar to the one foreseen for the ILD detector have been operated in two beam test campaigns: first at CERN in 2015, where 3 ASU mounted on test boards behaved as expected [17]; a signal to noise ratio (SNR) - defined as the Most Probable Value of a Landau fit on data, divided by the Gaussian width of the noise – reached typical values of 15-18, with a very limited number of masked channels.

More recently a campaign at DESY using 1-5 GeV electrons, punching through "short slabs", featuring all the elements of the slabs described in section 4.2.1.5 but limited to a single ASU on a single side, could reach a SNR of $\simeq 20$ in average [18].

The collected data is still under analysis for estimated calorimetric performances, but they are expected to be similar to the physics prototype.

The building of a "long slabs" is being actively pursued, and should be completed toward the end of year 2019; the R&D involves all the power, cooling and FE issues for an ILD near the ILC.

The results and design will have to be adapted for a circular collider, where operation *a priori* forbid power-pulsed operations.

4.2.2 Scintillator-Tungsten Sandwich Electromagnetic Calorimeter

4.2.2.1 Introduction

Alternatively, a sampling calorimeter with scintillator-tungsten structure is proposed. It can be built in a compact and cost effective way. The structure of the ScW ECAL is similar to the SiW ECAL. The major geometry parameters of the ScW ECAL are also studied and optimized, with the similar results of the SiW ECAL. The active layers of the ScW ECAL are consisting of $5\times45\text{mm}^2$ scintillator strips. The scintillator strips in adjacent layers are perpendicular to each other to achieve a $5\times5\text{mm}^2$ effective transverse readout cell size. Each strip is covered by a reflector film to increase collection efficiency and improve uniformity of the scintillation light. Photons from each scintillator strip are read out by a very compact photo-sensor, SiPM, attached at the end of the strip. The SiPM and highly integrated readout electronics make the dead area in the ScW ECAL almost negligible.

Plastic scintillator is a robust material which has been used in many high energy physics experiments. Production of the scintillator strips can be performed at low cost by the extrusion method. Moreover, the number of readout channels can also be significantly reduced due to the strip structure. So the total construction cost of the ScW ECAL is lower than the SiW ECAL. Some key issues which might affect the performance of the ScW ECAL were studied and optimized.

4.2.2.2 SiPM dynamic range study

Because each pixel on a SiPM can only detect one photon at once and a few nanoseconds are needed before recovery, the SiPM is not a linear photon detection device, especially in the case of high intensity light input. The application of the SiPM in the CEPC ScW ECAL is a challenge to its dynamic range, which need to be studied.

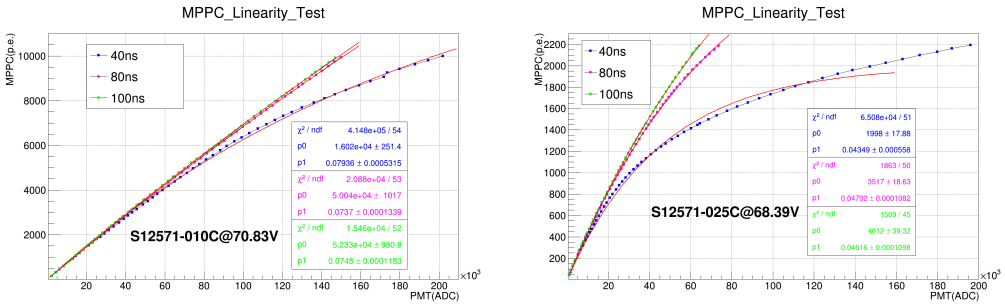

Figure 4.7: The response curve of 10000-pixel(left) and 1600-pixel(right) SiPM with different duration light.

For a short time light pulse, the response of the SiPM can be theoretically calculated as

$$N_{fired} = N_{pixel}(1 - e^{-N_{pe}/N_{pixel}}) \tag{4.1}$$

However, for the ScW ECAL, the width of the light pulse should not be ignored, and some pixels of the SiPM can detect more than one photon in an event. The response of the SiPM should be modified as

$$N_{fired} = N_{eff}(1 - e^{-N_{pe}/N_{eff}}) \tag{4.2}$$

The N_{eff} stands for the effective number of pixels on a SiPM, which is relative to the width of the input light pulse. Response curve of 10000 pixel (10μm pitch size)and 1600 pixel (25μm pitch size) SiPM with different duration light have been tested. As shown in Figure 4.7, the output linearity of the device is improved by the increase in the incident light width.

4.2.2.3 Scintillator strip test

Because the SiPM is coupled at one end of the scintillator strip, the light output will be non-homogeneous along the length of the scintillator, which will affect the performance of the ScW ECAL. By moving a Sr^{90} source along the length of the scintillator, we test the light pulses height read out by the SiPM to study the non-uniformity of the scintillator detector. Figure 4.8(left) is a typical test result of a scintillator module whose light output non-uniformity is 23%. The uniformity can be improved by optimizing the reflection material or the coupling methods of the SiPM to the scintillator strip. Figure 4.8(right) shows a result of a scintillator module with the SiPM embedded into the scintillator strip, and Figure 4.9 is the light output of another scintillator module with different reflector. Scintillators with ESR reflector can give much more light output. We have also test the light output of the scintillator coupled with the SiPM with different pitch size. Two kinds of SiPM have same sensitive area (1mm$\times$1mm), but have pitch size of 25μm and 10μm respectively. The light output of the scintillator with 25μm pitch SiPM is only about 1/3 of the scintillator with 10μm pitch SiPM, shown in Figure 4.10.

4.2.2.4 Beam test of a mini prototype

To study the layout, the coupling mode of the scintillator and the SiPM, and further test the minimum ionization particles (MIP). A mini prototype was constructed and tested by test beam. The test was carried out at the E3 beam at the IHEP, which could provide proton and pion mixed irradiation. The momentum of the particles was adjusted from 400MeV to 1.1GeV in the test.

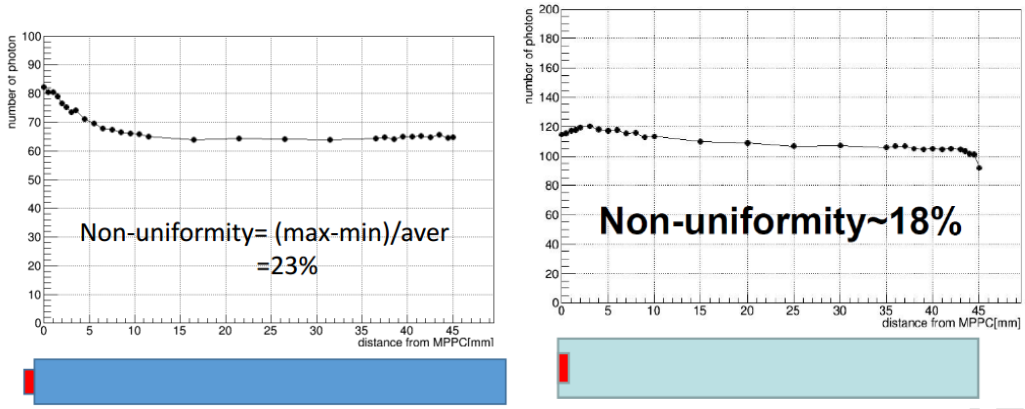

Figure 4.8: Scintillator module test results, with the SiPM coupled on the surface (left) or embedded into the strip(right).

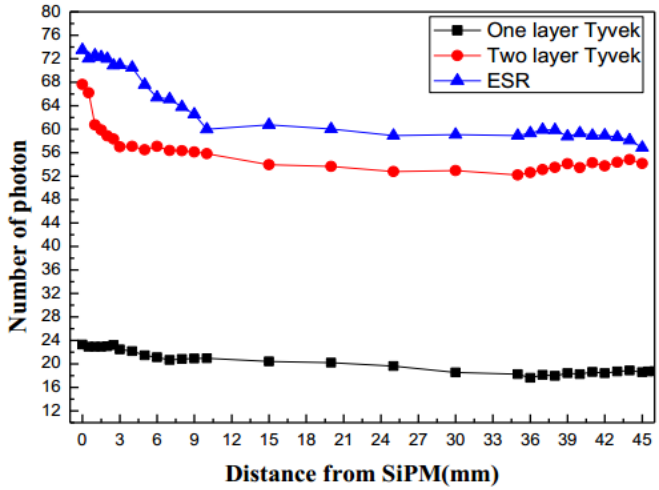

Figure 4.9: light output of scintillator with different reflector.

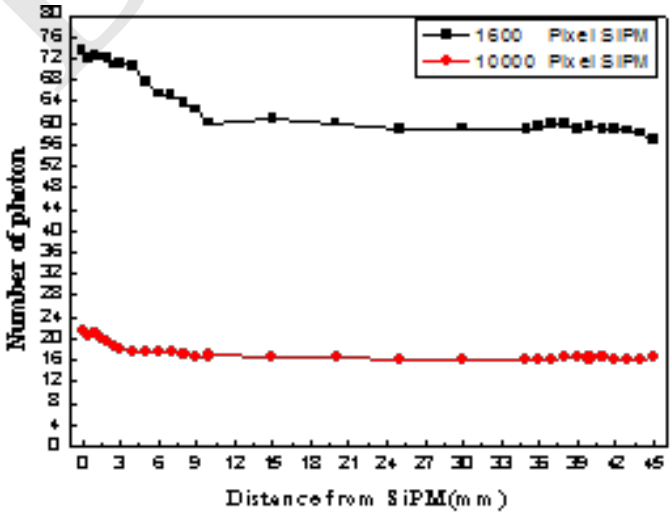

Figure 4.10: light output of the scintillator with different SiPM.

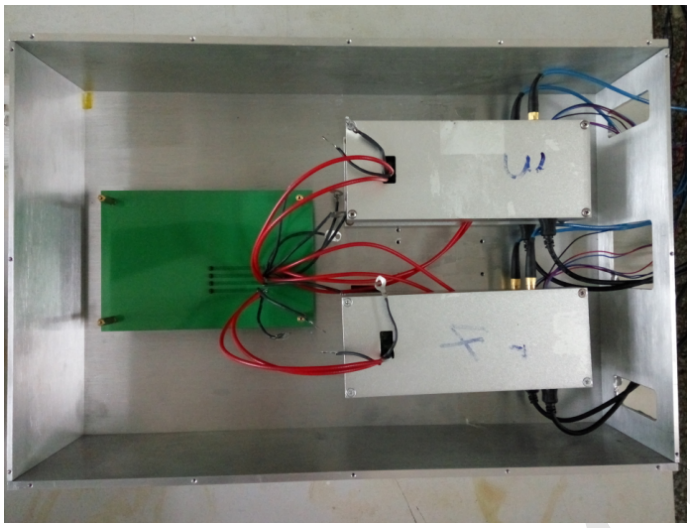

Figure 4.11: the picture of the prototype.

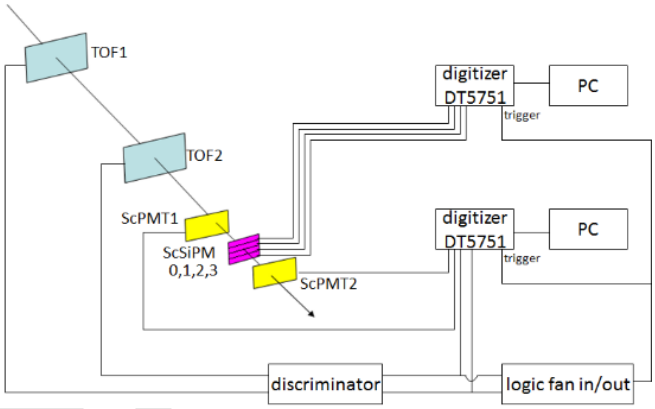

Figure 4.12: the schematic of the readout of the prototype.

The prototype includes four scintillator modules attached tightly to each other, as shown in Figure 4.11. Each module is composed of a BC408 scintillator with a dimension of 45mm×5mm×2mm, and a Hamamatsu S12571-025P SiPM coupled at the end of the scintillator as a photoelectric conversion device. The prototype is put into an aluminum box for electro-magnetic and light shielding. Figure 4.12 shows the detector layout in the test beam and the schematic of the readout. The beams first pass through two time of flight detectors (TOF) with the distance of 3m for particle identification, and then go through two scintillator counters with the same dimension of total of the four scintillator modules used to estimate the efficiency of the prototype. The prototype is located between the two scintillator counters. The signals from the TOFs and the scintillator counters are directly sent to a wave sampling digitizer (CAEN DT5751). The SiPM from each modules of the prototype is connected to a Hamamatsu driver board (C12332-01), which not only amplifies the signals from the SiPM, but also can eliminate the gain changes of the SiPM caused by the fluctuation of the temperature during the test thanks to its temperature compensation circuit. The signals from the four driver boards are sent to another CAEN DT5751 module to be digitized.

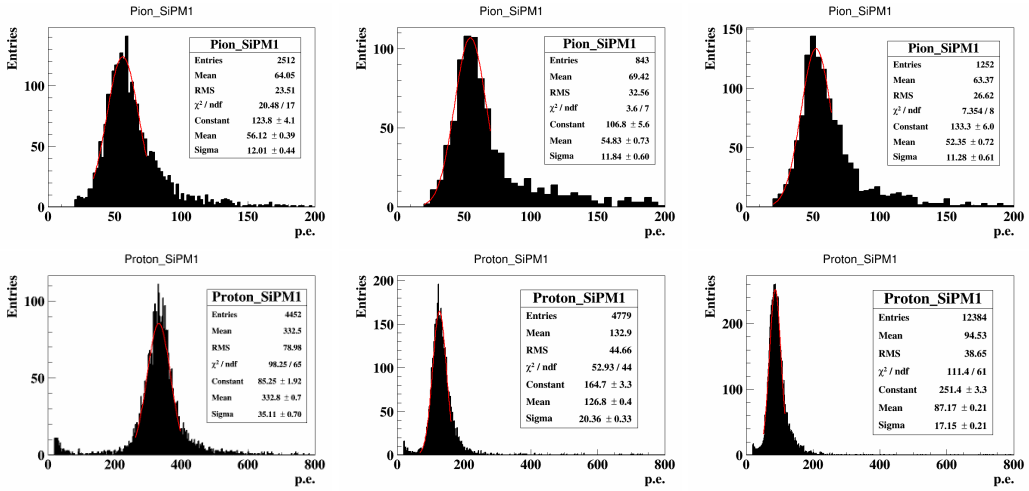

Figure 4.13: the energy spectrums of pions and protons with momentum of 400MeV/c, 700MeV/c and 1000MeV/c.

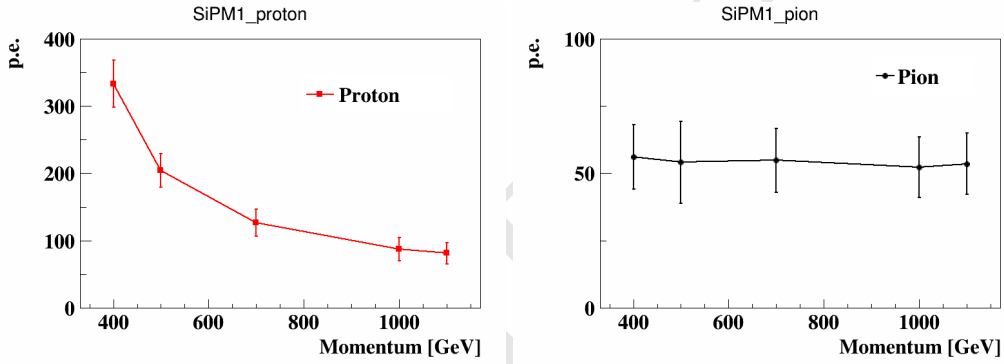

Figure 4.14: dE/dx of protons and pions change with the momentum.

Figure 4.13 are the energy spectrums of pions and protons with momentum of 400MeV/c, 700MeV/c and 1000MeV/c respectively after the system calibration, which indicate the energy deposition in a module. The dE/dx as a function of the momentum of the particles can be got from the energy spectrums of the module, as shown in Figure 4.14. The values of dE/dx of protons and pions are consistent with the expected ones with respect to the momentum of the particles. Based on the dE/dx of pions, we can know the signal of the MIPs from the scintillator module is about 50 photoelectrons.

4.2.2.5 Implementation Example for the Analog Calorimeter Readout

The readout electronics of the ECAL has to provide high dynamic range of energy, while showers of particle may deposit 1∼800 MIPs energy in single cell for 100GeV photon. As Particle Flow Algorithm (PFA) is being considered, high granularity requirement need be meet. Granularity of cells in ECAL need be finer than 10mm therefore a large amount of channels need be readout. So multiple-channels-readout-chip is considered.

Electronics consists of two parts: Front-End and Back-End. The Front-End-Electronics (FEE) is embedded into the layers of ECAL. It performs amplification, auto-triggering, digitization and zero-suppression, with local storage of data between the working phases.

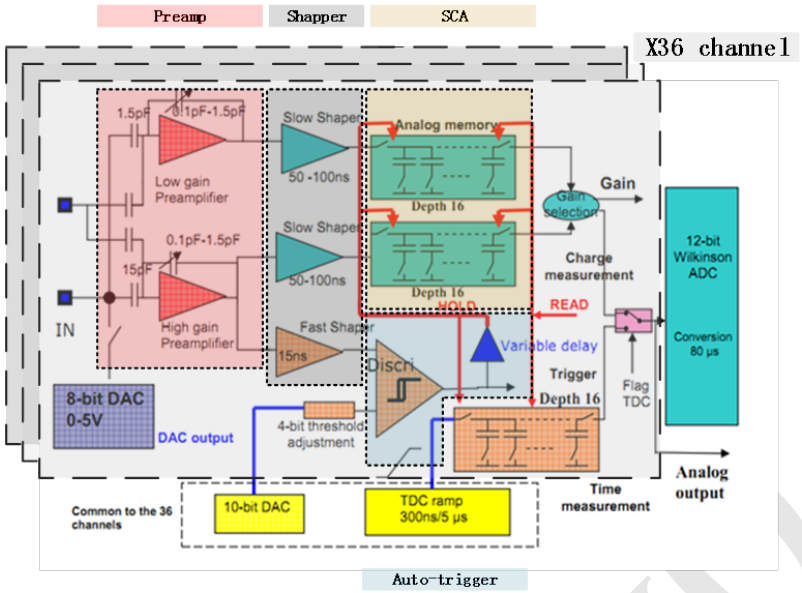

Figure 4.15: Schematic view of proposed readout ASIC.

The Back-End-Electronics play the role of collecting data and configuring chip before system running.

Several studies and existing calorimeter readout electronics have shown that one can obtain optimized energy resolutions using a preamplifier-shaper and digitizing the pulse at peak. For instance, a preamp-shaper-SCA structure of analog circuit applied on ILC HCAL which implemented in ASIC. A similar approach can be applied at CEPC-ECAL. An ASIC named SPIROC2b is considered in present stage. The analog part is schematically depicted in Figure 4.15.

The basic principle consists of a readout chain with an amplifier-shaper using a RCn-CRp filter delivering a pulse length of about 50-200ns duration for a SiPM pulse signal. This signal is also shaped by a fast shaper in the same time to generate fast and narrow pulse for discriminating. Then the discriminator gives the trigger to Switched-Capacitor-Array (SCA) for locking the peak value of slow-shaped signal. The locked voltage value is corresponding to the charge that circuit received. A 12bits Wilkinson ADC is used for digitizing analog voltage in SCA. Future detailed implementations of the calorimeter front-end electronics for CEPC is still considered using ROC series ASIC but newer version.

The maximum data rate can be estimated as follows. Assuming signal keep coming consistently, SPIROC2b will be continuously switched between three states called Acquisition, AD Converting and Readout. Only in Acquisition state can SPIROC2b receive signal from SiPM and stored in SCA in the rate of about 5MHz. Another two states should be seen as “dead-time" status. There is 16 depth in SCA, so 4us for Acquisition, according to measurement, ∼4ms for ADC & Readout. So data rate is 16 events per 4ms which equals to 4 kHz. Each fulfilled data packaged is 2 Kbytes in size.

More chip in one layer will multiply the duration of Readout. Assuming that there are 4 chips in one layer. So there is 16ms for Readout. Maximum events rate is reduced to 1kHz and leads to about a transmission of 5Mbyte/s. This can easily be managed with 100M links.

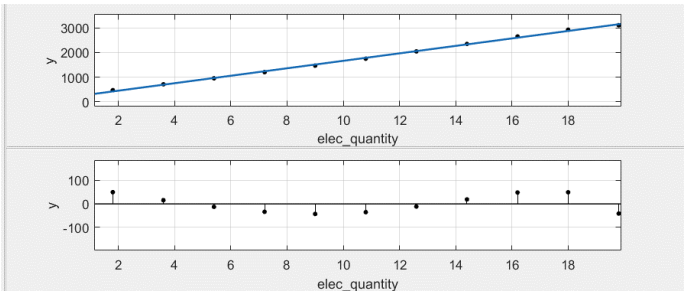

Figure 4.16: Pedestal noise.

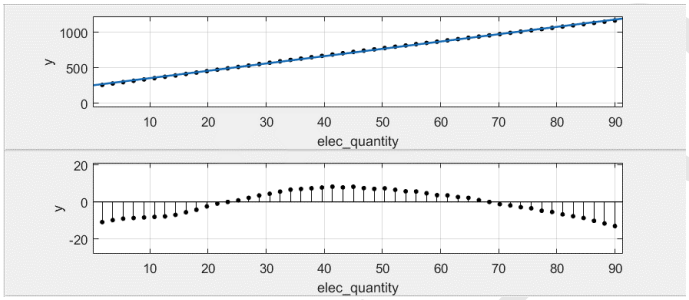

Figure 4.17: High gain calibration.

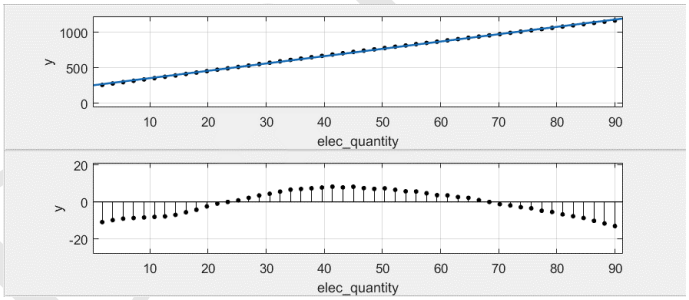

Figure 4.18: Low gain calibration.

The power consumption in the front-end will be dominated by ASIC and more specifically by analog part of ASIC. Opening all modules, one SPIROC2b is consuming 250.8mW of which about 150mW is consumed by analog part. In actual use, most of cycle is ADC and Readout. It leads to about 150mW power consumption per chip and 4mW per channels.

The electronic calibration and cosmic ray test have been done. From these electronic calibration Figure 4.16 - Figure 4.18, we can see that the noise of readout system is 46fC in RMS and high gain and low gain is 151/pC and 10.3/pC while maximum ADC range is 4096. So dynamic range that from 100fC-300pC of readout system is measured by electronic method. Cosmic ray results shows that the system can distinct MIPs signal from pedestal well and figure out that about 1pC.

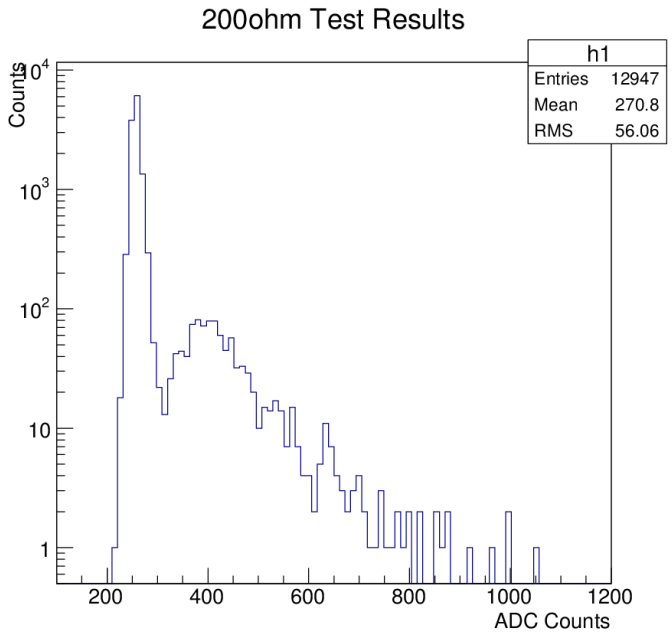

Figure 4.19: Cosmic Ray result.

4.3 Hadronic Calorimeter for Particle Flow Approach

4.3.1 Introduction

High-granularity hadronic calorimeter concept is to play an essential role in PFA-based experiments such as CEPC. It allows to separate the deposits of charged and neutral hadrons and to precisely measure the energy of the neutrals. The contribution of the neutrals to the jet energy, around 10% on average, fluctuates in a wide range from event to event, and the accuracy of the measurement is the dominant contribution to the particle flow resolution for jet energies up to about 100 GeV. For higher energies, the performance is dominated by confusion, and both topological pattern recognition and energy information are important for correct track cluster assignment. High-granularity hadronic calorimeter is thus needed to achieve excellent jet energy resolution.

HCAL are sampling calorimeters with steel as absorber and scintillator tiles or gaseous devices with embedded electronics for the active part. The steel was chosen due to its rigidity which allows to build self-supporting structure without auxiliary supports (dead regions). Moreover, the moderate ratio of hadronic interaction length ($\lambda_I = 17$ cm) to electromagnetic radiation length ($X_0 = 1.8$ cm) of iron, allows a fine longitudinal sampling in terms of X_0 with a reasonable number of layers in λ_I, thus keeping the detector volume and readout channel count small. This fine sampling is beneficial both for the measurement of the sizable electromagnetic energy part in hadronic showers as for the topological resolution of shower substructure, needed for particle separation.

The active detector element has very finely segmented readout pads, with 1×1 cm^2 size, for the entire HCAL volume. Each readout pad is read out individually, so the readout channel density is approximately 4×10^5/m^3. For the entire HCAL, with $\sim$100 m^3 total volume, the total number of channels will be 4×10^7 which is one of the biggest challenges for the HCAL system. On the other hand, simulation suggests that, for a

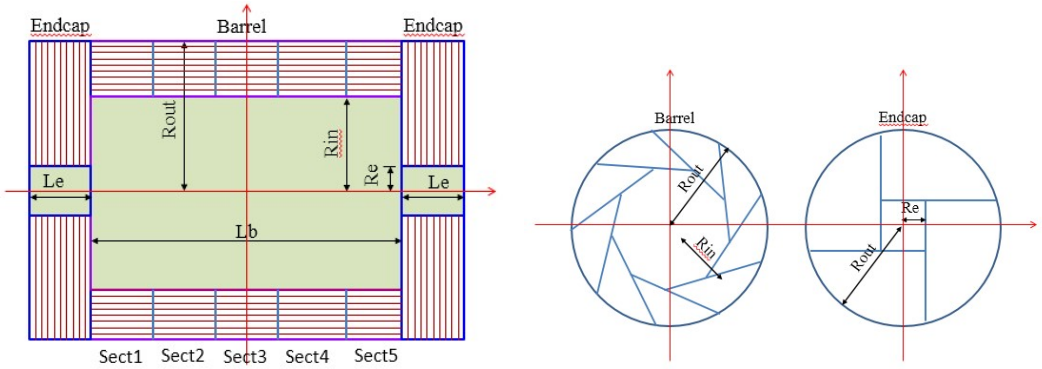

Figure 4.20: HCAL layout in Y-Z plane (left plot), HCAL Barrel layout in X-Y plane (middle plot) and HCAL Endcap layout in X-Y plane (right plot).

calorimeter with cell sizes as small as 1×1 cm^2, a simple hit counting is already a good energy measurement for hadrons. As a result, the readout of each channel can be greatly simplified and just record 'hit' or 'no hit' according to a single threshold (equivalent to a '1-bit' ADC). A hadron calorimeter with such kind of simplified readout is called a Digital Hadron Calorimeter (DHCAL). In a DHCAL, each readout channel is used to register a 'hit', instead of measure energy deposition, as in traditional HCAL. In this context, gas detectors (such as RPC, GEM) become excellent candidates for the active element of a DHCAL. Another technology option is Analog Hadron Calorimeter (AHCAL) which is based on scintillator with SiPM as active sensor.

A drawing of the HCAL structure is shown in Figure 4.20, the barrel part is made of 5 independent and self-supporting wheels along the beam axis. The segmentation of each wheel in 8 identical modules is directly linked with the segmentation of the ECAL barrel. A module is made of 40 stainless steel absorber plates with independent readout cassettes inserted between the plates. The absorber plates consist of a total of 20 mm stainless steel: 10 mm absorber from the welded structure and 10 mm from the mechanical support of the detector layer. Each wheel is independently supported by two rails on the inner wall of the cryostat of the magnet coil. The cables as well the cooling pipes will be routed outside the HCAL in the space left between the outer side of the barrel HCAL and the inner side of the cryostat.

4.3.2 Semi-Digital Hadronic Calorimeter (SDHCAL)

4.3.2.1 Introduction

For the CEPC, a SDHCAl based on gaseous detecor is proposed. This is motivated by the excellent efficiency and very good homogeneity the gaseous detectors could provide. Another important advantage of gaseous detectors is the possibility to have very fine lateral segmentation. Indeed, in contrast to scintillator tiles, the lateral segmentation of gaseous devices is determined by the readout electronics and not by the detector itself. Active layer thickness is also of importance for what concerns the CEPC hadronic calorimeter to be placed inside the magnetic field. Highly efficient gaseous detectors can indeed be built with a thickness of less than 3 mm. Other detectors could achieve such performance. However, gaseous detectors have the advantage of being cost-effective and discharge free. They are also known for their fast timing performance which could be used to perform 4D

construction of the hadronic showers. Such a construction can improve on hadronic showers separation by better associating the energy depots belonging to the same shower from those of other showers. It can also improve on the energy reconstruction by identifying the delayed neutrons and assigning them a different weight.

To obtain excellent resolution of hadronic shower energy measurement a binary readout of the gaseous detector is the simplest and most effective scenario. However, a lateral segmentation of a few millimeters is needed to ensure good linearity and resolution of the reconstructed energy. Such a lateral segmentation leads to a huge number of electronic channels resulting in a complicated readout system design and a too large power consumption. 1x1 cm^2 cells are found to be a good compromise that still provides a very good resolution at moderate energies. However, simulation studies show that saturation effects are expected to show up at higher energies ($> 40\,\mathrm{GeV}$). This happens when many particles cross one cell in the center of the hadronic shower. To reduce these effects, the choice of multi-threshold electronics (Semi-Digital) readout is chosen to improve on the energy resolution by exploiting the particle density in a more appropriate way. These elements were behind the development of a Semi-Digital Hadronic CALorimeter (SDHCAL) that we propose to equip one of the CEPC future experiments.

Even with a 1x1 cm^2 lateral granularity of the readout system, a huge number of electronic channels is still needed. This has two important consequences. The first is the power consumption and the resulting increase of temperature which affects the behavior of the active layers. The other consequence is the number of service cables needed to power, read out these channels. These two aspects can deteriorate the performance of the HCAL and destroy the principle of PFA if they are not addressed properly.

The R&D pursued by the CALICE SDHCAL groups has succeeded to pass almost all the technical hurdles of the PFA-based HCAL. The SDHCAL groups have succeeded to build the first technological prototype [19] of these new-generation calorimeters with 48 active layers of GRPC, $1m^2$ each. The prototype validates the concept of high-granularity gaseous detector and permits to study the energy resolution of hadrons one can obtains with such calorimeter. Figure 4.21 shows the energy resolution of SDHCAL with different number of layers using test beam data collected at CERN. It indicates that SDHCAL with 40 layers yield descent performance with pion energy up to 80 GeV which is suitable for CEPC detector.

A baseline detector of SDHCAL has been designed with 40 layers in total. Each layer contains 20 mm thick stainless steel, 3 mm thick GRPC and 3 mm for readout electronics with 1×1 cm^2 readout pads on PCB board.

In order to find out an appropriate option for the active detector of the SDHCAL, two parallel detector schemes, the Glass Resistive Plate Chamber (GRPC) and the Thick Gaseous Electron Multiplier (THGEM) are proposed for the active layers of the SDHCAL.

4.3.2.2 GRPC based SDHCAL

The GRPC scheme The structure of GRPC proposed as an active layer of the HCAL proposed for CEPC is shown in Figure 4.22. It is made out of two glass plates of 0.7 mm and 1.1 mm thickness. The thinner is used to form the anode while the the thicker forms the cathode. Ceramic balls of 1.2 mm diameter are used as spacers between the glass plates. The balls are glued on only one of the glass plates. In addition to those balls, 13 cylindrical fiber-glass buttons of 4 mm diameter are also used. Contrary to the ceramic balls the buttons are glued to both plates ensuring thus a robust structure. Special spacers

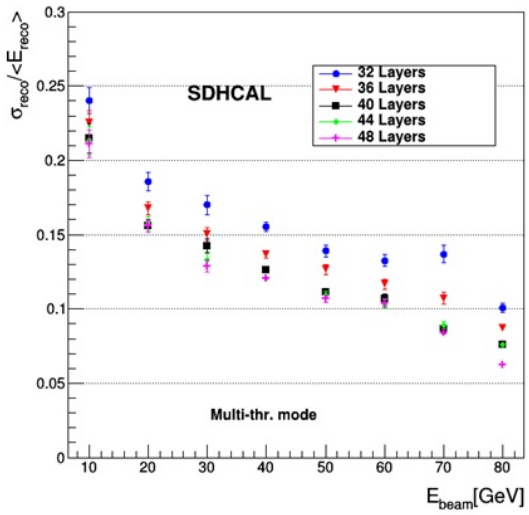

Figure 4.21: The energy resolution of SDHCAL with different number of layers using beam test data collected at CERN.

(ceramic balls) were used to maintain uniform gas gap of 1.2 mm. Their number and distribution were optimized to reduce the noise and dead zones (0.1%).

The distance between the spacers (10 cm) was fixed so that the deviation of the gap distance between the two plates under the glass weight and the electric force does not exceed 45 microns. The choice of these spacers rather than fishing lines was intended to reduce the dead zones (0.1%). It was also aimed at reducing the noise contribution observed along the fishing lines in standard GRPC chambers. The gas volume is closed by a 1.2 mm thick and 3 mm wide glass-fiber frame glued on both glass plates. The glue used for both the frame and the spacers was chosen for its chemical passivity and long term performance. The resistive coating on the glass plates which is used to apply the high voltage and thus to create the electric field in the gas volume was found to play important role in the pad multiplicity associated to a mip [20]. A product based on colloids containing graphite was developed. It is applied on the outer faces of the two electrodes using the silk screen print method, which ensures very uniform surface quality. The measured surface resistivity at various points over a $1m^2$ glass coated with the previous paint showed a mean value of 1.2 $M\Omega/cm^2$ and a ratio of the maximum to minimum values of less than 2 ensuring a good homogeneity of the detector.

Another important aspect of this development concerns the gas circulation within the GRPC taking into account that for the CEPC SDHCAL, gas outlets should all be on one side. A genuine system was proposed. It is based on channeling the gas along one side of the chamber and releasing it into the main gas volume at regular intervals. A similar system is used to collect the gas on the opposite side. A finite element model has been established to check the gas distribution. The simulation confirms that the gas speed is reasonably uniform over most of the chamber area. The GRPC and its associated electronics are housed in a special cassette which protects the chamber and ensures that the readout board is in intimate contact with the anode glass. The cassette is a thin box consisting of 2.5 mm thick stainless steel plates separated by 6 mm wide stainless steel spacers. Its plates are also a part of the absorber.

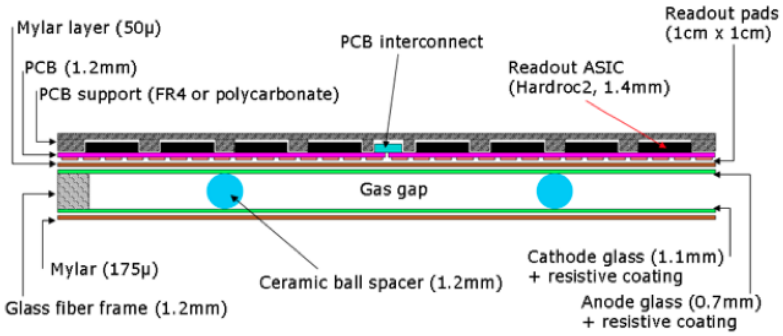

Figure 4.22: Cross-section through a 1 m^2 chamber.

The electronics board is assembled thanks to a polycarbonate spacer which is also used to fill the gaps between the readout chips and to improve the overall rigidity of the detector. The electronics board is fixed on the small plate of the cassette. Thanks to tiny screws and the new set is fixed on the other plate which hosts the detector and the spacers. The whole width of the cassette is 11 mm with only 6 of them corresponding to the sensitive medium including the GRPC detector and the readout electronics.

GRPC technological prototype An SDHCAL prototype fulfilling the efficiency, robustness and the compactness requirements of the future PFA-based leptonic collider experiments [19] was built. 48 cassettes as the one described above were built. They fulfilled a stringent quality control. It is worth mentioning that 10500 HR ASICs were produced and tested using a dedicated robot for this purpose. The yield was found to be higher than 92%. The ASICs were then fixed on the PCBs to make a $1m^2$ and itself fixed on the cassette cover once successfully tested. The cassettes were inserted in a self-supporting mechanical structure that was conceived and built in collaboration with the Spanish group of CIEMAT. The structure is made of Stainless Steel plates of 1.5 cm each. The plates were machined to have an excellent flatness and well controlled thickness. The flatness of the plates was measured using a laser-based interferometer system. It was found that the flatness of the plates are less than 500 microns. In April 2012 the prototype was exposed to pion, muon, electron beams of both the PS and the SPS of CERN Figure (4.23). The data were collected continuously in a triggerless mode. Figure 4.24 shows the efficiency (left) and pad multiplicity (right) of the prototype's GRPC chambers measured using the muon beam. Figure 4.25 shows a display of two events collected in the SDHCAL. One is a produced by a pion interaction (left) and the other by an electron interaction (right).

The SDHCAL prototype results obtained with a minimum data treatment (no grain correction) show clearly that excellent linearity and good resolution [21] could be achieved on large energy scale as can be shown in Figure 4.26 where results obtained in two different beam lines are obtained using the same detector configurations. Useless to mention that the high granularity of the SDHCAL allows one to study thoroughly the hadronic showers topology and to improve on the energy resolution by, among others, separating the electromagnetic and the hadronic contribution. The separation between close-by showers will also get big benefit thanks to the high granularity on the one hand and to the very clean detector response (< 1 Hz/cm^2) on the other hand. The results obtained with the the SDHCAL [22] confirm the excellent efficiency of such separation thanks to the SDHCAL performance.

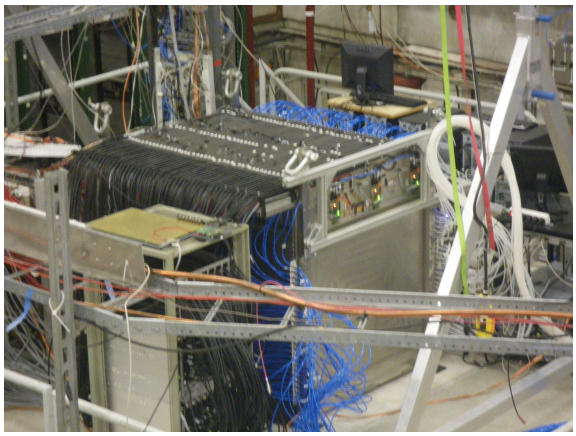

Figure 4.23: The SDHCAL prototype in beam test at CERN.

The quality of data obtained during several campaigns of data taking at the CERN PS and SPS beam lines validates completely the SDHCAL concept. This is especially encouraging since no gain correction was applied to the electronics channels to equalize their response. Still, improvement was further achieved by applying gain and threshold correction schemes in terms of the calorimeter response homogeneity.

A digitizer describing the response of the GRPC within the SDHCAL was developed [23]. It allows to study the SDHCAL behavior in a realistic manner in the future experiments.

In parallel to the prototype construction, a single cassette was tested in a magnetic field of 3 Tesla (H2 line at CERN) applying the power-pulsed mode. The TB results [24] indicated clearly that the use of the power-pulsed mode in such a magnetic field is possible. The behavior of the detector (efficiency, multiplicity..) was found to be similar to those obtained in the absence of both the magnetic field and the power-pulsed mode.

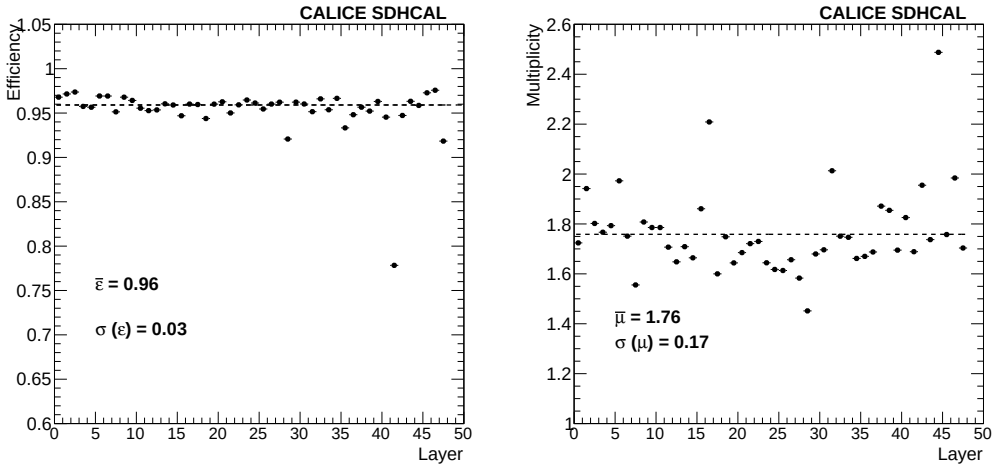

Figure 4.24: Left: Efficiency of the GRPC detectors of the SDHCAL. Right: the pad multiplicity of the GRPCs. One third of the chamber 42 was not instrumented.

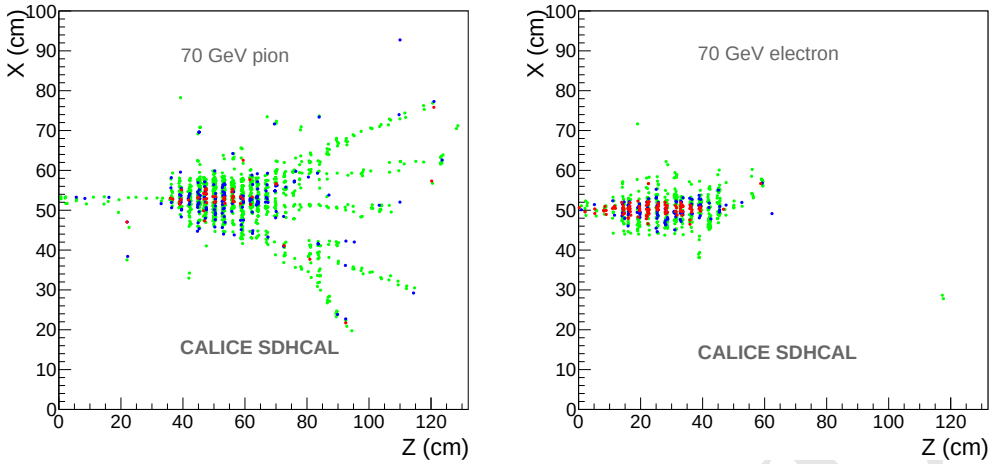

Figure 4.25: Left: event display of an 70 GeV pion interaction in the SDHCAL prototype. Right: Event display of a 70 GeV electron interaction in the SDHCAL prototype.

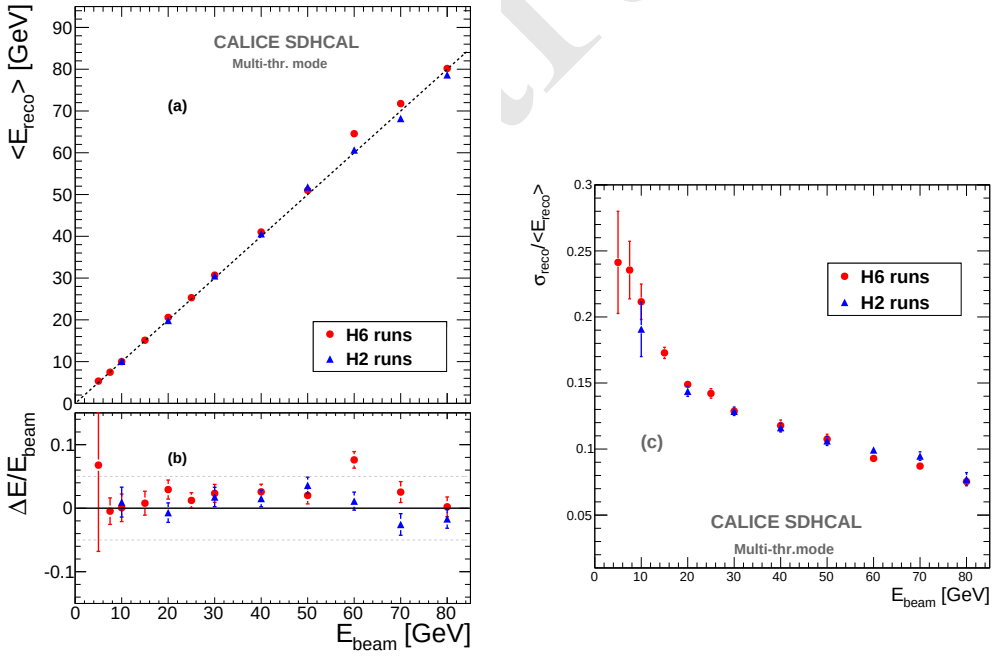

Figure 4.26: Left: a) Reconstructed energy of the hadronic showers collected in both H2 and H6 SPS beamlines. b) the relative deviation of the reconstructed energy with respect to the beam energy. Right: Relative energy resolution of the reconstructed hadronic shower.Pion beam of H6 beamline is largely contaminated by protons at high energy (>50 GeV).

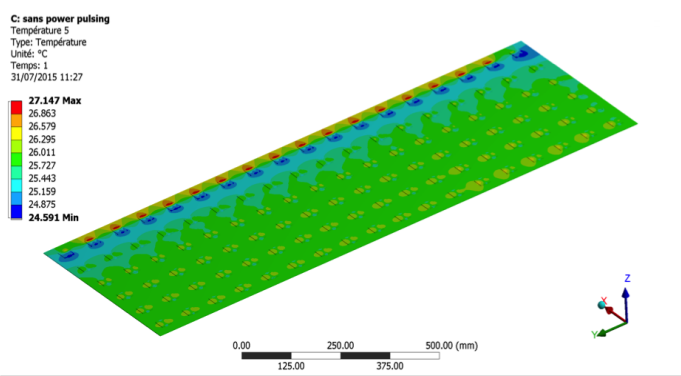

Figure 4.27: Temperature distribution in an active layer of the SDHCAL operated with no power-pulsing. The cooling system is made of a circulating water inside copper tubes in contact with the ASICs.

Current SDHCAL R&D Large GRPC of $1m^2$ were developed and built for the technological prototype. However, larger GRPC are needed in the SDHCAL proposed for future leptonic collider experiments. These large chambers with gas inlet and outlet on one side need a dedicated study to guarantee a uniform gas gap everywhere notwithstanding the angle of the plate. It is necessary also to ensure an efficient gas distribution as it was done for the 1m2 chambers. To obtain this different gas distribution systems were studied. A new scheme with two gas inlets and one outlet was found to ensure an excellent homogeneity of the gas distribution. This system will be used in the near future to build large detectors exceeding $2m^2$.

To cope with the heating produced by the embedded readout system in case of limited or even the absence of use of the Power Pulsing system, a new active cooling system is being studied. Figure 4.27 shows a study of a water-based cooling system to absorb the excess of heat in the SDHCAL. The cooling system is very simple but very effective as well. It allows to keep the average temperature as well as the temperature dispersion of the GRPC well under control.

4.3.2.3 THGEM-based DHCAL

The THGEM scheme The THGEM can be built in large quantities at low cost, which might make them suitable for the large CEPC HCAL. THGEM detectors can provide flexible configurations, which allow small anode pads for high granularity. They are robust and fast, with only a few nano-seconds rise time, and have a short recovery time which allows a higher rate capability compared to other detectors. They are operated at a relatively low voltage across the amplification layer with stable high gain. The ionisation signal from charged tracks passing through the drift section of the active layer is amplified using a sigle layer or WELL-type THGEM structure. The amplified charge is collected at the anode layer with pads at zero volts. As the HCAL is located within the coil, WELL-THGEM, a single layer structure with thinner thickness, as shown in Fig. 4.28, can be considered as the sensitive medium, to keep the HCAL compact.

Digital readout has been proposed to limit the total amount of data, which simplifies the data treatment without comprising the energy resolution performance. The readout electronics of the DHCAL will be integrated into the sensitive layer of the system, thus minimising dead areas. Large electronics boards are assembled together to form extralarge

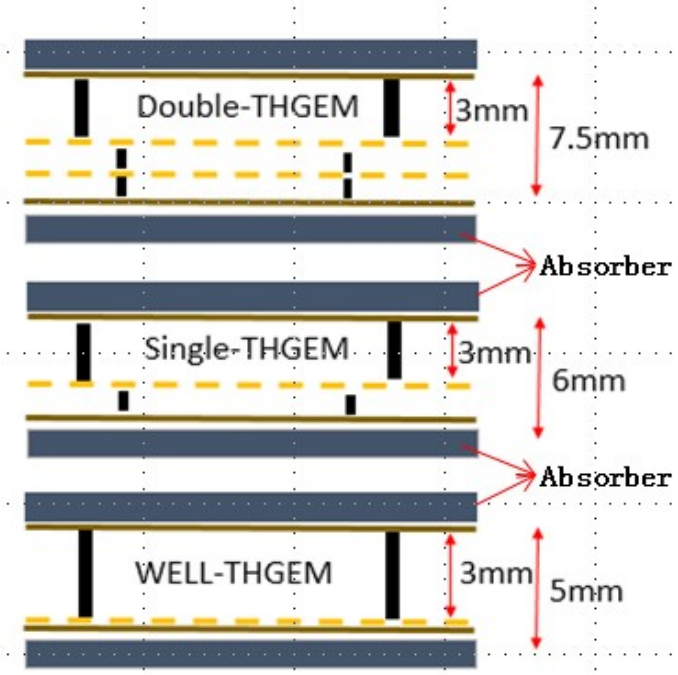

Figure 4.28: Structure of THGEM based detector for DHCAL.

boards before being attached to the THGEM. The board assembly will utilise a mechanical structure made of 4 mm stainless steel plate. In addition, to keep the HCAL as compact as possible, the fully equipped electronic boards are designed to be less than 2 mm thick in total.

A THGEM based detector for DHCAL has been designed with 40 layers in total. Each layer contains 2.0 cm thick stainless steel, 0.8 cm thick THGEM and readout electronics with 1×1 cm^2 readout pads. As THGEM production technology matures, the maximum area of THGEM is limited only by the size of the CNC drilling area. Its low price, robustness against occasional discharges, high gain and count rate capability of up to 10MHz/cm^2 make THGEM very attractive for building the DHCAL. As illustrated in Fig. 4.28, the total thickness of the sensitive medium is 5 mm, which consists of 3 mm drift gap, 1 mm transfer gap and 1 mm induction gap. The absorber between the active layers is made of 20 mm thick stainless steel. The thickness of the readout electronics board is about 3 mm, and the total thickness of a single sensitive layer is less than 10 mm. Each layer corresponds to about 1.2 radiation length and 0.65 nuclear interaction length. The whole DHCAL detector is evenly divided into 40 layers, with a total stainless steel absorber thickness of 4.7 nuclear interaction lengths.

THGEM prototype A THGEM with an area of 40×40 cm^2 has been successfully fabricated, as shown in Fig. 4.30, and a gain of 2×10^5 has been achieved with a double THGEM, with an energy resolution of about 20%. The THGEM produced has the following features: 1)standard PCB processes are used, which keeps the cost low; 2) excellent performance in terms of energy resolution, gas gain and stability (as shown in Fig. 4.29); 3) Rim around the hole formed by full-etching process, the size of which can be varied between 10 μm and 90 μm, as depicted in Fig. 4.29 - this allows adjustment according to gas requirements.

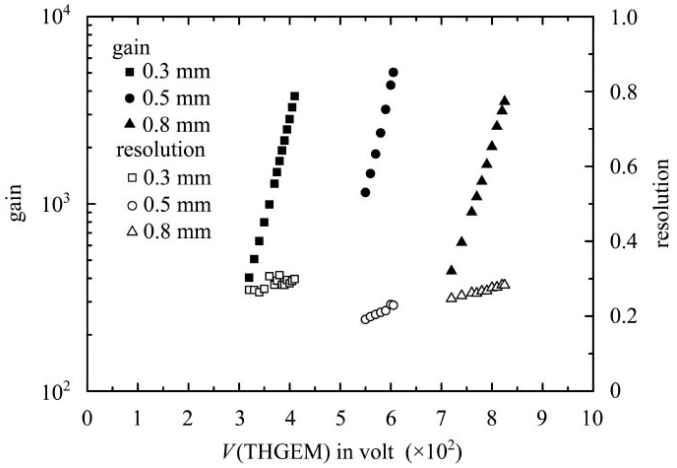

Figure 4.29: Gain and energy resolution of THGEM detector obtained with ^{55}Fe.

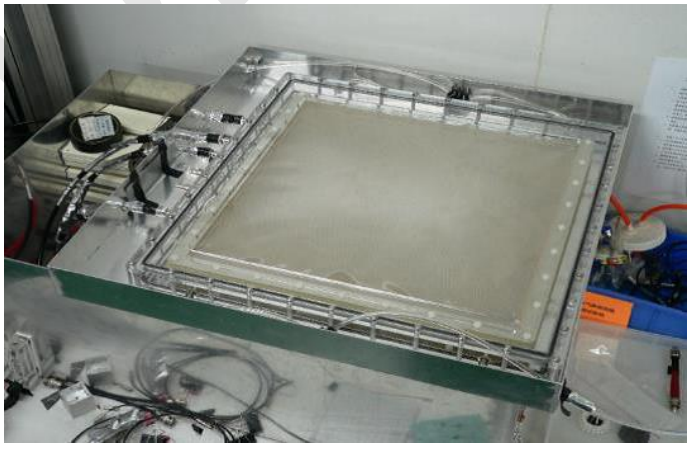

Figure 4.30: The maximum size of THGEM produced in domestic currently (40×40 cm^2).

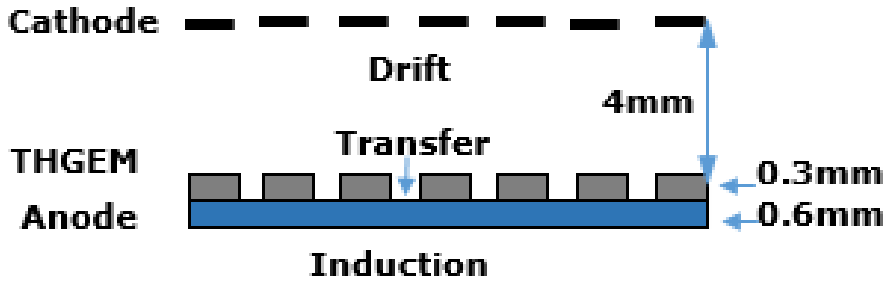

Figure 4.31: The schematic diagram of the WELL-THGEM.

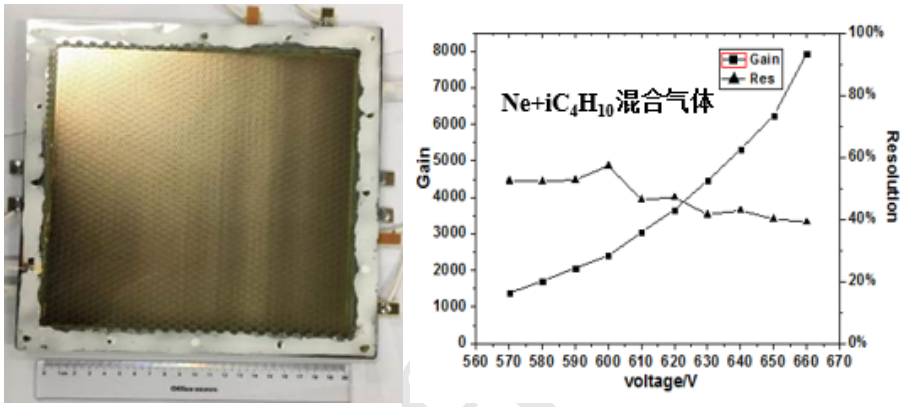

Figure 4.32: The photograph(left) and performance (right) of the WELL-THGEM detector.

Fig. 4.31 shows the schematic diagram of a new THGEM detector, where a micro-plate directly attached to the readout plate, since the micro-porous structure similar to a well, known as the well-type THGEM (WELL-THGEM). This structure contains of a single-layer THGEM, so that the thickness of detector can be reduced to $4 \sim 5$ mm, and the total thickness of the detector including ASIC electronics could be lowered to about 6 mm.

A $20cm \times 20cm$ WELL-THGEM detector using thin-type THGEM have been developed, and the basic performances such as the gain curve, uniformity and energy resolution were studied and shown in Fig. 4.32.

In addition, Researches on large THGEM detectors have been carried out. Single THGEM detectors and Well-THGEM detectors are being developed to reduce detector instability and inefficiency. Gas recycling systems are built to lower gas consumption and pollution. The achieved THGEM detection rate of 1 MHz/cm^2 with efficiency greater than 95% already meets the CEPC requirements.

THGEM digital readout system A MICRO-mesh gaseous structure Read-Out Chip (MICROROC), which is developed at IN2P3 by OMEGA/LAL and LAPP microelectronics groups was used to read out the THGEM-based SDHCAL. The MICROROC is a 64-channel mixed-signal integrated circuit based on 350 nm SiGe technology. Each channel of the MICROROC chip contains a very low noise fixed gain charge preamplifier which is optimized to cover a dynamic range from 1 fC to 500 fC and allow a input detector capacitance of up to 80 pF, two gain-adjustable shapers, three comparators for triple-threshold readout and a random access memory used as a digital buffer. Otherwise, it have a 10-bit DAC, a configuration register, a bandgap voltage reference, a LVDS receiver shared by 64

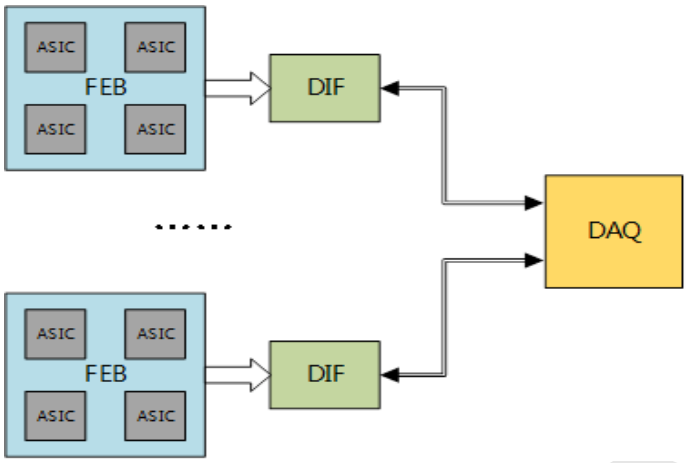

Figure 4.33: The schematic diagram of the readout system.

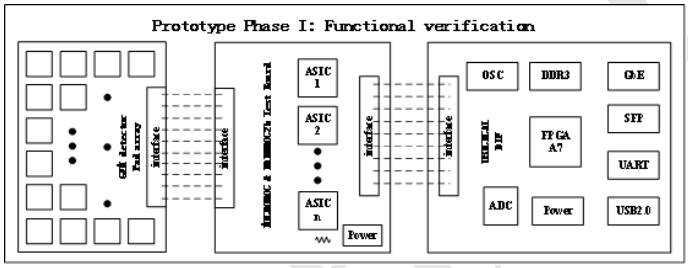

Figure 4.34: The diagram of the phase I design.

Figure 4.35: Pictures for the phase I design.

channels etc. A 1.4 mm total thickness is achieved by using the Thin Quad-Flat Packaging (TQFP) technology.

The readout system structure as shown in Fig. 4.33 is developed on the Scalable Readout System (SRS). It is composed of a front-end board (FEB), a detector interface board (DIF) and a data acquisition card (DAQ). The FEB (also called ASU-Active Sensor Unit) carries all the front-end ASIC, together with the readout plane of GEM detector. The DIF in charge of ASIC control and data connection, plugs to the FEB using high density connector. The DAQ card is designed to serve several DIF boards. It distributes the clock, command and trigger to different DIF and gather the data from DIF boards.

A phase I design (in Fig. 4.34 and Fig. 4.35) is completed to verify this kinds of readout structure and to test the performance of the MICROROC chip. In this design we separate the front-end ASIC from the detector readout plane for single test the ASIC. It contains the readout array of the GEM detector, front-end ASIC board and DIF board.

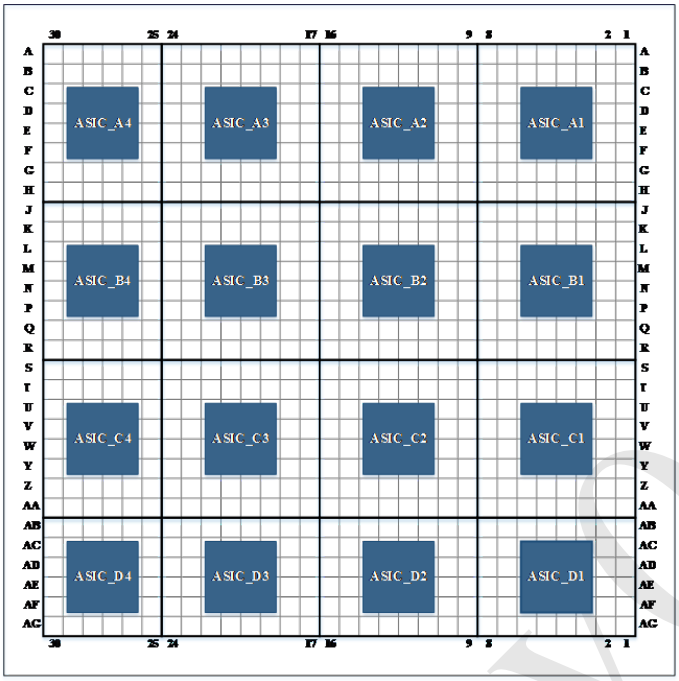

Figure 4.36: The Design scheme for next stage FEB.

In order to optimize the design, a next stage design (shown in Figure 4.36) based on the test results have been proposed and put into effort. In this version, the MICROROC chips are planed to be mounted on the bottom side of the readout plane, utilizing blind buried via technology. A 10-layer PCB with 3 ground plane and 2 power plane will ensure good signal integrity and low crosstalk.

4.3.3 AHCAL based on Scintillator and SiPM

A high-granularity hadronic calorimeter plays an essential role in PFA-based experiments such as CEPC. It allows separation of the energy deposits from charged and neutral hadrons. The contribution of the neutrals to the jet energy, around 10% on average, fluctuates over a wide range from event to event. The AHCAL (Analog Hadron CALorimeter) is a sampling calorimeter with steel as the absorber and scintillator tiles with embedded electronics. The moderate ratio of hadronic interaction length (I=17cm) to electromagnetic radiation length (X_0 = 1.8 cm) of steel, allows a fine longitudinal sampling in terms of X_0 with a reasonable number of layers.

Various calorimetry options are being developed to address challenges from the stringent performance requirements on future lepton collider experiments for precision measurements of the Higgs boson and for searches of physics beyond Standard Model. Within the CALICE collaboration, a large technological prototype [25] using scintillator tiles and SiPMs is currently being built to demonstrate the scalability to construct a final detector via automated mass assembly. The outcome of CALICE-AHCAL R&D activities can be an essential input for the conceptual design of the hadron calorimeter system at the future lepton colliders.

4.3.3.1 AHCAL geometry and simulation

The AHCAL will consist of 40 sensitive and absorber layers, and the total thickness is about 100cm. The AHCAL barrel consists of 32 super module, each super module consists 40 layers, figure 4.37 shows the AHCAL structure. Figure 4.38 shows the single layer structure of AHCAL. The scintillator tiles wrapped by reflective foil are used as sensitive medium, interleaved with stainless steel absorber. The thickness of active layer including the scintillator and electronics is about 4mm 5mm.

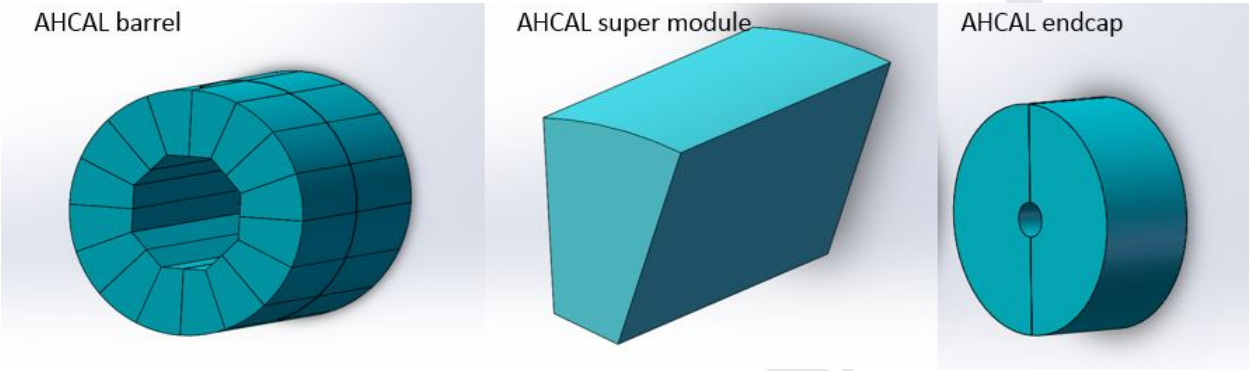

Figure 4.37: Side view of one layer in AHCAL

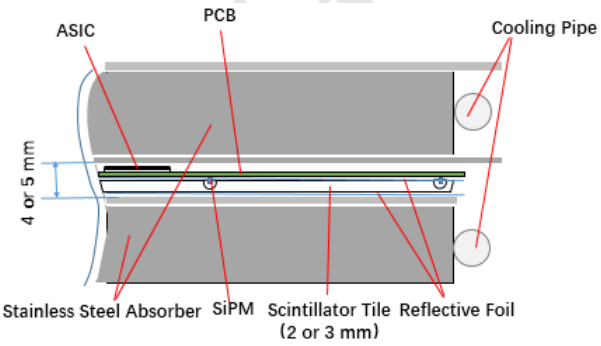

Figure 4.38: Side view of one layer in AHCAL

The structure of scintillator tiles is shown in Figure 4.39. A dome-shaped cavity was processed in the center of the bottom surface of each tile by injection molding technology. The diameter and height of cavity [26] are 6mm, 1.5mm, respectively, as shown in Figure 4.39 (right). Good response uniformity and low dead area will be achieved by the design of cavity. More optimizations of cavity structure will be done by Geant4 simulation.

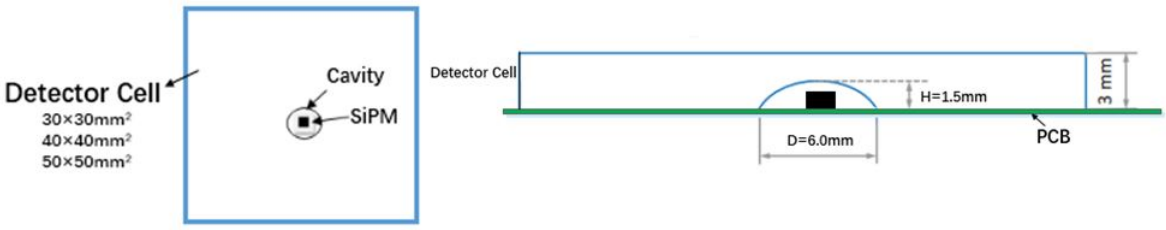

Figure 4.39: Top view of a detector cell (left) and sectional view of a detector cell with a dome-shaped cavity (right)

The AHCAL prototype detector was simulated by Geant4. The detector model used here was CEPC_v1 detector model. The geometry information was extracted by Mokka at runtime and the generated events were stored in Slcio, which contains primary information regarding the energy deposition, hit position, time and Monte Carlo particle causing the energy deposition. The ECAL was simulated with 30 layers, and the HCAL has 40 active layers interleaved with 20 mm stainless steel as absorber plates. Each active layer consists of plastic scintillator (3mm) and readout layer (2mm PCB), detector cell size is $30\times30\times3$ mm^3, as shown in Figure 4.40.

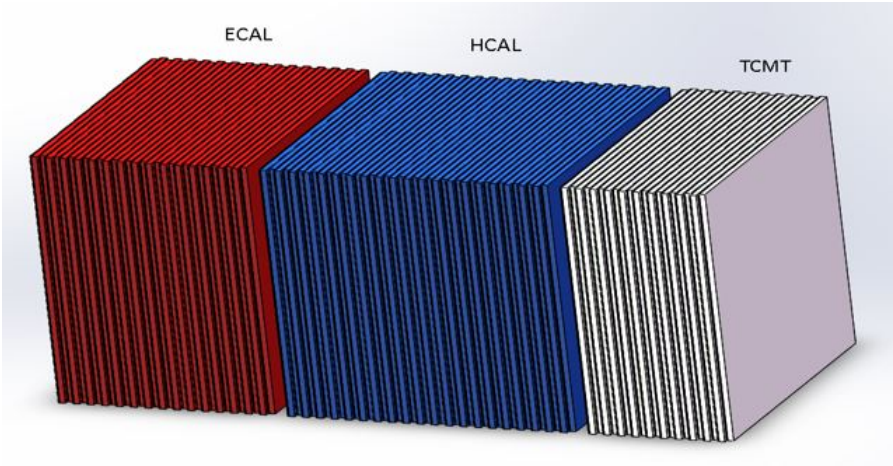

Figure 4.40: The structure of simulated calorimeters which is a part of the simplify geometry. Red part is the the Silicon ECAL, Blue part is the scintillator AHCAL

$$E_{REC} = a \times E_{ECAL} + b \times E_{HCAl} \tag{4.3}$$

In order to obtain the resolution of calorimeters (ECAL and AHCAL) as shown in figure 4.40, the energy reconstruction formula 4.3 is employed [27], the coefficients a and b in this formula represent ECAL and HCAl calibration constant, respectively. After optimization, the calibration constants are a=44.4 and b=44.2 respectively which were corrected by energy of 60GeV. Calibration constants can correct the energy leakage from the calorimeters. So one can use formula 4.4 [27] to calculate the resolution. The energy resolution result is shown in figure 4.41.

$$\frac{\sigma}{E} = \frac{p_0}{\sqrt{E}} + p_1 \tag{4.4}$$

4.3.3.2 Plastic Scintillator detector cell design and test

According to study of CALICE collaboration, 30×30mm^2 scintillator detector cell size is an optimal size. The simulation results of CALICE collaboration [28] also suggest that it is possible to use the detector cells of larger sizes. It will reduce nearly half electronics channels by using 40×40mm^2 size detector cell instead of 30×30mm^2 size. Therefore, the construction costs can be greatly reduced if the larger detector cells can meet the physics requirements. Two larger sizes of detector cells were considered. Four kinds of scintillator tiles with different sizes were fabricated and tested.

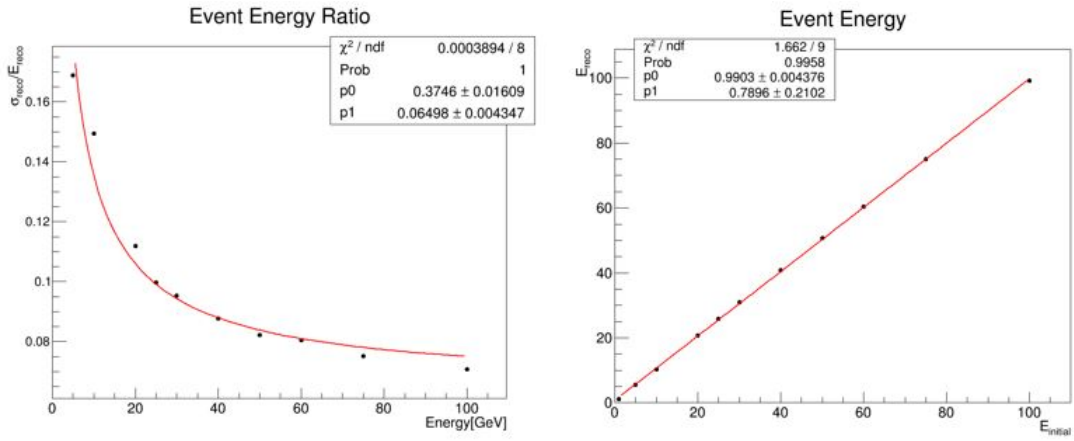

Figure 4.41: Left figure is energy resolution, right figure is the result of reconstruction energy linearity

The SiPM is soldered onto a readout Printed Circuit Board (PCB) and the scintillator tile wrapped by ESR reflective foil is directly glued onto the PCB. A cavity design provides enough space for the SiPM package and improves collection efficiency of the light produced by incident particles penetrating the tile at different positions.

A strongly non-uniform tile response can lead to a distortion of the energy reconstruction in a complete calorimeter, and also compromises the calibration of the detector cells based on single particle signals. Three different sizes tiles ($30\times30\times3mm^3$, $30\times30\times2mm^3$ and $50\times50\times3mm^3$) were tested by the Hamamatsu MPPC S12571-025P and S13360-025PE. The spatial distribution of photon equivalents number (p.e.) with different detector cell areas are shown in Figure 4.42. The result shows that the number of p.e. in the center area is slightly larger than that of the surrounding area. The 100% of the cell signal amplitude is within 10% deviation from the mean value for $30\times30mm^3$ cell. The 94% of the cell signal amplitude is within 10% deviation from the mean value for $50\times50\times3mm^3$ cell. The three detector cells show good response uniformity.

Seven detector cells of different sizes, polishing methods and wrapping foil types were measured. The larger the area of the cell is, the less p.e. are detected, and the results of same size cells varied greatly because of the polishing methods.

The detection efficiency of $30\times30\times3mm^3$ and $50\times50\times3mm^3$ were measured by the cosmic ray test. The detection efficiency of $30\times30\times3mm^3$ and $50\times50\times3mm^3$ cells are 99%, 98.2%, respectively. According the cosmic-ray test result, the detection efficiency of $30\times30\times2mm^3$ with S13360-025PE MPPC also can reach to 98%.

The good response uniformity and high detection efficiency results indicate that scintillator detector cells are acceptable for AHCAL. The size of $30\times30\times3mm^3$ detector cell is the baseline of AHCAL and more optimization of the detector cell size will be done by the simulation and experiment.

4.3.3.3 Development of SiPM

Several kinds of SiPM were developed by Hamamatsu and other company, they have been used for scintillator ECAL. The SiPM with epitaxial quenching resistors (EQR SiPM) is one of the main SiPM technologies under development in China. As shown in Figure 4.43, each APD cell (pixel) forms a high electric field, composing an enriched region between N-type epitaxial silicon substrate and P++ cap layer, and it employs the un-depleted

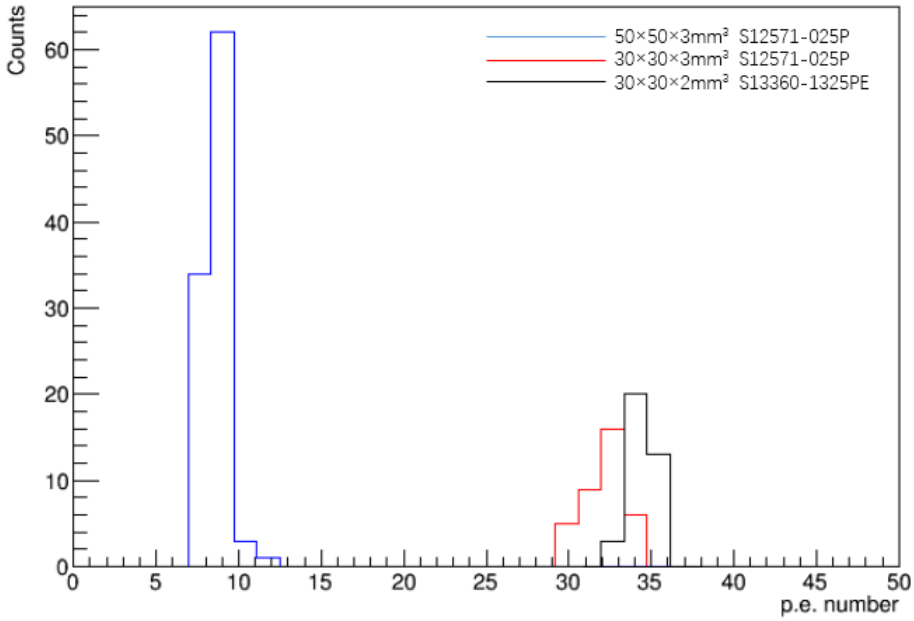

Figure 4.42: The uniformity measurement result of $30\times30\times3mm^3$, $50\times50\times3mm^3$ and $30\times30\times2mm^3$ detector cell

region in the epitaxial silicon layer below P/N junction as the quenching resistor. Compared to conventional SiPM configurations that employ poly-silicon quenching resistors on the device surface, it is easier to achieve high density and small micro APD cells, thus obtaining a small junction capacitor; It's expected to have short recovery time and high couting rate for EQR SiPM.

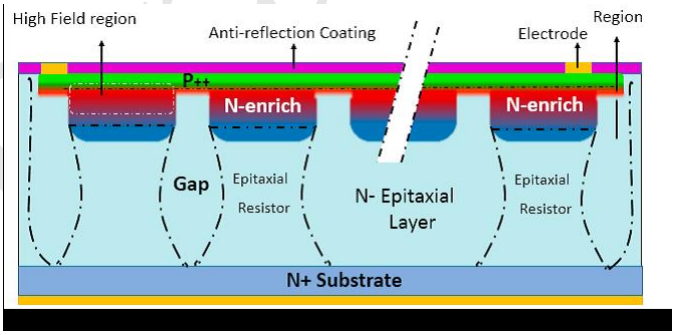

Figure 4.43: Schematic structure of EQR SiPM; APD cell consists of N-enriched regions forming high electric fields between the N-type epitaxial silicon wafer and the P++ surface layer, the un-depleted region in the epitaxial silicon layer below the P/N junction as the quenching resistor, and the APD cells are isolated from each other by the Gap depletion region.

4.3.3.4 Electronics and DAQ

Front-end electronics ASIC: High-density electronics is indispensable to instrumentation of high-granularity calorimetry. An ASIC chip named SPIROC, developed by the OMEGA group, is capable to handle 36 SiPMs. For each channel, it can be operated in an auto-trigger mode and has a dual-gain charge preamplifier with high dynamic range. It allows to measure the charge from 1 to 2000 photo-electron and the time within 1 ns using

a 12-bit digitizing circuit. With one 8-bit 5V input DAC per channel, the bias voltage for each SiPM can be adjusted to reach its optimum. In each channel, there are 16 analogue memory cells that can buffer both charge and timing signals to be digitized afterwards consecutively. The digitization circuit is shared for both charge and timing measurements to minimize the power consumption, which needs to be as low as 25 μW per channel.

4.3.3.5 Cooling system

Inside active layer, the total power consumption of SPIROC ASIC chip and SiPM is about 5 mW/channel [29]. The scintillator detector cell size is 30×30mm^2, and the total channel number is about 5 million. For whole AHCAL, the total power consumption from ASIC chip is about 30kW. The copper cooling water pipes is expected to embed in stainless steel absorber. It is shown in layer structure as in figure 4.38. Detailed design and optimization of a cooling system is needed.

4.4 Dual-readout calorimetry

4.4.1 Introduction

The dual-readout approach envisages designing a combined, homogeneus, detector with excellent performance for both electromagnetic and hadronic particle showers.

Till now, the performance obtained in hadronic energy measurements has been by far worse than for the electromagnetic ones, since showers from single hadrons or jets develop an electromagnetic component, from π^0 and η production, that exhibits large event-by-event fluctuations and dependence on the particle type and energy [30].

As a matter of fact, the em fraction depends on the kind of particle initiating the shower (e.g., π, K, p) since, for example, impinging $\pi^{\pm}$ mesons can undergo a charge-exchange reaction with a nucleon as first interaction and generate a pure em shower, while a p cannot do that due to baryon number conservation.

Moreover, since π^0 production happens at any stage of shower development, the $< f_{em} >$ increases with the energy as well as with the depth ("age") of the shower.

The em and $non-em$ components of a hadronic shower are normally sampled with very different sensitivity, producing large differences in the measured signals, heavily affecting the energy resolution capability.

To overcome the problem two methods have been exploited: compensation and dual readout (DR). The first relies on equalising the detector response to electromagnetic (e) and non-electromagnetic (h) shower particles (i.e. $h/e = 1$), but this requires a fixed ratio of absorber-to-sensor volumes, which limits the electromagnetic energy resolution, and the integration of the signals over large volumes and long times, to increase the response to the h component. The dual-readout method avoids these limitations by directly measuring f_{em} on an event-by-event basis. The showers are sampled through two independent processes, namely scintillation (S) and Čerenkov (C) light emissions. The former is sensitive to all ionizing particles, while the latter is produced by highly relativistic particles only, almost exclusively found inside the em shower component. By combining the two measurements, energy and f_{em} of each shower can be simultaneously reconstructed. The performance in hadronic calorimetry may be boosted toward its ultimate limit.

The results obtained so far with prototypes, support the statement that fibre-sampling DR calorimeters may reach resolutions of the order of $10\%/\sqrt{E}$ for em showers and

around $30 - 40\%/\sqrt{E}$ for hadronic showers, coupled with strong standalone particle-ID capabilities. This would allow $W \to jj$ separation from $Z \to jj$ by invariant mass, high-precision missing three-momentum reconstruction by subtraction, e-μ-π separation and particle tagging.

While the dual-readout concept has been extensively demonstrated and experimentally validated in a series of beam tests, the use of standard Photo-Multiplier (PM) tubes to read out the S and C light has so far limited its development towards a full-scale system compliant with the integration in a particle detector at a colliding beam machine. These limitations should be overcome using SiPM, low-cost solid-state sensors of light with single photon sensitivity, magnetic field insensitivity and design flexibility.

As it will be shown in the following, the high readout granularity in the plane perpendicular to the shower development and few other signal properties will probably make redundant or even inessential the need of a longitudinal segmentation into em and hadronic compartments (that is anyway possible). In case of a segmented calorimeter, both compartments need to provide dual-readout signals, in order to allow for the measurement of $< f_{em} >$.

4.4.2 Principle of dual-readout calorimetry

The independent sampling of hadronic showers, through scintillation and Čerenkov light emission, allows one to fully reconstruct, at the same time, energy and f_{em} of hadronic showers. In fact, the total detected signals, measured with respect to the electromagnetic energy scale, can be expressed as:

$$S \;=\; E\,[\; f_{em} \;+\; \eta_S \cdot (1 - f_{em})\;] \tag{4.5}$$

$$C \;=\; E\,[\; f_{em} \;+\; \eta_C \cdot (1 - f_{em})\;] \tag{4.6}$$

where $\eta_S = (h/e)_S$ is the ratio of the average S response for the non-em component to the em component in hadronic showers. The response being defined as the average signal per unit of deposited particle energy. $\eta_C = (h/e)_C$ is the same for the C signal. In a typical dual-readout calorimeter, $\eta_S \approx 0.7$ and $\eta_C \approx 0.2$. These two equations are easily solved giving:

$$\frac{C}{S} \;=\; \frac{[\; f_{em} \;+\; \eta_C \cdot (1 - f_{em})\;]}{[\; f_{em} \;+\; \eta_S \cdot (1 - f_{em})\;]} \tag{4.7}$$

$$E \;=\; \frac{S \;-\; \chi C}{1 \;-\; \chi} \tag{4.8}$$

where:

$$\chi \;=\; \frac{1 - \eta_S}{1 - \eta_C} \;=\; \cot\,\theta \tag{4.9}$$

This is the simplest formulation of hadronic calorimeter response: an em part with relative response of unity, and a $non - em$ part with relative response η.

There are two unknowns for each shower, E and f_{em}, and two measurements S and C. The electromagnetic fraction, f_{em}, is determined entirely by the ratio C/S, and the shower energy calculated as in Eq. 4.8. Both, S and C, $\eta = (h/e)$ ratios have event-by-event fluctuations and should be considered stochastic variables, nevertheless the average

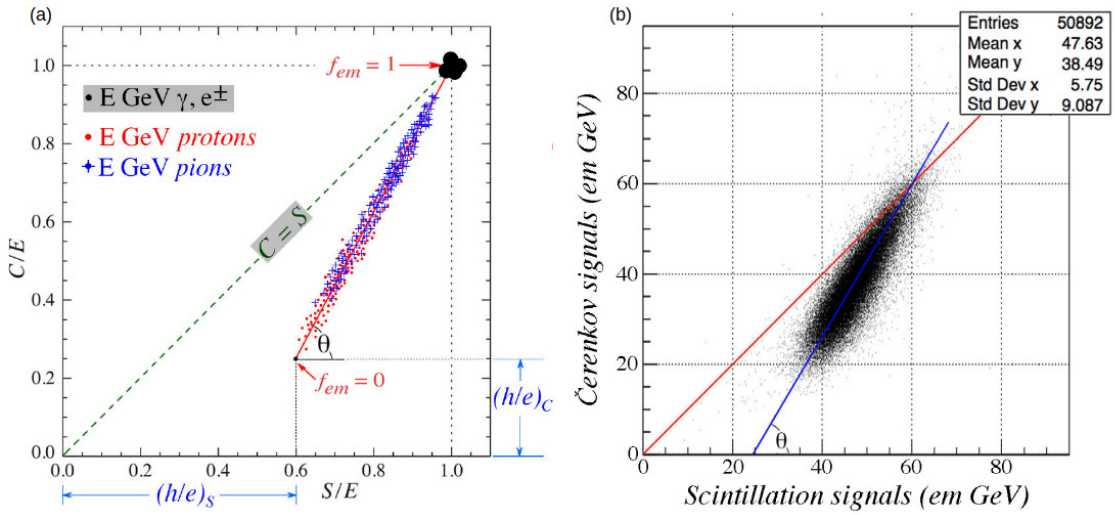

Figure 4.44: (a) Scatter plot of C/E versus S/E in a dual-readout calorimeter for p and π; (b) scatter plot of C and S signals for 60 GeV pions in the RD52 lead-fibre calorimeter.

$<h/e>$ values are essentially independent of hadron energy and species [31–33]. The global parameter χ can be extracted with a fit to calibration data:

$$\chi = \frac{E_0 - S}{E_0 - C} \tag{4.10}$$

$$S = (1-\chi)E_0 + \chi C \tag{4.11}$$

where E_0 is the beam energy.

The geometrical meaning of the θ angle in Eq. 4.9 can be understood by looking at the scatter plot of C versus S signals in Figure 4.44. An illustration of the prediction for the scatter plot for protons and pions is shown in Fig. 4.44(a) and the scatter plot for 60 GeV pions measured in the RD52 lead-fibre calorimeter is shown in Fig. 4.44(b).

The plot in Figure 4.44(b) shows that the data points are located on a locus, clustered around a line that intersects the $C/S = 1$ line at the beam energy of 60 GeV. In first approximation, the signal generated in the Čerenkov fibres is produced only by the em components of the hadron showers. The smaller the em fraction f_{em}, the smaller the C/S signal ratio.

All signals are relative to the em scale meaning that both the Čerenkov and the scintillation responses are calibrated with beam electrons only, i.e. no hadronic calibration is required. This is one of the most qualifying and important points of dual-readout calorimetry.

The effectiveness of this approach has been demonstrated by the DREAM/RD52 collaboration over a 15-year research program with a variety of detector solutions. Results and simulations [34–39] provide, so far, confidence that a fibre-sampling calorimeter, even without longitudinal segmentation, may meet the requirements of the CepC physics programme in a cost-effective way. Linearity and energy resolution, for both em and hadronic showers, $e/\pi/\mu$ separation, spatial resolution, all show adequate performance.

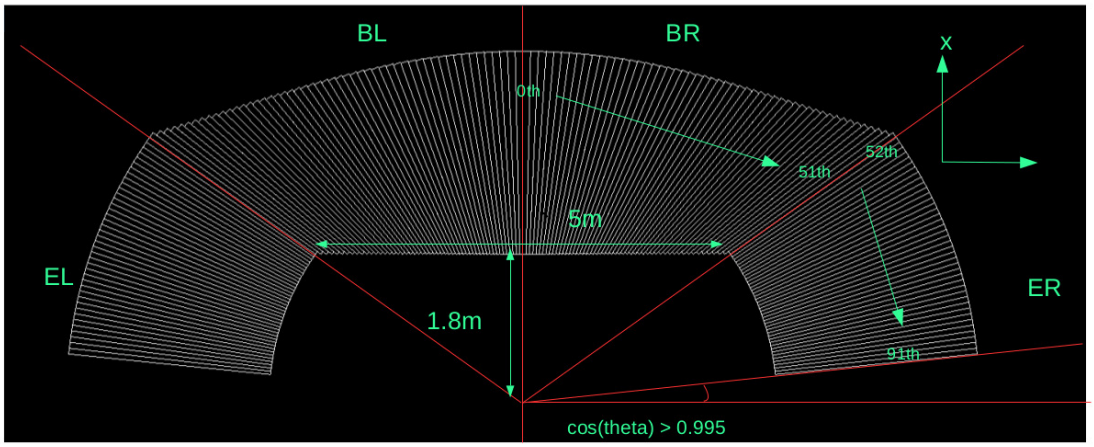

Figure 4.45: A possible 4π solution (called "wedge" geometry).

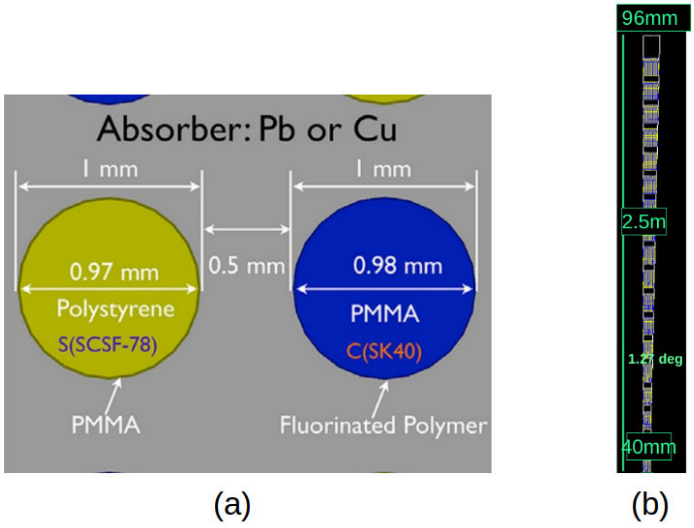

Figure 4.46: (a) Fibre arrangement inside the modules. (b) Dimensions of a module in the barrel region (at $\eta = 0$): from inside to outside the number of fibres more than doubles.

4.4.3 Layout and mechanics

4.4.3.1 Layout

A possible projective layout ("wedge" geometry, Figure 4.45) has been implemented in the simulations. Based on the work done for the 4th Detector Collaboration (described in its Letter of Intent [40]), it covers, with no cracks, the full volume up to $|cos(\theta)| = 0.995$, with 92 different types of towers (wedges). A typical one in the barrel region is shown in Figure 4.46(b), together with the fibre arrangement (Figure 4.46(a)): it has an acceptance of $\Delta\theta \times \Delta\phi = 1.27° \times 1.27°$, a depth of about 250 cm ($\sim 10\ \lambda_{\mathrm{Int}}$), and contains a total of about 4000 fibres.

The sampling fraction is kept constant by fibres starting at different depths inside each tower. This layout has been already imported in the simulations for the CepC detector. Preliminary results on performance are shown in the next chapters.

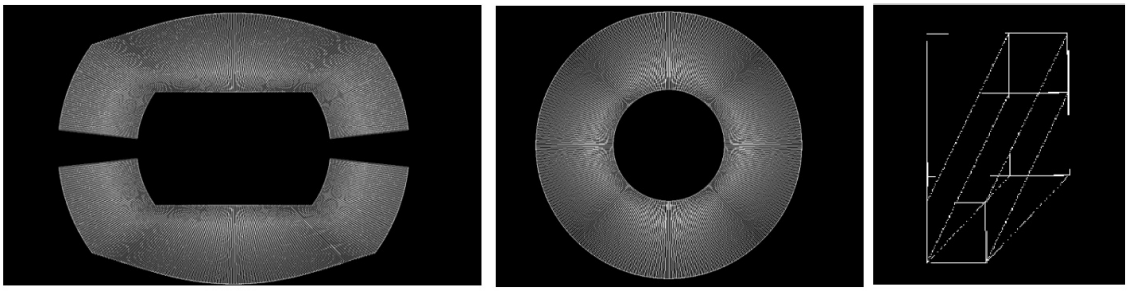

Figure 4.47: An alternative 4π solution (called "wing" geometry).

A different layout implementing the "wing" geometry (see Figure 4.47) is also under study and preliminary results on the em performance will also been shown in the next chapters. In this case, the calorimeter is made of rectangular towers coupled with triangular ones.

In both cases, the total number of fibres is of the order of 10^8 for a complete 4π calorimeter.

4.4.3.2 Mechanics (material choice and machining)

Copper, lead and brass (Cu260) have been used as absorber materials by the DREAM/RD52 collaboration. Their main properties are shown in the Table 4.1, that also reports the calculation for the RD52 lead-prototype geometry. The values for iron are also shown, for comparison. From the table it can be seen that, for hadronic showers, a full-coverage solution with lead (Pb) will give 6% broader and longer showers and a total mass 56% heavier than using brass. A full-containment $3 \times 3 \times 10\ \lambda^3$ prototype will need ~ 5 tons of material with lead (Pb) and ~ 3.2 tons with brass (Cu260).

A possibly stronger reason in favour of copper/brass is the fact that, since the e/mip ratio is 50% higher for copper than for lead, the Čerenkov light (almost exclusively produced by the em component of the shower) has a larger yield for copper, resulting in a better hadronic resolution [30]. However this statement needs to be quantified since it depends on the absolute level of the Čerenkov light yield(s).

On the other hand, lead is easily and accurately extruded, whereas forming copper into the desired shape, either by extrusion, molding, or machining, with the required tolerances in planarity and groove parallelism, is not yet an established industrial process. A variety of techniques (extrusion, rolling, scraping, and milling) for forming the converter layers have been tested. None has been qualified for a large-scale production and identifying an industrial and cost-effective process, including moulding, is a key point.

Alternative copper alloys (e.g. bronze) and/or materials (e.g. iron) may be investigated as well, both for addressing the production process issues and for optimising the detector performance.

4.4.4 Sensors and readout electronics

To separately read out the signals from the S and C fibre forest and avoid oversampling of late developing showers is an issue that may be successfully addressed through the use of Silicon Photo-Multipliers (SiPM). They would allow the separate reading of each fibre and provide magnetic field insensitivity. In principle, assuming powering and cooling do

Absorber Material	ρ (g/cm^3)	X_0 (cm)	$R_{\text{Molière}}$ (cm)	λ_{Int} (cm)	$\rho \times \lambda_{\text{Int}}^3$ (kg)
Copper (Cu)	8.96	1.44	1.57	15.3	32.2
Brass (Cu260)	8.53	1.49	1.64	16.4	37.8
Lead (Pb)	11.35	0.56	1.60	17.6	61.8
Iron (Fe)	7.874	1.76	1.72	16.8	37.1
Fibres:Copper (38:62)	5.98	2.26	2.28	21.9	62.8
Fibres:Brass (38:62)	5.72	2.35	2.38	23.3	72.1
Fibres:Lead (38:62)	7.46	0.90	2.33	24.7	112.8
Fibres:Iron (38:62)	5.31	2.75	2.48	23.7	70.8

Table 4.1: Main properties of lead, copper, brass and iron absorber material and of fibre sampling matrices (RD52 lead-fibre prototype geometry).

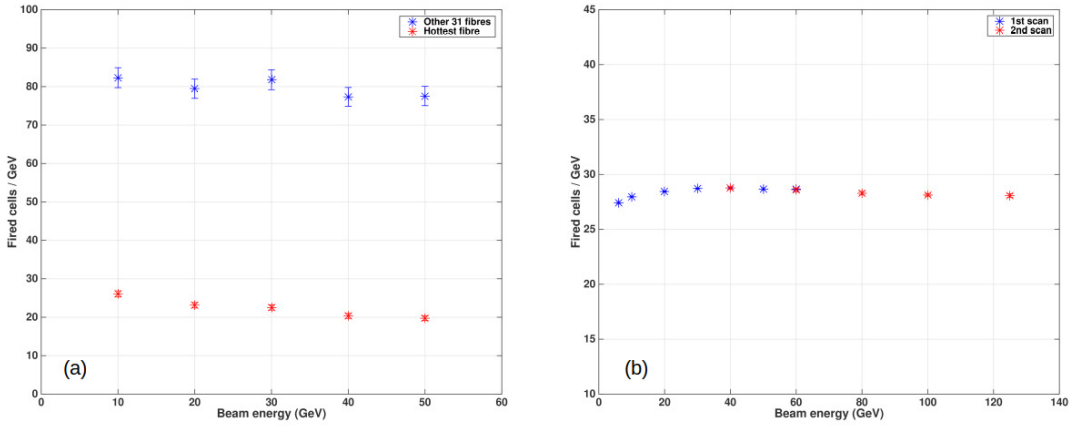

Figure 4.48: Number of photoelectrons per GeV (pe/GeV) for (a) S and (b) C signals, as a function of the electron energy, from 10 to 50 GeV, in a small 64-fibre brass module. In (a), the results are shown separately for the hottest fibre and for the sum of the signals measured by the other 31 scintillating fibres obtained at the (ultra low) PDE of $\sim 2\%$. The main sensor specifications were: 1600, $25 \times 25\ \mu m^2$, cells, and a 25% nominal PDE.

not pose issues, the transverse segmentation could be made as small as a fibre spacing, or 1.5 mm.

SiPMs are low-cost solid state light sensors with single photon sensitivity that underwent an impressive development over the last few years. Tests done in the last two years by the RD52 collaboration indicate that effective solutions for small-scale prototypes are very close already now. Thanks to their higher photon detection efficiency with respect to a standard PM, the higher number of Čerenkov (pe) should result in an improved resolution for both em and hadronic showers. On the other hand, the scintillation light spans a very large dynamic range and saturation and non-linearity effects were observed already for low-energy em showers.

In Figure 4.48, the number of photoelectrons per GeV (pe/GeV) measured, in July 2017, with a very small module ($\sim 1cm^2$ cross section, 32 + 32 fibres), is shown. The most relevant sensor characteristics are 1600, $25 \times 25\ \mu m^2$, cells, and a 25% nominal PDE. Due to the large S light yield, the data for the S signal were obtained at an (ultra low) PDE of $\sim 2\%$, and corrected for non-linearity. Rescaled to a 25% efficiency, the yield of S photoelectrons results in $\sim 108 \times 12.5 = 1350\ pe/GeV$. By removing from the sum the hottest fibre, more heavily affected by non-linearity effects, the estimate grows to $\sim 1530\ pe/GeV$.

The C signals show a linear response at $\sim 30\ pe/GeV$. It should be mentioned that the shower containment was estimated from GEANT4 simulations to be $\sim 45\%$. In addition, the problem of large light leaks from the S fibres into the neighbouring C SiPM channels, observed in the 2016 tests, seems to be largely but not completely solved by a staggered readout of the S and C fibres (Figure 4.49). The contamination of the C signal was estimated to be $\sim 16\% \pm 6\%$.

4.4.4.1 Sensor choice

As far as the scintillation light detection is concerned, saturation and non-linearity should be solvable using higher density devices (e.g. with 10000, $10 \times 10\ \mu m^2$, cells) in com-

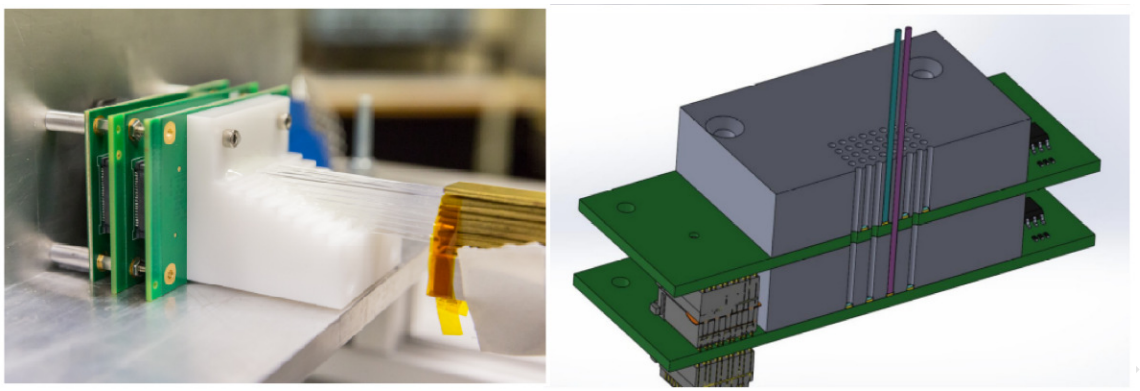

Figure 4.49: Staggered readout scheme: the scintillation and Čerenkov fibres are readout at different planes to minimise light leakage into neighbouring channels.

bination with some light filtering. The definition of the optimal dynamic range and the qualification of existing SiPMs in that regard, will be likely addressed in a short-term R&D phase.

For the Čerenkov light, improvements of the photon collection are possible with the use of an aluminised mirror on the upstream end of the fibres. The acceptance cone may also be enlarged with the use of cladding with a different refractive index. Over a longer term, it could be possible that the R&D on new devices, such as Silicon Carbide (SiC) sensors, expected to provide exclusive UV sensitivity (i.e. visible-light blindness), will allow us to obtain significantly larger pe yields.

4.4.4.2 Front-end electronics and readout

Concerning the front-end, the development shall certainly evaluate the use of Application Specific Integrated Circuits (ASIC) to handle and reduce the information to be transferred to the DAQ system. A major question is finding the optimal way for summing signals from a plurality of sensors into a single output channel. A dedicated feature-extracting processor, capable of extracting timing information such as time-over-threshold, peaking, leading and/or falling times, may allow to disentangle overlapping em and hadronic showers without the need for longitudinal segmentation. With the present fibres, a resolution of the order of 100 ps corresponds to a spatial resolution of about $\sim$ 6 cm along the fibre axis (relativistic particles take 200 ps to cover 6 cm while light needs 300 ps).

4.4.5 Performance studies with fibre-sampling prototypes

Different prototypes were built and studied by the DREAM/RD52 collaboration, with copper or lead as absorber and photomultipliers as light sensors [34–39]. With electrons and pions, in the range of $\sim$ 10-150 GeV, the response linearity was found at the level of 1% for both the em and the hadronic energy reconstruction (having applied the dual-readout formula, equation 4.8, for hadronic showers). The em resolution was estimated to be close to $\sim 10\%/\sqrt{E}$, while the hadronic resolution was found to be at the level of $60\text{-}70\%/\sqrt{E}$, to be corrected for the fluctuations introduced by lateral leakage and light attenuation in the fibres. None of the prototype was large enough to substantially contain hadronic showers and an R&D programme to assess the hadronic performance of a real

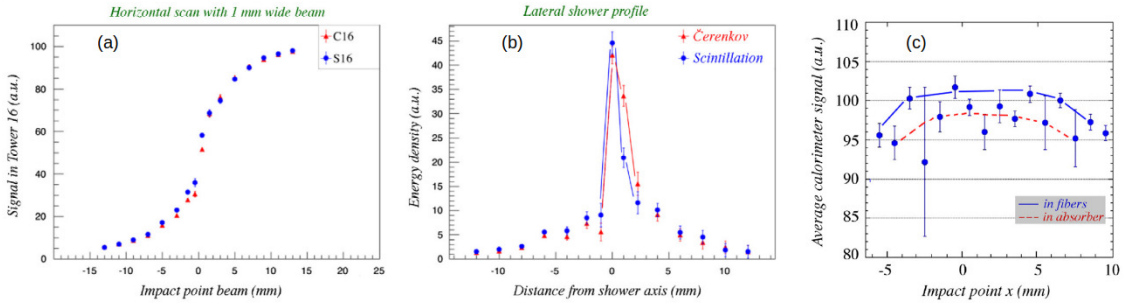

Figure 4.50: (a) The signal from a 1 mm wide beam of 100 GeV electrons, in the RD52 lead-fibre prototype, as a function of the impact point; (b) the lateral shower profiles derived from this measurement; (c) the dependence of the scintillation signal on impact point for a beam impinging parallel to the fibres.

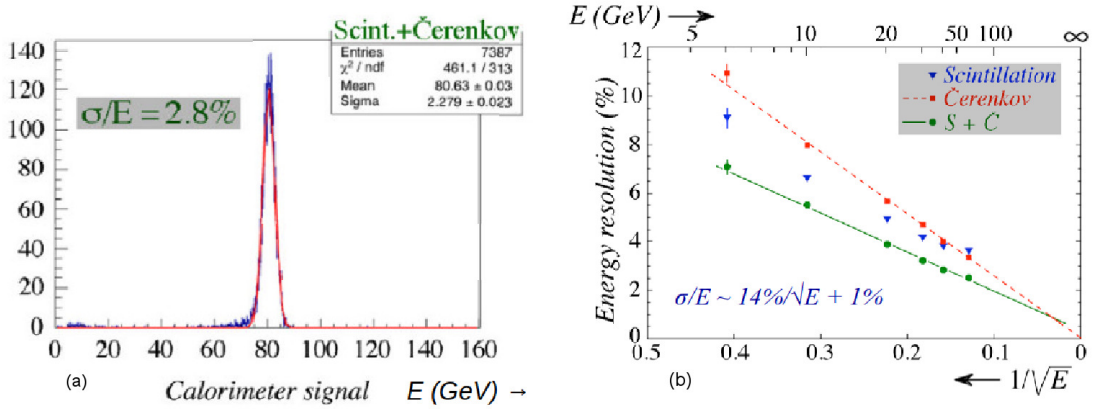

Figure 4.51: In the RD52 copper-fibre module: (a) signal distribution of the sum of all fibres for 40 GeV electrons; (b) the em energy resolution as a function of the beam energy. Shown are the results for the two types of fibres, and for the average combined signal.

detector, is under way. Preliminary simulations of standalone modules indicate a possible ultimate resolution of $\sim 30-40\%/\sqrt{E}$. More details can be found in the next paragraphs.

4.4.5.1 Electromagnetic performance

Figure 4.50(a) and 4.50(b) show the radial shower profile and the sensivity to the impact point: the core of the signal spans just a few mm. Figure 4.50(c) shows the dependence of the S signal on the impact point for particles entering parallel to the fibres. This introduces a constant term in the resolution that can be avoided with a small tilt of the fibre axis. In the C fibres, the problem does not show up since the early (collimated) part of the shower produces photons outside the fibre numerical aperture.

For the reconstruction of the energy of em showers, S and C signals provide independent uncorrelated measurements, with different sensitivity of the response. They are affected by different problems: S signals have photoelectron statistics one or two orders of magnitude higher than C signals, and their fluctuations are largely dominated by the sampling fluctuation of the energy deposits. C signal fluctuations are generally dominated by the limited photoelectron statistics, especially at low energies. Nevertheless, at high energies, the constant term for C signals is negligible, giving a better resolution. Averaging the two measurements improves the resolution up to a factor of $\sqrt{2}$. For the copper

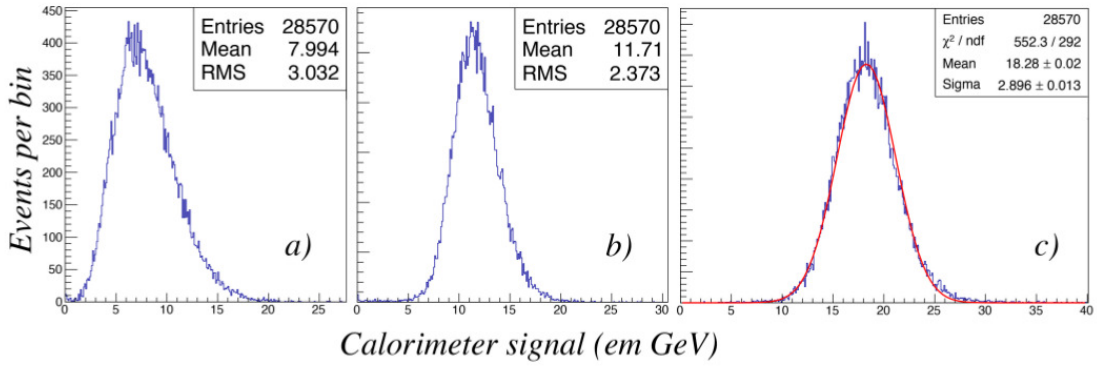

Figure 4.52: Signal distributions for 20 GeV π^- particles in the RD52 lead-fibre matrix. Shown are the measured (a) Čerenkov and (b) scintillation signal distributions as well as (c) the distribution obtained by combining the two signals according to Equation 4.8, with $\chi = 0.45$.

matrix, in Figure 4.51(a) the sum of S and C signals for 40 GeV electrons is plotted, while Figure 4.51(b) shows the em resolution, for S, C and the (average) combined signal.

4.4.5.2 Hadronic performance

The response of a lead-fibre matrix was studied with pion and proton beams [39]. The energy was reconstructed with the dual-readout relation (Eq. 4.8) and shows a restored gaussian response function (Figure 4.52) and linearity of the mean response.

The comparison of p and π^+ signals confirms that the dual-readout method largely compensates for the differences in shower composition, i.e., differences in the electromagnetic fraction, f_{em}, and between baryon-initiated and pion-initiated hadronic showers.

Due to the limited lateral size of the matrix (the effective diameter was $\sim 1\lambda_{\mathrm{Int}}$), the containment for hadronic showers was $\sim 90\%$ so that leakage fluctuations dominated the energy resolution. Selecting contained showers improved the resolution by a factor of ~ 2. Although that selection was introducing a bias in favour of high f_{em} showers, a significant improvement is expected for a realistic-size module.

The resolution was also affected by the finite light attenuation length of the fibres, causing early starting showers to be observed at lower signal values. The hadronic resolution, yet to be corrected for both effects, was reconstructed to be $\sim 70\%/\sqrt{E}$.

4.4.5.3 e/π separation

Four discriminating variables were identified for implementing e/π separation: the fraction of energy in the central tower, the C/S signal ratio, the signal starting time and the total charge/amplitude ratio, shown in Figure 4.53. The plots are relative to testbeam data taken with the RD52 lead-fibre prototype [34].

A multivariate neural network analysis showed that the best e/π separation achievable for 60 GeV beams was 99.8% electron identification efficiency with 0.2% pion misidentification. Further improvements may be expected by including the full time structure information of the pulses, especially if the upstream ends of the fibres are made reflective.

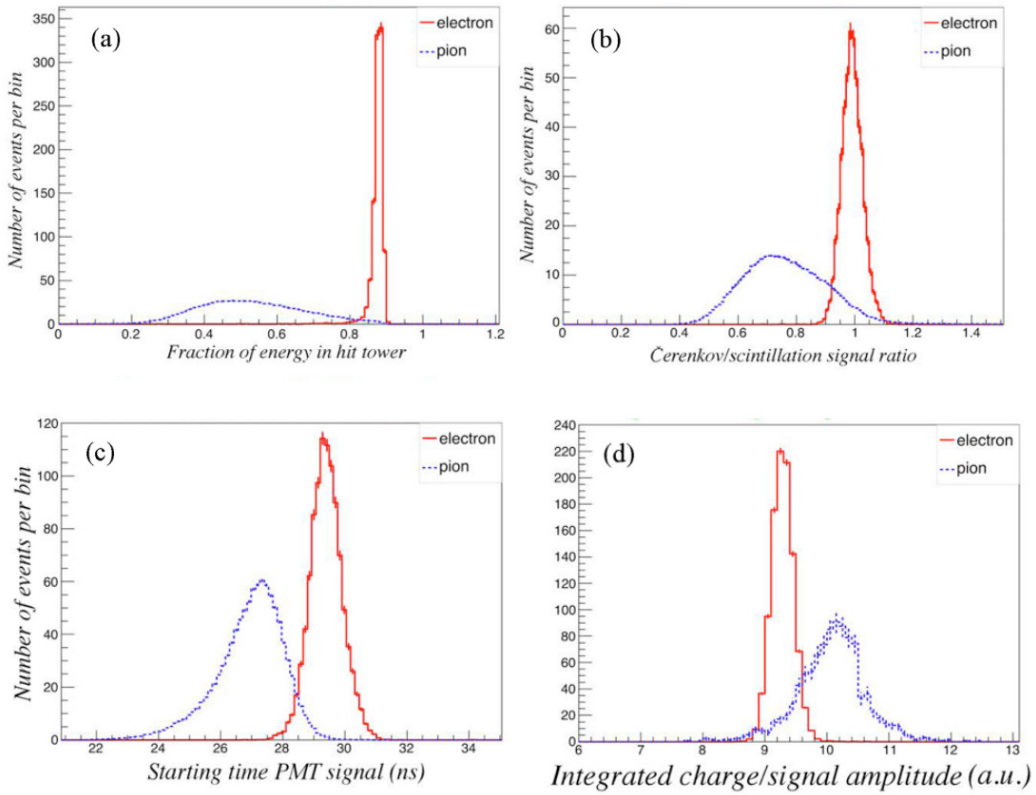

Figure 4.53: Distribution of four discriminating variables for 60 or 80 GeV electrons and pions, as measured with the RD52 lead-fibre prototype: (a) energy fraction deposited in the hit tower; (b) C/S signal ratio in the hit tower; (c) starting time of the PM signal; (d) ratio of the integrated charge and the amplitude of the signals.

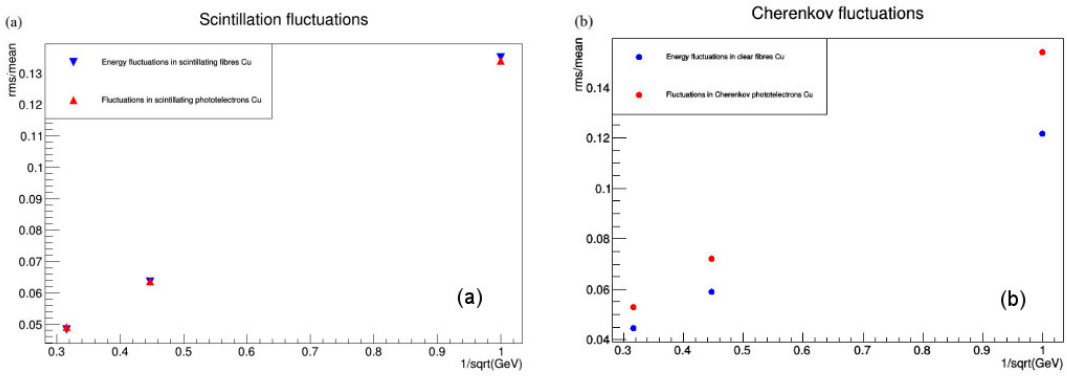

Figure 4.54: Relative fluctuation of the total signal detected in the (a) scintillating and (b) Čerenkov fibres, for both the energy deposit and the number of photoelectrons (MC simulations).

4.4.6 Montecarlo simulations

GEANT4 simulations [1] are under development and analysis for understanding the performance of both testbeam modules and a 4π calorimeter integrated in a detector, with magnetic field, tracking and preshower elements.

4.4.6.1 em performance

A Cu matrix of dimensions $\sim 31 \times 31 \times 100\ cm^3$, with 1 mm fibres at 1.4 mm distance, compatible with the RD52 prototypes, has been simulated for the evaluation of the electromagnetic performance. PMMA clear fibres and Polystyrene scintillating fibres, with a 3% thick cladding (C_2F_2 Fluorinated Polymer for clear and PMMA for scintillating fibres), were the sensitive elements.

A small ($\lesssim 1^\circ$) tilt angle was introduced to avoid large non-Gaussian tails in the scintillation signal due to channeling.

The energy containment for 20 GeV electrons was estimated to be $\geq 99\%$, with sampling fractions of 5.3% and 6.0% for scintillating and clear fibres, respectively.

Given the integral sampling fraction of 11.3% and the 1 mm diameter fibres, the contribution to the energy resolution due to sampling fluctuations can be estimated to be $\sim 9\%/\sqrt{E}$, ultimate limit on the em resolution for this detector.

The scintillation light yield is so large ($\sim$ 5500 pe/GeV) that the fluctuations of the S signals are dominated by the energy sampling process (Figure 4.54(a)). This is not true for the Čerenkov signals (Figure 4.54(b)), whose sensitivity is estimated to be $\sim 100\ pe/GeV$.

So, in the simulations, the process of generation and propagation of the scintillation light was switched off and the energy deposited in the fibres was taken as signal since this does not introduce any bias to the detector performance. This statement does not apply to the Čerenkov photons for which a parameterization that convolutes the effect of light attenuation, angular acceptance and PDE, was introduced.

In Figure 4.55 the resolutions are shown for both C and S signals, separately, and for the unweighted average value of the two. The variable on the horizontal axis and in

[1] version 10.02.p01-10.03.p01, with FTFP_BERT_HP physics list

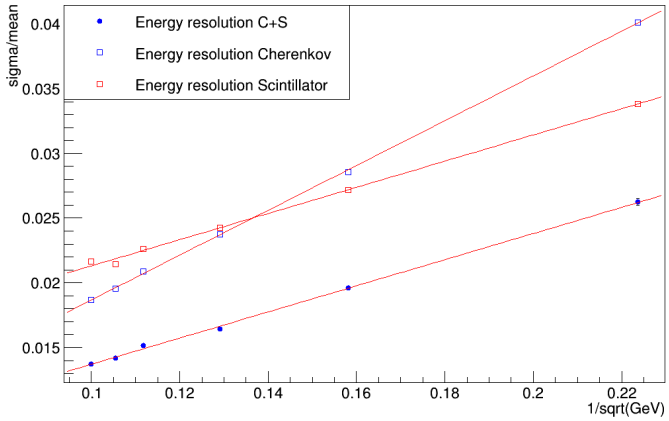

Figure 4.55: Relative resolution for em showers for the C and S signals, independently, and for the average of the two (MC simulations).

Fibers used	Fitted Gaussian electromagnetic energy resolution
S-fibres only	$\sigma/E = 10.1\%/\sqrt{E} \oplus 1.1\%$
C-fibres only	$\sigma/E = 17.3\%/\sqrt{E} \oplus 0.1\%$
S-fibres and C-fibres	$\sigma/E = 10.1\%/\sqrt{E} \oplus 0.4\%$

Table 4.2: Fit to the em resolution (MC simulations)

the formulae for the fitted resolutions is the beam energy. The results of the fit to the data points are shown in Table 4.2. A slightly better result may be obtained with a weighted average.

4.4.6.2 Hadronic performance

A simulation of larger ($\sim 72 \times 72 \times 250\ cm^3$) matrices was implemented in order to get a hadronic shower containment of $\sim 99\%$. Calibration was done with 40 GeV electron beams.

In Figure 4.56 GEANT4 predictions for the hadronic energy resolution, with copper absorber, are shown. Table 4.3 lists the results of the fit to the curves.
The large constant terms, for both S and C signals, are generated by the f_{em} correlated fluctuations. Simulations with lead absorber give equivalent but even slightly better results. The energy E in the plot (and in the expressions for the fitted resolutions) is the beam energy, corresponding in average to the energy reconstructed with the Equation 4.8 when the containment is properly accounted for (i.e., the reconstructed energy corresponds, in average, to the beam energy times the average containment). The fact that the exper-

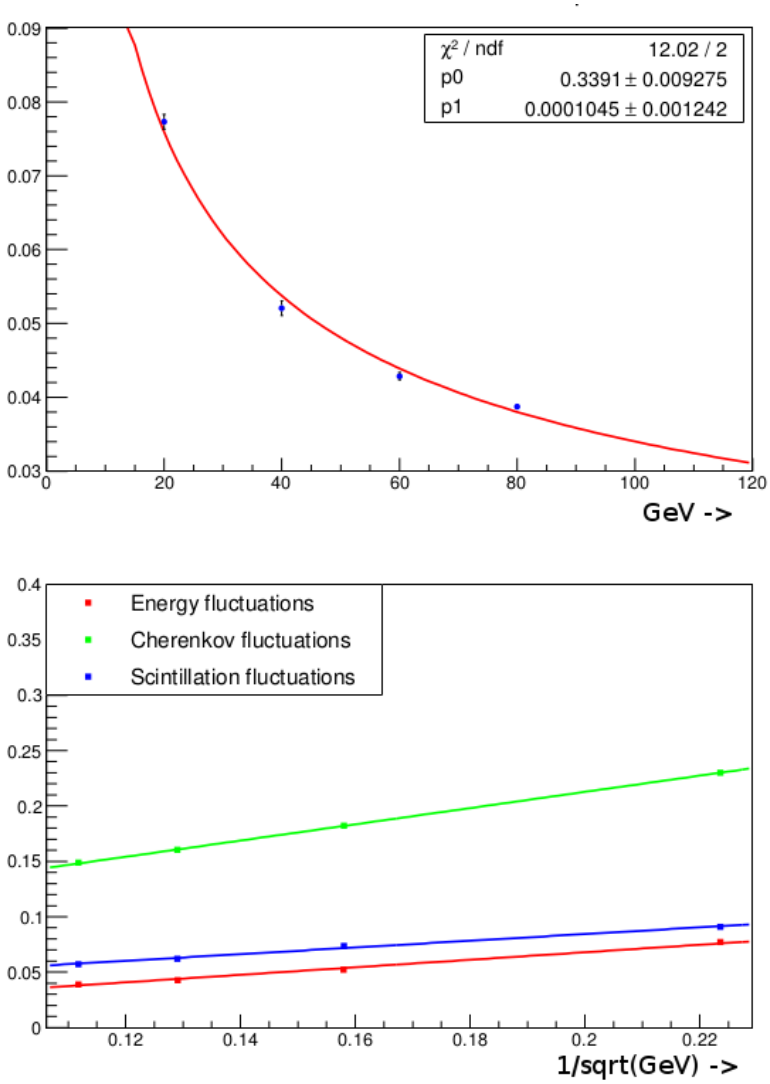

Figure 4.56: Montecarlo simulations showing: (top) the relative hadronic resolution as reconstructed with the dual-readout formula; (bottom) the relative hadronic resolution independendly for the C and S signals and for the dual-readout combination of the two.

Fiber used	Fitted Gaussian hadronic energy resolution
S-fibres only	$\sigma/E = 30\%/\sqrt{E} \oplus 2.4\%$
C-fibres only	$\sigma/E = 73\%/\sqrt{E} \oplus 6.6\%$
Dual-readout S-fibres and C-fibres	$\sigma/E = 34\%/\sqrt{E} \oplus (\text{negligible})\%$

Table 4.3: Fit to the hadronic resolution (MC simulations)

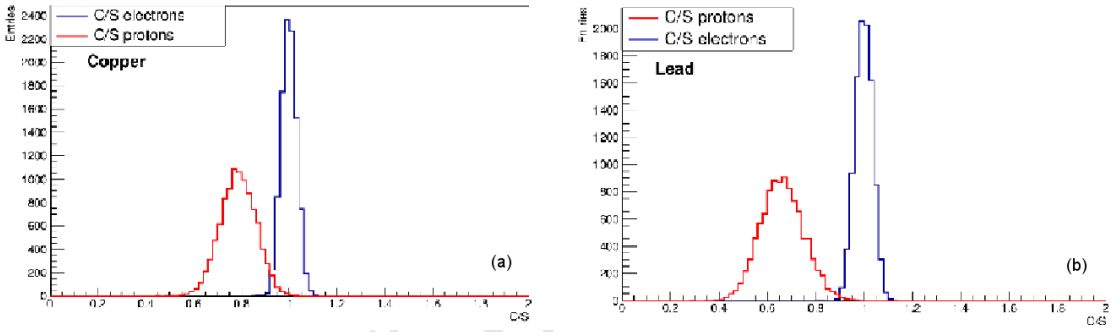

Figure 4.57: C/S ratio (MC simulations) for 80 GeV e^- and protons in (a) copper and (b) lead.

imental resolution was, so far, about a factor of two worse than simulations, is in our understanding, largely due to the small lateral size of the prototypes. In order to fully validate the MC predictions, an R&D programme is being pursued.

The correlation of the invisible energy with all the other components of hadronic showers was also analysed. Preliminary results seem to indicate that the most appropriate variable to account for the fluctuations of the invisible energy component is, by far, the f_{em}, with correlation coefficients of 90%, 92%, 94%, for copper, iron and lead respectively. The kinetic energy of the neutrons is predicted to be, at best, correlated at the 76% level. If confirmed, this would prove that compensation through neutron signal pickup or amplification will anyway give worse results than the dual-readout method [41].

About particle ID capabilities, in Figure 4.57 the C/S ratio is shown for 80 GeV e^- and protons in copper (left) and lead (right). For an electron efficiency of $\sim 98\%$, the rejection factor for protons is ~ 50 in copper and ~ 600 in lead. Of course, this is an ideal detector and in reality it is likely that the numbers will be worse. On the other hand, there are more variables that can be easily used in order to enhance the particle ID performance (namely the lateral shower profile, the starting time of the signal, the charge-to-amplitude ratio).

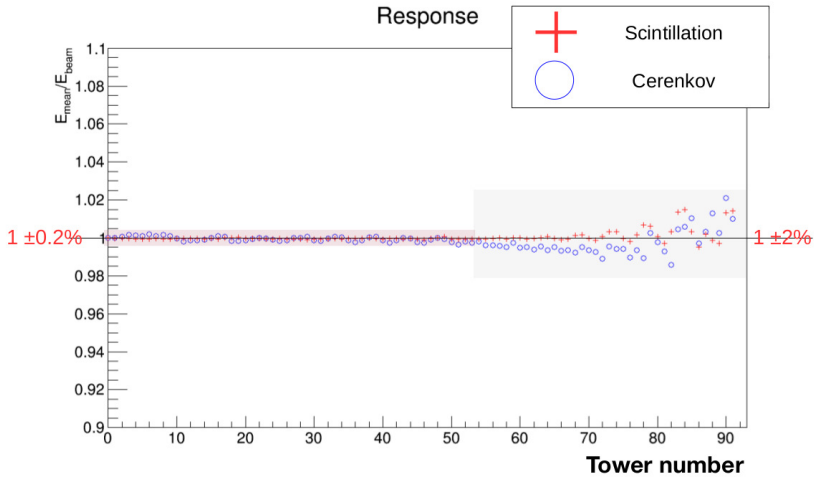

Figure 4.58: Ratio of reconstructed energy to the beam energy for 20 GeV e^-, as a function of the tower number, in the wedge geometry (MC simulations).

4.4.6.3 Projective geometry

Each tower, in the wedge geometry implementation, was exposed to 20 GeV electron beams, with an incident angle of $(1°, 1.5°)$, and the calibration constants calculated as the average deposit energy (in each tower) divided by the average C or S signal (of each tower). The response to an electron beam of the same energy is plotted in Figure 4.58. In the barrel region the response of all towers is within 0.2%, while in the forward the systematics are within 2%. All results were obtained with the quantum efficiency for the Čerenkov channel of each tower tuned to a light yield of $\sim 30\ pe/GeV$, as estimated in the RD52 beam tests.

The performance of a few towers was studied with electron beams in the range of 10-100 GeV. Figure 4.59 shows the linearity and em energy resolutions for towers #0 and #45. In both cases, the combined S and C signal shows a resolution of $\sim 14\%/\sqrt{E}$ with a constant term of $\sim 0.1\%$ while the average response is constant within 0.4%.

The hadronic resolution was studied with pions in the same energy range. A χ value of 0.29, the value measured for the DREAM calorimeter [42], was used to reconstruct the shower energy with Eq. 4.8. In the linearity plots for both tower #0 and #45 in Figure 4.60(a), the C and S responses to single pions increase non-linearly as the pion beam energy increases. On the other hand, the value reconstructed with the dual-readout formula shows a constant response to single pions $\sim 8\%$ lower than that to electrons (the reason being the shower containment). This effect in the GEANT4 simulations is described in reference [43]. In addition, the energy resolution after the correction (shown in Figure 4.60(b) for towers #0 and #45) is $\sim 26\%/\sqrt{E}$, with a constant term of less than 1%. These results support the statement that the hadronic energy resolution and the response to single hadrons should be constant (and appropriate) over the full barrel region. We may reasonably expect to obtain good performance over the entire 4π detector.

For the wing geometry, the results, at present, are limited to the em performance of few towers and the results (linearity and em resolution) substantially reproduce the wedge geometry ones.

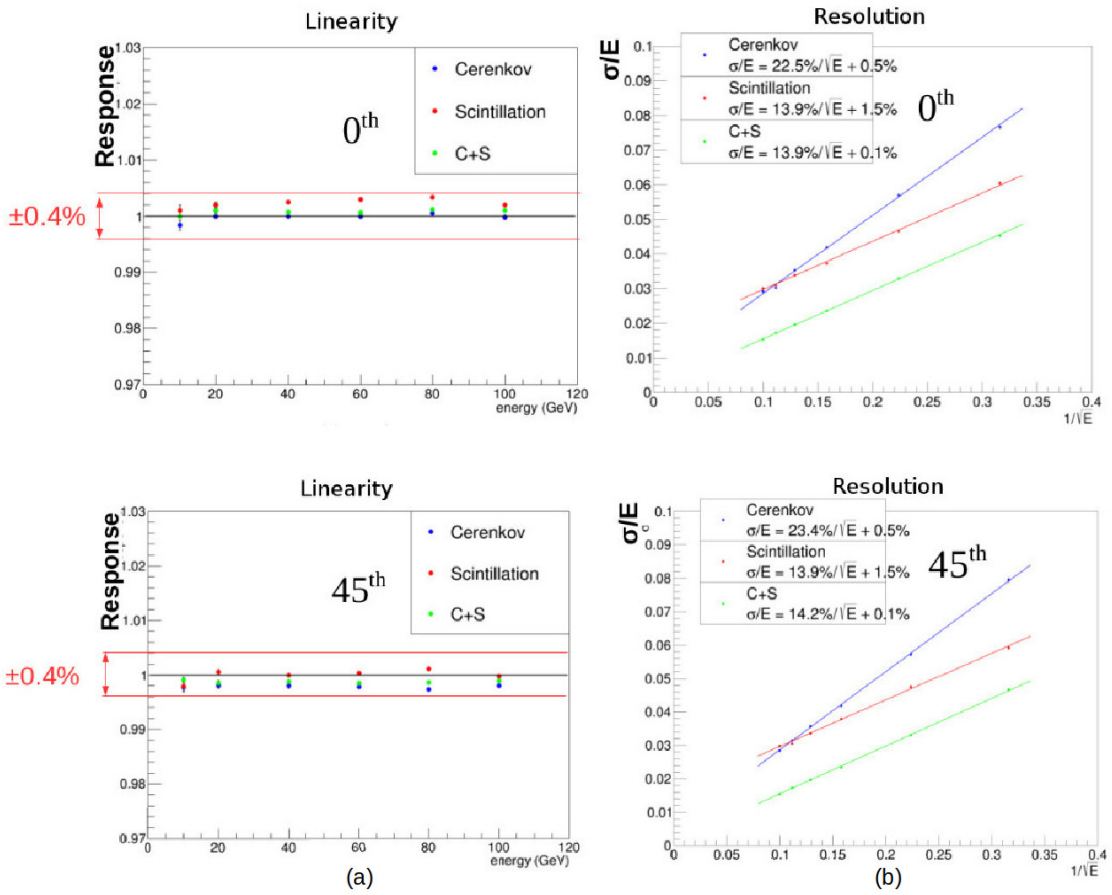

Figure 4.59: Linearity and em energy resolution for towers #0 (top) and #45 (bottom), in the wedge geometry (MC simulations).

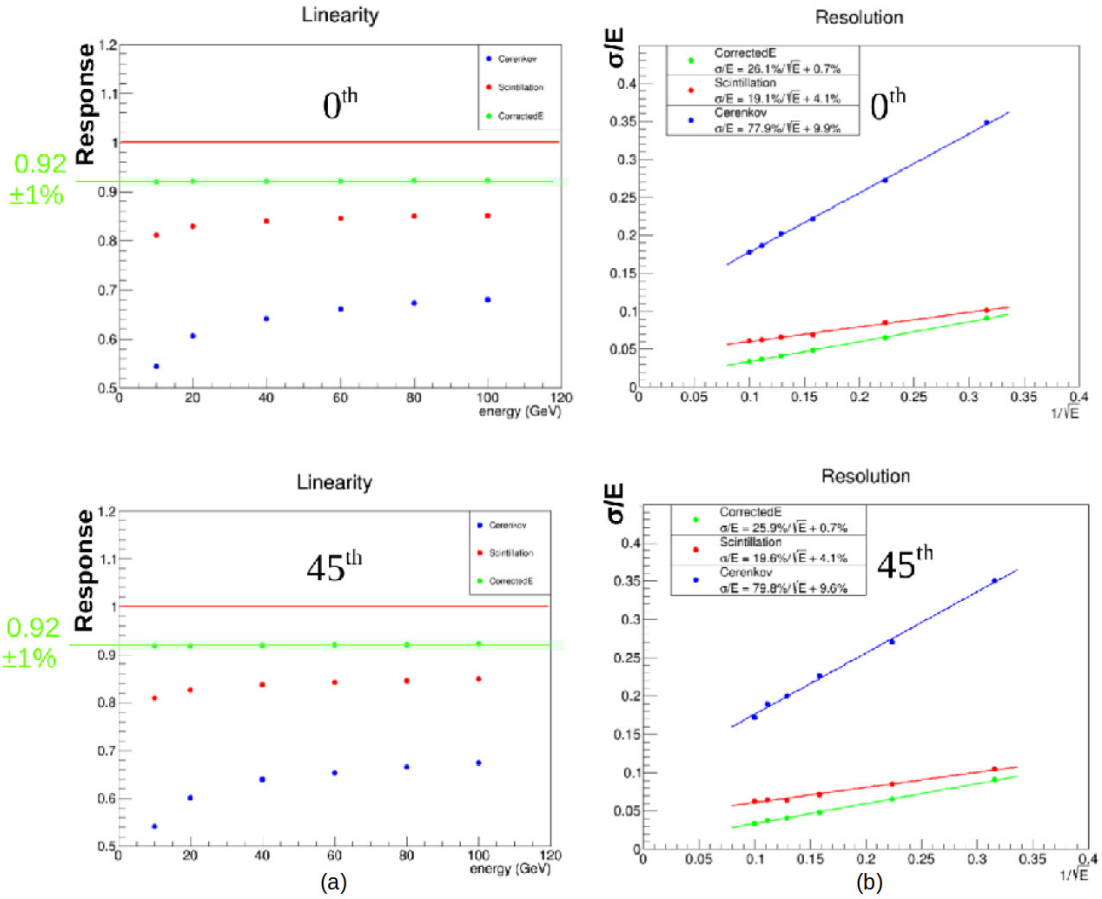

Figure 4.60: Linearity and energy resolution with pions, for towers #0 (top) and #45 (bottom), in the wedge geometry (MC simulations).

4.4.6.4 Short term planning and open issues

The performance for single hadrons, jets and τ leptons has to be understood and the work has just started. For validation, the comparison with a prototype with a non-marginal hadronic shower containment, like the RD52 lead matrix, will be pursued.

About em simulations, a program for the comparison with the 2017 RD52 data is ongoing. Some initial understanding of the absolute photoelectron scale for the Čerenkov light should be available in a very short time.

In general, light attenuation effects need also to be considered, for a $\sim 2-2.5m$ long fibre detector, that may introduce a constant term in the hadronic resolution as a function of the shower development point (late starting showers will give bigger and earlier signals).

The evaluation of advantages and disadvantages of filters (to dump the short attenuation-length components) and mirrors (to increase the number of photons that reach the photodetectors) may be relevant in this context.

The effects of the integration of a preshower detector have to be evaluated and the e/π separation capability assessed and quantified, for both isolated particles and particles within jets.

About physics, a (non exhaustive) list of benchmark channels to be studied is:

$H \to \gamma\gamma$
$H \to \tau\tau \to e/\mu + \rho\pi$
$H \to gg \to jj$
$Z \to jj$
$W \to jj$
$H \to ZZ^* \to 4j$
$H \to WW^* \to 4j$.

4.4.7 Final remarks

Thanks to a 15-year-long experimental research program on dual-readout calorimetry of the DREAM/RD52 collaboration, this technology looks mature for the application in future experimental programs. The results show that the parallel, independent, readout of scintillation and Čerenkov light, makes it possible to cancel the effects of the fluctuations of the electromagnetic fraction in hadronic showers, dominating the energy resolution of most (if not all) the calorimeters built so far. In conjunction with high-resolution em and hadronic energy measurements, excellent standalone particle-ID capability has been demonstrated as well.

Those results give increasing support to the conviction that a matrix of alternating scintillating and clear fibres, inserted in copper or lead strips and readout by Silicon PhotoMultipliers (SiPM), will be able to provide performance more than adequate for the physics programs at the proposed CepC collider.

Nevertheless, there is a series of technical and physics issues that need to be solved, within the next 2-3 years in order to arrive up to the design of a realistic 4π detector. A non-exhaustive list must include:

1. The industrial machining of foils of copper, lead or some other material, with the required precision.

2. The development of a mechanical integration design.

3. The readout of the high granularity matrices of SiPM that, in order to be effective, will require the development of a dedicated Application Specific Integrated Circuit (ASIC). Possible aggregations of more fibre outputs into a single channel have also to be implemented and studied.

4. The need and, in case, the way for a longitudinally segmented calorimeter system and the performance of Particle Flow Algorithms to further boost the performance of dual-readout.

5. The development of a modular solution and the assessment, at all levels, of its performance, through beam tests of small modules and simulations. An intensive program of simulations is already ongoing, targeted at the CepC experimental program. The response to single particles and jets is under study, in standalone configurations. The work for understanding the behaviour of a 4π calorimeter integrated in a full detector, with a tracking and a magnetic system, has also started. This will include, as well, the evaluation of the combined performance with a preshower detector in front.

References

[1] CALICE Wikipage. https://twiki.cern.ch/twiki/bin/view/CALICE/.

[2] J.-C. Brient, *Improving the jet reconstruction with the particle flow method: An introduction*, 2004. Calorimetry in particle physics. Proceedings, 11th International Conference, CALOR 2004, Perugia, Italy,.

[3] H. Videau and J. C. Brient, *Calorimetry optimised for jets*, in *Proc. 10th International Conference on Calorimetry in High Energy Physics (CALOR 2002), Pasadena, California* [44].

[4] H. Videau and J. C. Brient, *A Si-W calorimeter for linear collider physics*, in *Proc. 10th International Conference on Calorimetry in High Energy Physics (CALOR 2002), Pasadena, California* [44], pp. 309–320.

[5] CALICE Collaboration, R. Cornat, *Semiconductor sensors for the CALICE SiW EMC and study of the cross-talk between guard rings and pixels in the CALICE SiW prototype*, in *Proceedings CALOR'08*, vol. 160, p. 012067. 2009.

[6] ILD Collaboration, T. Behnke et al., *International Linear Collider – Detector Baseline Document*, , DESY / FERMILAB / CERN, 2013. https://edmsdirect.desy.de/edmsdirect/file.jsp?edmsid=D00000001021295.

[7] CMS Collaboration, A. M. Magnan, *HGCAL: a High-Granularity Calorimeter for the endcaps of CMS at HL-LHC*, JINST **12** (2017) no. 01, C01042.

[8] CMS Collaboration, A. Martelli, *The CMS HGCAL detector for HL-LHC upgrade*, in *5th Large Hadron Collider Physics Conference (LHCP 2017) Shanghai, China, May 15-20, 2017*. 2017. arXiv:1708.08234 [physics.ins-det]. http://inspirehep.net/record/1620207/files/arXiv:1708.08234.pdf.

[9] H. Zhao, *PFA Oriented ECAL Simulation and Geometry Optimization for the CEPC*, in *proceeding of the International Conference on Calorimetry for the High Energy Frontier (CHEF 2017)*. 2017.

[10] D. Jeans, *Simalution of the SiW-ECAL for ILD*, in *proceedings of LCWS 2017*. 2017.

[11] T. S. et al., *Performance study of SKIROC2/A ASIC for ILD Si-W ECAL*, in *proceeding of the International Conference on Calorimetry for the High Energy Frontier (CHEF 2017)*. 2017.

[12] D. Grondin, J. Giraud, and J.-Y. Hostachy, *CALICE Si/W ECAL: Endcap structures and cooling system*, in *Proceedings, International Workshop on Future Linear Colliders 2016 (LCWS2016): Morioka, Iwate, Japan, December 05-09, 2016*. 2017. arXiv:1702.03770 [physics.ins-det]. http://inspirehep.net/record/1513187/files/arXiv:1702.03770.pdf.

[13] V. Boudry, *SiW ECAL R&D*, in *Fourth International Workshop on Future High Energy Circular Colliders (CEPC2014)*. 2014. http://indico.ihep.ac.cn/event/4338/session/2/contribution/35/material/slides/0.pdf.

[14] CALICE Collaboration, J. Repond et al., *Design and Electronics Commissioning of the Physics Prototype of a Si-W Electromagnetic Calorimeter for the International Linear Collider*, JINST **3** (2008) P08001, arXiv:0805.4833 [physics.ins-det].

[15] C. Adloff et al., *Response of the CALICE Si-W electromagnetic calorimeter physics prototype to electrons*, Nucl. Instrum. Meth. **A608** (2009) 372–383.

[16] CALICE Collaboration Collaboration, R. Poschl, *A large scale prototype for a SiW electromagnetic calorimeter for a future linear collider*, in *Proceedings of International Workshop on Future Linear Colliders (LCWS11) 26-30 Sep 2011. Granada, Spain*. 2012. arXiv:1203.0249 [physics.ins-det].

[17] V. Balagura et al., *SiW ECAL for future e^+e^- collider*, in *Proceedings, International Conference on Instrumentation for Colliding Beam Physics (INSTR17): Novosibirsk, Russia*. 2017. arXiv:1705.10838 [physics.ins-det]. http://inspirehep.net/record/1601898/files/arXiv:1705.10838.pdf.

[18] A. Irles, *Latest R&D news and beam test performance of the highly granular SiW-ECAL technological prototype for the ILC*, in *proceeding of the International Conference on Calorimetry for the High Energy Frontier (CHEF 2017)*. 2017.

[19] G. B. *et.al.*, *Conception and construction of a technological prototype of a high-granularity digital hadronic calorimeter*, JINST **10** (2015) P10039.

[20] M. B. *et al.*, *Performance of Glass Resistive Plate Chambers for a high granularity semi-digital calorimeter*, JINST **6** (2011) P02001.

[21] C. Collaboration, *First results of the CALICE SDHCAL technological prototype*, JINST **11** (2016) P04001.

[22] C. Collaboration, *Separation of nearby hadronic showers in the CALICE SDHCAL prototype detector using ArborPFA*, CAN-054 (2016) .

[23] C. Collaboration, *Resistive Plate Chamber Digitization in a Hadronic Shower Environment*, JINST **11** (2016) P06014.

[24] L. Caponetto*et al.*, *First test of a power-pulsed electronics system on a GRPC detector in a 3-Tesla magnetic field*, JINST **7** (2012) P04009.

[25] F. Sefkow, *Prototype tests for a highly granular scintillator-based hadron calorimeter*, CHEF2017. https://indico.cern.ch/event/629521/contributions/2702990/.

[26] The CALICE Collaboration, Y. Liu et al., *A design of scintillator tiles read out by surface-mounted SiPMs for a future hadron calorimeter*, (NSS/MIC), IEEE (2014) 1–4.

[27] The CALICE Collaboration, C. Adloff et al., *hadronic energy resolution of a highly granular scintillator-steel hadron calorimeter using software compensation techniques*, Journal of Instrumentation **7(09)** (2012) 1–23.

[28] K. Krueger, *Software compensation and particle flow*, CHEF2017. https://indico.cern.ch/event/629521/contributions/2703038/.

[29] M. Bouchel et al., *Second generation Front-end chip for H-Cal SiPM readout :SPIROC*, ILC website. https://agenda.linearcollider.org/event/1354/contributions/2542/attachments/1826/3054/SPIROC_presentation_13_02_2007.pdf.

[30] R. Wigmans, *Calorimetry, Energy Measurement in Particle Physics*, vol. 168 (second edition). International Series of Monographs on Physics, Oxford University Press, 2017.

[31] C. Patrignani et al. (Particle Data Group) Chin. Phys. C **40** (2016) 479–482.

[32] D. E. Groom, *Energy flow in a hadronic cascade: Application to hadron calorimetry*, Nucl. Instrum. Methods A **572** (2007) 633–653.

[33] D. E. Groom, *Erratum to "Energy flow in a hadronic cascade: Application to hadron calorimetry" [Nucl. Instr. and Meth. A 572 (2007) 633-653]*, Nucl. Instrum. Methods A **593** (2008) 638.

[34] N. Akchurin et al., *Particle identification in the longitudinally unsegmented RD52 calorimeter*, Nucl. Instrum. Methods A **735** (2014) 120.

[35] N. Akchurin et al., *The electromagnetic performance of the RD52 fiber calorimeter*, Nucl. Instrum. Methods A **735** (2014) 130.

[36] N. Akchurin et al., *Lessons from Monte Carlo simulations of the performance of a dual-readout fiber calorimeter*, Nucl. Instrum. Methods A **762** (2014) 100.

[37] A. Cardini et al., *The small-angle performance of a dual-readout fiber calorimeter*, Nucl. Instrum. Methods A **808** (2016) 41.

[38] R. Wigmans, *New results from the RD52 project*, Nucl. Instrum. Methods A **824** (2016) 721.

[39] S. Lee et al., *Hadron detection with a dual-readout fiber calorimeter*, Nucl. Instrum. Methods A **866** (2017) 76.

[40] 4th Detector Collaboration Letter of Intent: http://www.4thconcept.org/4LoI.pdf.

[41] S. Lee, M. Livan, and R. Wigmans, *On the limits of the hadronic energy resolution of calorimeters*, Nucl. Instrum. Methods A **882** (2018) 148.

[42] N. Akchurin et al., *Hadron and jet detection with a dual-readout calorimeter*, Nucl. Instrum. Methods A **537** (2005) 537.

[43] N. Akchurin et al., *Lessons from Monte Carlo simulations of the performance of a dual-readout fiber calorimeter*, Nucl. Instrum. Methods A **762** (2014) 100.

[44] *10th International Conference on Calorimetry in High Energy Physics (CALOR 2002), Pasadena, California, 25-30 Mar 2002*. March, 2002.

CHAPTER 5

DETECTOR MAGNET SYSTEM

The CEPC detector magnet is an iron-yoke-based solenoid to provide an axial magnetic field of 3 Tesla. A room temperature bore is required with a diameter of 6.8 m. This chapter describes the conceptual design of magnet, including the design of field distribution, solenoid coil, cryogenics, quench protection, power supply and the yoke. In the end of this chapter, the R&D section 6.5 brings up other concept options and some reach projects.

Compensation magnets are discussed in the Accelerator CDR chapter 9.2.

5.1 Magnetic field design

5.1.1 Main parameters

The CEPC detector magnet follows the same design concepts of the CMS and ILD detector magnets [1, 2]. The magnet system consists of the superconducting coil and the iron yoke with a barrel yoke and two end-cap yokes. The superconducting coil is designed with 5 modules wound with 4 layers. The three middle coil modules and the two end coil modules are wound with 78 and 44 turns, respectively. The operating current is 15,779 A for each turn corresponding to 3 T at the interaction point. The geometrical layout of magnet are shown in Figure 5.1. The main magnetic and geometrical design parameters are given in Table 5.1.

5.1.2 Magnetic field design

The magnetic field simulation has been calculated in 2D FEA model, with fine structure of the barrel yokes and end-cap yokes. Figure 5.2 shows the magnetic field contour of the

The solenoid central field (T)	3	Working current (kA)	15779
Maximum field on conductor (T)	3.485	Total ampere-turns of the solenoid (MAt)	20.323
Coil inner radius (mm)	3600	Inductance (H)	10.46
Coil outer radius (mm)	3900	Stored energy (GJ)	1.3
Coil length (mm)	7600	Cable length (km)	30.35

Table 5.1: Main parameters of the solenoid coil

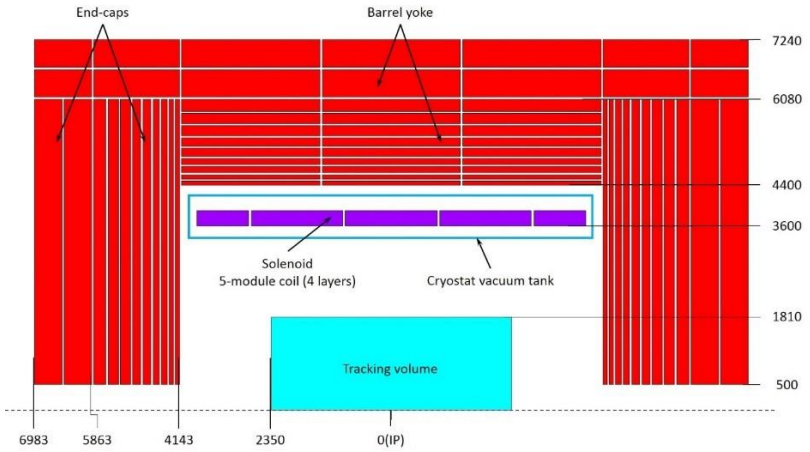

Figure 5.1: 2D layout of CEPC detector magnet (mm)

magnet. The maximum field on NbTi cable is 3.5 Tesla. The edge of 50 Gauss stray field is at 13.6 m from the beam axis and axial direction 15.8 m from the IP.

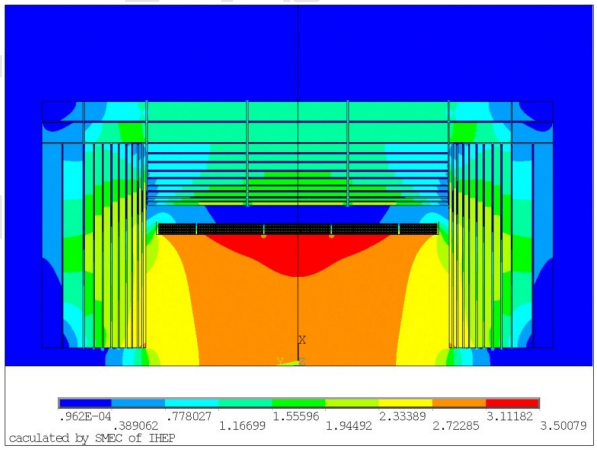

Figure 5.2: Field map of the magnet (T)

5.2 Solenoid Coil

The conceptual superconducting conductor is based on the self-supporting conductor design of CMS detector magnet, composed of NbTi Rutherford cable, the pure aluminum stabilizer and aluminum alloy reinforcement.

The coil windings is wound by inner winding technique with the support aluminum-alloy cylinder, which acts as an external supporting mandrel and taking away the quench induced heat energy. In order to maintain the operating temperature of LTS detector magnet, the cooling tubes for circular flow of LHe are welded on the outer surface of the aluminum-alloy cylinder.

5.3 Ancillaries (cryogenics, power supply, quench protection)

5.3.1 Cryogenics System

The coil cryogenic system is based on the CMS cryogenic system. The magnetic stored energy is 1.3 GJ. The thermosiphon principle is used for the coil indirect cooling mode using saturated liquid helium. A horizontal cryostat is designed, including a vacuum tank, an inner thermal shield, an outer thermal shield. The stainless steel vacuum vessel is 8.05 m length cylinder with diameter of 8.5 m. Two service towers are designed on the top of the cryostat in the central ring of the barrel yoke.

5.3.2 power supply

A low ripple DC current-stabilized power supply, with low output voltage and high output current, is requested for CEPC detector magnet. The power supply is expected to have a free-wheel diode system and to be cooled with demineralized water.The main circuit of a standard power supplyincludes 12 pulse diode rectifiers and 4 IGBT chopper units with a switching frequency of 10 kHz.

5.3.3 Quench Protection and Istrumentation

Selected voltage signals from the CEPC detector magnet coil and current leads are monitored by an FPGA board for quench detection. If a quench happened, the power supply is switched off and a dump resistor is switched into the electrical circuit, the huge stored energy will be extracted mainly by the dump resistor and partially by the coil itself. In order to monitor the status of the magnet, sensors or tools are added inside or outside to monitor temperature (busbar, current lead, valve box and etc), stress (tie rods), vacuum, coil current, liquid helium level, position (coil section) and etc.

5.4 Iron Yoke Design

The iron yoke is designed not only for field quality but also for resisting magnetic forces, as well as the mechanical support of the sub-detectors. Therefore high permeability material with high mechanical strength is required for the yoke material in account of mechanical performance and magnetic field. The yoke also provides room for the muon detector, which will sit between layers of the yoke, and allow space for data cables, cooling pipes, gas pipes and etc. through the yoke. The yoke is divided into two main components, one cylindrical barrel yoke and two end-cap yokes. The total weight of the yoke assembly is about 10,000 tons.

The barrel yoke is a dodecagonal shape structure with a length of 8,200 mm (Fig. 5.3). The outer diameter of the dodecagon and the inner diameter are 13,300 mm and 7,800 mm. The barrel yoke is subdivided along the beam axis into 3 rings, with 11 layers

in each ring. Each ring of the barrel yoke is composed of 12 segments. 40 mm gap is designed between the rings and the layers for placing the muon detector and the electronics cables and services. From the inner to the outer, the layer thicknesses are 80 mm, 80 mm, 120 mm, 120 mm, 160 mm, 160 mm, 200 mm, 200 mm, 240 mm, 540 mm, 540 mm, respectively.

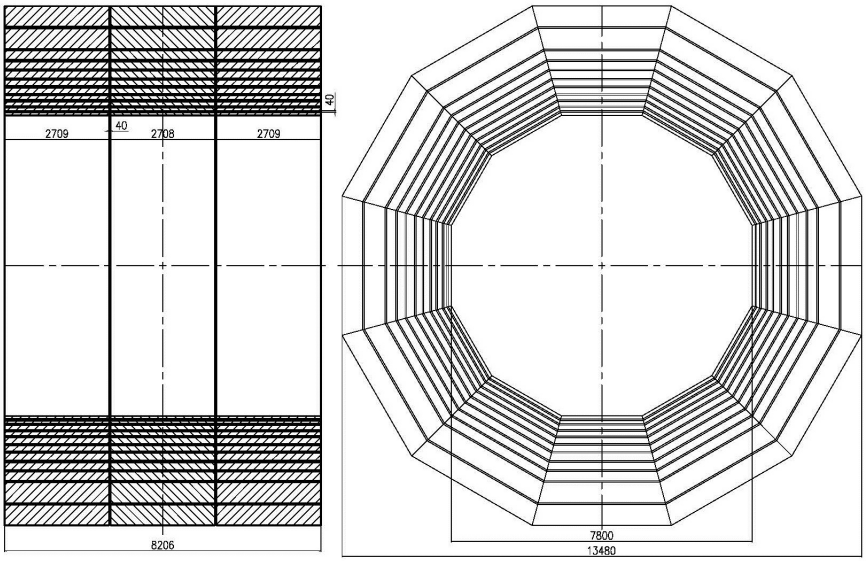

Figure 5.3: The barrel yoke design

The end-cap yokes is designed to dodecagonal structure with the out diameter of 13,300 mm. Each end-cap yoke will consist of 11 layers and one pole tip (Fig. 5.4). Each end-cap yoke is composed of 12 segments. The thickness of pole tip is 600 mm, and from the inner to the outer, the layer thicknesses are 80 mm, 80 mm, 120 mm, 120 mm, 160 mm, 160 mm, 200 mm, 200 mm, 240 mm, 540 mm, 540 mm, respectively.

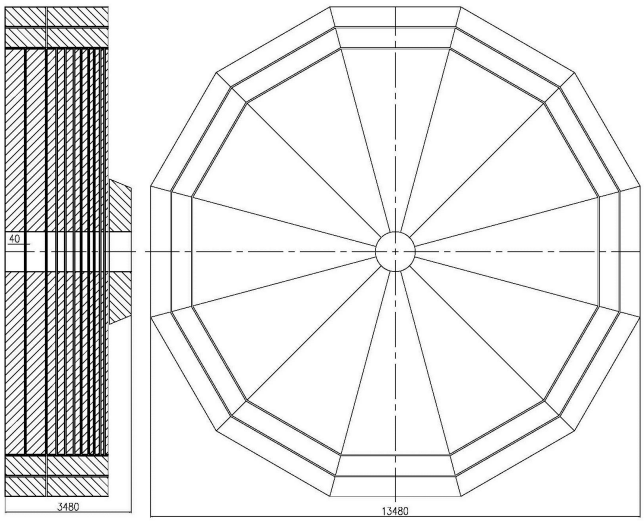

Figure 5.4: The end-cap yokes design

5.5 R&D

5.5.1 HTS solenoid concept for IDEA detector

A large HTS solenoid concept is proposed for the IDEA detector, which requires a thin solenoid with a magnetic field of 2 Tesla and a room temperature bore of 2.1 m diameter [chapter 3.2.2][3, 4]. The HTS solenoid is supposed to use YBCO stacked-tape cable as the conductor. The radiation length of single YBCO tape coated with 150 ŠÌm copper is about 0.014 X0. 35 YBCO tapes stacked together allows 25 kA and 0.49 X0. If the operation temperature of the cold mass is raised to 20 K, the heat conductivity parameters of all components are improved. In addition, the electricity consumption of cooling station will be much lower than that at 4.2 K. Therefore, the YBCO stacked-tape cable and the cryogenics are brought into R&D.

5.5.2 Dual Solenoid Design

The dual solenoid design is presented for a conceptual option for CEPC detector magnet, which contains two series connected superconducting solenoids carrying the opposite direction current, based on FCC twin solenoid [5]. The main solenoid provides central field within the room temperature bore. The outer solenoid provides the stray field shielding and a magnetic field between the two solenoids to facilitate muon tracking. The main advantage of this dual solenoid is that the system becomes comparatively light-weight and cost saving without iron yoke. The sketch is shown in Figure 5.5.

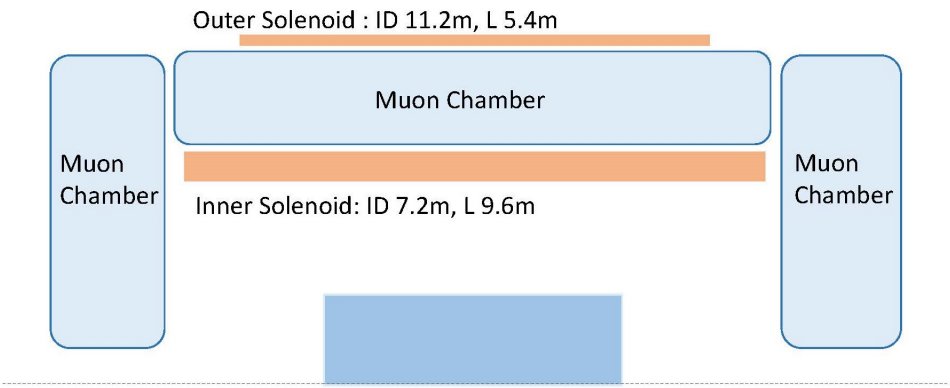

Figure 5.5: The sketch of dual solenoid design

5.5.3 Superconducting Conductor

The coil is simulated with an elasto-plastic 2D FE model. Mechanical analysis requires the experimental material properties of all conductor components. We have developed a 10 m long NbTi Rutherford cable embedded inside stabilizer from a manufacturer which provides Ic 5 kA at 4 T background magnetic field. Meanwhile we measured the material properties and the tensile stress of 10 m cable. Longer conductor with higher Ic 15 kA at 4 T background is ongoing.

5.5.4 Thermosyphon Circuit

Thermosyphon principle is used to cool CEPC detector superconducting magnet by the U-shaped circuit configuration carrying LHe on the outer surfaces of the coil supporting cylinders. The thermosyphon circuit consists of helium phase separator located in an elevated position and the cooling tubes. In order to study the phase transition process of helium in the circuit, the changes of the temperature distribution and the density distribution over the time, a 1:10 scale thermosyphon circuit will be established for simulation and experiment.

References

[1] T. Behnke, J. E. Brau, P. N. Burrows, J. Fuster, M. Peskin, M. Stanitzki, Y. Sugimoto, S. Yamada, and H. Yamamoto, *The International Linear Collider Technical Design Report*, vol. Detector. 2013.

[2] C. Collaboration, *The CMS magnet project: Technical Design Report*, CERN/LHCC, 1997.

[3] M. Mentink, A. Dudarev, H. F. P. D. Silva, C. P. Berriaud, G. Rolando, R. Pots, B. Cure, A. Gaddi, V. Klyukhin, H. Gerwig, U. Wagner, and H. ten Kate, *Design of a 56-GJ Twin Solenoid and Dipoles Detector Magnet System for the Future Circular Collider*, IEEE TRANSACTIONS ON APPLIED SUPERCONDUCTIVITY **26** (2016) no. 3, 4003506.

[4] *Progress in the FCC-ee Interaction Region Magnet Design*. 2017.

[5] M. Caccia, *An International Detector for Electron-Positron Accelerator(IDEA)*, Workshop on Circular Electron-Positron Colliders. Roma, May 24-26th, 2018.

CHAPTER 6

MUON SYSTEM

The muon system for a CEPC detector is designed to identify and measure muons, and will be located within the solenoid flux return yoke of the whole spectrometer. Two detector concepts are envisaged for the CEPC collider and they will likely employ different muon systems. A common requirement for the muon detectors will be to identify muons with very high efficiency ($\geq$95%) and high purity, over the largest possible solid angle and down to low p_T values ($\geq$3 GeV/c). A standalone muon momentum resolution from the muon detector could be required, translating in a good position resolution along the muon track which would add robusteness and redundancy to the whole detector design. In particular the muon system will significantly help in identifying muon produced within jets, for example from b decays.

The muon system plays an important role in measuring physics processes involving muon final states, e.g. $e^+e^- \to ZH$ with $Z \to e^+e^-$ or $\mu^+\mu^-$ and also for studying long-lived particles that would decay far from the primary vertex but still within the detector. In addition, the muon system compensates for leaking energetic showers and late showering pions from the calorimeters, which could help to improve the relative jet energy resolution[1].

In this chapter the baseline muon system design is described and then two possible technologies for realising the muon detector are presented, specifically the Resistive Plate Chamber (RPC) and an innovative type of Micro Pattern Gas detector (MPGD), the μ-RWELL detector. The main difference between the two technologies lies in the position resolution and the cost. More layers of RPC detectors are needed to achieve a good momentum resolution on the muon tracks with respect to the μ-RWELL case, where 3-4 layers would be sufficient. In terms of rate capability both technologies are more than adequate for the CEPC environment. If the requirement of a standalone muon momentum

resolution from the muon detector is relaxed, the number of layers of the RPC solution could be greatly reduced. Other gas detectors are also being considered as possible options, such as Gas Electron Multiplier (GEM), MicroMegas and Monitored Drift Tubes (MDT), although they are not described here.

6.1 Baseline Design

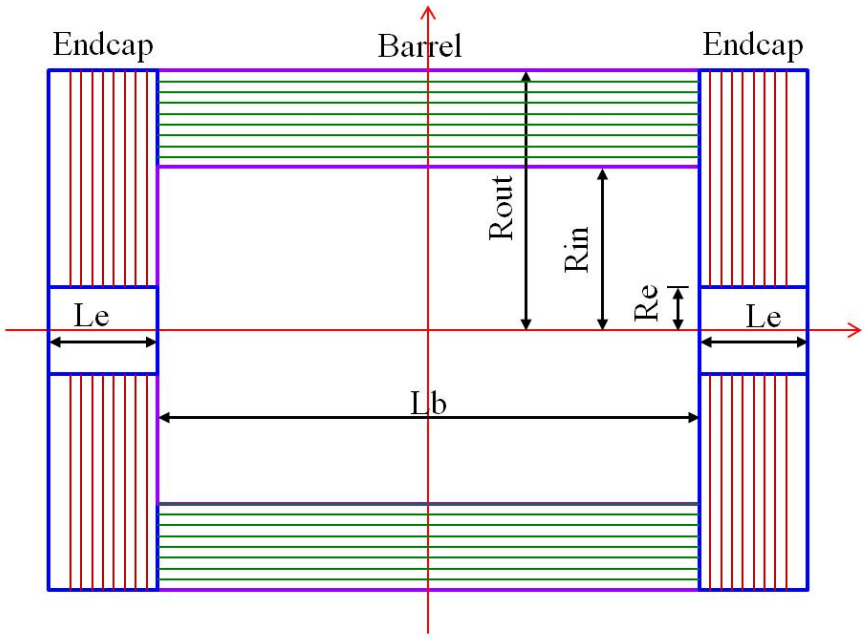

Figure 5.1: The basic layout of the muon system.

The CEPC muon system is the outermost component of the whole detector. It is divided into barrel and end-caps, as shown in Fig. 5.1. Both the barrel and end-caps consist of segmented modules. The segmentation is constrained by the maximum sizes of the module and sensitive unit (more segments are required for a larger detector), dodecagon segmentation is selected for the baseline design of the CEPC muon system. All baseline design parameters are summarised in Table 6.1. These parameters will be further optimised together with the inner detectors, in particular the ECAL and the HCAL.

The number of sensitive layers and the thickness of iron (or tungsten) in the absorbers are two critical parameters. For the baseline design, the total thickness of iron absorber is chosen to be 8λ (the nuclear interaction length of iron) distributed in 8 layers, which should be sufficient for effective muon tracking together in combination with the calorimeters. Gaps of 4 cm between neighbouring iron layers give adequate space for installing sensitive detectors.

The solid angle coverage of the CEPC muon system should be up to $0.98 \times 4\pi$ in accordance with the tracking system. Minimum position resolutions of $\sigma_{r\phi} = 2.0$ cm and $\sigma_z = 1.5$ cm are required. Since the particle flow algorithm calorimetry provides very good particle identification capabilities, the detection efficiency of 95% ($E_\mu > 5$ GeV) of the CEPC muon system should provide enough redundancy and complement in muon detection for most physics processes related to muons. The muon system should provide

Table 6.1: The baseline design parameters of the CEPC muon system

Parameter	**Possible range**	**Baseline**
Lb/2 [m]	3.6 – 5.6	4.0
Rin [m]	3.5 – 5.0	4.4
Rout [m]	5.5 – 7.2	7.0
Le [m]	2.0 – 3.0	2.6
Re [m]	0.6 – 1.0	0.8
Segmentation	8/10/12	12
Number of layers	3 – 10	8
Total thickness of iron	6 – 10λ ($\lambda = 16.77$ cm)	8λ (136 cm) (8/8/12/12/16/16/20/20/24) cm
Solid angle coverage	(0.94 – 0.98)$\times 4\pi$	0.98
Position resolution [cm]	$\sigma_{r\phi}$: 1.5 – 2.5	2
	σ_z : 1 – 2	1.5
Time resolution [ns]	< 10	1 – 2
Detection efficiency ($E_\mu > 5$ GeV)	92% – 99%	95%
Fake($\pi \to \mu$)@30GeV	0.5% – 3%	$< 1\%$
Rate capability [Hz/cm^2]	50 – 100	$\sim$60
Technology	RPC	RPC (super module, 1 layer readout, 2 layers of RPC)
	μRWell	
Total area [m^2]	Barrel	$\sim$4450
	Endcap	$\sim$4150
	Total	$\sim$8600

several hits each with a spatial resolution of a few cm, a time resolution of a few ns and a rate capability of 50 – 100 Hz/cm^2. Based on the dimensions and segmentation of the baseline design, the total sensitive area of the muon system amounts to 8600 m^2.

6.2 The Resistive Plate Chamber technology

Resistive Plate Chamber (RPC) is suitable for building large area detectors with centimeter spatial resolution. It has been applied in muon systems for experiments including BaBar [2], Belle [3], CMS [4] , ATLAS [5], BESIII [6], and Daya Bay [7]. It provides a common solution with the following advantages: low cost, robustness, easy construction of large areas, large signal, simple front-end electronics, good time and spatial resolution. It is chosen as the baseline design of the CEPC muon system.

RPCs can be built with glass or Bakelite, and run in avalanche or streamer mode. Bakelite RPCs of about 1200 m^2 and 3200 m^2 were produced for the BESIII and Daya Bay muon systems, respectively. Compared with glass RPC, Bakelite RPC has the advantages of easier construction, lower density, larger cell size and lower cost, especially if the event rate is below 100 Hz/cm^2 as required by the CEPC muon system. The characteristics of Bakeliete and glass RPCs are compared in Table 6.2. Further improvements are required for Bakelite RPCs, however, in terms of long-term stability, detection efficiency, readout technologies, lower resistivity ($< 10^{10}$) and higher rate capability.

Table 6.2: Comparison of Bakelite and glass RPC.

Parameters		Bakelite	Glass
Bulk resistivity [$\Omega\cdot$ cm]	Normal	$10^{10} \sim 10^{12}$	$> 10^{12}$
	Developing	$10^8 \sim 10^9$	
Max unit size (2 mm thick) [m]		1.2×2.4	1.0×1.2
Surface flatness [nm]		< 500	< 100
Density [g/cm^3]		1.36	2.4∼2.8
Min board thickness [mm]		1.0	0.2
Mechanical performance		Tough	Fragile
Rate capability [Hz/cm^2]	Streamer	100@92%	
	Avalanche	10K	100@95%
Noise rate [Hz/cm^2]	Streamer	< 0.8	0.05

6.3 The μ-RWELL technology

The μ-RWELL is a compact, spark-protected and single amplification stage Micro-Pattern Gas Detector (MPGD). A μ-RWELL detector [8] is composed of two PCBs: a standard GEM Drift PCB acting as the cathode and a μ-RWELL PCB that couples in a unique structure the electron amplification (a WELL patterned matrix) and the readout stages 6.2a). A standard GEM 50 μm polyimide foil is copper clad on one side and Diamond Like Carbon (DLC) sputtered on the opposite side. The thickness of the DLC layer is adjusted

according to the desired surface resistivity value (50-200 MΩ/□) and represents the bottom of the WELL matrix providing discharge suppression as well as current evacuation. The foil is then coupled to a readout board 6.2b). A chemical etching process is then performed on the top surface of the overall structure in order to create the WELL pattern (conical channels 70 um (50 um) top (bottom) in diameter and 140 μm pitch) that constitutes the amplification stage 6.3. The high voltage applied between the copper and the resistive DLC layers produces the required electric field within the WELLs that is necessary to develop charge amplification. The signal is capacitively collected at the readout strips/pads. Two main schemes for the resistive layer can be envisaged: a *low-rate* scheme (for particles fluxes lower than 100 kHz/cm^2) based on a simple resistive layer of suitable resistivity; and an *high-rate* scheme (for a particle flux up to 1 MHz/cm^2) based on two resistive layers intra-connected by vias and connected to ground through the readout electrodes. Finally, a drift thickness of 3-4 mm allows for reaching a full efficiency while maintaining a versatile detector compactness.

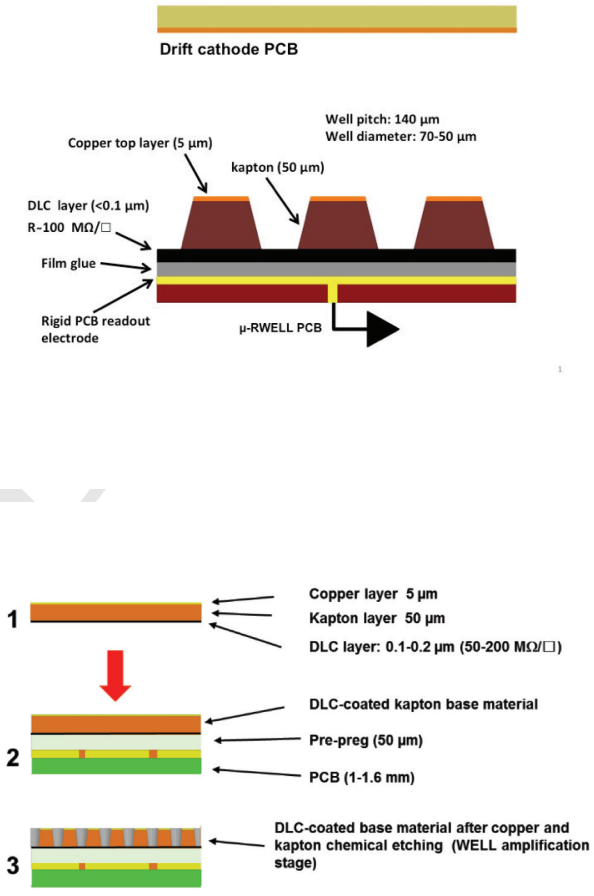

Figure 6.2: a) Layout of a μ-RWELL detector module; b) Coupling steps of the μ-RWELL PCB c) Amplification stage directly coupled with the readout.

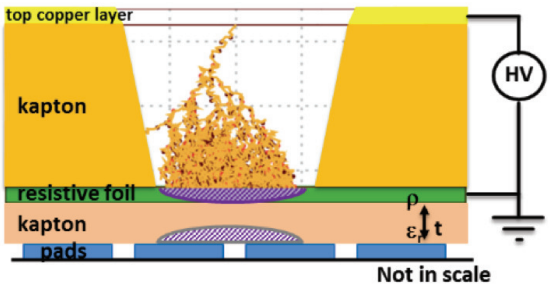

Figure 6.3: Amplification stage directly coupled with the readout.

A distinctive advantage of the proposed μ-RWELL technology is that the detector does not require complex and time-consuming assembly procedures (neither stretching nor gluing), and is definitely much simpler than many other existing MPGDs, such as GEMs or MicroMegas. Being composed of only two main components, the cathode and anode PCBs, is extremely simple to be assembled. This makes the cost of a μ-RWELL detector typically less than half the cost of a triple-GEM detector of the same size and the same strip pitch.

The μ-RWELL technology, especially in its *low-rate* version, is a mature solution, with whom single detectors of a 0.5 m^2 have been realised and succesfully operated in the laboratory as well as in test beams. They can withstand particle rates up to a few tens of kHz/cm^2, providing a position resolution as good as $\sim$60 μm with a time resolution of 5-6 ns. The detailed results are presented in the Appendix. The requirements of a muon detector for CEPC are not as stringent and therefore can be easily and cost-effectively achieved with the μ-RWELL technology. Moreover the μ-RWELL technology is a robust solution, intrinsically safer against sparks than, for example, the widely used GEM detectors. The muon system could be realised by using tiles of μ-RWELL detectors of a size 50x50 cm^2. This would make the whole muon detector very modular with components bought directly from industry. A CEPC muon detector made of μ-RWELL tiles could consist of three or four detector layers stations, each equipped with a couple of layers of μ-RWELL detectors in order to provide a very precise, of the order of 200-300μm, position resolution on the coordinates of a muon track.

6.4 Future R&D

The baseline conceptual design and most promising technologies for the CEPC muon system have been discussed. Future R&D requires detailed studies of different technologies and further optimization of baseline design parameters. Several critical R&D items have been identified, including:

- **Long-lived particles optimization**: Explore new physics scenario of long-lived particles and exotic decays. Optimize detector parameters and technologies.
- **Layout and geometry optimization**: Detailed studies on the structure of the segments and modules need to be carried out to minimise the dead area and to optimise the interface for routing, support and assembly. The geometry and dimensions need to be optimized together with the inner detectors, in particular the ECAL and the HCAL.
- **Detector optimization**: Study aging effects, improve long-term reliability and stability, readout technologies.
- **Detector industrialization**: Improve massive and large area production procedures for all technologies. One example is the engineering and the following industrialization of the μ-RWELL technology. The engineering of the detector essentially coincides with the technological transfer of the manufacturing process of the anode PCB and the ecthing of the kapton foil to suitable industrial partners.

References

[1] CALICE Collaboration, *Construction and performance of a silicon photomultiplier/extruded scintillator tail-catcher and muon-tracker*, JINST **7** (2012) no. 04, P04015, arXiv:1201.1653. http://stacks.iop.org/1748-0221/7/i=04/a=P04015.

[2] Babar Collaboration, *The BaBar detector*, Nucl. Instrum. Meth. **A479** (2002) 1–116, arXiv:hep-ex/0105044.

[3] A. Abashian et al., *The Belle Detector*, Nucl. Instrum. Meth. **A479** (2002) 117–232. KEK-PROGRESS-REPORT-2000-4.

[4] CMS Collaboration, *The CMS muon project: Technical Design Report*. Technical Design Report CMS. CERN, Geneva, 1997. http://cds.cern.ch/record/343814.

[5] ATLAS Collaboration, *ATLAS muon spectrometer: Technical Design Report*. Technical Design Report ATLAS. CERN, Geneva, 1997. http://cds.cern.ch/record/331068.

[6] Y.-G. XIE, J.-W. ZHANG, Q. LIU, J.-F. HAN, S. QIAN, N. YAO, J.-B. ZHAO, J. CHEN, and J.-C. LI, *Performance Study of RPC Prototypes for the BESIII Muon Detector*, Chinese Physics C **31** (2007) no. 01, 70–75. http://cpc-hepnp.ihep.ac.cn:8080/Jwk_cpc/EN/abstract/abstract7618.shtml.

[7] J.-L. Xu, M.-Y. Guan, C.-G. Yang, Y.-F. Wang, J.-W. Zhang, C.-G. Lu, K. McDonald, R. Hackenburg, K. Lau, L. Lebanowski, C. Newsom, S.-K. Lin, J. Link, L.-H. Ma, and P. Viktor, *Design and preliminary test results of Daya Bay RPC modules*, Chinese Physics C **35** (2011) no. 9, 844. http://stacks.iop.org/1674-1137/35/i=9/a=011.

[8] G. Bencivenni, R. D. Oliveira, G. Morello, and M. P. Lener, *The micro-Resistive WELL detector: a compact spark-protected single amplification-stage MPGD*,

Journal of Instrumentation **10** (2015) no. 02, P02008.
http://stacks.iop.org/1748-0221/10/i=02/a=P02008.

CHAPTER 7

READOUT ELECTRONICS AND DATA ACQUISITION

This [1] is an example with plots, please edit ...

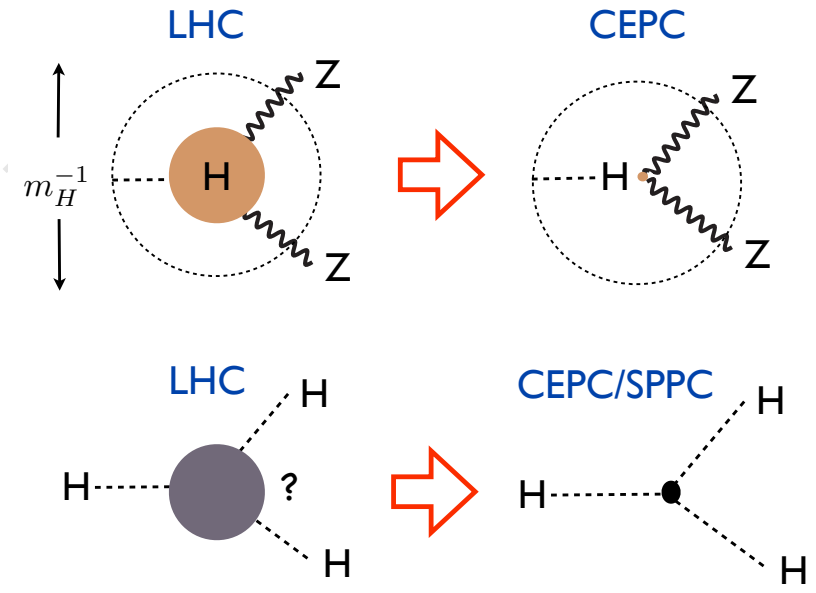

Figure 7.1: A sketch of two of the central goals of the CEPC and SPPC. The CEPC will probe whether the Higgs is truly “elementary", with a resolution up to a hundred times more powerful than the LHC. The SPPC will see, for the first time, a fundamentally new dynamical process — the self-interaction of an elementary particle — uniquely associated with the Higgs.

7.1 New Colliders for a New Frontier

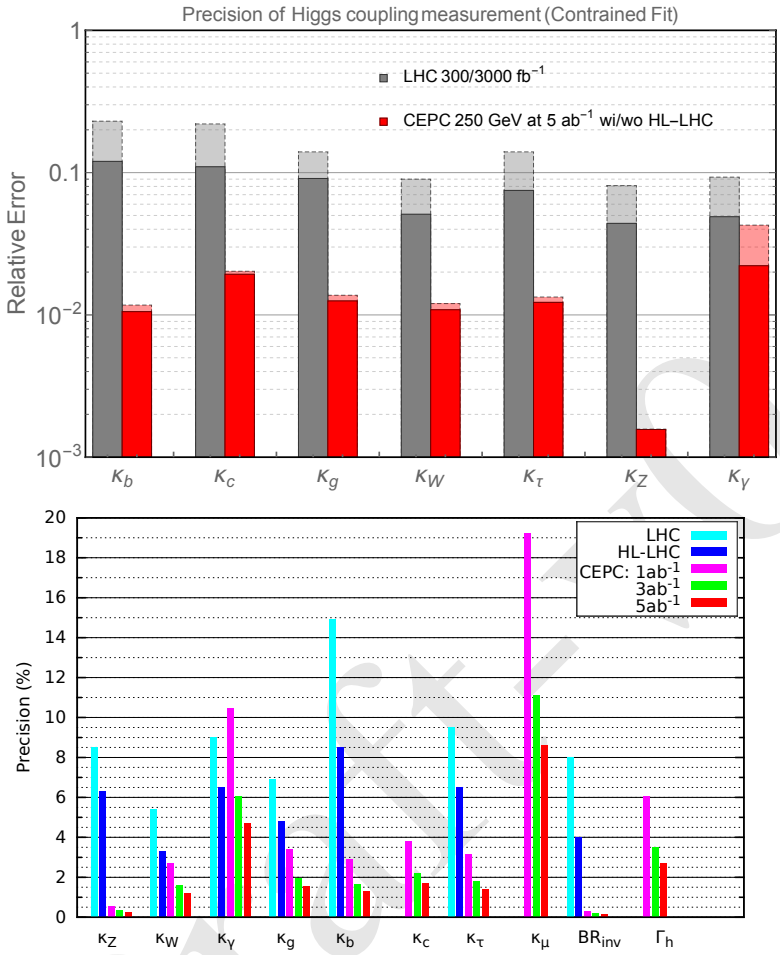

Figure 7.2: Top: The 7 parameter fit, and comparison with the HL-LHC, discussed in detail in Chapter **??**. The projections for CEPC at 250 GeV with 5 ab^{-1} integrated luminosity are shown. The CEPC results without combination with HL-LHC input are shown with dashed edges. The LHC projections for an integrated luminosity of 300 fb^{-1} are shown in dashed edges. Bottom: Comparison between the LHC and several benchmark luminosities of the CEPC.

References

[1] CEPC project website. http://cepc.ihep.ac.cn.

CHAPTER 8

MACHINE DETECTOR INTERFACE

Machine-Detector Interface (MDI) represents one of the most challenging topics for the CEPC projects. In general, it will have to cover all common issues relevant to both the machine and detector. Topics summarized in this chapter include the interaction region, the final focusing magnets, the detector radiation backgrounds and the luminosity instrumentation. Integration of all the machine and detector components in the interaction region is also briefly discussed. It is critical to achieve comprehensive understanding of MDI issues and assure the optimal performance of the machine and detector.

8.1 Interaction region

The interaction region (IR) has to focus both electron and positron beams to small spot sizes at the interaction point (IP) to maximize the machine luminosity, and merge but subsequently separate the two beams which travel in two separate storage rings. The IR layout, as illustrated in Fig. 8.1, has received several necessary updates with respect to the published preliminary CDR [1], to cope with the latest double-ring design and a beam-crossing angle of 33 mrad. The two final focusing magnets, QD0 and QF1, sits inside the detector. The focal length (L^*), defined as the distance from the final focusing magnet (*i.e.* QD0) to the IP, has increased from 1.5 m to 2.2 m. This allows enlarged separation between the two single apertures of the QD0. Compensating magnets are positioned in front of the QD0 and surrounding both the QD0 and QF1 magnets. They are introduced to cancel out the detector solenoid field and minimize the disturbance on the focusing beams. Furthermore, the outer radius of the compensating magnets defines the detector acceptance to be $|\cos\theta| \leq 0.993$. The luminosity calorimeter (so called "LumiCal"), located right in front of the compensating magnets, is designed to measure the integrated

luminosity to a precision of 10^{-3} or even higher. Tracking disks, labeled as FTD, are designed to measure charged particle trajectories in the forward region.

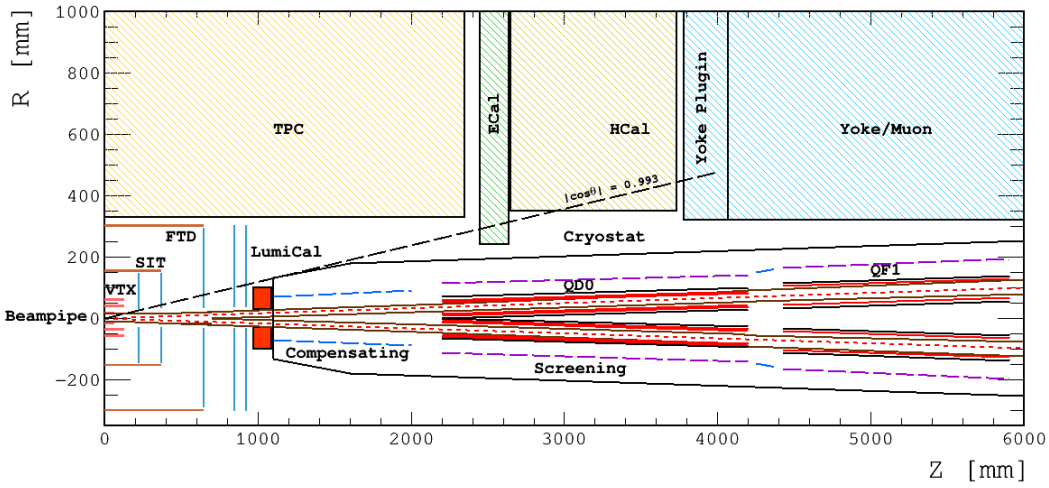

Figure 8.1: Layout of the CEPC interaction region.

8.2 Final focusing magnets

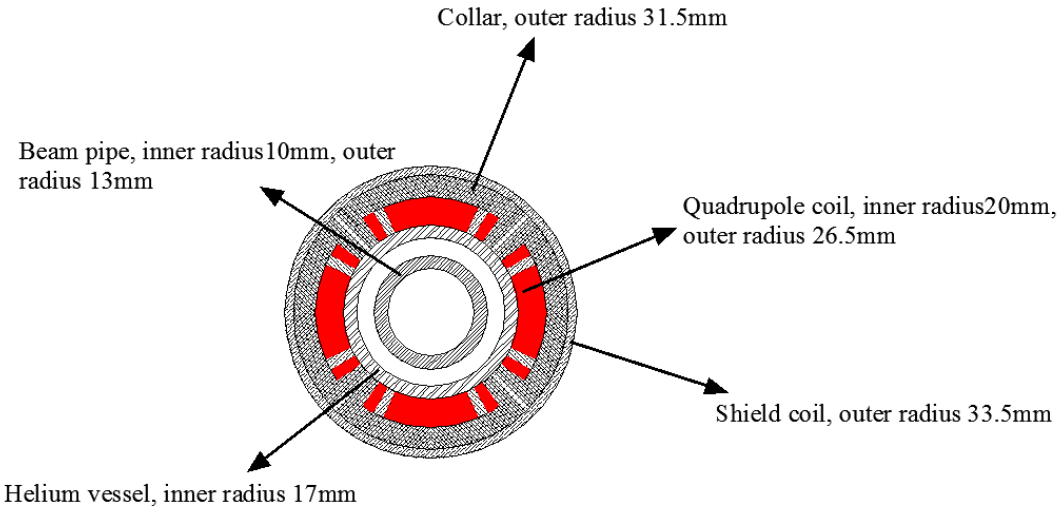

Figure 8.2: Schematic view of the single aperture of the QD0 superconducting magnet.

In the interaction region, compact high gradient quadrupole magnets are designed to focus the electron and positron beams. The two final focusing quadrupoles (QD0 and QF1), are placed inside the CEPC detector and must operate in the background field of the detector solenoid. QD0 is the quadrupole magnet close to the interaction point, with a distance of 2.2 m to the IP. It is designed as a double aperture superconducting magnet and can be realized with two layers of Cos-Theta quadrupole coil using NbTi Rutherford cables without iron yoke. The cross-sectional view of the single aperture of the QD0 is shown in Fig. 8.2. It is designed to deliver a gradient field of 136 T/m and control the filed

harmonics in the sensitive area to be below 3×10^{-4}. Design parameters are summarized in Table 8.1. The QF1 magnet is similar to the QD0, except that there is an iron yoke around the quadrupole coil for the QF1.

Table 8.1: Main design parameters of QD0 and QF1.

Magnet	QD0	QF1
Field gradient [T/m]	136	110
Magnetic length [m]	2.0	1.48
Coil turns per pole	23	29
Excitation current [A]	2510	2250
Coil layers	2	2
Stored energy [kJ]	25.0	30.5
Inductance [H]	0.008	0.012
Peak field in coil [T]	3.3	3.8
Coil inner diameter [mm]	40	56
Coil outer diameter [mm]	53	69
X direction Lorentz force/octant [kN]	68	110
Y direction Lorentz force/octant [kN]	-140	-120

Additional compensating magnets are introduced to minimize the disturbance from the detector solenoid on the incoming and outgoing beams. The compensating magnets in front of the QD0 is designed to achieve an almost zero integral longitudinal field before entering the QD0. And the compensating magnet right outside the QD0 and QF1 is necessary to screen the detector field. The magnets are based on wound of rectangular NbTi-Cu conductors. To minimize the magnet size, the compensating magnets are segmented into 22 sections with different inner coil diameters. Inside the first section, the central field reaches the peak value of 7.2 Tesla. More detailed design of the final focusing magnets and the compensating magnets can be found in [2].

8.3 Detector backgrounds

Beam and machine induced radiation backgrounds can be the primary concern for the detector design [3–6]. They can cause various radiation damages to the detectors and electronic components, and degrade the detection performance or even kill the detector completely in the extreme case. During data-taking, high rate radiation backgrounds may significantly increase the detector occupancy and exaggerate the data-taking capability of the impaired detector. Therefore it is always desirable to characterize the potential backgrounds at the machine and detector design stage and mitigate their impacts with effective measures. Detailed Monte Carlo simulation, along with lessons and experience learned from other experiments, can serve as the basis for such studies.

The deleterious effects of the radiation backgrounds can be represented with hit density, total ionizing dose (TID), and non-ionizing energy loss (NIEL). The expected hit

density can be used to evaluate the detector occupancy. TID is an important quantity for understanding surface damage effects in electronics. NIEL, represented in the 1 MeV neutron equivalent fluence, is important for understanding the bulk damage to silicon devices. The background simulation starts with either generating background particles directly in the IR (e.g. pair production) or propagating them to the region close enough to the IR (e.g. SR photons and off-energy beam particles). Particle interactions with detector components are simulated with Geant4 [7–9]. The characterization methodology for the ATLAS detector background estimation [10] has been adopted. In the following, main radiation backgrounds originating from synchrotron radiation, beam-beam interactions, and off-energy beam particles, are discussed and their contributions are carefully evaluated.

8.3.1 Synchrotron radiation

Synchrotron radiation (SR) photons are vital at circular machines. At the CEPC, they are mostly produced in the last bending dipole magnets and in the focusing quadrupoles inside the interaction region. The innermost tracking detectors can be sensitive to photons above 10 keV and vulnerable to high levels of soft photon radiation [1]. In order to reduce the energy and flux of SR photons that enter the straight sections, the field strength of the last bending dipole magnet has been reduced and becomes much weaker than the normal arc dipole fields. This controls the critical energy of SR photons to be below 100 keV and makes the collimation design less difficult.

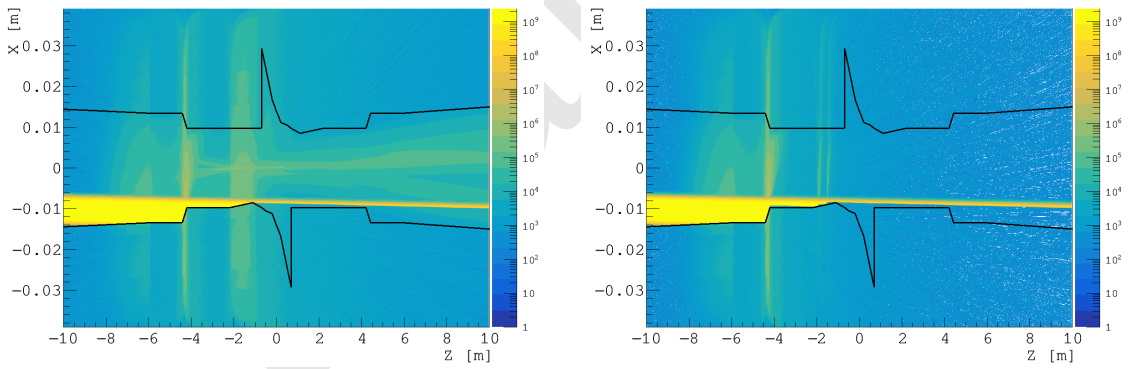

Figure 8.3: Distribution of the synchrotron photon flux formed by the upstream bending magnet on the left side before (a) and after (b) introducing collimators.

The BDSim [11] software based on GEANT4 has been deployed for the detailed studies. It allows generating SR photons from the relevant magnetic elements and transports them to the region of the experimental detectors. Particular care has been taken for a realistic simulation in the tails of the beam density distributions (up to 10 $\sigma_{x/y}$) and for both beam core and halo, as particles form the tails are most effective in producing background particles. SR photons from the last dipole magnet form the light yellow band in Fig. 8.3 and can hit the beam pipe in the interaction region. A considerable amount of

[1] It should be noted that the SR photon energy increases rapidly with the beam energy and additional measures might have to be introduced to allow detector operation at higher operation energies.

them are scattered and can hit the central Beryllium beam pipe ($z = \pm 7$ cm) as shown in Fig. 8.3(a). Collimators made with high-Z materials (e.g. tungsten) and particular shapes are designed to block those scattering photons. Three sets of mask tips, located at $|z| = 1.51$, 1.93 and 4.2 m along the beam pipe to the interaction point, are introduced to suppress such SR photons. They can effectively reduce the number of SR photons hitting the central beam pipe from nearly 40, 000 to below 80. This reduction leads to much lower power deposition in the beam pile and allows a simplified cooling design for the beam pipe. The resulting photon flux distribution after collimation is shown in Fig. 8.3(b). SR photons generated in the final focusing magnets are also carefully evaluated. They are highly forward and do not strike directly the central beam pipe unless the particles are 40 σ_x off the central orbit.

Table 8.2: The input machine parameters to the GUINEA-PIG simulation.

Machine Parameters	**H** (240 GeV)	**W** (160 GeV)	**Z** (91 GeV)
Beam energy [GeV]	120	80	45.5
Particles per bunch [10^{10}]	15	12	8
Transverse size σ_x/σ_y [μm]	20.9/0.068	13.9/0.049	6.0/0.078
Bunch length σ_z [μm]	3260	5900	8500
Emittance $\varepsilon_x/\varepsilon_y$ [nm]	12.1/0.0031	0.54/0.0016	0.18/0.004

8.3.2 Beam-beam interactions

Beamstrahlung and its subsequent process of pair production are important background at the CEPC. Due to the pinch effect in the beam-beam interaction, the trajectories of beam particles in the bunches are bent, which causes the emission of beamstrahlung photons. This process has been studied with the Monte Carlo simulation program GUINEA-PIG [12], which takes into account dynamically changing bunch effects, reduced particle energies and their impacts on the electric and magnetic fields. In addition, the simulation program has be customized to implement the external detector field for the charged particle tracking. This allows improved determination of the positions and momenta of the out-going charged particles before interfacing to the GEANT4 detector simulation. Machine parameters for operation at different energies are listed in Table 8.2, and serve as the input to the GUINEA-PIG simulation. It should be noted that compared to other consequent processes, electron-positron pair production generates most significant detector backgrounds. The processes can be categorized as:

- *Coherent Production*: e^+e^- pairs are produced via the interaction of virtual or real photons (e.g. beamstrahlung photons) with the coherent field of the oncoming bunch. Particles can be highly energetic but are dominantly produced with small angle and confined in the beam pipe.
- *Incoherent Production*: e^+e^- pairs are produced through interactions involving two real and/or virtual photons. Most of the particles are confined in the beam pipe by the strong detector solenoid field. However, a small fraction of them are produced with high transverse momentum and large polar angle.

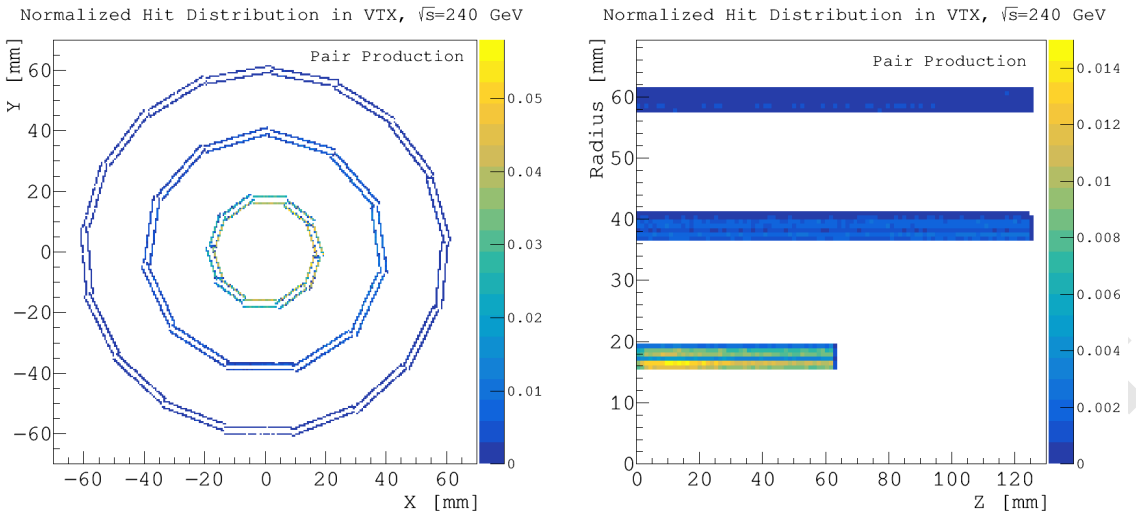

(a) (b)

Figure 8.4: Hit distributions due to the pair production in the $x-y$ and $r-z$ planes of the vertex detector.

As shown in Fig. 8.4(a), the resulting hit distribution is nearly uniform in the $\phi-$ direction, even though the beam squeezing is different in the x and y directions. On the other hand, the hit distribution is more dense in the central region as shown in Fig. 8.4(b), but decreases rapidly with the increased radius.

Table 8.3: Maximum radiation backgrounds originating from the pair production at each vertex detector layer.

	Hit Density [hits/BX]	TID [kRad/year]	NIEL [1 MeV n_{eq}/ cm^2·year]
Layer 1 ($r = 1.6$ cm)	2.2	620	1.2×10^{12}
Layer 2 ($r = 1.8$ cm)	1.5	480	9.1×10^{11}
Layer 3 ($r = 3.7$ cm)	0.18	60	1.2×10^{11}
Layer 4 ($r = 3.9$ cm)	0.15	45	1.0×10^{11}
Layer 5 ($r = 5.8$ cm)	0.03	9.7	3.3×10^{10}
Layer 6 ($r = 6.0$ cm)	0.02	6.8	3.0×10^{10}

8.3.3 Off-energy beam particles

Circulating beam particles can lose significant amounts of energy in scattering processes. If exceeding 1.5% of the nominal energy (defined as the machine energy acceptance), scattered particles can be kicked off their orbit. A fraction them will get lost close to or in the interaction region. They can interact with machine and/or detector components and contribute to the radiation backgrounds. There are three main scattering processes that

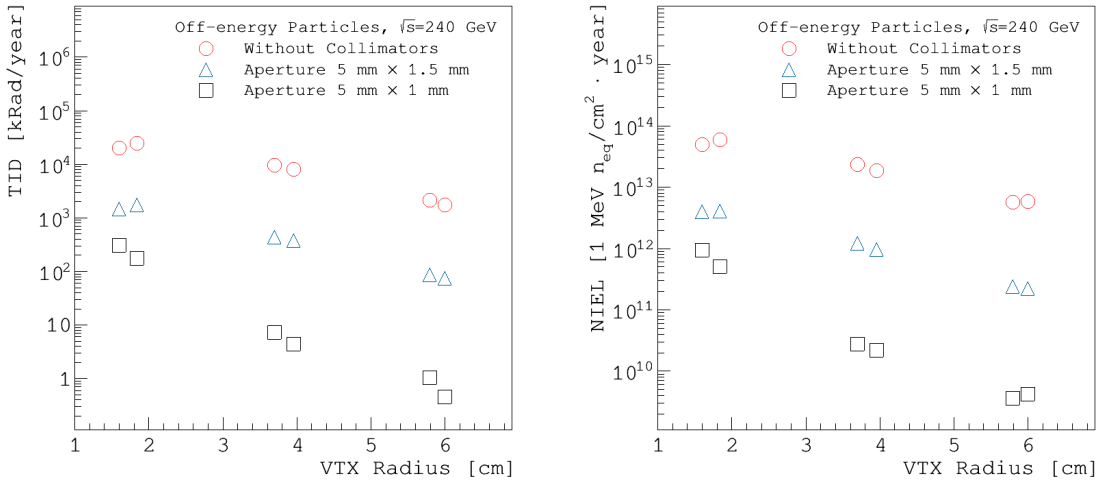

(a) (b)

Figure 8.5: Contributions to TID and NIEL from off-energy beam particles are effectively reduced after introducing the two sets of collimators.

are almost entirely responsible for the losses of beam particles, including beamstrahlung, radiative Bhabha scattering and beam-gas interaction.

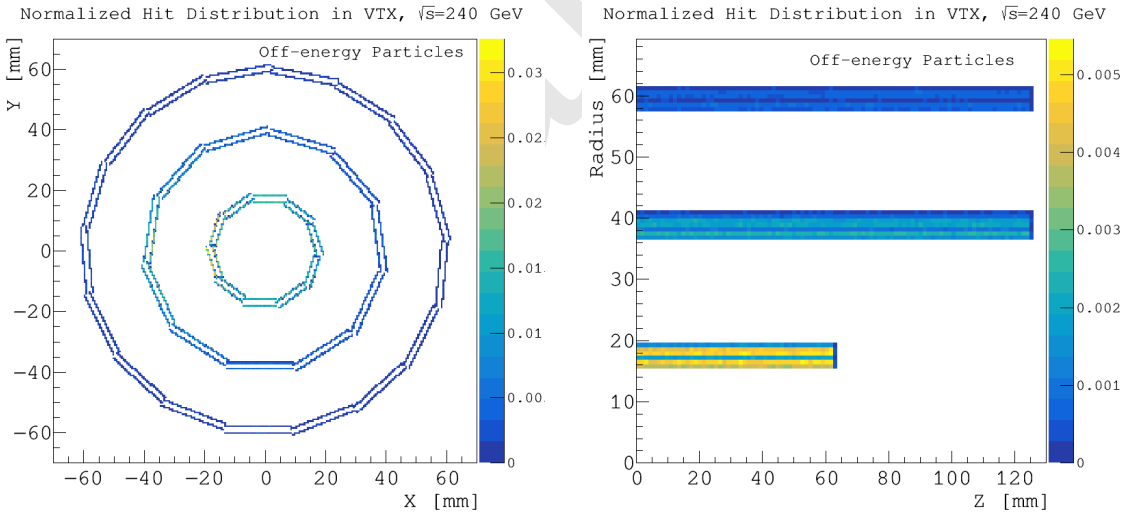

(a) (b)

Figure 8.6: Hit distributions due to the radiative Bhabha scattering process in the $x - y$ and $r - z$ planes of the vertex detector.

While beamstrahlung events out of beam-beam interactions are generated with GUINEA-PIG, radiative Bhabha events with small angles are generated with the BBBREM program [13]. Interactions between the beam particles and the residual gas in the beam pipe are simulated with custom code, assuming the gas pressure to be 10^{-7} mbar. The backgrounds originating from the beam-gas interaction is much smaller compared to that from the Radiative Bhabha scattering. Beam particles after interactions are tracked with

SAD [14] and transported to the interaction region. Particles lost close to the interaction region, either right after the bunch crossing or after traveling multiple turns, are interfaced to detector simulation.

Backgrounds introduced by off-energy beam particles can be effectively suppressed with proper collimation. The designed collimator aperture has to be small enough to stop as much as possible the off-energy beam particles, but must be sufficiently large without disturbing the beam. Two sets of collimator pairs, APTX1/Y1 and APTX2/Y2 are placed in the arch region, with aperture size of 5 mm and 1 mm, in the horizontal and vertical planes, respectively. They are equivalently 14 σ_x and 39 σ_y, which are sufficiently away from the beam clearance region. Fig. 8.5 shows off-energy beam particles entering the IR are reduced significantly after introducing the collimation system. As shown in Fig. 8.6(a), the resulting hit distribution maximizes towards the $-x$ direction due to the nature of the off-energy beam particles that are swept away by the magnets. But along the z direction, the hit distribution is more or less uniform with the additional contribution of the back-scattered particles by the LumiCal in the downstream. For the background estimation, the maximum values in the $-x$ direction are taken. At the first vertex detector layer ($r = 1.6$ cm), the hit density is about 0.22 hits/cm^2 per bunch crossing from the radiative Bhabha scattering. The TID and NIEL are 310 kRad per year and 9.3×10^{11} 1 MeV n_{eq}/cm^2 per year, respectively.

8.3.4 Summary of radiation backgrounds

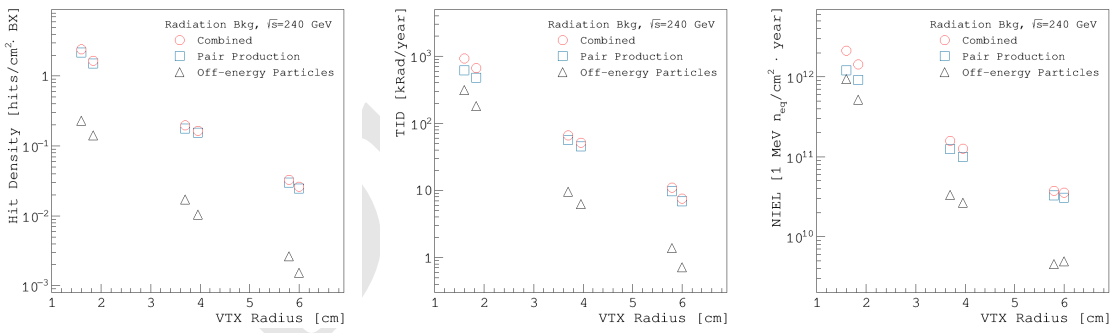

(a) (b) (c)

Figure 8.7: Hit density, TID and NIEL at different vertex detector layers due to the pair production, off-energy beam particles and the two combined.

When operating the machine at the center-of-mass energy of $\sqrt{s} = 240$ GeV, the main detector backgrounds come from the pair-production. The contribution from the off-energy particles is nearly an order of magnitude lower. Fig 8.7 shows the hit density, TID and NIEL at different vertex detector layers, originating from the pair production, off-energy beam particles and the two combined. In addition, TID and NIEL distributions covering the silicon detectors in $r - z$ are shown in Fig. 8.7.

At lower operation energies, *i.e.* $\sqrt{s} = 160$ GeV for W and $\sqrt{s} = 91$ GeV for Z, the background particles are usually produced with lower energies but with higher rates given the higher machine luminosities. In addition, the pair-production dominates the radiation backgrounds and contributions from other sources become negligible. The

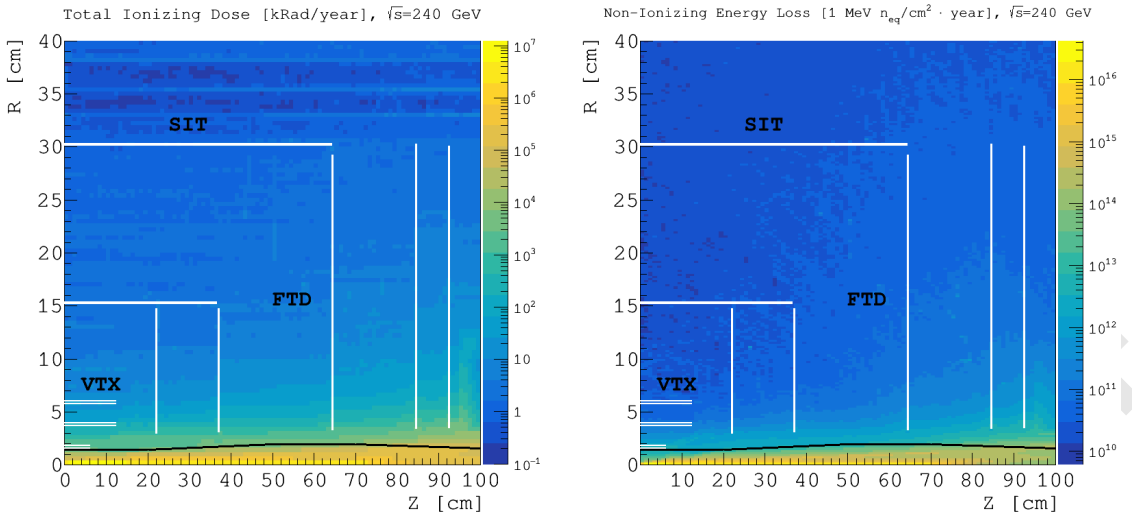

(a) (b)

Figure 8.8: TID and NIEL distribution in $r - z$ for the machine operation at $\sqrt{s} = 240$ GeV.

resulting radiation backgrounds at the first vertex detector layer at different operation energies are summarized in Table 8.4.

Table 8.4: Summary of radiation background levels at the first vertex detector layer ($r = 1.6$ cm) at different machine operation energies.

	H (240)	**W** (160)	**Z** (91)
Hit Density [hits/BX]	2.4	2.3	0.25
TID [MRad/year]	0.93	2.9	3.4
NIEL [10^{12} 1 MeV n_{eq}/cm^2·year]	2.1	5.5	6.2

8.4 Luminosity instrumentation

Very forward region at CEPC will be instrumented with a luminometer (LumiCal), aiming to measure integral luminosity with a precision of 10^{-3} and 10^{-4} in e^+e^-collisions at the center-of-mass energy of 240 GeV and at the Z pole, respectively. The precision requirements on the integral luminosity measurement are motivated by the CEPC physics program, intended to test the validity scale of the Standard Model through precision measurements in the Higgs and the electroweak sectors with 10^6 Higgs and 10^{10} Z bosons. Many sensitive observables for such measurements critically depend on the uncertainty of the integral luminosity.

Luminosity at an e^+e^- collider is best measured by counting the Bhabha events of elastic e^+e^- scattering. Its theoretical interpretation is better than 0.05% at the Z pole [15]. The scattered electrons are distributed in the forward direction with a $1/\theta^3$ dependence. The cross section of the BHLUMI [16] simulation is illustrated in Fig. 8.9(a).

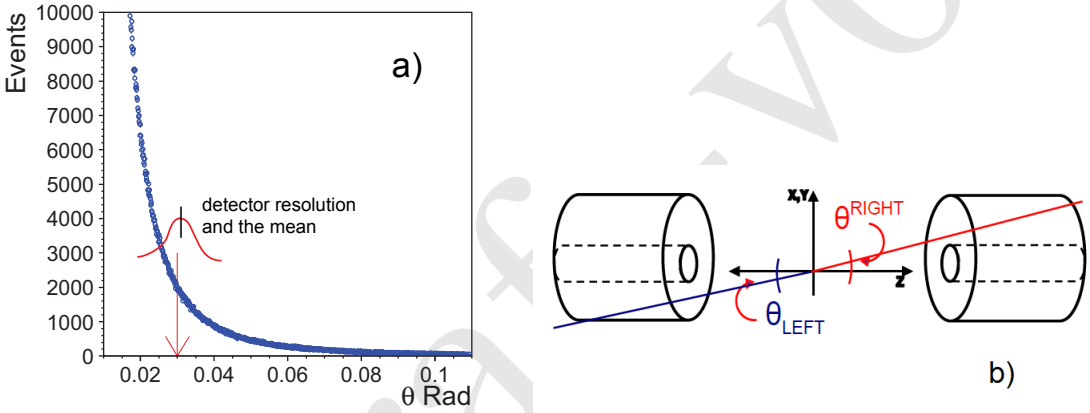

Figure 8.9: a) Distribution of scattered electrons in azimuthal angle of the BHLUMI simulation. The Gaussian curve illustrates the detector resolution to θ measured at a given fiducial edge. The offset of the mean in measurement contributes to the systematic errors. b) Bhabha events is measured preferably in the forward direction of the e^+e^-collision characterized by the back-to-back of elastic scattering and the electromagnetic shower of the electrons.

A Bhabha event is detected with a pair of scattered electrons back-to-back in direction, and the momenta of beam energy. Therefore the luminosity detector is consists of a pair of forward calorimeters with high precision on detecting electron impact positions. The configuration is sketched in Fig. 8.9(b). Bhabha events are detected in the angular coverage ($\theta_{min} < \theta < \theta_{max}$) of the forward calorimeters. The integrated luminosity (L) of the leading order calculation is

$$\sigma^{vis} = \frac{16\pi\alpha^2}{s}\left(\frac{1}{\theta^2_{min}} - \frac{1}{\theta^2_{max}}\right), \quad \mathcal{L} = \frac{1}{\epsilon}\frac{N_{acc}}{\sigma^{vis}}, \quad \frac{\Delta\mathcal{L}}{\mathcal{L}} \sim \frac{2\Delta\theta}{\theta_{min}}, \tag{8.1}$$

where ϵ is the detection efficiency to be evaluated. The systematic uncertainties are contributed mostly by the error on θ_{min}, mainly due to mechanical alignment and the detector resolution. The error propagates to the luminosity is about twice on magnitude.

The dimension of the detector is favorable to have the θ_{min} as low as possible to optimize coverage of the Bhabha cross section. The position of the luminosity detector is planned to be mounted in front of the quadruple magnets at $z = \pm 100$ cm. With the

θ_{min} of ∼30 mrad, corresponding to a radius of 30 mm to the beam pipe at $z = 100$ cm, the cross-section, σ^{vis}, after event selection will reach ~ 50 nb. A large detector coverage of σ^{vis} is necessary for statistics required for the Z line-shape study, where the $Z \to qq$ cross section is 41 nb. The precision required for 10^{-4} makes a strong demand on the detector resolution. At $\theta = 30$ mrad, it corresponds to an offset of $\Delta\theta \sim 1.5$ μrad, which is equivalent to 1.5 μm in radius at $z = 100$ cm.

Several technological options for LumiCal design are under study, as described in Sec. 8.4.1, with emphases on the precision of polar angle and energy reconstruction of Bhabha particles scattered in the t-channel $V(V = \gamma, Z)$ exchange. The dual beam-pipe configuration with the beam-crossing at 33 mrad results to a boost to particles of e^+e^- collisions. The back-to-back characteristics of Bhabha electrons is shifted by approximately a horizontal offset of 33 mm. The impact to LumiCal design is discussed. The LumiCal together with the quadruple magnet are inserted into the tracking volume that extended to $z = \pm 200$ cm. Shower leakage of electrons off the LumiCal to central tracker is studied by simulation, which is also discussed.

Luminometer at CEPC is a precision device with challenging requirements on the mechanics and position control. Precision requirements on integral luminosity measurement set the precision of the opening aperture and positioning control of the LumiCal. Various sources of luminosity uncertainty in this respect are reviewed in Sec. 8.4.2. Encouraging estimations on feasibility of the luminosity precision goals are presented. Detailed studies are ongoing, to include the full simulation of physics and machine induced processes and of the detector itself, for various luminometer positioning and technology choices.

8.4.1 Technological and design options

In the current design of the very forward region at CEPC, luminometer is foreseen to cover the polar angle region between 26 mrad and 105 mrad what translates into the detector aperture of 25 mm for the inner radius and 100 mm for the outer, at $z = \pm 100$ cm of the LumiCal front plane from the IP. The detector options shall be considered for

1. precision of the electron impact position to $r \sim 10$ μ m (1 μ m) for the errors on luminosity, corresponding to the systematic errors on luminosity of $\Delta L \sim 10^{-3}$ (10^{-4}) in the Higgs (Z-pole) operations;

2. monitoring of the detector alignment and calibration of detector position by tracking of Bhabha electrons with upstream detectors;

3. energy resolution and separation of e/γ for measurements of single photons and radiative Bhabha events;

4. maximum coverage and segmentation of the LumiCal to accommodate the dual beam-pipe and the beam crossing of 33 mrad;

5. minimizing shower leakage into the central tracking volume.

The detector option for the 1 μm precision on electron impact position is very much limited silicon detectors segmented in strips or pixels. Silicon strip detectors of 50 μm readout pitch is commonly reaching a resolution of $\sigma \sim 5$ μm. The mean on error

($\bar{\sigma} = \sigma/\sqrt{n}$) would be much smaller. The selection of Bhabha events is set on a fiducial edge of θ_{min}, for example, center in the gap between two silicon strips. The systematic error is therefore the number of events being selected with an error of $\bar{\sigma}$ despite the detector resolution, and would be relatively small, which is indicated by the Gaussian curve in Fig.8.9(a). The alignment of the detector position would be the major systematic requirement for an absolute precision of 1 μm.

A conceptional Luminosity detector is illustrated in Fig. 8.10 for the combination of a silicon detector and a calorimeter around the beam pipe for measurement of the electron impact position energy. The segmentation of the calorimeter is considered for the back-to-back resolution detecting a pair of Bhabha electrons, and for separation of e/γ in case of radiative photon accompanied with the electron or from beam background. The thickness is determined for the energy resolution favorable of $> 20X_0$ for shower containment of a 50 GeV electron. The option on the calorimeter is limited by the space affordable. The traditional crystal or scintillator-based calorimeter will require more than 20 cm in length for $> 20X_0$. The most compact design would be a sandwiched stack of Silicon samplers with Tungsten in $1X_0$ (3.5 mm thick), to a total of about 10 cm that weights about 400 kg.

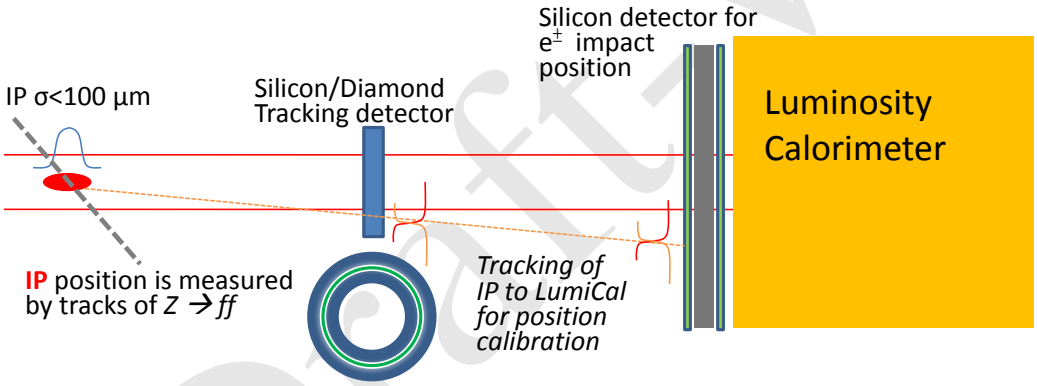

Figure 8.10: A conceptional luminosity detector combination with a upstream silicon/diamond detector for tracking Bhabha electrons to calibrate position of the luminosity detector.

The alignment precision of the front-layer Silicon detector is the most critical issue to reach 1 μm in radius for the luminosity measurement of 10^{-4}. For the precision at the 1 μm level, a monitoring system with laser alignment is required to calibrate the detector position. The θ angle of a detected electron is calculated assuming an IP position measured by the beam steering and the central tracking system. The IP position relative to the luminosity detector could be limited to survey relative to central tracking devices or beam pipe. If feasible, a tracking system on the Bhabha electrons will improve very the measurement precision of the electron theta angle. This is illustrated in Fig. 8.10 for the option that a ring of silicon or diamond detector is mounted in front of the Luminosity detector. Such that a electron track is measure from the IP, the ring detector, and the LumiCal impact position. The ring detector offers a second survey, and by extrapolation, to calibrate the LumiCal silicon strip positions.

The front silicon layer of the luminosity detector will measure electron impact positions to a few micron. If this will be a fine-pitch strip detector, the position is measured by strips collecting the ionization charges generated by a traversing electron. In Fig. 8.11,

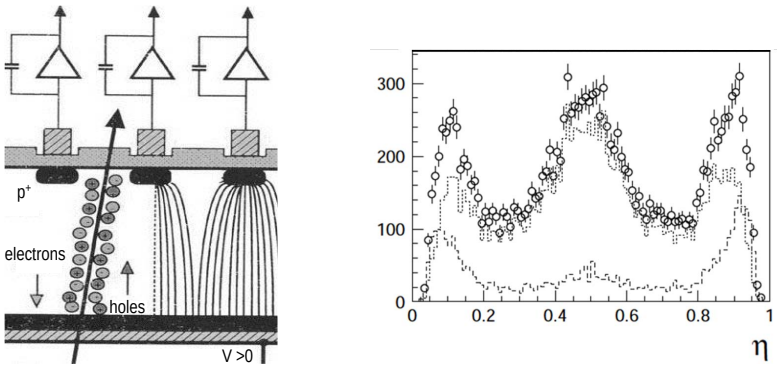

Figure 8.11: Charge collection by silicon strips is illustrated for ionization charges generated by a traversing particle. The $\eta = Q_r/(Q_r + Q_l)$ distributions are made for charge sharing to left and right strips to the impact position, for a test devices with strips implementation in 25 μm pitch and the readout of every other strips in 50 μm pitch. The η distributions are also plotted for contents with charges collected by two-strip (dotted) and three-strip (dashed) cases. The middle bump corresponds to the position of the floating strip between two readout strips.

the charge sharing is illustrated for $\eta = Q_r/(Q_r + Q_l)$ with the ionization charges collected by the strips on the right (left) of the impact position. The distribution is collected for a test device having the strips implanted in 25 μm pitch, and the readout in 50 μm pitch by wire bonding to every other strips. The floating strip between two readout strips attracts charges drifting towards it and results to the bump at $\eta \sim 0.5$, in particular for a wide cluster of charges collected by three strips (dotted line). The impact position of a particle is approximated by center-of-gravity weighted on the charges between two strips. With the η distribution, the non-linear distribution can be corrected to achieve a position resolution of better than ~ 5 μm for the readout pitch of 50 μm. With the strip detectors placed in a magnetic field, the ionization charge in the silicon wafer is drifted toward one side, and therefore the η distribution is tilted un-evenly. Without a proper correction for the η, the true impact position the off-set can be as large as half the readout pitch.

If the luminosity detector will be assembled in a sandwiched silicon-tungsten calorimeter with the type of silicon wafer for the front layer. Wide silicon strips may be chosen in a case like the OPAL LumiCal [17], applying 2.5 mm wide strips in circular span of 11.25°. The resolution on detection of an electron, as well as for e/γ separation is at the 1 mm level. Assuming that the event counting of Bhabha electrons has the fiducial edge, θ_{min}, chosen at the middle between two strips, and the events are evenly divided to left and right strips without charge sharing. The systematic error to luminosity measurement is by the alignment error of the strip position of a few microns, and is not by the resolution.

Charge sharing between the gap of two-strips have been studied with prototype wafers[18] shown in Fig. 8.12. The wafer dimension is 65×65 mm^2 implemented with 2 mm wide strips and the gaps from 50 μm to 160 μm. The beam test was conducted with a set of find-pitch strip detectors as a telescope to provide reference positions of incident electrons scattered across strips and gaps. The charge sharing for electrons in the gaps are compared for η distributions in Fig. 8.12, which are found compatible for the different gap widths. Charge collection shows no loss, and are drifted toward the near strips with the η peaking at the edges. The dispelling charges in the middle of a gap is difficult for deriving

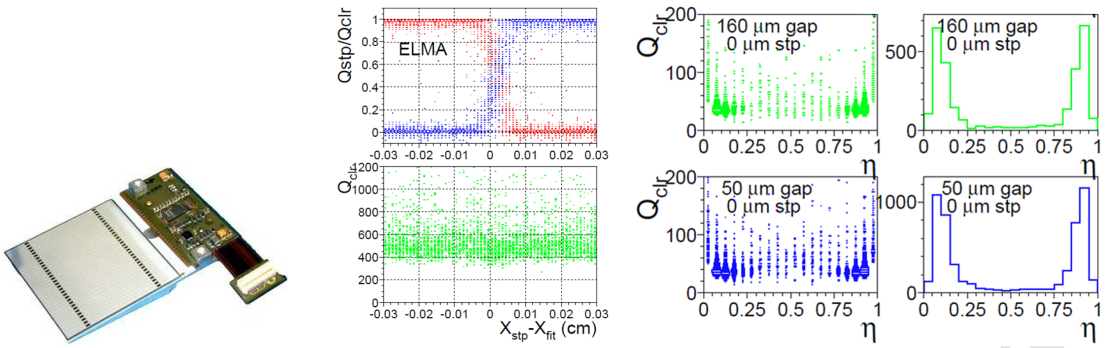

Figure 8.12: Beam tests using prototype silicon wafer of the CMS pre-shower detector (right) were conducted for collection of ionization charges generated by traversing particles across the gap between strips. The charge sharing by adjacent strips are plotted (middle) to the reference impact position (extrapolation of a upstream telescope). The sum strip charges (middle plots) is compatible to the hits on a strip. The charge sharing in $\eta Q_r/(Q_r + Q_l)$ peaks near 0 and 1, indicating non-linear response to the randomly distributed beam particles across the gap.

the position of an incident electron in the gap. But, it does divide the event fraction cleanly to the near side of the strips.

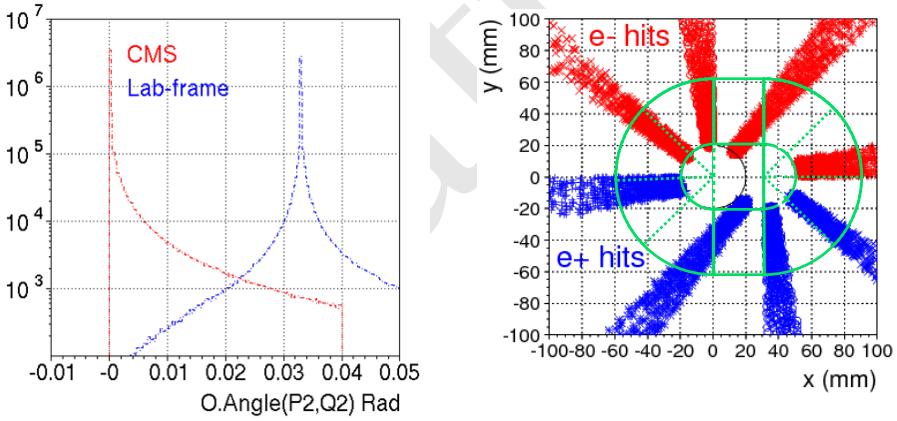

Figure 8.13: Bhabha events of BHLUMI simulation at the Z-pole are plotted for the back-to-back opening angle of scattered electron-position pairs in Center-of-Mass and the laboratory frames (left). The impact positions on the LumiCal front face are plotted in slides of ϕ angles every 45 degrees (right). The detector coverage is illustrated in green lines indicating a beam-pipe of 20 mm, extended from beam center at $x = \pm 16.5$ mm.

The double ring configuration of the CEPC machine design at the interaction point has a beam crossing angle of 33 mrad. The effect to the electrons of Bhabha interaction is a boost off the accelerator ring center, by maximum 16.5 mrad in horizontal direction. The distribution is simulated with the BHLUMI program. The shift on back-to-back angle is plotted in Fig. 8.13. The boost is toward $+x$ direction of the laboratory frame. The electron impact positions on the LumiCal front-layer at $z = 100$ cm are also plotted in Fig. 8.13, in slices of every 45 degrees to indicate the dependence on p_T direction. The beam-pipe centers are at $x = \pm 16.5$ mm. The green lines indicate the beam-pipe area of 20 mm in radius extending horizontally, and the coverage of the LumiCal in segmentation

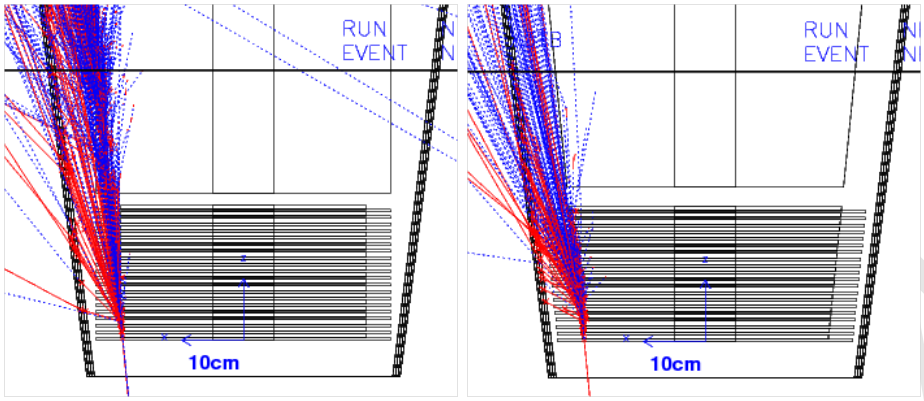

Figure 8.14: Event display of a GEANT simulation for electron shower on the LumiCal configuration stacked with 20 decks of silicon and Tungsten layers in TUBE and CONE shapes.

of circular and rectangular silicon wafers. The electron impact positions are illustrated for >20 mrad to the laboratory frame. Electrons of low scattering angles, in particular for those in $-x$ direction, are lost into beam-pipe. To have both scattered electrons and positrons detected, the corresponding θ_{min} on the horizontal axis is the beam-pipe acceptance plus 16.5 mrad. The loss of vents on vertical direction is much less. With a beam pipe as indicated with $\pm y$ dimension equals radius, the horizontal boost is not losing electrons with a larger y-position. A large detector coverage for Bhabha events is most favorable. The large opening of beam-pipe position is inevitable. We shall pursue the vertical dimension to be low as possible for a total integrated Bhabha cross section of larger than 50 nb.

The LumiCal mounted in front of the quadruple magnet at $z = \pm 100$ cm is half way in the tracking volume of $z = \pm 200$ cm. Shower leakage of electrons at the edge of LumiCal is investigated with a GEANT simulation witn parameters cross-checked with a lateral shower study [19]. The LumiCal is configured assuming a sandwiched Silicon-Tungsten calorimeter stacked in twenty decks of 2 mm air-gap and $1X_0$ tungsten (3.5 mm thick). The air-gap has a layer of silicon wafer of 0.3 mm thick. The front layer of the LumiCal is positioned at $z = 100$ cm. The geometry of the LumiCal is tested in two configurations: a TUBE with uniform inner and outer radii of 25 and 100 mm, respectively; and a CONE shape with the outer edge at a constant angle of $\arctan 0.1$ to the interaction point. The CONE shape is intended for well separated absorption of electron shower in a theta threshold. Illustrated in Fig. 8.14 are the event display of the simulations. Out of the LumiCal, a 5 mm iron cone at $|\cos\theta| = 0.992$ is implemented for absorption of low energy shower secondaries massing into the center tracking volume.

The TUBE configuration leaves a corner of about 5 mrad on the outer edge, where the shower leakage of an incident electron is with energetic shower secondaries. The CONE shape allows the shower fully developed once the electron enters the calorimeter coverage. The shower leakage reaching the Fe-cone is recorded for the particle energies arriving and penetrating through, which are listed in Table 8.5 for 50 GeV and 125 GeV electrons. When the shower is well contained, the leakage is just a few dozens of less than 30 MeV particles. A shower on the edge creates up to 3k secondaries into the tracking

volume mostly of less than 100 MeV. The 5 mm iron layer can filter a large fraction of them, to less than 1k particles traversing through.

8.4.2 Systematic effects

The main measure of luminosity at CEPC is the count of Bhabha events N_{Bh} detected in coincidence in the two halves of the luminosity calorimeter LumiCal. The luminosity figure is then obtained from the equation of $\mathcal{L} = N_{acc}/\sigma^{vis}$. The cross section for the Bhabha process, σ_{vis}, should be integrated over the same phase space as used for the counting of Bhabha events. The limited precision with which the experimental acceptance region is defined gives rise to a number of systematic effects. Further, other processes misidentified as Bhabha and the limited accuracy of the theoretical calculation of σ_{vis} contribute to the overall systematic uncertainty.

A generator-level study was performed to assess the effects related to the precision of the Bhabha acceptance region on Bhabha counting. An underlying assumption of the study is that the LumiCal is centered on the outgoing beam axis. This assumption is essential for data-driven control of the radial offset of Lumical with respect to the IP, as well as for Bhabha event counting based on the mirrored asymmetric polar-angle acceptance regions on the left and right side of the detector [17] (in further text, *OPAL-style selection*). OPAL-style counting cancels out biases due to left-right asymmetries of the experimental angular acceptance. It is further assumed that for the final state particles hitting the radial region between 50 mm and 75 mm, corresponding to the detector fiducial volume (FV), shower leakage has a negligible effect on the reconstruction of the polar angle and the energy.

Bhabha event samples are generated using the BHLUMI generator [16]. Center-of-mass (CM) energy of 240 GeV is assumed, roughly corresponding to the peak of the Higgs production cross section. The particles are generated in the range of polar angles including a ~ 7 mrad margin outside the FV to allow non-collinear final state radiation (FSR) to contribute to the events. After event generation, smearing is applied to the final particle vertices and momenta according to the nominal CEPC parameters. Additional smearing or bias is then applied according to one systematic effect at a time. Four mo-

Table 8.5: Number of particles leaking out of the LumiCal outer radius (N_{enter}) and number of particles passing through the Fe-cone (N_{pass}). Two different detector designs (TUBE and CONE) and two shower energies (50 GeV and 125 GeV) are simulated.

	50 GeV electrons		125 GeV electrons	
	TUBE	CONE	TUBE	CONE
θ (mrad)	$N_{\mathrm{enter}}/N_{\mathrm{pass}}$	$N_{\mathrm{enter}}/N_{\mathrm{pass}}$	$N_{\mathrm{enter}}/N_{\mathrm{pass}}$	$N_{\mathrm{enter}}/N_{\mathrm{pass}}$
40	15.4/5.6	13.6/5.8	38.0/16.0	35.8/14.7
90	392/155	173/76	1028/399	434/19.7
95	501/290	367/152	2389/720	937/382
98	762/216	860/284	1718/473	2176/725
99	553/140	1331/367	1102/273	3306/915

menta of close-by particles are summed up to account for cluster merging in LumiCal. The selection criteria to count an event consist of the OPAL-style angular selection and the requirement that the energy of both detected showers is above 50% of the nominal beam energy. The relative acceptance bias is determined as the relative difference between the Bhabha count $N_{\mathrm{Bh},i}$ obtained with the inclusion of the considered effect i and N_{Bh} obtained with the nominal set of parameters.

Table 8.6 lists the requirements on beam delivery, MDI and LumiCal installation, needed to limit individual systematic effects in the luminosity measurement to 1×10^{-3}, such as required for the Higgs program at CEPC. Parameters influencing the integral luminosity precision are given as follows:

- ΔE_{CM}, uncertainty of the available CM energy affecting the Bhabha cross-section,
- $E_{e^+} - E_{e^-}$, asymmetry of the incident beam energies resulting in a net longitudinal boost of the event,
- $\frac{\delta\sigma_{E_{beam}}}{\sigma_{E_{beam}}}$, uncertainty of the beam energy spread,
- Δx_{IP} and Δz_{IP}, radial and axial offsets of the IP w.r.t. the LumiCal,
- Beam synchronization, resulting in axial offset of the IP w.r.t. the LumiCal,
- $\sigma_{x_{\mathrm{IP}}}$ and $\sigma_{z_{\mathrm{IP}}}$, radial and axial fluctuations of the scattering position,
- r_{in}, inner radius of the LumiCal acceptance region,
- $\sigma_{r_{\mathrm{shower}}}$, reconstruction precision of the radial shower coordinate,
- Δd_{IP}, uncertainty of the distance between the luminometer halves.

Most requirements are technically feasible with the present state of the art of accelerator and detector technology. The most important challenge identified is the precision of the inner acceptance radius r_{in} of LumiCal. In order to keep the luminosity precision of 1 permille, r_{in} must be known to within $10\,\mu\mathrm{m}$. The precision requirement of r_{in} scales linearly with the required luminosity precision, implying a correspondingly stricter requirement for the Z-pole run.

8.4.3 Summary on LumiCal

Instrumentation of the very forward region is very important for the realization of the CEPC physics program. Several technology options are under consideration. Some of them have been successfully applied at LEP or are under study at other future projects. We argue that a tracker placed in front of the luminometer can improve polar angle measurement accuracy, facilitate LumiCal alignment and enable electron-photon separation. Luminometer must be centered on the outgoing beam axis to allow control of the systematic effects at the required level. Precision requirements on beam delivery, MDI and LumiCal installation have been addressed by simulation, and proven to be feasible with the present state-of-the-art of accelerator and detector technology.

Table 8.6: Requirements on beam delivery, MDI and LumiCal installation, needed to limit individual systematic effects to 1×10^{-3}.

Parameter	Unit	Limit
ΔE_{CM}	MeV	120
$E_{e^+} - E_{e^-}$	MeV	240
$\frac{\delta\sigma_{E_{beam}}}{\sigma_{E_{beam}}}$		effect canceled
Δx_{IP}	mm	>1
Δz_{IP}	mm	10
Beam synchronization	ps	7
$\sigma_{x_{\text{IP}}}$	mm	1
$\sigma_{z_{\text{IP}}}$	mm	10
r_{in}	mm	10
$\sigma_{r_{\text{shower}}}$	mm	1
Δd_{IP}	μm	500

8.5 Detector integration

Both QD0 and QF1 are located inside the detector, which drastically complicates the support and alignment of the detector and machine components in the interaction region. The two final focus magnets and the LumiCal will possibly be mounted on a dedicated support structure, extended from a pillar outside the detector and suspended from the solenoid cryostat. They might have to been integrated together before being pushed into the interaction region. The amount of material in front of the LumiCal must be minimized so that the high precision of the LumiCal can be maintained. This shall inventively introduce more difficulties to the detector integration. Furthermore, he shaped beam pipe and surrounded silicon detectors will possibly be supported from a structure of carbon fiber reinforced plastic, which can hang at the flanges of the field cage of the Time Projection Chamber (TPC). Significant effort is required to realize a solid mechanical design and to define a reasonable procedure for the detector and machine installation scheme.

References

[1] CEPC-SPPC Study Group, *CEPC-SPPC Preliminary Conceptual Design Report. 1. Physics and Detector*, . IHEP-CEPC-DR-2015-01, IHEP-TH-2015-01, IHEP-EP-2015-01.

[2] CEPC-SPPC Study Group, *CEPC-SPPC Conceptual Design Report. 1 . Accelerator*, . IHEP-CEPC-DR-2018-01, IHEP-AC-2018-01, to be published.

[3] G. von Holtey et al., *Study of beam-induced particle backgrounds at the LEP detectors*, Nucl. Instr. and Meth. **A403** (1998) 205 – 246.

[4] P. M. Lewis et al., *First Measurements of Beam Backgrounds at SuperKEKB*, arXiv:1802.01366 [physics.ins-det].

[5] D. S. Denisov et al., *Machine-Related Backgrounds in the SiD Detector at ILC*, JINST **1** (2006) P12003, arXiv:hep-ex/0608001 [hep-ex].

[6] B. Dalena, J. Esberg, and D. Schulte, *Beam-induced backgrounds in the CLIC 3 TeV CM energy interaction region*, in *International Workshop on Future Linear Colliders (LCWS11) Granada, Spain, September 26-30, 2011*. 2012. arXiv:1202.0563 [physics.acc-ph].

[7] GEANT4 Collaboration, S. Agostinelli et al., *GEANT4: A Simulation toolkit*, Nucl. Instrum. Meth. **A506** (2003) 250–303.

[8] J. Allison et al., *Geant4 developments and applications*, IEEE Trans. Nucl. Sci. **53** (2006) 270.

[9] Geant4 Collaboration, M. Asai et al., *Recent developments in Geant4*, Annals Nucl. Energy **82** (2015) 19–28.

[10] S. Baranov et al., *Estimation of Radiation Background, Impact on Detectors, Activation and Shielding Optimization in ATLAS*, . ATL-GEN-2005-001, ATL-COM-GEN-2005-001, CERN-ATL-GEN-2005-001.

[11] I. Agapov, G. A. Blair, S. Malton, and L. Deacon, *BDSIM: A particle tracking code for accelerator beam-line simulations including particle-matter interactions*, Nucl. Instrum. Meth. **A606** (2009) 708–712.

[12] D. Schulte, *Beam-beam simulation with GUINEA-PIG*, In 5th International Computational Accelerator Physics Conference (1998) . CLIC-NOTE 387.

[13] R. Kleiss and H. Burkhardt, *BBBREM – Monte Carlo simulation of radiative Bhabha scattering in the very forward direction*, Comput. Phys. Commun. **81** (1994) 372 – 380.

[14] K. Oide and H. Koiso, *Anomalous equilibrium emittance due to chromaticity in electron storage rings*, Phys. Rev. **E49** (1994) 4474–4479.

[15] S. Jadach, *Theoretical error of luminosity cross-section at LEP*, in *Electroweak precision data and the Higgs mass. Proceedings, Workshop, Zeuthen, Germany, February 28-March 1, 2003*, pp. 85–95. 2003. arXiv:hep-ph/0306083 [hep-ph].

[16] S. Jadach et al., *Upgrade of the Monte Carlo program BHLUMI for Bhabha scattering at low angles to version 4.04*, Comput. Phys. Commun. **102** (1997) 229–251.

[17] OPAL Collaboration, G. Abbiendi et al., *Precision luminosity for Z0 line shape measurements with a silicon tungsten calorimeter*, Eur. Phys. J. **C14** (2000) 373–425, arXiv:hep-ex/9910066 [hep-ex].

[18] P. Bloch et al., *Performance Study of Non-Irradiated Prototype Silicon Preshower Samplers for CMS*, . CMS-NOTE-2000-042.

[19] Y. Chang et al., *Lateral development of electron showers measured by silicon microstrip detectors*, Nucl. Instr. and Meth. **A388** (1997) 135 – 143.

CHAPTER 9

BENCHMARK PHYSICS

The historic discovery of a Higgs boson in 2012 by the ATLAS and CMS collaborations [1, 2] and the subsequent studies of the properties of the particle [3–9] indicate the compatibility with the Standard Model (SM) predictions. Although all of the particles in the SM have been discovered, some fundamental questions, e.g. vast difference between the Planck scale and the weak scale, the nature of electroweak phase transition have not been fully understood. The attempt to further address those questions will involve the new physics beyond the SM which could lead a deviation from SM expectations for the precision measurement of the SM. A circular electron positron collider will provide an unique opportunity to have precise measurements of the Higgs, W and Z properties.

The CEPC produces huge statistics of massive SM Bosons. Its physics potential is explored on two different classes of physics benchmarks, the Higgs physics, the precision EW physics. Using the software tools introduced in section **??**, the physics potential on Higgs physics is analyzed at full simulation level, see section **??**. The accuracies on the EW precision measurements are mainly limited by systematic errors and are estimated in section 9.2. The synergies of these different physics measurements, the complimentary and comparison to the HL-LHC and other high energy physics programs are discussed in Chapter 10.

References

[1] ATLAS Collaboration Collaboration, *Observation of a new particle in the search for the Standard Model Higgs boson with the ATLAS detector at the LHC*, Phys. Lett. B **716** (2012) 1, arXiv:1207.7214 [hep-ex].

[2] CMS Collaboration Collaboration, *Observation of a new boson at a mass of 125 GeV*

with the CMS experiment at the LHC, Phys. Lett. **B716** (2012) 30, arXiv:1207.7235 [hep-ex].

[3] ATLAS Collaboration, G. Aad et al., *Measurements of Higgs boson production and couplings in diboson final states with the ATLAS detector at the LHC*, Phys. Lett. **B726** (2013) 88–119, arXiv:1307.1427 [hep-ex]. [Erratum: Phys. Lett.B734,406(2014)].

[4] ATLAS Collaboration, G. Aad et al., *Evidence for the spin-0 nature of the Higgs boson using ATLAS data*, Phys. Lett. **B726** (2013) 120–144, arXiv:1307.1432 [hep-ex].

[5] CMS Collaboration Collaboration, S. Chatrchyan et al., *Observation of a new boson with mass near 125 GeV in pp collisions at* $\sqrt{s}$ *= 7 and 8 TeV*, JHEP **1306** (2013) 081, arXiv:1303.4571 [hep-ex].

[6] CMS Collaboration Collaboration, *Evidence for the direct decay of the 125 GeV Higgs boson to fermions*, Nature Phys. **10** (2014) , arXiv:1401.6527 [hep-ex].

[7] CMS Collaboration, V. Khachatryan et al., *Constraints on the spin-parity and anomalous HVV couplings of the Higgs boson in proton collisions at 7 and 8 TeV*, Phys. Rev. **D92** (2015) no. 1, 012004, arXiv:1411.3441 [hep-ex].

[8] ATLAS, CMS Collaboration, G. Aad et al., *Combined Measurement of the Higgs Boson Mass in* pp *Collisions at* $\sqrt{s} = 7$ *and 8 TeV with the ATLAS and CMS Experiments*, Phys. Rev. Lett. **114** (2015) 191803, arXiv:1503.07589 [hep-ex].

[9] ATLAS, CMS Collaboration, G. Aad et al., *Measurements of the Higgs boson production and decay rates and constraints on its couplings from a combined ATLAS and CMS analysis of the LHC pp collision data at* $\sqrt{s} = 7$ *and 8 TeV*, JHEP **08** (2016) 045, arXiv:1606.02266 [hep-ex].

9.1 Higgs Boson Physics

JQ: Need to improve the summary and the flow, fill missing info and check numbers, reconcile with the white paper, notation consistency... otherwise it is in a reasonable good shape for proof reading... will resume editing from July 31 onwards...

At the CEPC, in contrast to the LHC, Higgs boson candidate events can be identified through a technique known as the recoil mass method without tagging its decays. Therefore, Higgs boson production can be disentangled from its decay in a model independent way. Moreover, the cleaner environment at a lepton collider allows much better exclusive measurement of Higgs boson decay channels. All of these give the CEPC impressive reach in probing Higgs boson properties. In this section, the results of the current CEPC simulation studies on the precision of the Higgs boson property measurements are summarized. In addition, reaches based on phenomenological studies in searching for exotic decays and in CP admixture of the Higgs boson are also included.

9.1.1 Higgs boson production and decay

Production processes for a 125 GeV SM Higgs boson at the CEPC are $e^+e^- \to ZH$ (ZH or Higgsstrahlung), $e^+e^- \to \nu\bar{\nu}H$ ($\nu\bar{\nu}H$ or W fusion) and $e^+e^- \to e^+e^-H$ (eeH or Z fusion) as illustrated in Fig. 9.1. The W and Z fusion processes are collectively referred to as vector-boson fusion (VBF) production.

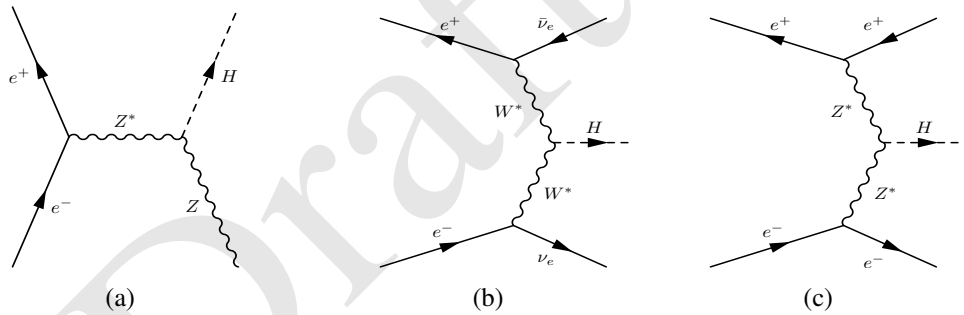

Figure 9.1: Feynman diagrams of the Higgs boson production processes at the CEPC: (a) $e^+e^- \to ZH$, (b) $e^+e^- \to \nu\bar{\nu}H$ and (c) $e^+e^- \to e^+e^-H$.

The total and individual cross sections for the production of a SM Higgs boson with a mass of 125 GeV as functions of center-of-mass energy are plotted in Fig. 9.2 while its decay branching ratios and total width are shown in Table 9.1. As an s-channel process, the cross section of the $e^+e^- \to ZH$ process reaches its maximum at $\sqrt{s} \sim 250$ GeV, and then decreases asymptotically as $1/s$. The VBF production processes are through t-channel exchanges of vector bosons. Their cross sections increase logarithmically as $\ln^2(s/M_V^2)$. Because of the accidental small neutral-current Zee coupling, the VBF cross section is dominated by the W fusion process. Numerical values of these cross sections at $\sqrt{s} = 240$ GeV are listed in Table 9.2.

The CEPC as a Higgs boson factory is designed to deliver a total of 5 ab^{-1} integrated luminosity to two detectors in 7 years. Over 10^6 Higgs boson events will be produced during this period. The large statistics, well-defined event kinematics and clean collision environment will enable the CEPC to measure Higgs boson production cross sections as

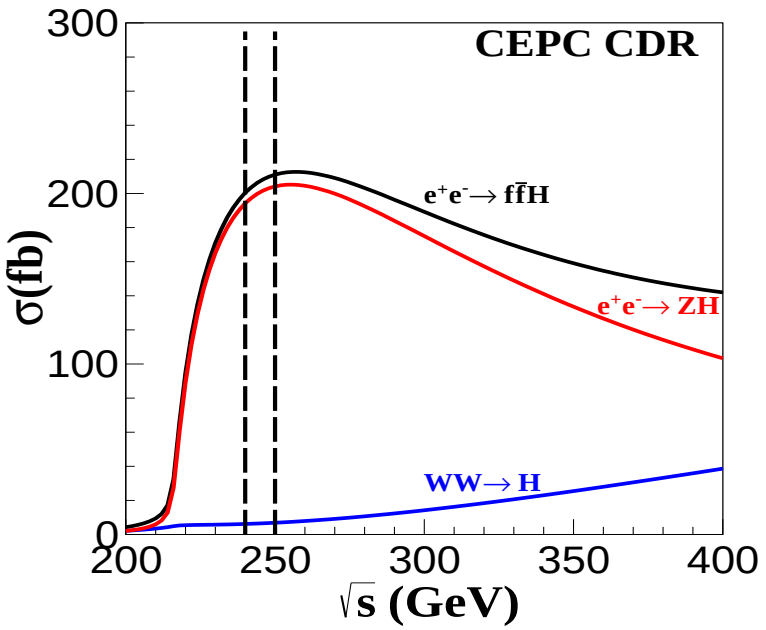

Figure 9.2: Production cross sections of $e^+e^- \to ZH$ and $e^+e^- \to (e^+e^-/\nu\bar{\nu})H$ as functions of $\sqrt{s}$ for a 125 GeV SM Higgs boson. Can still use some improvements...

Table 9.1: Standard model predictions of the decay branching ratios and total width of a 125 GeV Higgs boson. These numbers are obtained from Refs. [1, 2].

Decay mode	Branching ratio	Relative uncertainties
$H \to b\bar{b}$	57.7%	$+3.2\%, -3.3\%$
$H \to c\bar{c}$	2.91%	$+12\%, -12\%$
$H \to \tau^+\tau^-$	6.32%	$+5.7\%, -5.7\%$
$H \to \mu^+\mu^-$	2.19×10^{-4}	$+6.0\%, -5.9\%$
$H \to WW^*$	21.5%	$+4.3\%, -4.2\%$
$H \to ZZ^*$	2.64%	$+4.3\%, -4.2\%$
$H \to \gamma\gamma$	2.28×10^{-3}	$+5.0\%, -4.9\%$
$H \to Z\gamma$	1.53×10^{-3}	$+9.0\%, -8.8\%$
$H \to gg$	8.57%	$+10\%, -10\%$
Γ_H	4.07 MeV	$+4.0\%, -4.0\%$

well as its properties (mass, decay width and branching ratios, etc.) with precision far beyond those achievable at the LHC. Compared with hadron collisions, e^+e^- collisions are unaffected by underlying event and pile-up effects. Theoretical calculations are less dependent on higher order QCD radiative corrections. Therefore, more precise tests of theoretical predictions can be performed at the CEPC. The tagging of $e^+e^- \to ZH$ events

Table 9.2: Cross sections of Higgs boson production and other SM processes at $\sqrt{s} = 250$ GeV and numbers of events expected in 5 ab^{-1}. The cross sections are calculated using the Whizard program [3]. Note that cross sections do not include potential interference effects between the same final states from different processes after W and Z boson decays (see text). The numbers need to be updated to 240 GeV.

Process	Cross section	Events in 5 ab^{-1}
Higgs boson production, cross section in fb		
$e^+e^- \to ZH$	204.7	1.02×10^6
$e^+e^- \to \nu\bar{\nu}H$	6.85	3.43×10^4
$e^+e^- \to e^+e^-H$	0.63	3.15×10^3
Total	212.1	1.06×10^6
Background processes, cross section in pb		
$e^+e^- \to e^+e^-$ (Bhabha)	25.1	1.3×10^8
$e^+e^- \to q\bar{q}\,(\gamma)$	50.2	2.5×10^8
$e^+e^- \to \mu^+\mu^-\,(\gamma)$ [or $\tau^+\tau^-\,(\gamma)$]	4.40	2.2×10^7
$e^+e^- \to WW$	15.4	7.7×10^7
$e^+e^- \to ZZ$	1.03	5.2×10^6
$e^+e^- \to e^+e^-Z$	4.73	2.4×10^7
$e^+e^- \to e^+\nu W^-/e^-\bar{\nu}W^+$	5.14	2.6×10^7

using the invariant mass of the system recoiling against the Z boson, independent of the Higgs boson decay, is unique to lepton colliders. It provides a powerful tool for the model-independent measurements of the inclusive $e^+e^- \to ZH$ production cross section, $\sigma(ZH)$, and of Higgs boson decay branching ratios. Combinations of these measurements will enable to determine the total Higgs boson decay width and to extract the Higgs boson couplings to fermions and vector bosons, providing sensitive probes to potential new physics beyond the SM.

SM background processes include $e^+e^- \to e^+e^-$ (Bhabha scattering), $e^+e^- \to Z\gamma$ (ISR return), $e^+e^- \to WW/ZZ$ (diboson) as well as the single boson production of $e^+e^- \to e^+e^-Z$ and $e^+e^- \to e^+\nu W^-/e^-\bar{\nu}W^+$. Their cross sections and expected numbers of events for an integrated luminosity of 5 ab^{-1} at $\sqrt{s} = 240$ GeV are shown in Table 9.2 as well. The energy dependence of the cross sections for these and the Higgs boson production processes are shown Fig. **??**. Note that many of these processes can lead to identical final states and thus can interfere. For example, $e^+e^- \to e^+\nu_e W^- \to e^+\nu_e e^-\bar{\nu}_e$ and $e^+e^- \to e^+e^-Z \to e^+e^-\nu_e\bar{\nu}_e$ have the same final state. Unless otherwise noted, these processes are simulated together to take into account interference effects for the studies presented in this paper.

9.1.2 Higgs boson tagging

Perhaps the most striking difference between hadron-hadron and e^+e^- collisions is that electron and positron are fundamental particle whereas hadrons are composite particles. Consequently the energy of e^+e^- collisions is known. Therefore through the energy and momentum conservation, the energy and momentum of a Higgs boson can be inferred from other particles in an event without examining the Higgs boson itself. For a Higgsstrahlung event where the Z boson decays to a pair of visible fermions (ff), the mass of the system recoiling against the Z boson, commonly known as the recoil mass, can be calculated assuming the event has a total energy $\sqrt{s}$ and zero total momentum:

$$M^2_{\text{recoil}} = (\sqrt{s} - E_{ff})^2 - p^2_{ff} = s - 2E_{ff}\sqrt{s} + m^2_{ff}. \tag{9.1}$$

Here E_{ff}, p_{ff} and m_{ff} are, respectively, the total energy, momentum and invariant mass of the fermion pair. The M_{recoil} distribution should show a peak at the Higgs boson mass m_H for $e^+e^- \to ZH$ and $e^+e^- \to e^+e^-H$ processes, and is expected to be smooth without a resonance structure for background processes in the mass region around 125 GeV. Two important measurements of the Higgs boson can be performed from the M_{recoil} mass spectrum. The Higgs boson mass can be determined from the position of the resonance in the spectrum. The width of the resonance structure is dominated by the beam energy spread (including ISR effects) and energy/momentum resolution of the detector as the natural Higgs boson width is only 4.07 MeV. The best precision of the mass measurement can be achieved from the leptonic $Z \to \ell\ell\,(\ell = e, \mu)$ decays. The height of the resonance is a measure of the Higgs boson production cross section $\sigma(ZH)$[1]. Through the fitting to the M_{recoil} spectrum, the $e^+e^- \to ZH$ event yield, and therefore $\sigma(ZH)$, can be extracted, independent of Higgs boson decays. Higgs boson decay branching ratios can then be determined by measuring the ZH cross sections for individual Higgs boson decay modes. The recoil mass spectrum has been investigated for both leptonic and hadronic Z boson decays as presented below.

The leptonic Z decay is ideal for studying the recoil mass spectrum of the $e^+e^- \to ZX$ events. The decay is easily identifiable and the lepton momenta can be precisely measured. Figure 9.3 shows the reconstructed recoil mass spectra of $e^+e^- \to ZX$ candidates for the $Z \to \mu\mu$ and $Z \to ee$ decay modes. The analyses are based on the full detector simulation for the signal events and on the fast detector simulation for background events. They are performed with event selections entirely based on the information of the two leptons, independent of the final states of Higgs boson decays. This approach is essential for the measurement of the inclusive $e^+e^- \to ZH$ production cross section and the model-independent determination of the Higgs boson branching ratios. SM processes with at least 2 leptons in their final states are considered as backgrounds. As shown in Fig. 9.3, the analysis has a good signal-to-background ratio. The long high-mass tail is largely due to the initial-state radiation. Leading background contributions after the selection are from ZZ, WW and $Z\gamma$ events. Compared to the analysis of the $Z \to \mu\mu$ decay, the analysis of the $Z \to ee$ decay suffers from additional and large background contributions from Bhabha and single boson production.

The recoil mass technique can also be applied to the hadronic Z boson decays ($Z \to q\bar{q}$) of the $e^+e^- \to ZX$ candidates. This analysis benefits from a larger $Z \to q\bar{q}$ decay

[1]For the $Z \to ee$ decay, there will be a small contribution from $e^+e^- \to e^+e^-H$ production.

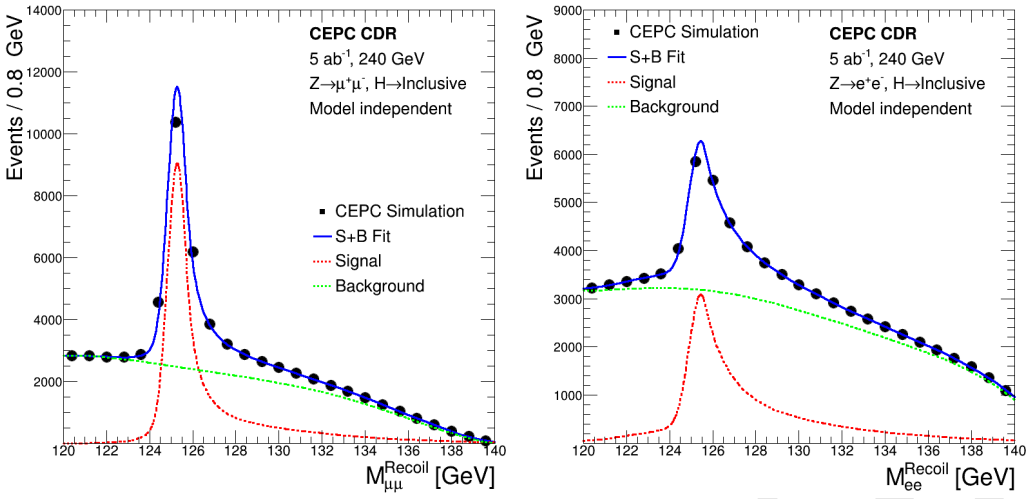

(a) (b)

Figure 9.3: The recoil mass spectra of $e^+e^- \to ZX$ candidates for (a) $Z \to \mu\mu$ and (b) $Z \to ee$ with an integrated luminosity of 5 ab^{-1}.

branching ratio, but suffers from worse jet energy resolution compared with the track momentum and electromagnetic energy resolutions. In addition, ambiguity in selecting jets from the $Z \to q\bar{q}$ decay, particularly in events with hadronic decays of the Higgs boson, can degrade the analysis performance and also introduce model dependences. Therefore, the measurement is highly dependent on the performance of the PFA and the jet clustering algorithm. Following the same approach as the ILC study [4], an analysis based on the fast simulation has been performed. After the event selection, main backgrounds arise from $Z\gamma$'s and WW production.

9.1.3 Measurements of $\sigma(ZH)$ and m_H

The inclusive $e^+e^- \to ZH$ production cross section $\sigma(ZH)$ and Higgs boson mass m_H can be extracted from fits to the recoil mass distributions of the $e^+e^- \to ZX \to (\ell^+\ell^-/q\bar{q})X$ candidates. For the leptonic $Z \to \ell\ell$ decays, the recoil mass distribution of the signal process $e^+e^- \to ZH$ (and also $e^+e^- \to e^+e^-H$ in case of the $Z \to ee$ decay) is modeled with a Crystal Ball function [5] whereas the total background is modeled with a polynomial function in the fit. As noted above, the recoil mass distribution is insensitive to the intrinsic Higgs boson width if it were as small as predicted by the SM. The Higgs boson mass can be determined with precision of 6.5 MeV and 14 MeV from the $Z \to \mu\mu$ and $Z \to ee$ decay modes, respectively. In combination, an uncertainty of 5.9 MeV can be achieved. $e^+e^- \to ZX \to q\bar{q}X$ events contribute little to the precision of the m_H measurement due to the poor $Z \to q\bar{q}$ mass resolution, but dominates the precision of the $e^+e^- \to ZH$ cross section measurement benefiting from its large statistics. A relative precision of 0.65% of $\sigma(ZH)$ is predicted from a simple event counting analysis. In comparison, the corresponding precision from the $Z \to ee$ and $Z \to \mu\mu$ decays is estimated to be 2.1% and 0.9%, respectively. The combined precision of the three measurements is 0.5%.

For the model-independent measurement of $\sigma(ZH)$, event selections independent of the Higgs boson decays are essential. However, additional selections using the Higgs boson decay information can be applied to improve the Higgs boson mass measurement. This will be particularly effective in suppressing the large backgrounds in the $Z \to ee$ and $Z \to q\bar{q}$ decay modes. This improvement is not implemented in the current study.

9.1.4 Analyses of individual Higgs boson decay modes

A bit too wordy, repetitive? Too many plots?

Different decay modes of the Higgs boson can be identified through their unique signatures, enabling the measurements of production rates for these decays. For the Higgs boson production through the $e^+e^- \to ZH$ process in particular, candidate events can be tagged from the visible decays of the Z bosons, Higgs boson decays can then be probed by studying the rest of the events. Simulation studies of the CEPC conceptual detector have been performed for the Higgs boson decay modes of $H \to b\bar{b}/c\bar{c}/gg$, $H \to WW^*$, $H \to ZZ^*$, $H \to \gamma\gamma$, $H \to Z\gamma$, $H \to \tau^+\tau^-$, $H \to \mu^+\mu^-$ and $H \to$ inv. The large numbers of the decay modes of H, W and Z boson as well as the τ-lepton lead to a very rich variety of event topologies. This complexity makes it impractical to investigate the full list of final states descending from the Higgs boson decays. Instead, a limited number of final states of individual Higgs boson decay mode is considered. The dominant backgrounds come from SM diboson production and Z production with initial or final state radiations.

The studies are optimized for the dominant ZH process, however the $e^+e^- \to \nu\bar{\nu}H$ and $e^+e^- \to e^+e^-H$ processes are included whenever applicable. The production cross sections of individual decay mode, $\sigma(ZH) \times \mathrm{BR}$, are extracted. Combined with the inclusive $\sigma(ZH)$ measurement, these measurements will permit the determinations of the Higgs boson decay branching ratios in a model-independent way. Below main features of these studies are described and their results are presented in Section 9.1.5.

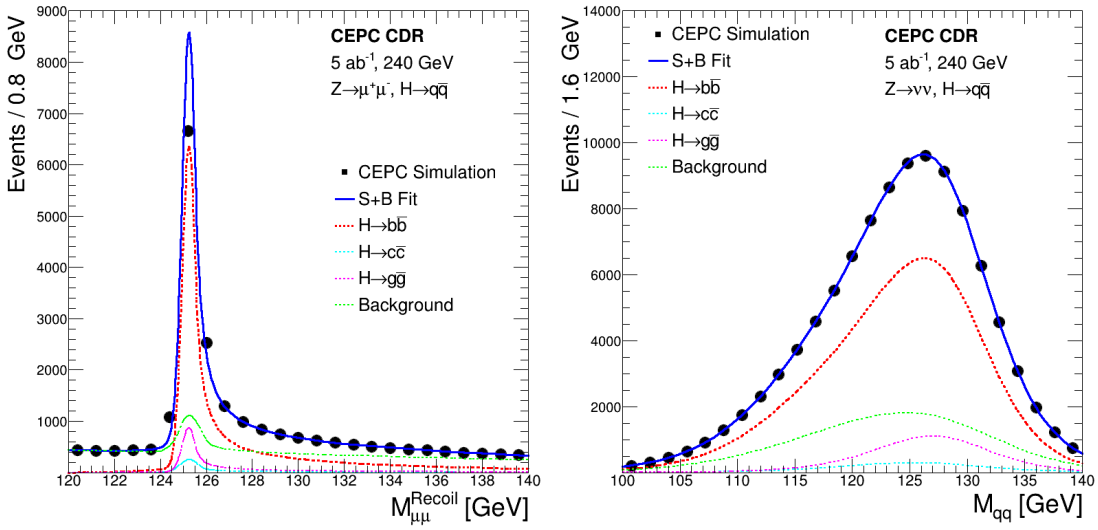

(a) (b)

Figure 9.4: (a) ZH production with $H \to b\bar{b}/c\bar{c}/gg$ decays: distributions of (a) the recoil mass of $Z \to \mu\mu$ and (b) the dijet invariant mass distribution the $Z \to \nu\bar{\nu}$ analysis.

For a SM Higgs boson with a mass of 125 GeV, nearly 70% of all Higgs bosons decay into a pair of jets: b-quarks (57.7%), c-quarks (2.9%) and gluons (8.6%). While the $H \to b\bar{b}$ decay has been observed at the LHC, the $H \to c\bar{c}$ and $H \to gg$ decays are difficult, if not impossible, to be conclusively identified even at the HL-LHC due to large backgrounds. In comparison, these three decays can be isolated and studied at the CEPC in detail. This is important as the $H \to c\bar{c}$ decay is likely the only vehicle for investigating Higgs boson coupling to the second-generation quarks. The study considers all Z boson decay modes except $Z \to \tau^+\tau^-$. The $H \to b\bar{b}/c\bar{c}/gg$ candidates are identified through the dijet invariant mass, or the recoil mass of the visible Z boson decays, or both. Jet flavor tagging is employed to statistically separate $H \to b\bar{b}, c\bar{c}, gg$ contributions. Figure 9.5(a) shows the recoil mass distribution of the $Z \to \mu\mu$ analysis. Compared with the distribution of the analysis of inclusive Higgs boson decays shown in Fig. 9.3(a), the background is significantly reduced through the selection of specific Higgs boson decays. Figure 9.5(b) is the dijet mass distribution of the $Z \to \nu\bar{\nu}$ analysis, showing excellent signal-to-background ratio and good dijet mass resolution.

The W-fusion process of $e^+e^- \to \nu\bar{\nu}H$ has a cross section of XX% of that of the ZH process at $\sqrt{s} = 240$ GeV in the SM. This process has been explored for the $H \to b\bar{b}$ decay mode. The analysis suffers from large backgrounds from $ZH \to \nu\bar{\nu}b\bar{b}$ as it has the same final state. However, the $\nu\bar{\nu}H$ and $Z(\nu\bar{\nu})H$ contributions can be separated through the exploration of their kinematic differences. Higgs bosons are produced with different polar angular distributions. Moreover, the recoil mass distribution should exhibit a resonance structure at the Z boson mass for $Z(\nu\bar{\nu})H$ and show a continuum spectrum for $e^+e^- \to \nu\bar{\nu}H$. The $\nu\bar{\nu}H$ contribution is extracted through a fit to the two-dimensional distribution of the cosine of the polar angle and the recoil mass.

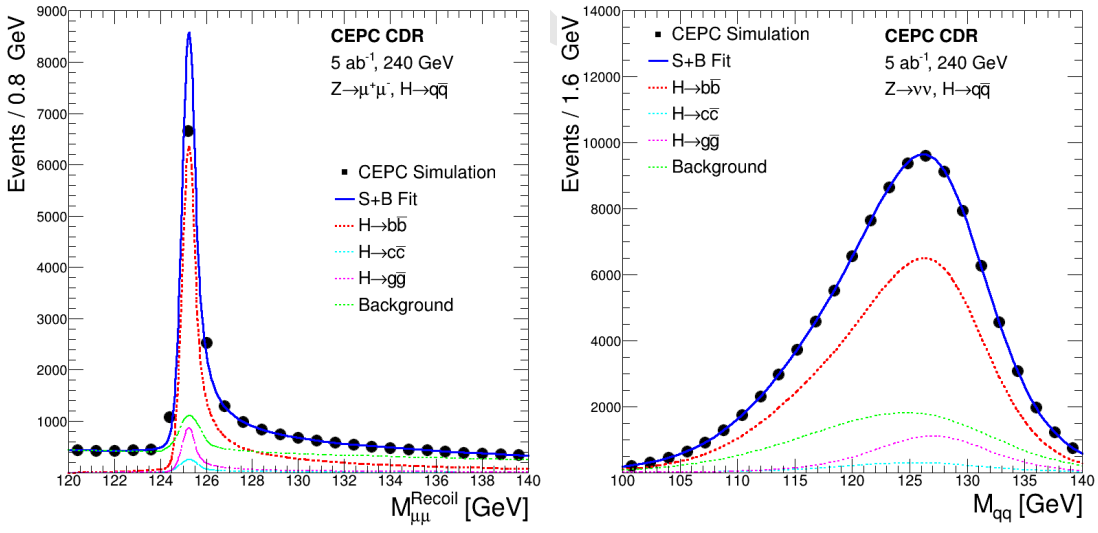

(a) (b)

Figure 9.5: (a) ZH production with $H \to b\bar{b}/c\bar{c}/gg$ decays: distributions of (a) the recoil mass of $Z \to \mu\mu$ and (b) the dijet invariant mass distribution the $Z \to \nu\bar{\nu}$ analysis.

The $H \to WW^*$ and $H \to ZZ^*$ decays are among the first decay modes studied at the LHC and are critical for the discovery of the Higgs boson thanks to the clean leptonic signatures of the W or Z boson decays. However due to their large backgrounds, hadronic

final states of the $H \to WW^*$ and $H \to ZZ^*$ decays are out of reach at the LHC despite of their larger branching ratios than leptonic final states. This is not the case at the CEPC. In fact, most of the sensitivities to these two Higgs boson decay modes at the CEPC are expected to be from final states with one or both vector bosons decay hadronically. A number of selected final states have been studied. For $H \to WW^*$, the final states included are $Z \to \ell\ell$, $H \to WW^* \to \ell\nu\ell\nu, \ell\nu q\bar{q}$; $Z \to \nu\bar{\nu}$, $H \to WW^* \to \ell\nu\ell\nu, q\bar{q}q\bar{q}$ and $Z \to q\bar{q}$, $H \to WW^* \to q\bar{q}q\bar{q}$. For $H \to ZZ^*$, they are $Z \to \mu\mu$, $H \to ZZ^* \to \nu\bar{\nu}q\bar{q}$ and $Z \to \nu\bar{\nu}$, $H \to ZZ^* \to \ell\ell q\bar{q}$. A combination of the recoil mass, the invariant mass of the $W \to q\bar{q}$ and $Z \to q\bar{q}$ decay as well as the leptonic decay signatures of W and Z bosons are used to identify ZH events. Some of these analyses suffer from large backgrounds as shown, for example, in Fig. 9.6(a), while others are almost background free as illustrated in Fig. 9.6(b).

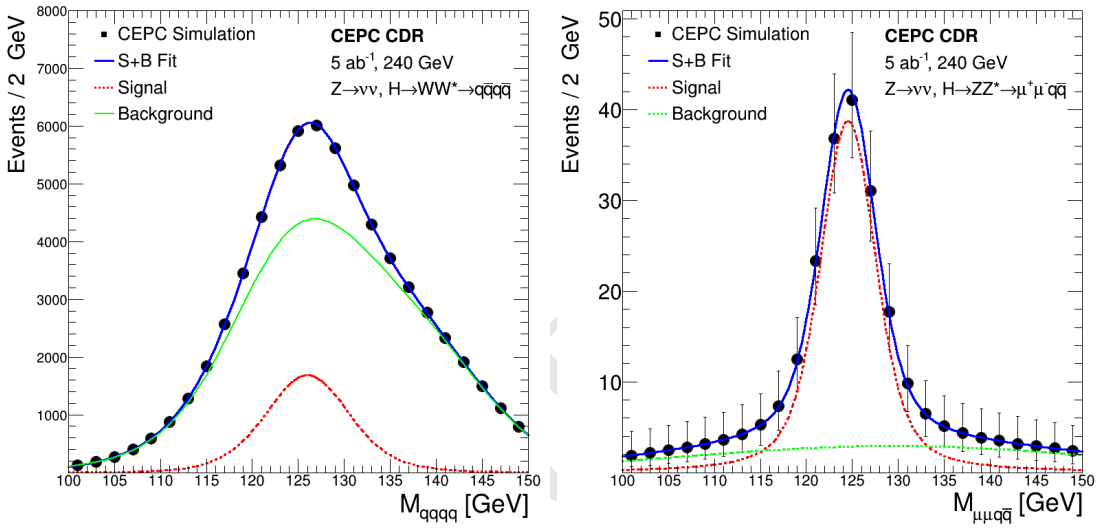

(a) (b)

Figure 9.6: (a) ZH production with $H \to WW^* \to q\bar{q}q\bar{q}$ and $Z \to \nu\bar{\nu}$: the invariant mass of the 4-jet system. (b) ZH production with $H \to ZZ^* \to \mu^+\mu^- q\bar{q}$ and $Z \to \nu\bar{\nu}$: the invariant mass distribution of the dimuon and dijet system.

The $H \to \gamma\gamma$ and $H \to Z\gamma$ decays have small branching ratios in the SM as they proceed through W boson and top quark triangular loops. CEPC's sensitivities to these two decay modes have been examined.The $H \to \gamma\gamma$ analysis of ZH production suffers from large $e^+e^- \to (Z/\gamma^*)\gamma\gamma$ background where γ's arise from the initial and final state radiations. All Z boson decay modes other than the $Z \to ee$ decay are considered for the $H \to \gamma\gamma$ studies. The $ZH \to e^+e^-\gamma\gamma$ decay has additional large backgrounds from Bhabha processes. As shown in Fig. 9.7(a), the $H \to \gamma\gamma$ signal is expected to appear as a resonance over a smooth background in the diphoton mass distribution. ZH production with $H \to Z\gamma$ decay will lead to events with two on-shell Z bosons and one photon. The $H \to Z\gamma$ study targeted the signal process of $ZH \to ZZ\gamma \to \nu\bar{\nu}q\bar{q}\gamma$. In this final state, the energy and momentum of the $\nu\bar{\nu}$ system can be calculated from the visible energy and momentum of the event. The mass difference between the Higgs boson candidate and the candidate of the associated Z boson can then be calculated. For signal events, this mass difference is expected to be $m_H - m_Z \sim 35$ GeV for correct combinations as

shown in Fig. 9.8(b). For background events and wrong combinations of signal events, the distribution should be smooth.

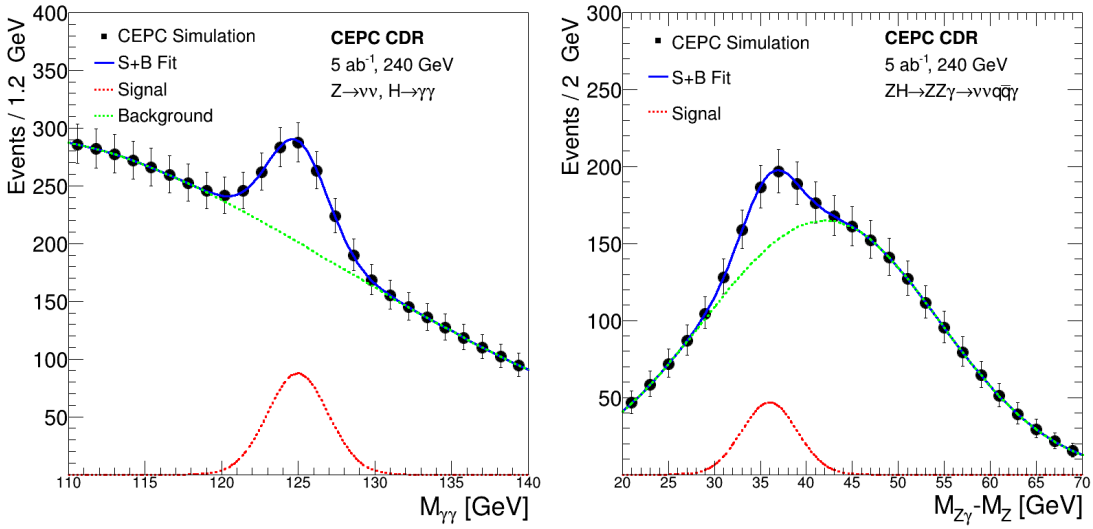

(a) (b)

Figure 9.7: (a) ZH production with $H \to \gamma\gamma$: the invariant mass distribution of the selected photon pairs for $Z \to \nu\bar{\nu}$. (b) ZH production with $H \to Z\gamma$: the distribution of the mass difference between the reconstructed $Z\gamma$ and Z system.

Leptonic Higgs boson decays are accessible for $H \to \tau^+\tau^-$ and $H \to \mu^+\mu^-$ at the CEPC. Simulation studies of ZH production with the $H \to \tau^+\tau^-$ decay have been performed for all Z boson decay modes except $Z \to ee$. A boosted decision tree utilizing particle multiplicity and their separations is used to select di-tau candidates from $H \to \tau^+\tau^-$. An impact-parameter based variable of the leading track of the di-tau candidate is used as the final discriminant for the signal extraction. An example distribution of this variable for $Z \to \nu\bar{\nu}$ is shown Fig. 9.8(a). Similar to $H \to \gamma\gamma$, the $H \to \mu^+\mu^-$ decay also allows the reconstruction of the Higgs boson with high resolution. The signal is expected to appear as a resonance structure at m_H over the smooth background in the dimuon mass spectrum. Good dimuon mass resolution is essential for the performance. For this study, all Z boson decay modes are considered. Figure 9.8 shows the dimuon mass distribution combining all Z boson decay modes.

In the SM, the Higgs boson can decay invisibly via $H \to ZZ^* \to \nu\bar{\nu}\nu\bar{\nu}$ with a branching ratio of 1.06×10^{-3}. In many extensions to the SM, the Higgs boson can decay directly to invisible particles with significantly higher branching ratio. At the CEPC, the $H \to \text{inv}$ decay be directly identified the recoil mass of Z boson decays. The sensitivity is estimated for $Z \to \ell\ell$ and $Z \to q\bar{q}$ decays. The SM $H \to ZZ^* \to \nu\bar{\nu}\nu\bar{\nu}$ decay is used to model the $H \to \text{inv}$ decay in both the SM and its extension. This is made possible by the fact that the Higgs boson is narrow scalar in the SM so that the production and decay are factorized.

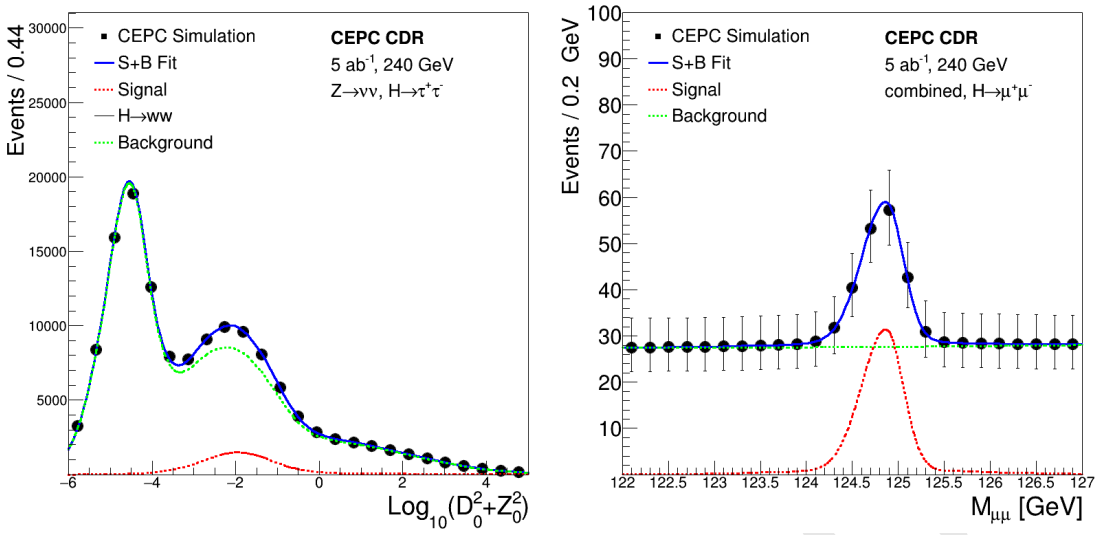

(a) (b)

Figure 9.8: (a) ZH production with $H \to \tau^+\tau^-$: the distribution of impact parameter variable of the leading track of the di-tau candidates for the $Z \to \nu\bar{\nu}$ decay mode. (b) ZH production with $H \to \mu^+\mu^-$: the invariant mass distribution of the selected muon pairs combining all Z boson decay modes.

9.1.5 Combination of individual analyses

With the measurements of inclusive cross section $\sigma(ZH)$ and the cross sections of individual Higgs boson decay mode $\sigma(ZH) \times \mathrm{BR}$, the Higgs boson decay branching ratio, BR, can be extracted. Most of the systematic uncertainties associated with the measurement of $\sigma(ZH)$ cancels in this procedure. A maximum likelihood fit is used to estimate the precision on BRs. For a given Higgs boson decay mode, the likelihood has the form:

$$L(\mathrm{BR}, \theta) = \mathrm{Poisson}\left[N^{\mathrm{obs}} \middle| N^{\mathrm{exp}}(\mathrm{BR}, \theta)\right] \cdot G(\theta), \tag{9.2}$$

where BR is the parameter of interest and θ represent nuisance parameters associated with systematic uncertainties. N^{obs} is the number of the observed events, $N^{\mathrm{exp}}(\mathrm{BR}, \theta)$ is the expected number of events, and $G(\theta)$ is a set of constraints on the nuisance parameters within their estimated uncertainties. The number of expected events is the sum of signal and background events. The number of signal events is calculated from the integrated luminosity, the $e^+e^- \to ZH$ cross section $\sigma(ZH)$ measured from the recoil method, Higgs boson branching ratio BR, the event selection efficiency ϵ. The number of the expected background events, N^b, is estimated from Monte Carlo samples. Thus

$$N^{\mathrm{exp}}(\mathrm{BR}, \theta) = \mathrm{Lumi}(\theta^{\mathrm{lumi}}) \times \sigma_{ZH}(\theta^{\sigma}) \times \mathrm{BR} \times \epsilon(\theta^{\epsilon}) + N^b(\theta^b), \tag{9.3}$$

where θ^X ($X = \mathrm{lumi}, \sigma$, ϵ and b) are the nuisance parameters of their corresponding parameters or measurements. Even with 10^6 Higgs boson events, statistical uncertainties are expected to be dominant and thus systematic uncertainties are not taken into account for the current studies. Thus the nuisance parameters are fixed to their nominal values.

Table 9.3 summarizes the estimated precision of Higgs boson property measurements, combining all studies described above and taking into account cross-feeds between different Higgs boson production processes and decay modes. For the leading

Table 9.3: Estimated precision of Higgs boson property measurements expected from a CEPC dataset of 5 ab^{-1} at $\sqrt{s} = 240$ GeV. All precision are relative except for m_H and BR($H \to$ inv) for which Δm_H and 95% CL upper limit on the BSM physics contribution are quoted respectively. Missing BR precision

Property	Estimated Precision
m_H	5.9 MeV
Γ_H	3.3%
$\sigma(ZH)$	0.50%
$\sigma(\nu\bar{\nu}H)$	3.05%

Decay mode	$\sigma(ZH) \times$ BR	BR
$H \to b\bar{b}$	0.29%	%
$H \to c\bar{c}$	3.45%	%
$H \to gg$	1.37%	%
$H \to WW^*$	1.04%	%
$H \to ZZ^*$	5.21%	%
$H \to \gamma\gamma$	7.38%	%
$H \to Z\gamma$	21%	%
$H \to \tau^+\tau^-$	0.87%	%
$H \to \mu^+\mu^-$	16.8%	%
$H \to$ inv	–	$< 0.33\%$

Higgs boson decay modes, namely $b\bar{b}$, $c\bar{c}$, gg, WW^*, ZZ^* and $\tau^+\tau^-$, percent level precision are expected. The best achievable statistical uncertainties for 5 ab^{-1} are 0.28% for $\sigma(e^+e^- \to ZH) \times \text{BR}(H \to b\bar{b})$ and 0.5% for $\sigma(e^+e^- \to ZH)$. Even for these measurements, statistics is likely the dominant source of uncertainties. Systematic uncertainties from the efficiency/acceptance of the detector, the luminosity and the beam energy determination are expected to be small. The integrated luminosity can be measured with a 0.1% precision, a benchmark already achieved at the LEP [6], and can be potentially improved in the future. The center-of-mass energy will be known better than 1 MeV, resulting negligible uncertainties on the theoretical cross section predictions and experimental recoil mass measurements.

9.1.6 Higgs boson width

The Higgs boson width (Γ_H) is of special interest as it is sensitive to BSM physics in Higgs boson decays that are not directly detectable or searched for. However, the 4.07 MeV width predicted by the SM is too small to be measured with a reasonable precision from the distributions of either the invariant mass of the Higgs boson decay products or the recoil mass of the system produced in association with the Higgs boson. Unique to lepton colliders, the width can be determined from the measurements of Higgs boson production

cross sections and its decay branching ratios. This is because the inclusive $e^+e^- \to ZH$ cross section $\sigma(ZH)$ can be measured from the recoil mass distribution, independent of Higgs boson decays.

Measurements of $\sigma(ZH)$ and BR's have been discussed in Sections 9.1.2 and 9.1.4. Combining these measurements, the Higgs boson width can be calculated in a model-independent way:

$$\Gamma_H = \frac{\Gamma(H \to ZZ^*)}{\mathrm{BR}(H \to ZZ^*)} \propto \frac{\sigma(ZH)}{\mathrm{BR}(H \to ZZ^*)} \tag{9.4}$$

Here $\Gamma(H \to ZZ^*)$ is the partial width of the $H \to ZZ^*$ decay. Because of the small expected $\mathrm{BR}(H \to ZZ^*)$ value for a 125 GeV Higgs boson (2.64% in the SM), the precision of Γ_H is limited by the $H \to ZZ^*$ statistics. It can be improved using the decay final states with the expected large BR values, for example the $H \to b\bar{b}$ decay:

$$\Gamma_H = \frac{\Gamma(H \to b\bar{b})}{\mathrm{BR}(H \to b\bar{b})} \tag{9.5}$$

$\Gamma(H \to b\bar{b})$ can be independently extracted from the cross section of the W fusion process $e^+e^- \to \nu\bar{\nu}H \to \nu\bar{\nu}\, b\bar{b}$:

$$\sigma(\nu\bar{\nu}H \to \nu\bar{\nu}\, b\bar{b}) \propto \Gamma(H \to WW^*) \cdot \mathrm{BR}(H \to b\bar{b}) = \Gamma(H \to b\bar{b}) \cdot \mathrm{BR}(H \to WW^*) \tag{9.6}$$

Thus the Higgs boson total width

$$\Gamma_H = \frac{\Gamma(H \to b\bar{b})}{\mathrm{BR}(H \to b\bar{b})} \propto \frac{\sigma(e^+e^- \to \nu\bar{\nu}H)}{\mathrm{BR}(H \to WW^*)} \tag{9.7}$$

Here $\mathrm{BR}(H \to b\bar{b})$ and $\mathrm{BR}(H \to WW^*)$ are measured from the $e^+e^- \to ZH$ process. The limitation of this method is the precision of the $\sigma(e^+e^- \to \nu\bar{\nu}H)$ measurement.

The expected precision on Γ_H is 5.1% from the measurements of $\sigma(ZH)$ and $\mathrm{BR}(H \to ZZ^*)$ and is 3.4% from the measurements of $\sigma(\nu\bar{\nu}H \to \nu\bar{\nu}b\bar{b})$, $\mathrm{BR}(H \to b\bar{b})$ and $\mathrm{BR}(H \to WW^*)$. The former is dominated by the precision of the $\mathrm{BR}(H \to ZZ^*)$ measurement while the latter by the $\sigma(e^+e^- \to \nu\bar{\nu}H)$ measurement. The combined Γ_H precision of the two measurements is 3.2%, taking into account correlations between the two measurements.

9.1.7 Higgs Boson Coupling Measurements

To understand the implications of the predicted measurement precision shown in Table **??** on possible new physics models, one would need to translate them into constraints on the parameters in the Lagrangian. This is frequently referred to as Higgs boson coupling measurement, even though this way of phrasing it can be misleading as discussed in the following.

There are different ways of presenting the constraints. Before going into CEPC results, we briefly comment on the reasons behind choices of schemes in this section. First, the goal of theory interpretation is different from analyzing actual data, where a lot of detailed work will be done to derive the extended sets of observables. Instead, obtaining a broad brushed big picture of the basic capability of the Higgs boson coupling measurement at the CEPC is the goal. Ideally, the presentation would be simple with a intuitive

connection with the observables. The presentation would ideally also be free of underlying model assumptions. In addition, it would be convenient if the result presentation can be interfaced directly with higher order computations, RGE evolutions, and so on. However, achieving all of these goals simultaneously is not possible. Two of the most popular and balanced approaches are the so-called κ-framework and the Effective Field Theory (EFT) analysis. As discussed in more detail later, none of these is perfect. At the same time, neither of these is wrong as long as one is careful not to over interpreting the result. Another important aspect of making projections on the physics potential of a future experiment is that they will be compared with other possible future experiments. Hence, CEPC follows the most commonly used approaches to facilitate such comparisons.

Motivated by these arguments, in the following, CEPC presents the projections using both the κ-framework and EFT approach. In the later part of this section, Higgs physics potential beyond coupling determination will be discussed.

9.1.7.1 Coupling fits in the κ-framework

The Standard Model makes specific predictions for the Higgs boson couplings to the SM fermions, $g(Hff;\mathrm{SM})$, and to the SM gauge bosons $g(HVV;\mathrm{SM})$. [2] In the κ-framework, the potential deviations are parameterized by

$$\kappa_f = \frac{g(Hff)}{g(Hff;\mathrm{SM})},\ \kappa_V = \frac{g(HVV)}{g(HVV;\mathrm{SM})}, \tag{9.8}$$

with $\kappa_i = 1$ indicating agreement with the SM prediction.

In addition to couplings which are present at tree level, the Standard Model also predicts effective couplings $H\gamma\gamma$ and Hgg, in terms of other SM parameters. Changes in the gluon and photon couplings can be induced by the possible shifts in the Higgs boson couplings described above. In addition, these couplings can also be altered by loop contributions from new physics states. Hence, these couplings will be introduced as two independent couplings, with their ratios to the SM predictions denoted as κ_γ and κ_g.

Furthermore, it is possible that the Higgs boson can decay directly into new physics particles. In this case, two type of new decay channels will be distinguished:

1. Invisible decay. This is a specific channel in which Higgs boson decay into invisible particles. This can be searched for and, if detected, measured.

2. Exotic decay. This includes all the other new physics channels. Whether they can be observed, and, if so, to what precision, depends sensitively on the particular final states. In one extreme, they can be very distinct and can be measured very well. In another extreme, they can be in a form which is completely swamped by the background. Whether postulating a precision for the measurement of the exotic decay or treating it as an independent parameter (essentially assuming it can not be measured directly) is an assumption one has to make. In the latter case, it is common to use the total width Γ_H as an equivalent free parameter.[3]

In general, possible deviations of all Standard Model Higgs boson couplings should be considered. However, in the absence of obvious light new physics states with large

[2] For the discussion of coupling fits and their implications, "H" is used to denoted the 125 GeV Higgs boson.
[3] Total width is a very useful parameter in understanding and deriving parameter precisions in the κ-scheme.

couplings to the Higgs boson and other SM particles, a very large deviation ($> \mathcal{O}(1)$) is unlikely. In the case of smaller deviations, the Higgs boson phenomenology will not be sensitive to the deviations [7]κ_e, κ_u, κ_d and κ_s. Therefore, they will not be considered here and set to be their SM values.

The CEPC will not be able to directly measure the Higgs boson coupling to top quarks. A deviation of this coupling from its SM value does enter $H\gamma\gamma$ and Hgg amplitudes. However, this can be viewed as parametrized by κ_γ and κ_g already. Therefore, we will not include κ_t as an independent parameter. Hence, the following set of 10 independent parameters is considered:

$$\kappa_b,\ \kappa_c,\ \kappa_\tau,\ \kappa_\mu,\ \kappa_Z,\ \kappa_W,\ \kappa_\gamma,\ \kappa_g,\ \mathrm{BR}_{\mathrm{inv}},\ \Gamma_H. \tag{9.9}$$

Several assumptions can be made that can lead to a reduced number of parameters (see also [8, 9]). It can be reduced to a 7-parameter set, by assuming lepton universality, and the absence of exotic and invisible decays (excluding $H \to ZZ^* \to \nu\bar{\nu}\nu\bar{\nu}$) [8, 10]:

$$\kappa_b,\ \kappa_c,\ \kappa_\tau = \kappa_\mu,\ \kappa_Z,\ \kappa_W,\ \kappa_\gamma,\ \kappa_g. \tag{9.10}$$

This is useful for hadron collider studies since it can not measure the Higgs boson total width with precision; it is more useful for models in which this assumption is satisfied.

There are some pros and cons of the κ-framework. κ_is give a simple and intuitive parameterization of potential deviations. It has a direct connection with the observables shown in Table **??**. It does cover a lot of possible modifications of the coupling. At the same time, κ-framework has its limitations. Strictly speaking, it should not be understood as modifying the SM renormalizable Lagrangian by a multiplicative factor. For instance, individual κ modifications violates gauge invariance. The higher order corrections in the κ framework is not easily defined. κ_is do not summarize all possible effects of new physics neither. For example, in addition to the overall size, potential new physics can also introduce form factors which can change the kinematics of particles connected to a vertex. Manifestations of this effect will be seen in the discussion of the EFT approach. It is useful to pause here and compare with the EFT scheme introduced in detail in the next subsection. The EFT scheme relates κ_Z and κ_W, and further expanse them into three different Lorentz structures. In addition, some of these higher dimensional HVV coupling are also in connection with κ_γ and anomalous trilinear gauge couplings. The current EFT scheme does not include important new degree of freedom $\mathrm{BR}_{\mathrm{inv}}$ and Γ_H as independent parameters. Overall, κ-framework does capture the big picture of the capability of precision Higgs boson measurement at CEPC. It is useful as long as we understand its limitation.

The LHC and especially the HL-LHC will provide valuable and complementary information about the Higgs boson properties. For example, the LHC is capable of directly measure the ttH process [11, 12]. In addition, the LHC could use differential cross sections to differentiate top-loop contributions and other heavy particle-loop contributions to the Higgs boson to gluon coupling [13–16], and similarly to separate contributions from different operators to the Higgs boson to vector boson couplings [17]. For the purpose of the coupling fit in the κ-framework, the LHC with its large statistics, helps improving precision on rare processes such as Higgs to diphoton couplings. Note that a large portion of the systematics intrinsic to a hadron collider would be canceled by taking ratios of measured cross sections. For example, combining the ratio of the rates $pp \to H \to \gamma\gamma$

and $pp \to H \to ZZ^*$ and the measurement of HZZ coupling at the CEPC can significantly improve the measurement of κ_γ. These are the most useful inputs from the LHC to combine with the CEPC. Similar studies of combination with the LHC for the ILC can be found in Refs. [18–22].

Table 9.4: Coupling measurement precision in percentage from the 7-parameter fit and 10-parameter fit described in the text for the CEPC, and corresponding results after combination with the HL-LHC. All the numbers refer to are relative precision except for $\mathrm{BR}_{\mathrm{inv}}^{\mathrm{bsm}}$ of beyond standard model for which 95% CL upper limit are quoted respectively. Some entries are left vacant for the 7-parameter fit to stress them being dependent parameter under the fitting assumptions of the 7-parameter fit scheme.

	10-parameter fit		7-parameter fit	
	CEPC	+HL-LHC	CEPC	+HL-LHC
Γ_H	3.4	2.6	–	–
κ_b	1.7	1.3	1.6	1.2
κ_c	2.4	2.0	2.3	2.0
κ_g	1.7	1.3	1.7	1.3
κ_W	1.5	1.1	1.5	1.1
κ_τ	1.6	1.2	1.6	1.2
κ_Z	0.25	0.25	0.16	0.16
κ_γ	4.3	1.7	4.2	1.7
κ_μ	8.6	5.0	–	–
$\mathrm{BR}_{\mathrm{inv}}^{\mathrm{bsm}}$	0.31	0.31	–	–

The 10-parameter fit and the 7-parameter fit for CEPC with integrate luminosity of $5\ \mathrm{ab}^{-1}$ are shown in Table 9.4. In addition, the combinations with expectations (optimistically assuming no theoretical uncertainties) from the HL-LHC from Ref. [23] are shown in the same tables as well.[4] We assume the HL-LHC will operate at 14 TeV center-of-mass energy and accumulate an integrated luminosity of 3000 fb^{-1}.

The CEPC Higgs boson properties measurements mark a giant step beyond the HL-LHC. First of all, in contrast to the LHC, a lepton collider Higgs factory is capable of measuring the absolute width and coupling strengths of the Higgs boson. A comparison with the HL-LHC is only possible with model dependent assumptions. One of such comparison is within the framework of a 7-parameter fit, shown in Fig. 9.9. Even with this set of restrictive assumptions, the advantage of the CEPC is still significant. The measurement of κ_Z is more than a factor of 10 better. The CEPC can also improve significantly on a set of channels which suffers from large background at the LHC, such as κ_b, κ_c, and κ_g. Note that this is in comparison with the HL-LHC projection with aggressive assumptions about systematics. Such uncertainties are typically under much better control at lepton colliders. Within this 7-parameter set, the only coupling which the HL-LHC can give a competitive measurement is κ_γ, for which the CEPC's accuracy is limited by statistics.

[4] We note here that the LHC and the CEPC have different sources of theoretical uncertainties, for detailed discussion, see Refs. [9, 10, 24–26].

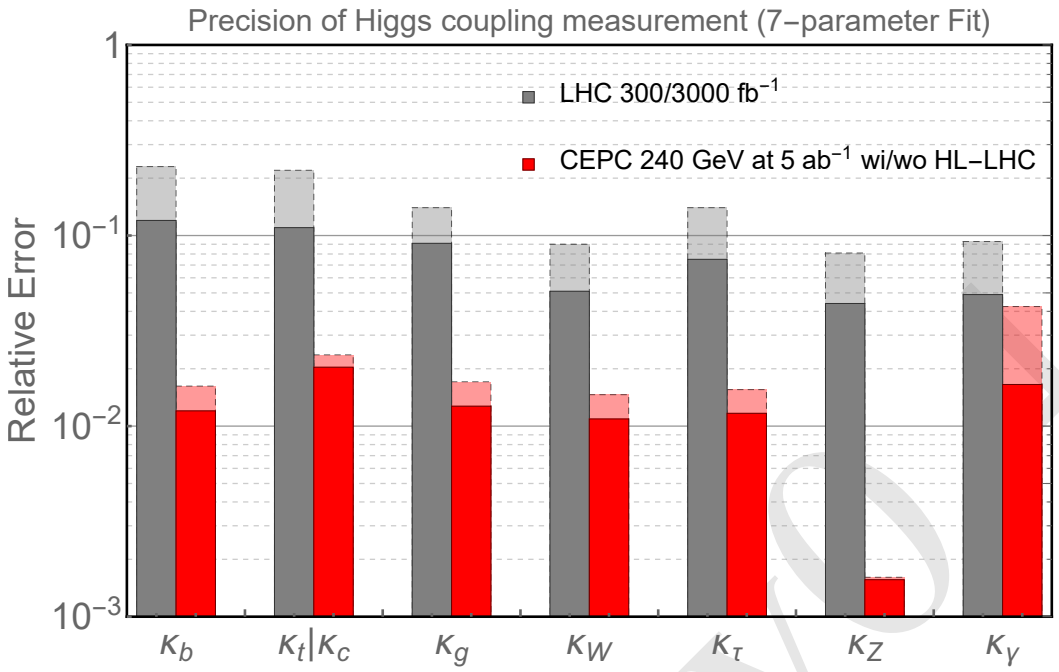

Figure 9.9: The 7 parameter fit result, and comparison with the HL-LHC [23]. The projections for the CEPC at 240 GeV with 5 ab^{-1} integrated luminosity are shown. The CEPC results without combination with the HL-LHC input are shown with dashed edges. The LHC projections for an integrated luminosity of 300 fb^{-1} are shown in dashed edges.

This is also the most valuable input that the HL-LHC can give to the Higgs boson coupling measurement at the CEPC, which underlines the importance of combining the results of these two facilities.

The direct search limit for BSM Higgs decay into invisibles $\mathrm{BR}_{\mathrm{inv}}^{\mathrm{bsm}}$ is well motivated, in close connection to dark sectors. The CEPC with 5 ab^{-1} can measure this to a high accuracy as 95% upper limit 0.31%, as shown in Table 9.4. At the same time, the HL-LHC can only manage a much lower accuracy 6-17% [10] and some improved analysis may reach 2-3.5% [27].

As discussed above, one of the greatest advantages of lepton collider Higgs boson factory is the capability of determining the Higgs boson coupling *model independently*. The projection of such a determination at the CEPC is shown in Fig. 9.10. The advantage of the higher integrated luminosity at a circular lepton collider is apparent. The CEPC has a clear advantage in the measure of κ_Z. It is also much stronger in κ_μ and $\mathrm{BR}_{\mathrm{inv}}$ measurements.

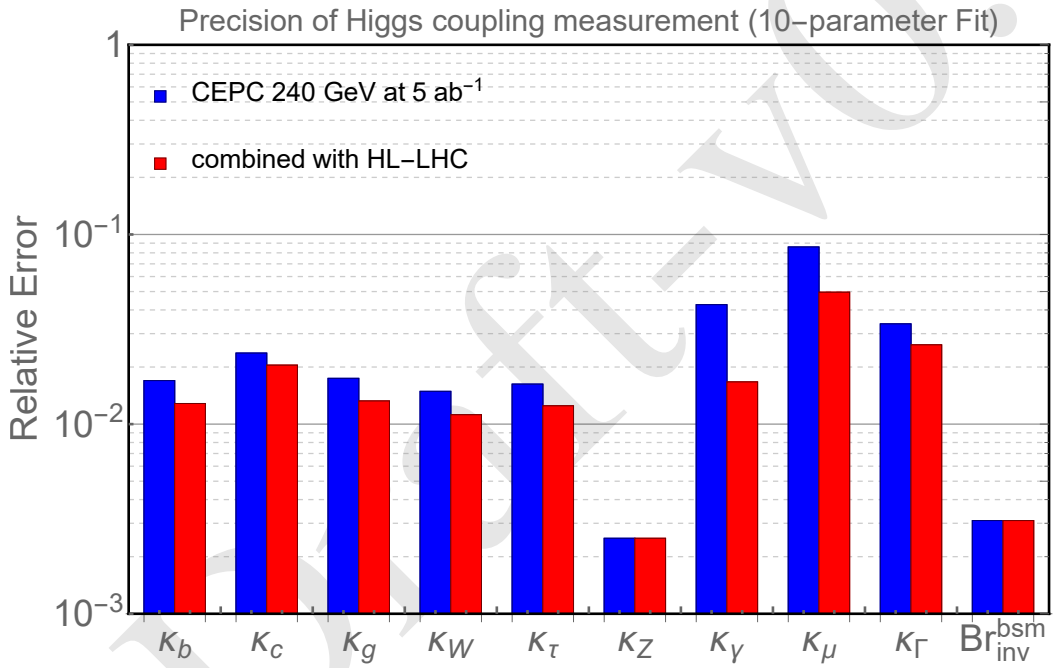

Figure 9.10: The 10 parameter fit result for CEPC at 240 GeV with 5 ab^{-1} integrated luminosity (blue) and in combination with HL-LHC inputs (red). All the numbers refer to are relative precision except for $\mathrm{BR}_{\mathrm{inv}}^{\mathrm{bsm}}$ for which 95% CL upper limit are quoted respectively.

9.1.7.2 Effective-field-theory analysis

With the assumption that the new physics particles are heavier than the relevant energy of the Higgs factory, their effect can be characterized in the effective-field-theory (EFT) framework, in which higher dimensional operators supplement the Standard Model Lagrangian. Imposing baryon and lepton numbers conservations, all higher dimensional operators are of even dimension:

$$\mathcal{L}_{\rm EFT} = \mathcal{L}_{\rm SM} + \sum_i \frac{c_i^{(6)}}{\Lambda^2}\mathcal{O}_i^{(6)} + \sum_j \frac{c_j^{(8)}}{\Lambda^4}\mathcal{O}_j^{(8)} + \cdots \tag{9.11}$$

The leading effects of new physics at the electroweak scale would be the dimension-six operators. To obtain robust constraints on the Wilson coefficients c_i, a global analysis is required which includes the contributions from all possible dimension-six operators. While a large number of dimension-six operators can be written down, only a subset of them contribute to the Higgs boson processes at leading order. Among these operators, some are much better constrained by other measurements. It is thus reasonable to focus on the operators that primarily contribute to the Higgs boson processes and reduce the parameter space by making appropriate assumptions, as done in many recent studies of EFT global analysis at future lepton colliders [22, 28–33]. Following these studies, the CP-violating operators as well as the ones that induce fermion dipole interactions are discarded in this analysis. At leading order, CP-violating operators do not have linear contributions to the rates of Higgs processes. While they do contribute to the angular observables at the leading order [34, 35], these operators are usually much better constrained by EDM experiments [36–38], though some rooms are still possible for the CP-violating couplings of Higgs boson to the heavy flavor quarks and leptons [39, 40]. The interference between the fermion dipole interactions with SM terms are suppressed by the fermion masses. The corresponding operators also generate dipole moments, which are stringently constrained especially for light fermions. For the operators that modify the Yukawa matrices, only the five diagonal ones that correspond to the top, charm, bottom, tau, and muon Yukawa couplings are considered, which are relevant for the Higgs boson measurements at CEPC.

Before presenting the projections, some brief comments on the EFT framework are in order. In comparison with the κ-framework, a significant advantage of the EFT framework is that it gives physical parameterizations of the new physics effect. EFT operators can be used directly in computations. It also allows natural inclusions of new observables, with possible correlations automatically taken into account. At the same time, the connections with experimental observables are less direct and intuitive. Sometimes, the EFT approach is referred to as model-independent. This is only accurate to a certain extent. At least, it assumes that there are no new light degrees of freedom. In practice, assumptions are often made to simplify the set of EFT operators, as also done here.

The electroweak precision observables are already tightly constrained by the LEP Z-pole and W mass measurements. The CEPC Z-pole run can further improve the constraints set by LEP, thanks to the enormous amount ($\sim 10^{11}$) of Z bosons that can be collected. The W mass can also be constrained within a few MeVs at CEPC even without a dedicated WW threshold run. Given that the expected precisions of the Z-pole observables and the W mass are much higher than the ones of Higgs boson observables, in the Higgs boson analysis, it is assumed that the former ones are perfectly constrained, which significantly simplifies the analysis. In particular, in a convenient basis all the contact

CEPC 240 GeV ($5\,\mathrm{ab}^{-1}$)				
	uncertainty	correlation matrix		
		$\delta g_{1,Z}$	$\delta\kappa_\gamma$	λ_Z
$\delta g_{1,Z}$	1.3×10^{-3}	1	0.08	-0.90
$\delta\kappa_\gamma$	1.0×10^{-3}		1	-0.42
λ_Z	1.4×10^{-3}			1

Table 9.5: The estimated constraints on aTGCs from the measurements of the diboson process ($e^+e^- \to WW$) in the semi-leptonic channel at CEPC 240 GeV with $5\,\mathrm{ab}^{-1}$ data and unpolarized beams. All angular distributions are used in the fit. Only the statistical uncertainties of the signal events are considered, assuming a selection efficiency of 80%.

interaction terms of the form $hVf\bar{f}$ can be discarded since they also modify the fermion gauge couplings. Realistic Z-pole constraints have also been considered in recent studies [22, 31, 33], but certain assumptions (such as flavor-universality) and simplifications are made. Future studies with more general frameworks are desired to fully determine the impact of the Z-pole measurements on the Higgs boson analysis.

The measurements of the triple gauge couplings (TGCs) from the diboson process ($e^+e^- \to WW$) play an important role in the Higgs boson coupling analysis under the EFT framework. Focusing on CP-even dimension-six operators, the modifications to the triple gauge vertices from new physics can be parameterized by three anomalous TGC parameters (aTGCs), conventionally denoted as $\delta g_{1,Z}$, $\delta\kappa_\gamma$ and λ_Z [41, 42]. Among them, $\delta g_{1,Z}$ and $\delta\kappa_\gamma$ are generated by operators that also contribute to the Higgs boson processes. At 240 GeV, the cross section of $e^+e^- \to WW$ is almost two orders of magnitude larger than the one of the Higgsstrahlung process. The measurements of the diboson process thus provide strong constraints on the operators that generate the aTGCs. A dedicated study on the TGC measurements at CEPC is not available at the current moment. A simplified analysis is thus performed to estimate the precision reaches on the aTGCs. The results are shown in Table 9.5. The analysis roughly follows the methods in Refs. [30, 43]. Only the WW events in the semi-leptonic (electron or muon) channel are used, which have good event reconstructions and also a sizable branching fraction ($\approx 29\%$). In particular, the production polar angle, as well as the two decay angles of the leptonic W, can be fully reconstructed, which contain important information on the aTGCs. The two decay angles of the hadronic W can only be reconstructed with a two-fold ambiguity. A χ^2 fit of the three aTGC parameters to the binned distribution of all five angles is performed, from which the one-sigma precisions of the three aTGCs as well as the correlations among them are extracted. A signal selection efficiency of 80% is assumed. The effects of systematics and backgrounds are not considered, assuming they are under control after the selection cuts.

Under the assumptions specified above, the contributions to the Higgs boson and diboson processes from dimension-six operators consist of a total number of twelve degrees of freedom. While all non-redundant basis are equivalent, it is particularly convenient to choose a basis in which the twelve degrees of freedom can be mapped to exactly twelve operators, while the rest are removed by the assumptions. Two such bases are considered in our analysis, one is defined by the set of dimension-six operators in Table 9.6, the other is the so-called "Higgs basis," proposed in Ref. [44]. In the Higgs basis, the parameters are

$\mathcal{O}_H = \frac{1}{2}(\partial_\mu \lvert H^2 \rvert)^2$	$\mathcal{O}_{GG} = g_s^2 \lvert H \rvert^2 G^A_{\mu\nu} G^{A,\mu\nu}$
$\mathcal{O}_{WW} = g^2 \lvert H \rvert^2 W^a_{\mu\nu} W^{a,\mu\nu}$	$\mathcal{O}_{y_u} = y_u \lvert H \rvert^2 \bar{Q}_L \tilde{H} u_R \quad (u \to t, c)$
$\mathcal{O}_{BB} = g'^2 \lvert H \rvert^2 B_{\mu\nu} B^{\mu\nu}$	$\mathcal{O}_{y_d} = y_d \lvert H \rvert^2 \bar{Q}_L H d_R \quad (d \to b)$
$\mathcal{O}_{HW} = ig(D^\mu H)^\dagger \sigma^a (D^\nu H) W^a_{\mu\nu}$	$\mathcal{O}_{y_e} = y_e \lvert H \rvert^2 \bar{L}_L H e_R \quad (e \to \tau, \mu)$
$\mathcal{O}_{HB} = ig'(D^\mu H)^\dagger (D^\nu H) B_{\mu\nu}$	$\mathcal{O}_{3W} = \frac{1}{3!} g \epsilon_{abc} W^{a\,\nu}_{\mu} W^b_{\nu\rho} W^{c\,\rho\mu}$

Table 9.6: A complete set of CP-even dimension-six operators that contribute to the Higgs and TGC measurements, assuming there is no correction to the Z-pole observables and the W mass, and also no fermion dipole interaction. For $\mathcal{O}_{y_u}$, $\mathcal{O}_{y_d}$ and $\mathcal{O}_{y_e}$, only the contributions to the diagonal elements of the Yukawa matrices that corresponds to the top, charm, bottom, tau, and muon Yukawa couplings are considered.

defined in the broken electroweak phase, and can be directly interpreted as the size of the Higgs couplings. Different from the original Higgs basis, this analysis follows Ref. [30], with the parameters associated with the Hgg, $H\gamma\gamma$ and $HZ\gamma$ vertices normalized to the SM one-loop contributions, and denoted as $\bar{c}_{gg}$, $\bar{c}_{\gamma\gamma}$ and $\bar{c}_{Z\gamma}$. The parameter $\bar{c}_{gg}^{\text{eff}}$ is further defined to absorb all contributions to the Hgg vertex, as shown in Eq. **??**. These redefined parameters can be more conveniently interpreted as the precisions of the Higgs couplings analogous to those in the κ framework. The exact definitions of the Higgs basis and the translation to the basis in Table 9.6 can be found in the end of the section.

The estimated precisions of all the Higgs rate measurements in Section **??** (Table **??**), along with the correlations among them, are included as inputs for the EFT global analysis. In addition, the angular observables of the channel $e^+e^- \to HZ$, $Z \to \ell^+\ell^-$, $H \to b\bar{b}$ are included, following the studies in Refs. [34, 35]. This channel is almost background-free after the selection cuts, with a signal selection efficiency of about 40%. For the TGC measurements, the results in Table 9.5 are used as inputs. The global χ^2 is obtained by summing over the χ^2 of all the measurements. Due to the high precision of the measurements, it is shown that for all observables, keeping only the linear terms of all EFT parameters gives a very good approximation [30]. This greatly simplifies the fitting procedure, as the total χ^2 can be written as

$$\chi^2 = \sum_{ij} (c - c_0)_i \, \sigma_{ij}^{-2} \, (c - c_0)_j \,, \qquad \text{where} \quad \sigma_{ij}^{-2} \equiv (\delta c_i \, \rho_{ij} \, \delta c_j)^{-1} \,, \tag{9.12}$$

where c_i's are the EFT parameters, c_0's are the corresponding central values which are zero by construction, as the measurements are assumed to be SM-like. The one-sigma uncertainties δc_i and the correlation matrix ρ can be obtained from $\sigma_{ij}^{-2} = \partial^2 \chi^2 / \partial c_i \partial c_j$.

For comparison, the reaches of the LHC 14 TeV are also considered, with a total luminosities of $300\,\text{fb}^{-1}$ or $3000\,\text{fb}^{-1}$, which are combined with the diboson ($e^+e^- \to WW$) measurements at LEP as well as the LHC 8 TeV Higgs measurements. For the LHC 14 TeV Higgs measurements, the projections by the ATLAS collaboration [23] are used, while the composition of each channel is obtained from Refs. [45–49]. The constraints from the LHC 8 TeV Higgs measurements and the diboson measurements at LEP are obtained directly from Ref. [50]. While the LHC diboson measurements could potentially improve the constraints on aTGCs set by LEP [51], they are not included in this analysis due to the potential issues related to the validity of the EFT [52, 53] and the TGC dominance assumption [54].

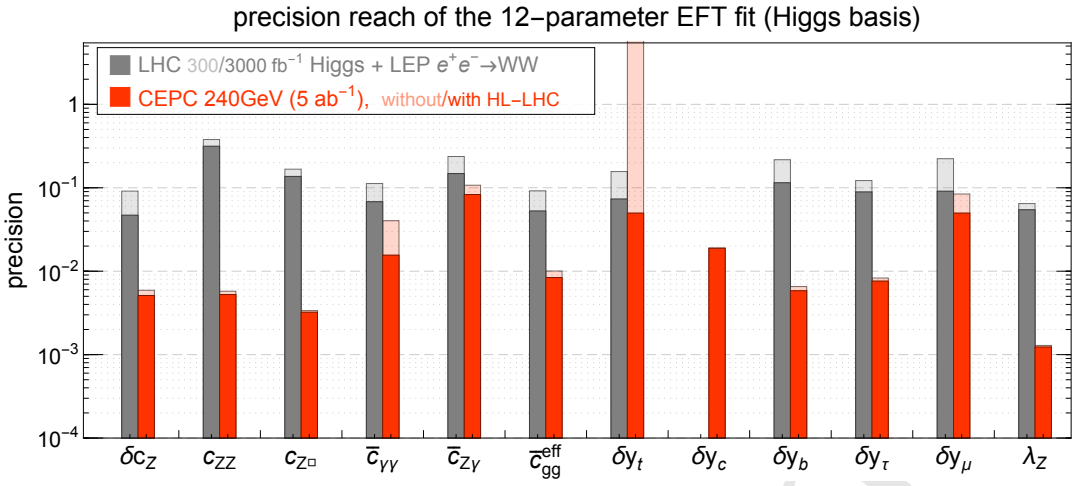

Figure 9.11: One-sigma precision reach of the twelve parameters in the Higgs basis. The first column shows the results from the LHC Higgs measurements with $300\,\mathrm{fb}^{-1}$ (light shade) and $3000\,\mathrm{fb}^{-1}$ (solid shade) combined with LEP diboson ($e^+e^- \to WW$) measurement. The second column shows the results from CEPC with $5\,\mathrm{ab}^{-1}$ data collected at 240 GeV with unpolarized beam. The results from CEPC alone are shown in light shades, and the ones from a combination of CEPC and HL-LHC are shown in solid shades. δy_c is fixed to zero for the LHC fits.

The results of the 12-parameter fit at CEPC are shown in Fig. 9.11 for the Higgs basis and Fig. 9.12 for the basis in Table 9.6. The results from LHC Higgs measurements (both $300\,\mathrm{fb}^{-1}$ and $3000\,\mathrm{fb}^{-1}$) combined with LEP diboson measurements are shown in comparison. The results of the combination of CEPC with HL-LHC ($3000\,\mathrm{fb}^{-1}$) are also shown in addition to the ones of CEPC alone. In Fig. 9.11, the results are shown in terms of the one-sigma precision of each parameter. The LHC results are shown with gray columns with $300\,\mathrm{fb}^{-1}$ ($3000\,\mathrm{fb}^{-1}$) in light (solid) shades, while the CEPC ones are shown with the red columns, with the CEPC-alone (combination with HL-LHC) results shown in light (solid) shades. In Fig. 9.12, the results are presented in terms of the reaches of $\Lambda/\sqrt{|c_i|}$ at 95% confidence level (CL), where Λ is the scale of new physics and c_i is the corresponding Wilson coefficient for each operator, defined in Eq. 9.11. Four columns are shown separately for LHC $300\,\mathrm{fb}^{-1}$, LHC $3000\,\mathrm{fb}^{-1}$, CEPC alone and CEPC combined with HL-LHC. The results of the global fits are shown with solid shades. The results from individual fits are shown with light shades, which are obtained by switching on one operator at a time with the rest fixed to zero.

It is transparent from Fig. 9.11 that CEPC provides very good reaches on the precisions of Higgs couplings, which are of one order of magnitude better than the ones at the LHC. For the parameters $\bar{c}_{\gamma\gamma}$, $\bar{c}_{Z\gamma}$ and δy_μ, the clean signal and small branching ratios of the corresponding channels ($H \to \gamma\gamma/Z\gamma/\mu\mu$) makes the HL-LHC precisions comparable with the CEPC ones. The combination with additional LHC measurements thus provides non-negligible improvements, especially for those parameters. It should be noted that, while δy_t modifies the Hgg vertex via the top loop contribution, CEPC alone could not discriminate it from the Hgg contact interaction ($\bar{c}_{gg}$ in Eq. **??**) obtained from integrating out a heavy new particle in the loop. The parameter $\bar{c}_{gg}^{\mathrm{eff}}$ absorbs both contributions and reflects the overall precision of the Hgg coupling. The combination with the LHC $t\bar{t}H$ measurements could resolve this flat direction. The CEPC measurements, in turn, could improve the constraint on δy_t set by the LHC by providing much better con-

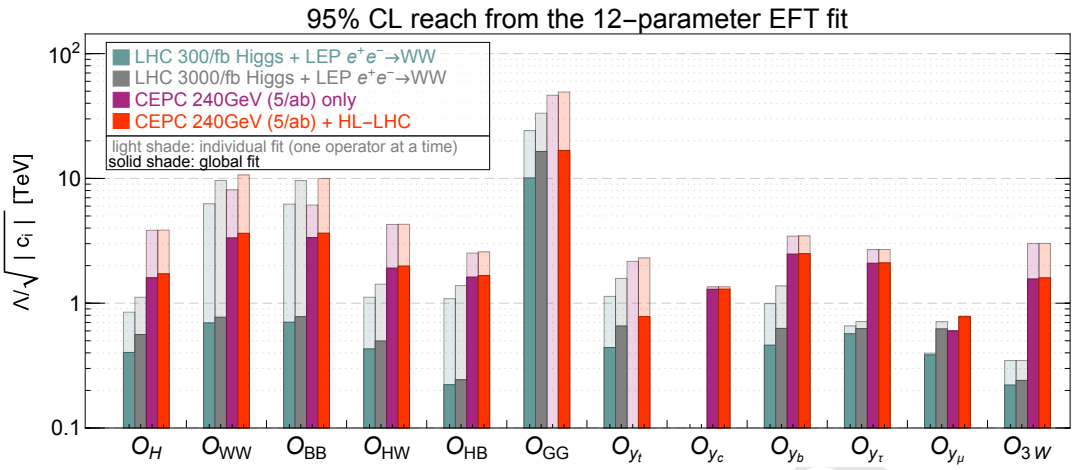

Figure 9.12: The 95% CL reach on $\Lambda/\sqrt{|c_i|}$ for the operators in the basis defined in Table 9.6. The first two columns show the results from LHC Higgs measurements with 300 fb^{-1} and 3000 fb^{-1} combined with LEP diboson ($e^+e^- \to WW$) measurement. The last two columns show the results from CEPC alone and the combination of CEPC and HL-LHC (3000 fb^{-1}). The results of the global fits are shown with solid shades. The results from individual fits (by switching on one operator at a time) are shown with light shades. δy_c is fixed to zero for the LHC fits.

straints on the other parameters that contribute to the $t\bar{t}H$ process. It should also be noted that the measurement of the charm Yukawa coupling is not reported in Ref. [23], while the projection of its constraint has a large variation among different studies and can be much larger than one [55–60]. Therefore, δy_c is fixed to be zero for the LHC-only fits, as treating δy_c as an unconstrained free parameter generates a flat direction in the fit which makes the overall reach much worse. The CEPC, on the other hand, provides excellent measurements of the charm Yukawa and can constrain δy_c to a precision of $\sim 2\%$.

Regarding the reaches of $\Lambda/\sqrt{|c_i|}$ in Fig. 9.12, it is also clear that CEPC has a significantly better performance than the LHC. If the couplings are naïvely assumed to be of order one ($c_i \sim 1$), the Higgs measurements at CEPC would be sensitive to new physics scales at multiple TeVs. While the individual reach for some of the operators at the LHC can be comparable to the ones at CEPC (*e.g.*, O_{WW} and O_{BB} from the measurement of $H \to \gamma\gamma$), the reaches of CEPC are much more robust under a global framework thanks to its comprehensive measurements of both the inclusive HZ cross section and the exclusive rates of many Higgs decay channels. Operators O_{GG} and O_{y_t} both contribute to the Hgg vertex. While the CEPC could provide strong constraints on either of them if the other is set to zero, they can only be constrained in a global fit if the $t\bar{t}h$ measurements at the LHC are also included. It is also important to note that the validity of EFT could be a potential issue for the LHC measurements [52]. Depending on the size of the couplings, the inferred bounds on the new physics scale Λ could be comparable with or even smaller than the energy scale probed by the LHC. The CEPC has a smaller center of mass energy and much better precisions, which ensures the validity of EFT for most new physics scenarios.

In Table 9.7 and Fig. **??**, the numerical results of the global fit are presented for CEPC in terms of the one-sigma precisions of the 12 parameters and the correlations among them. The results assume an integrated luminosity of 5 ab^{-1} at 240 GeV with unpolarized beams, both without and with the combination of HL-LHC (3000 fb^{-1}) Higgs measurements. With both the one-sigma bounds and the correlation matrix, the corre-

sponding *chi-squared* can be reconstructed, which can be used to derive the constraints in any other EFT basis or any particular model that can be matched to the EFT. This offers a convenient way to study the reaches on new physics models, as detailed knowledge of the experimental measurements are not required.

Higgs basis											
δc_Z	c_{ZZ}	$c_{Z\Box}$	$\bar{c}_{\gamma\gamma}$	$\bar{c}_{Z\gamma}$	$\bar{c}_{gg}^{\rm eff}$	δy_t	δy_c	δy_b	δy_τ	δy_μ	λ_Z
0.0059	0.0058	0.0034	0.040	0.11	0.010	–	0.019	0.0065	0.0083	0.084	0.0013
0.0051	0.0053	0.0032	0.016	0.083	0.0084	0.050	0.019	0.0058	0.0076	0.050	0.0012
c_i/Λ^2 [TeV^{-2}] of dimension-six operators											
c_H	c_{WW}	c_{BB}	c_{HW}	c_{HB}	c_{GG}	c_{y_t}	c_{y_c}	c_{y_b}	c_{y_τ}	c_{y_μ}	c_{3W}
0.20	0.045	0.044	0.14	0.19	–	–	0.30	0.082	0.11	1.4	0.20
0.17	0.038	0.038	0.13	0.18	0.0018	0.82	0.30	0.080	0.11	0.82	0.20

Table 9.7: The one-sigma uncertainties for the 12 parameters from CEPC (240 GeV, $5\,\mathrm{ab}^{-1}$) in the Higgs basis and the basis of dimension-six operators. For both cases, the upper (lower) row correspond to results without (with) the combination of the HL-LHC Higgs measurements.. Note that, without the $t\bar{t}h$ measurements, δy_t can not be constrained in a global fit, thus c_{GG} and c_{y_t} can not be resolved.

In the EFT framework, it is explicitly assumed that the Higgs total width is the sum of all the widths of its SM decay channels. This is because the EFT expansion in Eq. 9.11 relies on the assumption that the new physics scale is sufficiently large, while any potential Higgs exotic decay necessarily introduces light BSM particles, thus in direct conflict with this assumption. One could nevertheless treat the Higgs total width as a free parameter in the EFT global fit and obtain an indirect constraint of it, as done in Ref. [22]. With this treatment, the CEPC could constrain the Higgs total width to a precision of 1.8% (1.7% if combined with HL-LHC). This result is significantly better than the one from the 10-parameter coupling fit in Table 9.4 ($3.4\%/2.6\%$). The improvement is mainly because the HWW and HZZ couplings are treated as being independent in the 10-parameter coupling fit, while in the EFT framework they are related to each other under gauge invariance and custodial symmetry. It should also be noted that the Higgs width determined using Eq. (9.4) and (9.7) explicitly assumes that the HWW and HZZ couplings are independent of the energy scale. Such an assumption is not valid in the EFT framework with the inclusion of the anomalous couplings.

9.1.7.3 The Higgs self-coupling

The Higgs boson self-coupling is a critical parameter governing the dynamics of the electroweak symmetry breaking. In the Standard Model, the Higgs trilinear and quadrilinear couplings are fixed once the values of the electroweak VEV and the Higgs mass are known. Any deviation from the SM prediction is thus clear evidence of new physics beyond the SM. The Higgs trilinear coupling is probed at the LHC with the measurement of the double-Higgs process, $pp \to HH$. Current bounds on the Higgs trilinear coupling is at the $\mathcal{O}(10)$ level, while the HL-LHC is expected to improve the precision to the level of $\mathcal{O}(1)$ [61]. The prospects for extracting the Higgs quadrilinear coupling are much less promising, even for a 100 TeV hadron collider [62].

To measure the double-Higgs processes at a lepton collider, a sufficiently large center of mass energy ($\gtrsim 400$ GeV) is required, which is likely to be achieved only at a linear collider. The CEPC, instead, can probe the Higgs trilinear coupling via its loop contributions to the single Higgs processes. This indirect approach nevertheless provides competitive reaches since the loop suppression is compensated by the high precision of

the Higgs measurements at CEPC [63]. With a precision of 0.5% on the inclusive HZ cross section at 240 GeV, the Higgs trilinear coupling can be constrained to a precision of 35%, assuming all other Higgs couplings that contributes to $e^+e^- \to HZ$ are SM-like. [5] While this indirect bound is comparable to the direct ones at linear colliders, it relies on strong assumptions which are only applicable to some specific models. A more robust approach is to include all possible deviations on the Higgs couplings simultaneously and constrain the Higgs trilinear coupling in a global fit. The EFT framework presented in Section 9.1.7.2 is ideal for such an analysis. Under this framework, the one-loop contributions of the trilinear Higgs coupling to all the relevant Higgs production and decay processes are included, following Ref. [32]. The new physics effect is parameterized by the quantity $\delta\kappa_\lambda \equiv \kappa_\lambda - 1$, where κ_λ is the ratio of the Higgs trilinear coupling to its SM value,

$$\kappa_\lambda \equiv \frac{\lambda_3}{\lambda_3^{\rm sm}}\,, \qquad \lambda_3^{\rm sm} = \frac{m_H^2}{2v^2}\,. \tag{9.13}$$

The global fit is performed simultaneously with $\delta\kappa_\lambda$ and the 12 EFT parameters in Section 9.1.7.2. The results are presented in Table 9.8. The results for HL-LHC are also shown, which were obtained in Ref. [64] under the same global framework. For CEPC 240 GeV, the one-sigma bound on $\delta\kappa_\lambda$ is around ± 3, significantly worse than the 35% in the $\delta\kappa_\lambda$-only fit. This is a clear indication that it is difficult to resolve the effects of $\delta\kappa_\lambda$ from those of other Higgs couplings. For HL-LHC, the reach on $\delta\kappa_\lambda$ is still dominated by the double-Higgs process. However, as a result of the destructive interferences among diagrams, the double-Higgs process at LHC could not constrain $\delta\kappa_\lambda$ very well on its positive side, even with the use of differential observables [65]. The combination of HL-LHC and CEPC 240 GeV thus provides a non-trivial improvement to the HL-LHC result alone, in particular for the two-sigma bound on the positive side, which is improved from $+6.1$ to $+2.8$. This is illustrated in Fig. 9.13, which plots the profiled χ^2 as a function of $\delta\kappa_\lambda$ for the two colliders.

bounds on $\delta\kappa_\lambda$	$\Delta\chi^2 = 1$	$\Delta\chi^2 = 4$
CEPC 240 GeV $(5\,\text{ab}^{-1})$	$[-3.2, +3.3]$	$[-6.3, +6.7]$
HL-LHC	$[-0.9, +1.3]$	$[-1.7, +6.1]$
HL-LHC + CEPC 240 GeV	$[-0.8, +1.0]$	$[-1.5, +2.8]$
240 GeV $(5\,\text{ab}^{-1})$ + 350 GeV $(1.5\,\text{ab}^{-1})$	$[-0.48, +0.48]$	$[-0.96, +0.96]$

Table 9.8: The $\Delta\chi^2 = 1$ (one-sigma) and $\Delta\chi^2 = 4$ (two-sigma) bounds of $\delta\kappa_\lambda$ for various scenarios, obtained in a global fit by profiling over all other EFT parameters. The results for HL-LHC are obtained from Ref. [64].

It is also important to note that the reach on $\delta\kappa_\lambda$ in the global framework is significantly improved if an additional run at a higher energy, such as 350 GeV, is available. The global constraint on $\delta\kappa_\lambda$ is improved by almost one order of magnitude with $1.5\,\text{ab}^{-1}$ data collected at the 350 GeV on top of the $5\,\text{ab}^{-1}$ at 240 GeV. The usefulness of the 350 GeV run in discriminating different EFT parameters is thoroughly discussed in Ref. [30]. In

[5] A better precision can be obtained by also using the exclusive channels, such as $\sigma(HZ) \times \text{BR}(H \to b\bar{b})$, but would require an even stronger assumption that all Higgs couplings contributing to the branching ratios are also SM-like except the Higgs trilinear coupling.

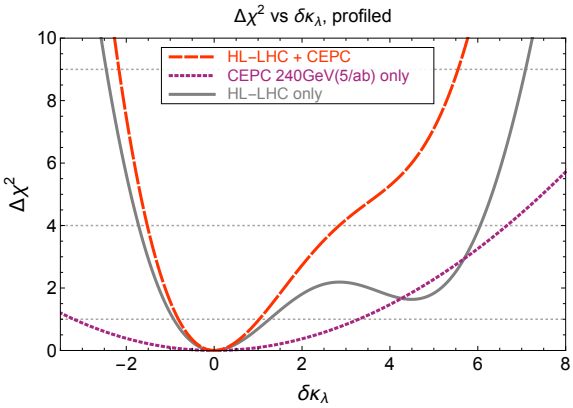

Figure 9.13: Chi-square as a function of $\delta\kappa_\lambda$ after profiling over all other EFT parameters for HL-LHC, CEPC and their combination.

addition, it was pointed out in Refs. [32, 63] that the sensitivity of $\sigma(HZ)$ to $\delta\kappa_\lambda$ is maximized near the HZ threshold and decreases as the center of mass energy increases – a feature not exhibited by the other EFT parameters. Measuring $e^+e^- \to HZ$ at two different energies is thus particularly helpful in discriminating $\delta\kappa_\lambda$ with other EFT parameters.

9.1.7.4 Higgs and top couplings

Interactions of the Higgs boson with the top quark are widely viewed as a window to new physics beyond the Standard Model. Parameterizing effects of new physics in terms of dimension-six gauge-invariant operators modifying the Higgs-top interactions [66, 67], the Higgs top couplings physics potential at CEPC can be evaluated [68–71]. This EFT basis enlarges the Higgs EFT considered above. Moreover, the CP violation effects in the third generation Yukawas can be reflected as the complexity of the Wilson coefficients of operator $\mathcal{O}_{y_t}$ and $\mathcal{O}_{y_b}$,

$$\Delta y_t = y_t^{\rm SM}\left(\Re[C_{y_t}]\frac{v^3}{2m_t\Lambda^2} + i\Im[C_{y_t}]\frac{v^3}{2m_t\Lambda^2}\right) \tag{9.14}$$

$$\Delta y_b = y_t^{\rm SM}\left(\Re[C_{y_b}]\frac{v^3}{2m_b\Lambda^2} + i\Im[C_{y_b}]\frac{v^3}{2m_b\Lambda^2}\right). \tag{9.15}$$

In this section, the effect of introducing CP phases in the Yukawa operators in Higgs physics are discussed. For more detailed discussion on a complete set of Higgs and Top operators, see Ref. [68]. The dominant sources of constraints are from $H \to \gamma\gamma$ and $H \to gg$ for $\mathcal{O}_{y_t}$, and $H \to gg$ and $H \to b\bar{b}$ for $\mathcal{O}_{y_b}$. Given that $H \to gg$ measurements are sensitive to both operators, a joint analysis of $\mathcal{O}_{y_t}$ and $\mathcal{O}_{y_b}$ will yield a significantly different result comparing to individual operator analysis. A joint analysis for these two operators in terms of Yukawa coupling strengths and the associated CP phases is performed at CEPC. The important physics cases for such considerations are highlighted.

In Fig. 9.14 constraints on the top and bottom Yukawa coupling strengths and their CP phases are presented in the left panel and right panel, respectively. The 68% and 95% exclusion bands are shown in solid and dashed lines. The limits for CEPC are shown in *bright* black and magenta lines for individual operator analysis and the *bright* green and yellow shaded regions representing the 68% and 95% allowed parameter space, respectively. The *dimmed* thick black curves represent the results after turning on both operators

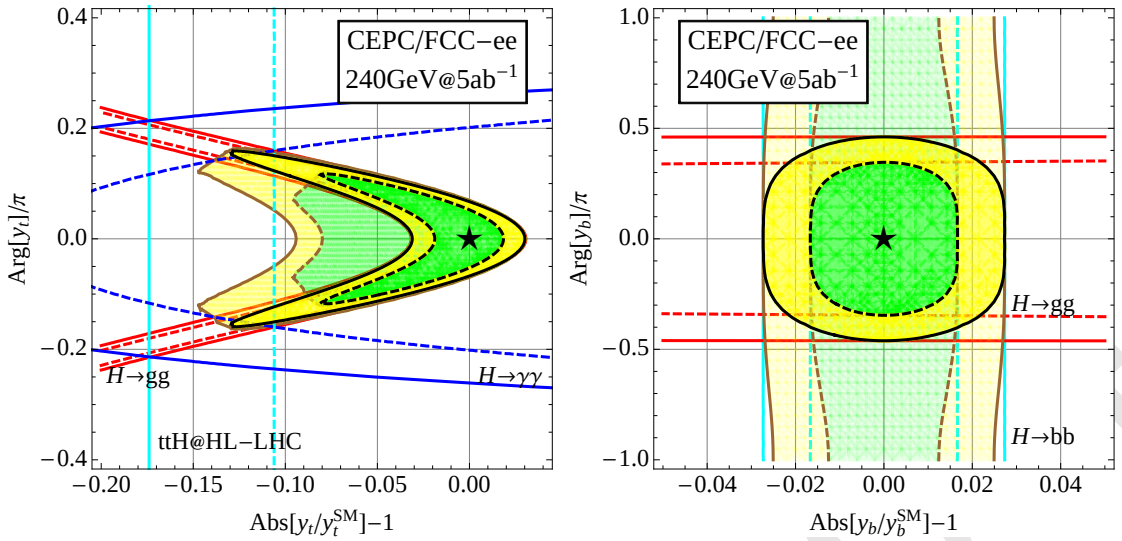

Figure 9.14: Results for analysis on C_{y_t} and C_{y_b} in the projected allowed regions for modification to top and bottom Yukawa couplings in magnitude and CP phase at 68% and 95% confidence level. The combined results for CEPC are shown in black curves. The source of individual constraints for the single operator analysis are labeled correspondingly. For a joint analysis of simultaneous appearance of both $\mathcal{O}_{y_t}$ and $\mathcal{O}_{y_b}$ operators, the results for CEPC are shown in the enlarged yellow (95%) and green regions (68%) with thick brown boundary lines.

$\mathcal{O}_{tH}$ and $\mathcal{O}_{bH}$ at the same time, using a profile-likelihood method profiling over other parameters. Furthermore, in the left panel the cyan band represents constraints from HL-LHC $t\bar{t}H$ measurements, red bands are constraints from CEPC $H \to gg$ measurements and blue bands are constraints from CEPC $H \to \gamma\gamma$ measurements. Similarly in the right panel, the cyan bands are constraints from $H \to b\bar{b}$ and the red bands are constraints from $H \to gg$ at CEPC.

The left panel of Fig. 9.14 shows that the expected sensitivity on the modification in the magnitude of top Yukawa is at around $\pm 3\%$ for the single operator analysis, which is relaxed to $[-9.5\%, +3\%]$ for the joint analysis allowing the bottom Yukawa and the associated CP phase to vary freely, in the case of zero CP phase in the top Yukawa. The phase of the top Yukawa could be constrained to be $\pm 0.16\pi$. The constraints on the phase of the top Yukawa is driven by the $H \to \gamma\gamma$ measurements, where a sizable phase shift will enlarge the Higgs to diphoton rate via reducing the interference with SM W-loop. The constraints on the magnitude of the top Yukawa modification is driven by the $H \to gg$ measurements due to the dominant contribution to $H \to gg$ being from top-loop. Note that constraints from $H \to gg$ measurement is not entirely vertical, this is a result of the different sizes of the top-loop contribution to Hgg through scalar and pseudoscalar couplings. Similarly, as shown in the right panel of Fig. 9.14 for the bottom Yukawa magnitude modification, the constraint is $\pm 2.5\%$ and, for the bottom Yukawa CP phase, the constraints changes from $\pm 0.47\pi$ to no constraint for simultaneous modification to top Yukawa.

9.1.8 Searches for exotic decays

Higgs boson can be an important portal to new physics beyond the Standard Model. Such new physics could manifest itself through Higgs boson exotic decays if some of the de-

grees of freedom are light. The Higgs boson BSM decays have a rich variety of possibilities. To organize this study on Higgs boson BSM decays, on two-body Higgs boson decays into BSM particles, dubbed as X_i, $H \to X_1 X_2$, which are allowed to subsequently decay further, up to four-body final states, are considered in this section. The cascade decay modes are classified into four cases, schematically shown in Fig. 9.15. These processes can be motivated by SM+singlet extensions, two-Higgs-doublet-models, SUSY models, Higgs portals, gauge extensions of the SM [72–74].

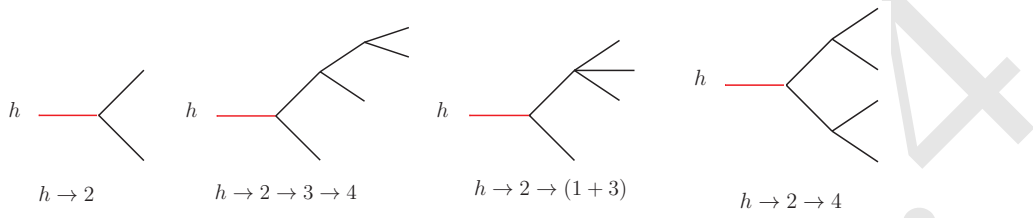

Figure 9.15: The topologies of the SM-like Higgs boson exotic decays.

For CEPC running at the center of mass energy 240 GeV, the most important Higgs boson production mechanism is Z-Higgs associated production $e^+e^- \to Z^* \to ZH$. The Z boson with visible decays enables Higgs boson tagging using the "recoil mass" technique. A cut around the peak of the recoil mass spectrum would remove the majority of the SM background. Further selection and tagging on the Higgs boson decay product can hence archive high signal efficiency, and the major background would be from the Higgs boson SM decays. The details of these analysis can be found in Ref. [74]. The set of Higgs boson exotic decays with their projected LHC constraints and limits from the CEPC with 5 ab^{-1} integrated luminosity are summarized in Table 9.9. For the LHC constraints, both the current limits and projected limits on these exotic decay channels from various references are tabulated. The comparison are performed for particular benchmark points, which is sufficient to demonstrate the qualitative difference between the LHC and CEPC.

In the summary in Table 9.9 and the corresponding Fig. 9.16, the exotic Higgs boson decay channels are selected such that they are hard to be constrained at the LHC. The

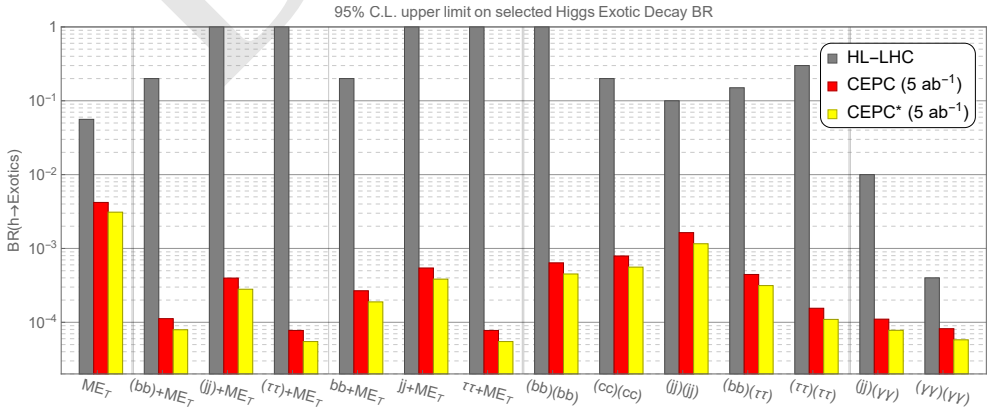

Figure 9.16: The 95% C.L. upper limit on selected Higgs boson exotic decay branching fractions at HL-LHC and CEPC, based on Ref [74]. The benchmark parameter choices are the same as in Table 9.9. The red bars correspond to the results using leptonically decaying spectator Z-boson alone. The yellow bars further include extrapolation with the inclusion of the hadronically decaying Z-bosons. Several vertical lines are drawn in this figure to divide different types of Higgs boson exotic decays.

Table 9.9: The current and projected limits on selected Higgs boson exotic decay modes for the (HL-)LHC and CEPC with $5\ \mathrm{ab}^{-1}$ integrated luminosity, based upon results from Ref. [74]. The projections for the HL-LHC are collected in the third column, where the limits for $100\ \mathrm{fb}^{-1}$ and $300\ \mathrm{fb}^{-1}$ alone are shown in parentheses and square brackets respectively.

Decay Mode	95% C.L. limit on Br		
	LHC	HL-LHC	CEPC
$E_{\mathrm{T}}^{\mathrm{miss}}$	0.23	0.056	0.014
$(b\bar{b}) + E_{\mathrm{T}}^{\mathrm{miss}}$	–	[0.2]	1×10^{-4}
$(jj) + E_{\mathrm{T}}^{\mathrm{miss}}$	–	–	4×10^{-4}
$(\tau^+\tau^-) + E_{\mathrm{T}}^{\mathrm{miss}}$	–	[1]	8×10^{-5}
$b\bar{b} + E_{\mathrm{T}}^{\mathrm{miss}}$	–	[0.2]	2×10^{-4}
$jj + E_{\mathrm{T}}^{\mathrm{miss}}$	–	–	5×10^{-4}
$\tau^+\tau^- + E_{\mathrm{T}}^{\mathrm{miss}}$	–	–	8×10^{-5}
$(b\bar{b})(b\bar{b})$	1.7	(0.2)	6×10^{-4}
$(c\bar{c})(c\bar{c})$	–	(0.2)	8×10^{-4}
$(jj)(jj)$	–	[0.1]	2×10^{-3}
$(b\bar{b})(\tau^+\tau^-)$	[0.1]	[0.15]	4×10^{-4}
$(\tau^+\tau^-)(\tau^+\tau^-)$	[1.2]	$[0.2 \sim 0.4]$	2×10^{-4}
$(jj)(\gamma\gamma)$	–	[0.01]	1×10^{-4}
$(\gamma\gamma)(\gamma\gamma)$	$[7\times10^{-3}]$	4×10^{-4}	8×10^{-5}

red bars correspond to the results using leptonic decaying Z-boson that is produced in association with the Higgs boson. The hadronic decaying Z-boson provides around ten times more statistics and hence further inclusion will definitely improve the results significantly. Based upon the study of the $H \to WW^*,\ ZZ^*$ and invisibles, hadronic decaying Z bosons are conservatively assumed to provide same upper limit on these channels from leptonic Z and hence improve the limits by around 40% when combined. This extrapolated results are shown in yellow bars. The improvements on the limits of the Higgs boson exotic decay branching fractions vary from one to four orders of magnitude for these channels. The CEPC can improve the limits on the BSM Higgs boson invisible decays beyond the HL-LHC projection by one order of magnitude, to 0.31% at 95% CL, after subtracting the SM invisible decay branching fraction of 0.12% from $H \to ZZ^* \to \nu\bar{\nu}\nu\bar{\nu}$ [9]. For the Higgs boson exotic decays into hadronic particle plus missing energy, $b\bar{b} + E_{\mathrm{T}}^{\mathrm{miss}}$, $jj + E_{\mathrm{T}}^{\mathrm{miss}}$ and $\tau^+\tau^- + E_{\mathrm{T}}^{\mathrm{miss}}$, CEPC improves on the HL-LHC sensitivity for these channels by roughly three to four orders of magnitude. This great advantage benefits a lot from low QCD background and the Higgs boson tagging from recoil mass technique at CEPC. As for the Higgs boson exotic decays without missing energy, the improvement varies between two to three orders of magnitude, except for the one order of magnitude improvement for the $(\gamma\gamma)(\gamma\gamma)$ channel. Being able to reconstruct the Higgs boson mass from the final state particles at the LHC does provide additional signal-background discrimination power and hence the improvement from CEPC on Higgs boson exotic decays without missing energy is less impressive than for those with missing energy. Furthermore, as discussed earlier, leptons and photons are relatively clean objects at the LHC and the sensitivity at the LHC on these channels will be very good. CEPC complements the HL-LHC for hadronic channels and channels with missing energy.

9.1.9 Tests of Higgs boson spin/CP

Need further editing...

The CP parity of a Higgs boson, and more generally its anomalous couplings to gauge bosons in the presence of BSM physics, can be measured at the CEPC based on the $e^+e^-(\to Z^*) \to ZH \to \mu^+\mu^- b\bar{b}$ process. It is convenient to express the anomalous coupling measurements in terms of physical quantities of effective fractions of events of the anomalous contribution relative to the SM predictions as detailed in Refs. [75–77], which are invariant under independent re-scalings of all couplings.

Two of the anomalous HZZ coupling measurements are of particular interest at the CEPC: the fraction of the high-order CP-even contribution due to either SM contribution or new physics, f_{a2}, and the fraction of a CP-odd contribution due to new physics, f_{a3}. The following two types of observables can be used to measure these anomalous couplings of the Higgs bosons.

1. The dependence of the $e^+e^- \to Z^* \to ZH$ cross section on $\sqrt{s}$ is different for different CP property of the Higgs boson [77]. Therefore, measurements of the cross section at several different energies will yield useful information about anomalous HZZ couplings. However this has non-trivial implications to the accelerator design and is not included in this study as a single value of $\sqrt{s}$ assumed for the CEPC operating as a Higgs boson factory.

2. Angular distributions, $\cos\theta_1$ or $\cos\theta_2$ and Φ as defined in Ref. [77]. These angles are also sensitive to interference between CP-even and CP-odd couplings. In particular forward-backward asymmetry with respect to $\cos\theta_1$ or $\cos\theta_2$ and non-trivial phase in the Φ distributions can lead to an unambiguous interpretation of CP violation.

To estimate the sensitivities on the anomalous couplings, a maximum likelihood fit [77] is performed to match observed three-dimensional angular distributions to theory predictions including signal and background processes. In this likelihood fit, the signal probability density functions are from analytical predictions that are validated using a dedicated MC program, the JHU generator [75, 76], which incorporates all the anomalous couplings, spin correlations, interference of all contributing amplitudes. The background probability density function is modeled from simulation based on $e^+e^- \to ZZ \to \ell^+\ell^- b\bar{b}$ process in Madgraph. The total integrated luminosity is assumed to be 5 ab^{-1}.

Several thousand statistically-independent experiments are generated and fitted to estimate the sensitivity to f_{a2} and f_{a3}, defined as the smallest values that can be measured with 3σ away from 0. All other parameters in the fit, including the number of expected signal and background events, are fixed. Figure 9.17 shows precision on f_{a2} and f_{a3} obtained with generated experiments. The expected sensitivity on f_{a2} and f_{a3} are 0.018 and 0.007 respectively.

The sensitivities of f_{a2} and f_{a3} are then converted to the equivalent parameters defined for the on-shell $H \to ZZ^*$ decays, $f_{a2}^{\rm dec}$ and $f_{a3}^{\rm dec}$, in order to compare with the sensitivities from other experiments as described in Ref. [77]. The corresponding sensitivities of $f_{a2}^{\rm dec}$ and $f_{a3}^{\rm dec}$ are 2×10^{-4} and 1.3×10^{-4} respectively. The much smaller values in the $f_{a2,a3}^{\rm dec}$ are due to the much larger $m^2_{Z^*}$ in the $Z^* \to ZH$ production compared to the value in the $H \to ZZ^*$ decays. A simultaneous fit of f_{a2} and f_{a3} can also performed with the 68% and 95% confidence level contours shown in Figure 9.17.

Compared to the ultimate sensitivity from HL-LHC experiments as shown in Ref. [77], the sensitivities in the f_{a2} and f_{a3} at the CEPC are a factor of 300 and 3 better. Further improvements can be achieved by exploring kinematics in the $H \to b\bar{b}$ decays, including other Z decay final states, and combining with the overall cross-section dependence of the signal with a threshold scan in $\sqrt{s}$.

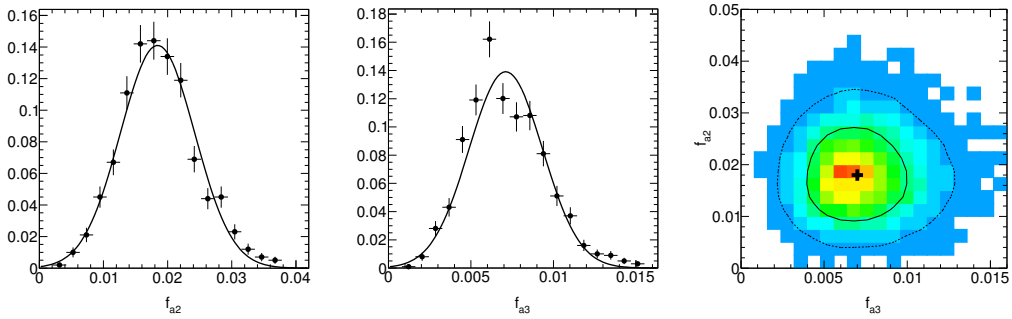

Figure 9.17: Distribution of fitted values of f_{a2} and f_{a3} in a large number of generated experiments. In the left and middle plots, only the parameter shown is floated. Other parameters are fixed to SM expectations. Right plot: simultaneous fit of non-zero f_{a2} and f_{a3}, with 68% and 95% confidence level contours shown. Keep the right plot only?

9.1.10 Summary

To do: need to actually summarize what is described above.

The Higgs boson is responsible for the electroweak symmetry breaking. It is the only fundamental scalar particle in the Standard Model observed so far. The discovery of such a particle at the LHC is a major breakthrough on both theoretical and experimental fronts. However, the Standard Model is likely only an effective theory at the electroweak scale. To explore potential new physics at the electroweak scale and beyond, complementary approaches of direct searches at the energy frontier as well as precision measurements will be needed. The current LHC and the planned HL-LHC have the potential to significantly extend its new physics reach and to measure many of the Higgs boson couplings with precision of a few percents.

However, many new physics models predict Higgs boson coupling deviations at the sub-percent level, beyond those achievable at the LHC. The CEPC complements the LHC and will be able to study the properties of the Higgs boson in great details with unprecedented precision. Therefore it is capable of unveiling the true nature of this particle. At the CEPC, most Higgs boson couplings can be measured with precision at a sub-percent level. More importantly, the CEPC will able to measure many of the key Higgs boson properties such as the total width and decay branching ratios model independently, greatly enhancing the coverage of new physics searches. Furthermore, the clean event environment of the CEPC will allow the detailed study of known decay modes and the identification of potential unknown decay modes that are impractical to test at the LHC.

This paper provides a snapshot of the current studies, many of them are ongoing and more analyses are needed to fully understand the physics potential of the CEPC. Nevertheless, the results presented here have already built a strong case for the CEPC as a Higgs factory. The CEPC has the potential to "undress" the Higgs boson as what the LEP has done to the Z boson, and shed light on new physics.

References

[1] LHC Higgs Cross Section Working Group, *Handbook of LHC Higgs Cross Sections: 1. Inclusive Observables*, arXiv:1101.0593 [hep-ph].

[2] LHC Higgs Cross Section Working Group, *Handbook of LHC Higgs Cross Sections: 2. Differential Distributions*, arXiv:1201.3084 [hep-ph].

[3] W. Kilian, T. Ohl, and J. Reuter, *WHIZARD: Simulating Multi-Particle Processes at LHC and ILC*, Eur. Phys. J. **C71** (2011) 1742, arXiv:0708.4233 [hep-ph].

[4] Y. Haddad, *Feasibility of a minimum bias analysis of* $e^+e^- \to ZH \to q\bar{q} + X$ *at a 250 GeV ILC*, arXiv:1404.3164 [hep-ph].

[5] M. Oreglia, *A Study of the Reactions* $\psi' \to \gamma\gamma\psi$, SLAC-R-0236 (1980) . http://www.slac.stanford.edu/cgi-wrap/getdoc/slac-r-23\6.pdf.

[6] ALEPH, DELPHI, L3, OPAL, LEP Electroweak Collaboration, *Electroweak Measurements in Electron-Positron Collisions at W-Boson-Pair Energies at LEP*, Phys. Rept. **532** (2013) 119, arXiv:1302.3415 [hep-ex].

[7] J. Gao, *Probing light-quark Yukawa couplings via hadronic event shapes at lepton colliders*, JHEP **01** (2018) 038, arXiv:1608.01746 [hep-ph].

[8] LHC Higgs Cross Section Working Group, *LHC HXSWG interim recommendations to explore the coupling structure of a Higgs-like particle*, arXiv:1209.0040 [hep-ph].

[9] LHC Higgs Cross Section Working Group, *Handbook of LHC Higgs Cross Sections: 3. Higgs Properties*, arXiv:1307.1347 [hep-ph].

[10] S. Dawson, A. Gritsan, H. Logan, J. Qian, C. Tully, et al., *Working Group Report: Higgs Boson*, arXiv:1310.8361 [hep-ex].

[11] CMS Collaboration, *Search for the associated production of the Higgs boson with a top-quark pair*, JHEP **1409** (2014) 087, arXiv:1408.1682 [hep-ex].

[12] ATLAS Collaboration, *Search for* $H \to \gamma\gamma$ *produced in association with top quarks and constraints on the Yukawa coupling between the top quark and the Higgs boson using data taken at 7 TeV and 8 TeV with the ATLAS detector*, Phys. Lett. **B740** (2015) 222, arXiv:1409.3122 [hep-ex].

[13] A. Banfi, A. Martin, and V. Sanz, *Probing top-partners in Higgs+jets*, JHEP **1408** (2014) 053, arXiv:1308.4771 [hep-ph].

[14] A. Azatov and A. Paul, *Probing Higgs couplings with high* p_T *Higgs production*, JHEP **1401** (2014) 014, arXiv:1309.5273 [hep-ph].

[15] C. Grojean, E. Salvioni, M. Schlaffer, and A. Weiler, *Very boosted Higgs in gluon fusion*, JHEP **1405** (2014) 022, arXiv:1312.3317 [hep-ph].

[16] M. Buschmann, C. Englert, D. Goncalves, T. Plehn, and M. Spannowsky, *Resolving the Higgs-Gluon Coupling with Jets*, Phys. Rev. **D90** (2014) 013010, arXiv:1405.7651 [hep-ph].

[17] J. Ellis, V. Sanz, and T. You, *Complete Higgs Sector Constraints on Dimension-6 Operators*, JHEP **1407** (2014) 036, arXiv:1404.3667 [hep-ph].

[18] T. Han, Z. Liu, and J. Sayre, *Potential Precision on Higgs Couplings and Total Width at the ILC*, Phys. Rev. **D89** (2014) 113006, arXiv:1311.7155 [hep-ph].

[19] M. Klute, R. Lafaye, T. Plehn, M. Rauch, and D. Zerwas, *Measuring Higgs Couplings at a Linear Collider*, Europhys. Lett. **101** (2013) 51001, arXiv:1301.1322 [hep-ph].

[20] M. E. Peskin, *Estimation of LHC and ILC Capabilities for Precision Higgs Boson Coupling Measurements*, arXiv:1312.4974 [hep-ph].

[21] K. Fujii et al., *Physics Case for the 250 GeV Stage of the International Linear Collider*, arXiv:1710.07621 [hep-ex].

[22] T. Barklow, K. Fujii, S. Jung, R. Karl, J. List, T. Ogawa, M. E. Peskin, and J. Tian, *Improved Formalism for Precision Higgs Coupling Fits*, arXiv:1708.08912 [hep-ph].

[23] ATLAS Collaboration, *Projections for measurements of Higgs boson signal strengths and coupling parameters with the ATLAS detector at a HL-LHC*, ATL-PHYS-PUB-2014-016 (2014) . http://cds.cern.ch/record/1956710.

[24] A. Denner, S. Heinemeyer, I. Puljak, D. Rebuzzi, and M. Spira, *Standard Model Higgs-Boson Branching Ratios with Uncertainties*, Eur. Phys. J. **C71** (2011) 1753, arXiv:1107.5909 [hep-ph].

[25] L. G. Almeida, S. J. Lee, S. Pokorski, and J. D. Wells, *Study of the standard model Higgs boson partial widths and branching fractions*, Phys. Rev. **D89** (2014) 033006, arXiv:1311.6721 [hep-ph].

[26] G. P. Lepage, P. B. Mackenzie, and M. E. Peskin, *Expected Precision of Higgs Boson Partial Widths within the Standard Model*, arXiv:1404.0319 [hep-ph].

[27] C. Bernaciak, T. Plehn, P. Schichtel, and J. Tattersall, *Spying an invisible Higgs boson*, Phys. Rev. **D91** (2015) 035024, arXiv:1411.7699 [hep-ph].

[28] J. Ellis and T. You, *Sensitivities of Prospective Future e+e- Colliders to Decoupled New Physics*, JHEP **03** (2016) 089, arXiv:1510.04561 [hep-ph].

[29] J. Ellis, P. Roloff, V. Sanz, and T. You, *Dimension-6 Operator Analysis of the CLIC Sensitivity to New Physics*, arXiv:1701.04804 [hep-ph].

[30] G. Durieux, C. Grojean, J. Gu, and K. Wang, *The leptonic future of the Higgs*, JHEP **09** (2017) 014, arXiv:1704.02333 [hep-ph].

[31] T. Barklow, K. Fujii, S. Jung, M. E. Peskin, and J. Tian, *Model-Independent Determination of the Triple Higgs Coupling at e^+e^- Colliders*, arXiv:1708.09079 [hep-ph].

[32] S. Di Vita, G. Durieux, C. Grojean, J. Gu, Z. Liu, G. Panico, M. Riembau, and T. Vantalon, *A global view on the Higgs self-coupling at lepton colliders*, JHEP **02** (2018) 178, arXiv:1711.03978 [hep-ph].

[33] W. H. Chiu, S. C. Leung, T. Liu, K.-F. Lyu, and L.-T. Wang, *Probing 6D operators at future e^-e^+ colliders*, JHEP **05** (2018) 081, arXiv:1711.04046 [hep-ph].

[34] M. Beneke, D. Boito, and Y.-M. Wang, *Anomalous Higgs couplings in angular asymmetries of $H \to Z\ell^+\ell^-$ and $e^+e^- \to HZ$*, JHEP **11** (2014) 028, arXiv:1406.1361 [hep-ph].

[35] N. Craig, J. Gu, Z. Liu, and K. Wang, *Beyond Higgs Couplings: Probing the Higgs with Angular Observables at Future e^+ e^- Colliders*, JHEP **03** (2016) 050, arXiv:1512.06877 [hep-ph].

[36] S. M. Barr and A. Zee, *Electric Dipole Moment of the Electron and of the Neutron*, Phys. Rev. Lett. **65** (1990) 21–24. [Erratum: Phys. Rev. Lett.65,2920(1990)].

[37] J. Fan and M. Reece, *Probing Charged Matter Through Higgs Diphoton Decay, Gamma Ray Lines, and EDMs*, JHEP **06** (2013) 004, arXiv:1301.2597 [hep-ph].

[38] ACME Collaboration, J. Baron et al., *Order of Magnitude Smaller Limit on the Electric Dipole Moment of the Electron*, Science **343** (2014) 269–272, arXiv:1310.7534 [physics.atom-ph].

[39] Y. T. Chien, V. Cirigliano, W. Dekens, J. de Vries, and E. Mereghetti, *Direct and indirect constraints on CP-violating Higgs-quark and Higgs-gluon interactions*, JHEP **02** (2016) 011, arXiv:1510.00725 [hep-ph]. [JHEP02,011(2016)].

[40] R. Harnik, A. Martin, T. Okui, R. Primulando, and F. Yu, *Measuring CP violation in $h \to \tau^+\tau^-$ at colliders*, Phys. Rev. **D88** (2013) no. 7, 076009, arXiv:1308.1094 [hep-ph].

[41] K. Hagiwara, S. Ishihara, R. Szalapski, and D. Zeppenfeld, *Low-energy effects of new interactions in the electroweak boson sector*, Phys. Rev. **D48** (1993) 2182–2203.

[42] G. Gounaris et al., *Triple gauge boson couplings*, arXiv:hep-ph/9601233 [hep-ph].
http://alice.cern.ch/format/showfull?sysnb=0215385. [,525(1996)].

[43] L. Bian, J. Shu, and Y. Zhang, *Prospects for Triple Gauge Coupling Measurements at Future Lepton Colliders and the 14 TeV LHC*, JHEP **09** (2015) 206, arXiv:1507.02238 [hep-ph].

[44] A. Falkowski, *Higgs Basis: Proposal for an EFT basis choice for LHC HXSWG*, LHCHXSWG-INT-2015-001 (March, 2015) .
https://cds.cern.ch/record/2001958.

[45] ATLAS Collaboration, *Projections for measurements of Higgs boson cross sections, branching ratios and coupling parameters with the ATLAS detector at a HL-LHC*, ATL-PHYS-PUB-2013-014 (2013) . https://cds.cern.ch/record/1611186.

[46] ATLAS Collaboration, *HL-LHC projections for signal and background yield measurements of the $H \to \gamma\gamma$ when the Higgs boson is produced in association with t quarks, W or Z bosons*, ATL-PHYS-PUB-2014-012 (2014) . https://cds.cern.ch/record/1741011.

[47] ATLAS Collaboration, *Update of the prospects for the $H \to Z\gamma$ search at the High-Luminosity LHC*, ATL-PHYS-PUB-2014-006 (2014) . https://cds.cern.ch/record/1703276.

[48] ATLAS Collaboration, *Prospects for the study of the Higgs boson in the VH(bb) channel at HL-LHC*, ATL-PHYS-PUB-2014-011 (2014) . https://cds.cern.ch/record/1740962.

[49] ATLAS Collaboration, *Studies of the VBF $H \to \tau_l\tau_{had}$ analysis at High Luminosity LHC conditions*, ATL-PHYS-PUB-2014-018 (2014) . https://cds.cern.ch/record/1956732.

[50] A. Falkowski, M. Gonzalez-Alonso, A. Greljo, and D. Marzocca, *Global constraints on anomalous triple gauge couplings in effective field theory approach*, Phys. Rev. Lett. **116** (2016) no. 1, 011801, arXiv:1508.00581 [hep-ph].

[51] A. Butter, O. J. P. Éboli, J. Gonzalez-Fraile, M. C. Gonzalez-Garcia, T. Plehn, and M. Rauch, *The Gauge-Higgs Legacy of the LHC Run I*, JHEP **07** (2016) 152, arXiv:1604.03105 [hep-ph].

[52] R. Contino, A. Falkowski, F. Goertz, C. Grojean, and F. Riva, *On the Validity of the Effective Field Theory Approach to SM Precision Tests*, JHEP **07** (2016) 144, arXiv:1604.06444 [hep-ph].

[53] A. Falkowski, M. Gonzalez-Alonso, A. Greljo, D. Marzocca, and M. Son, *Anomalous Triple Gauge Couplings in the Effective Field Theory Approach at the LHC*, JHEP **02** (2017) 115, arXiv:1609.06312 [hep-ph].

[54] Z. Zhang, *Time to Go Beyond Triple-Gauge-Boson-Coupling Interpretation of W Pair Production*, Phys. Rev. Lett. **118** (2017) no. 1, 011803, arXiv:1610.01618 [hep-ph].

[55] ATLAS Collaboration, *Search for the Standard Model Higgs and Z Boson decays to $J/\psi\,\gamma$: HL-LHC projections*, ATL-PHYS-PUB-2015-043 (2015) . http://cds.cern.ch/record/2054550.

[56] G. T. Bodwin, F. Petriello, S. Stoynev, and M. Velasco, *Higgs boson decays to quarkonia and the $H\bar{c}c$ coupling*, Phys. Rev. **D88** (2013) no. 5, 053003, arXiv:1306.5770 [hep-ph].

[57] G. Perez, Y. Soreq, E. Stamou, and K. Tobioka, *Constraining the charm Yukawa and Higgs-quark coupling universality*, Phys. Rev. **D92** (2015) no. 3, 033016, arXiv:1503.00290 [hep-ph].

[58] I. Brivio, F. Goertz, and G. Isidori, *Probing the Charm Quark Yukawa Coupling in Higgs+Charm Production*, Phys. Rev. Lett. **115** (2015) no. 21, 211801, arXiv:1507.02916 [hep-ph].

[59] F. Bishara, U. Haisch, P. F. Monni, and E. Re, *Constraining Light-Quark Yukawa Couplings from Higgs Distributions*, arXiv:1606.09253 [hep-ph].

[60] L. M. Carpenter, T. Han, K. Hendricks, Z. Qian, and N. Zhou, *Higgs Boson Decay to Light Jets at the LHC*, Phys. Rev. **D95** (2017) no. 5, 053003, arXiv:1611.05463 [hep-ph].

[61] ATLAS Collaboration Collaboration, *Study of the double Higgs production channel $H(\to b\bar{b})H(\to \gamma\gamma)$ with the ATLAS experiment at the HL-LHC*, ATL-PHYS-PUB-2017-001, CERN, Geneva, Jan, 2017. https://cds.cern.ch/record/2243387.

[62] R. Contino et al., *Physics at a 100 TeV pp collider: Higgs and EW symmetry breaking studies*, CERN Yellow Report (2017) no. 3, 255–440, arXiv:1606.09408 [hep-ph].

[63] M. McCullough, *An Indirect Model-Dependent Probe of the Higgs Self-Coupling*, Phys. Rev. **D90** (2014) 015001, arXiv:1312.3322 [hep-ph].

[64] S. Di Vita, C. Grojean, G. Panico, M. Riembau, and T. Vantalon, *A global view on the Higgs self-coupling*, JHEP **09** (2017) 069, arXiv:1704.01953 [hep-ph].

[65] A. Azatov, R. Contino, G. Panico, and M. Son, *Effective field theory analysis of double Higgs boson production via gluon fusion*, Phys. Rev. **D92** (2015) no. 3, 035001, arXiv:1502.00539 [hep-ph].

[66] J. A. Aguilar-Saavedra, *A Minimal set of top anomalous couplings*, Nucl. Phys. **B812** (2009) 181–204, arXiv:0811.3842 [hep-ph].

[67] J. A. Aguilar-Saavedra, *A Minimal set of top-Higgs anomalous couplings*, Nucl. Phys. **B821** (2009) 215–227, arXiv:0904.2387 [hep-ph].

[68] Z. Liu, I. Low, and L.-T. Wang, *Higgs-Top Interactions at Future Circular e^+e^- Colliders*, arXiv:2018.nnnn.

[69] G. Li, H.-R. Wang, and S.-h. Zhu, *Probing CP-violating $h\bar{t}t$ coupling in $e^+e^- \to h\gamma$*, arXiv:1506.06453 [hep-ph].

[70] E. Vryonidou and C. Zhang, *Dimension-six electroweak top-loop effects in Higgs production and decay*, arXiv:1804.09766 [hep-ph].

[71] G. Durieux, *Precision constraints on the top-quark effective field theory at future lepton colliders*, PoS **DIS2017** (2018) 088, arXiv:1708.09849 [hep-ph].

[72] D. Curtin, R. Essig, S. Gori, P. Jaiswal, A. Katz, et al., *Exotic decays of the 125 GeV Higgs boson*, Phys.Rev. **D90** (2014) 075004, arXiv:1312.4992 [hep-ph].

[73] LHC Higgs Cross Section Working Group Collaboration, D. de Florian et al., *Handbook of LHC Higgs Cross Sections: 4. Deciphering the Nature of the Higgs Sector*, arXiv:1610.07922 [hep-ph].

[74] Z. Liu, L.-T. Wang, and H. Zhang, *Exotic decays of the 125 GeV Higgs boson at future e^+e^- lepton colliders*, arXiv:1612.09284 [hep-ph].

[75] Y. Gao, A. V. Gritsan, Z. Guo, K. Melnikov, M. Schulze, and N. V. Tran, *Spin determination of single-produced resonances at hadron colliders*, Phys. Rev. **D81** (2010) 075022, arXiv:1001.3396 [hep-ph].

[76] S. Bolognesi, Y. Gao, A. V. Gritsan, K. Melnikov, M. Schulze, N. V. Tran, and A. Whitbeck, *On the spin and parity of a single-produced resonance at the LHC*, Phys. Rev. **D86** (2012) 095031, arXiv:1208.4018 [hep-ph].

[77] I. Anderson et al., *Constraining anomalous HVV interactions at proton and lepton colliders*, Phys. Rev. **D89** (2014) no. 3, 035007, arXiv:1309.4819 [hep-ph].

9.2 W, Z measurements at the CEPC

With high production cross sections and large integrated luminosity, the CEPC will reach a new level of precision for measurements of the properties of the W and Z bosons. Precise measurements of the W and Z boson masses, widths, and couplings are critical to test the consistency of the SM [1]. In addition, many BSM models predict new couplings of the W and Z bosons to other elementary particles. Precise electroweak measurements performed at the CEPC could discover deviations from the SM predictions and reveal the existence of new particles that are beyond the reach of current experiments.

Significant improvements are expected from the CEPC measurements. Table 9.10 lists the expected precision from CEPC compared to achieved precisions from the LEP experiments for various measurements. Details about the estimation of these uncertainties are described in this section.

Table 9.10: The expected precision in a selected set of EW precision measurements in CEPC and the comparison with the precision from LEP experiments. The CEPC accelerator running mode and total integrated luminosity expected for each measurement are also listed. Depending on detector solenoid field during Z pole operation, the integrated luminosity varied from $8ab^{-1}$ to $16ab^{-1}$.

Observable	LEP precision	CEPC precision	CEPC runs	$\int \mathcal{L}$ needed in CEPC
m_Z	2 MeV	0.5 MeV	Z threshold scan	$8ab^{-1} - 16\text{ab}^{-1}$
$A_{FB}^{0,b}$	1.7%	0.1%	Z threshold scan	$8ab^{-1} - 16\text{ab}^{-1}$
$A_{FB}^{0,\mu}$	7.7%	0.3%	Z threshold scan	$8ab^{-1} - 16\text{ab}^{-1}$
$A_{FB}^{0,e}$	17%	0.5%	Z threshold scan	$8ab^{-1} - 16\text{ab}^{-1}$
$\sin^2\theta_W^{\text{eff}}$	0.07%	0.001%	Z threshold scan	$8ab^{-1} - 16\text{ab}^{-1}$
R_b	0.3%	0.02%	Z pole	$8ab^{-1} - 16\text{ab}^{-1}$
R_μ	0.2%	0.01%	Z pole	$8ab^{-1} - 16\text{ab}^{-1}$
N_ν	1.7%	0.05%	ZH runs	5.6ab^{-1}
m_W	33 MeV	2-3 MeV	ZH runs	5.6ab^{-1}
m_W	33 MeV	1 MeV	WWthreshold	2.6ab^{-1}

9.2.1 Z pole measurements

The CEPC offers the possibility of dedicated low-energy runs at the Z pole for at least two years with a high instant luminosity ($1.6 - 3.2 \times 10^{35} cm^{-2} s{-}1$). The expected integrated luminosity for CEPC Z pole runs is more than 8 ab^{-1}, and it is expected to produce about 10^{12} Z bosons (Tera-Z).

These runs allow high precision electroweak measurements of the Z boson decay partial widths, e.g. the parameters $R_b = \Gamma_{Z\to b\bar{b}}/\Gamma_{\text{had}}$ and $R_\ell = \Gamma_{\text{had}}/\Gamma_{Z\to \ell\bar{\ell}}$. (Notice that R_ℓ is defined as the ratio to any *one* charged lepton flavor, assuming lepton universality, not the ratio to the sum of all lepton flavors.) It would also perform high precision measurements of the forward-backward charge asymmetry (A_{FB}), the effective weak mix-

ing angle ($\sin^2\theta_W^{\rm eff}$), number of light neutrino species (N_ν), and the mass of the Z boson (M_Z). It is also possible to perform some measurements with the Z boson without these dedicated low-energy runs near or at the Z pole. For example, the direct measurement of the number of light neutrino species can be performed in ZH runs at 240 GeV.

9.2.1.1 R_b

The width of the Z boson to each of its decay channels is proportional to the square of the fundamental Z-fermion couplings. The partial width R_b is sensitive to electroweak radiative corrections from new physics particles. For example, the existence of the scalar tops or charginos in supersymmetry could lead to a visible change of R_b from the SM prediction.

Precise measurements of R_b have been made by LEP collaborations [2–6] and by the SLD collaboration [7] at SLAC using hadronic Z events.

Decays of b-hadrons were tagged using tracks with large impact parameters and/or reconstructed secondary vertices, complemented by event shape variables. The combination of LEP and SLD measurements yields a value of 0.21629 ± 0.00066 for R_b. The relative statistical uncertainty of R_b is above 0.2%, and systematic uncertainty is about 0.2%.

A precision of 0.05% can be achieved for the measurement of R_b at CEPC, and it will improve the current precision in experimental measurement by one order of magnitude. The statistical uncertainty improves by two order of magnitude and the systematic uncertainties will also reduce. The main systematic uncertainty is the uncertainty due to hemisphere tag correlations in $Z \to b\bar{b}$ events (0.05%).The uncertainty due to hemisphere tag correlations will be reduced to a level of 0.05% due to the expected improvement in the b-tagging performance of the CEPC detector. The improvement of b-tagging efficiency is important to reduce this corrections, and this correlation becomes irrelevant in the limit of 100% b-tagging efficiency. Due to that fact that a next-generation vertex detector will be used in the CEPC detector, the b-tag efficiency is expected to be around 70% with a b-jet purity of 95% as shown in Fig. **??**, which is about 15%-20% higher than the efficiency in than previous measurements. The uncertainty due to hemisphere tag correlations can be reduce to 0.05% level, which is a factor of four lower than previous measurements.

9.2.1.2 The partial decay width of $Z \to \mu^+\mu^-$

The $\mu^+\mu^-$ channel provides the cleanest leptonic final state. Combining the measurements from all four LEP experiments [8–11], the overall uncertainty of R_μ is 0.2%. The statistical uncertainty of R_μ is 0.15%.

A precision of 0.01% can be achieved at the CEPC. The main systematic is the uncertainty of photon energy scale in the $Z \to \mu^+\mu^-\gamma$ process. About 2% of the $Z \to \mu^+\mu^-$ sample are classified as $Z \to \mu^+\mu^-\gamma$ events with a photon detected in ECAL. For this class of events, the most critical cut is that on the difference between the expected and measured photon energy ($|E_\gamma^{expected} - E_\gamma^{expected}| < 5\sigma_\gamma$), which is very efficient in removing the $Z \to \tau\tau$ background. The

The energy resolution in the EM calorimeter of the CEPC detector is expected to be 16%/sqrt(E), which is significantly better than the resolution in previous measurements. Therefore, the uncertainty due to photon energy scale and resolution in $Z \to \mu^+\mu^-\gamma$ process can be reduced to 0.01%. The main challenge in this measurement is to reduce the systematics due to QED ISR events. More detailed studies of radiative events in Z

threshold scan runs are expected. Benefitting from high statistics in Z threshold scan runs, the source of uncertainty can be reduced to a level of 0.03%.

9.2.1.3 The forward-backward asymmetry A_{FB}^{b} at the Z pole

The measurement of the forward-backward asymmetry in $e^+e^- \to b\bar{b}$ events at the Z pole, $A_{FB}^{b,0}$, gives an important test of the Standard Model. $A_{FB}^{b,0}$ offers the most precise determination of the weak mixing angle. The measurements have been made at SLD and LEP experiments [12–16].

$Z \to b\bar{b}$ events were identified by tagging two b jets. Each event was divided into forward and backward categories by the plane perpendicular to the thrust axis which contains the interaction point. The combination of the LEP and SLD measurements gives a measured value of $A_{FB}^{b,0} = 0.1000 \pm 0.0017$. The statistical uncertainty is 1.2% and the main systematic uncertainties come from hemisphere tag correlations for b events (1.2%), tracking resolution and vertex detector alignment (0.8%), charm physics modeling (0.5%), and QCD and thrust axis correction (0.7%).

A precision of 10^{-4} can be achieved for the measurement of $A_{FB}^{b,0}$ at the CEPC, improving the current precision by more than a factor of 10. The expected statistical uncertainty is at a level of 0.05%. The uncertainty due to hemisphere tag correlations for b events can be reduced to 0.1% due to high b-tagging efficiency. The uncertainty due to charm physics modeling can be reduced to 0.05% by choosing a tighter b-tagging working point. The uncertainty due to tracking resolution and vertex detector alignment can be reduced to 0.05%. The expected tracking momentum resolution in the CEPC detector is $\sigma/p_T = 2 \times 10^{-4} \times p_T + 0.005$, which is 10 times better than the resolutions of the LEP detectors. The uncertainty due to QCD and thrust axis correction can be reduced to 0.1% due to at least 10 times better granularity in the CEPC calorimeters. Overall, the expected systematics at CEPC measurement can be reduced to a level of 0.15%.

9.2.1.4 The prospects for the effective weak mixing angle measurement

The weak mixing angle $\sin^2\theta_W^{\rm eff}$ is a very important parameter in the electroweak theory of the SM. It is the only free parameter that fixes the relative couplings of all fermions to the Z. It describes the rotation of the original W^0 and B^0 vector boson states into the observed γ and Z bosons as a result of spontaneous symmetry breaking. The weak mixing angle is very sensitive to electroweak radiative corrections, and it can be used perform a precise test of the SM theory. Furthermore, if there is any new heavy gauge boson Z', the weak mixing angle is expected to deviate from the SM prediction due to the contribution from physics in loop corrections. Therefore $\sin^2\theta_W^{\rm eff}$ is very sensitive to new physics as well.

The centre-of-mass energy dependence of the forward-backward asymmetry arises from the interference of the Z boson with the virtual photon and thus depends on $\sin^2\theta_W^{\rm eff}$. In other words, the effective weak mixing angle can be extracted by studying the $\sqrt{s}$ dependence of the forward-backward asymmetry.

The effective weak mixing angle measurement has been performed in LEP using $Z \to b\bar{b}$ events and $Z \to \ell^+\ell^-$ events. The forward-backward asymmetry A_{FB} in one Z-pole dataset and two off Z-pole datasets ($\sqrt{s}$ = 89.4 GeV , $\sqrt{s}$ = 93.0 GeV) are used to extract $\sin^2\theta_W^{\rm eff}$. The current experimental result is $\sin^2\theta_W^{\rm eff} = 0.23153 \pm 0.00016$. $Z \to b\bar{b}$ events were identified by tagging two b jets. The main uncertainty includes uncertainty on

the A_{FB}^{b} measurement as described in Sec. 9.2.1.3. and the statistical uncertainty in off Z-pole datasets.

Both Z-pole and off Z-pole runs are needed to perform the effective weak mixing angle measurement at the CEPC. The Z off-peak runs are expensive, therefore we need to optimize the integrated luminosity for off-peak runs. In order to improve the precision of $\sin^2\theta_W^{\rm eff}$ by a factor of 3, the required CEPC integrated luminosity for Z-pole runs are $8-16$ ab^{-1} and at least $2-4$ ab^{-1} integrated luminosity is needed for off Z-pole runs.The expected precision of effective weak mixing angle measurement in CEPC using $Z \to b\bar{b}$ events is expected to be 0.02%.

9.2.1.5 Z mass measurement

The mass m_Z is a fundamental parameter in the SM and was determined with an overall uncertainty of 2 MeV by four LEP experiments. The mass scan around the Z peak was performed from 88 GeV to 94 GeV. The Z mass was measured by a combined fit to the hadronic and leptonic cross sections in the on-peak and off-peak datasets. Most of the m_Z information is extracted from the off-peak runs. Taking the OPAL measurement as one example, six off-peak datasets were used to complete the m_Z scan. The main uncertainty of m_Z includes the statistical uncertainty (1 MeV/c^2), and the LEP beam energy (about 1 MeV/c^2).

A precision of 0.5 MeV can be achieved in CEPC measurement. The mass scan around the Z peak is the key for improving m_Z measurements.

The LEP measurement was limited by the statistics in their off-peak runs, therefore the luminosity in Z off-peak runs plays an important role in the m_Z measurement. We propose six off-peak runs and one on-peak run in CEPC Z mass scan, as listed in Table **??**. The expected m_Z uncertainty in CEPC due to statistics is about 0.1 MeV.

Another important systematic is beam momentum scale uncertainty. The beam momentum uncertainty in the CEPC accelerator is expected to be accurate to the 10 ppm level, which is about five times better than LEP. The uncertainty on m_Z due to the uncertainty on the beam energy can be reduced to less than 0.5 MeV.

Hadronic decay channels of the Z events are also expected to be used to measure m_Z since the leptonic decay channels suffer from low statistics. The uncertainty due to jet energy scale and resolution results in about 0.1 MeV in the m_Z measurement.

9.2.1.6 Neutrino species counting

Two different methods have been used to determine the number of neutrino species (N_ν) at LEP.

The first method is an indirect method using the analysis of the Z lineshape, and it uses the data collected by the Z threshold scan runs. The second method is a direct measurement, which is based on the measurement of the cross section for the radiative process $e^+e^- \to \nu\nu\gamma$. The second method at CEPC is supposed to use the ZH runs.

These two methods use different theoretical inputs from the Standard Model and also use completely different datasets, therefore they are independent and complementary. The sensitivity to new physics will be different for these two methods. In the direct method, one can measure N_ν as a function of $sqrts$. This is very sensitive to new physics at high energy scales. Possible contributions include WIMP dark matter particles, and other weakly coupled particles such as exotic neutrinos, gravitinos, or KK gravitons in theories

with large extra dimensions. Thus, when we refer to the number of neutrino species, we actually include any number of possible invisible particles other than neutrinos.

Indirect method from Z line shape The indirect method assumed all contributions from invisible channels are coming from the $Z \to \nu\bar{\nu}$. This method used the analysis of Z line-shape, subtracting the visible partial widths of the hadrons ($\Gamma_{\rm had}$), and the partial widths of the leptons (Γ_ℓ) from the total width Γ_Z. The invisible width $\Gamma_{\rm inv}$ can be written as:

$$\Gamma_{\rm inv} = N_\nu \Gamma_\nu = \Gamma_Z - \Gamma_{\rm had} - 3\Gamma_\ell. \tag{9.16}$$

We take as our definition of the number of neutrinos $N_\nu = \Gamma_{\rm inv}/\Gamma_\nu$, i.e. the ratio of the invisible width to the Standard Model expectation for the partial width to a single neutrino species.

Using the input from SM model, we can rewrite equation 9.16 as the following:

$$N_\nu = \frac{\Gamma_\ell}{\Gamma_\nu}\left(\sqrt{\frac{12\pi R_\ell}{M_Z^2 \sigma^0_{\rm had}}} - R_\ell - 3\right). \tag{9.17}$$

As shown in equation 9.17, the precision of N_ν depends on the the lepton partial width R_ℓ measurement, the Z mass measurement, and the hadronic cross section of the Z boson on its mass peak ($\sigma^0_{\rm had}$). The precision of $\sigma^0_{\rm had}$ gives the largest impact to N_ν measurement, and it is very sensitive to the precision of the luminosity. Therefore the precise luminosity measurement is the key to determine N_ν.

Precise measurements of N_ν have been made by LEP collaborations, and they obtained a precision of 0.27% using this indirect method. The main systematics of the N_ν measurement is coming from the uncertainty of luminosity (0.14%) and the theory uncertainty in the predicted cross section of the small angle Bhabha process (0.11%).

The precision of 0.1% in N_ν measurement with the indirect method can be achieved in CEPC measurement, which improves the current precision by a factor of three. Benefitting from the recent development of luminosity detector technology, the uncertainty due to luminosity can be reduced to 0.05%. The uncertainty from the small angle Bhabha process can be reduced to 0.05% due to recent progress in studying this process.

Direct method using $e^+e^- \to \nu\bar{\nu}\gamma$ events The most precise direct N_ν measurements at LEP were carried out by the L3 collaboration and Delphi collaboration. By combining the direct measurements at LEP, the current experimental result is $N_\nu = 2.92 \pm 0.05$. The statistical uncertainty of N_ν in the previous measurement is 1.7%. The main systematic uncertainty from the L3 measurement includes the uncertainty in single photon trigger efficiency (0.6%), and photon identification efficiency (0.3%), and the uncertainty in identifying the converted photons (0.5%).

A precision of 0.2% can be achieved for the direct measurement of N_ν at CEPC, and it will improve the current precision by a factor of 10. Due to the excellent performance of the CEPC inner tracker, the uncertainty due to converted photons' selection efficiency is expected to be negligible. The granularity of the CEPC EM calorimeter is expected to be 10 to 100 times better than the detectors at LEP. Therefore photons can be identified with high purity with loose EM shower shape based selection. The uncertainty of photon efficiency can be reduced to less than 0.05%.

9.2.2 Measurement of the W boson mass

In e^+e^- collisions, W bosons are mainly produced in pairs, through the reaction $e^+e^- \to W^+W^-$. At threshold, $\sqrt{s} \sim 2m_W$, the cross section of this process is very sensitive to m_W, providing a natural method for the measurement of this parameter. At centre-of-mass energies above the W^+W^- production threshold, m_W can be determined from the peak of the invariant mass distribution of its decay products. Both methods are very complementary : while the former requires an accurate theoretical prediction of the W^+W^- production cross section as a function of m_W and a precise determination of the collider luminosity, the latter mostly relies on a good resolution in the reconstruction of the hadronic invariant mass, and a precise control of the detector calibration.

Both methods have been used at LEP. With only about 40 pb^{-1} collected by the four LEP experiments at $\sqrt{s} \sim 161.3$ GeV and given the low cross section at threshold, the former is limited by a significant statistical uncertainty of about 200 MeV. The final state reconstruction method exploited the full LEP2 dataset, about 2.6 fb^{-1} collected between $\sqrt{s} \sim 161.3$ GeV and 206 GeV, and achieved a total uncertainty of 33 MeV. While this measurement used both the $W^+W^- \to \ell\nu qq$ and $W^+W^- \to qqqq$ channels, the fully hadronic channel is limited by uncertainties in the modeling of hadronization and interactions between the decaying W bosons, and the semi-leptonic final state dominates the precision of the final result.

Accounting for results from the CDF and D0 experiments at the TeVatron, and from ATLAS at the LHC, the present world-average value of m_W has an uncertainty estimated between 12 and 13 MeV. The uncertainty is expected to fall below 10 MeV when including final LHC measurement results. A natural goal for CEPC is thus to reach a precision well below 5 MeV, making optimal use of W^+W^- cross section data around $\sqrt{s} \sim 161$ GeV, and of the final state invariant mass distributions at $\sqrt{s} \sim 240$ GeV. The achievable precision of both methods is described below.

Determination of m_W from the W^+W^- production cross section

Using the threshold scan method, a precision of 1.0 MeV can be achieved for the measurement at the CEPC. We assume that the CEPC can provide a 4-point threshold scan with 2.6 ab^{-1} integrated luminosity. The $\sqrt{s}$ values of threshold scan runs are assumed to be 157.5, 161.5, 162.5, and 172.0 GeV. The proposed run plan is shown in Table 9.11. The list of systematic uncertainties is summarized in Table 9.12.

Table 9.11: Using threshold scan measurement method in dedicated WW threshold scan runs, The proposed 4 $e^+e^- \to W^+W^-$ threshold scan runs and their integrated luminosity.

Beam Energy (GeV)	Lumiosity (ab^{-1})	Cross section(pb)	Number of WW pairs (million)
157.5	0.5	1.3	0.6
161.5	0.2	3.9	0.8
162.5	1.3	5.0	6.5
172.0	0.5	12.2	6.1

Table 9.12: Using threshold scan measurement method in dedicated WW threshold scan runs, the expected precision in m_W measurement in CEPC detectors and the comparison with LEP experiments.

ΔM_W(MeV)	LEP	CEPC
$\sqrt{s}$(GeV)	161	240
$\int \mathcal{L}$(fb^{-1})	3	2600
beam energy scale	13	0.4
luminosity,background,signal acceptance	10	0.5
statistics	20	0.8
total	36	1.0

Determination of m_W by kinematic reconstruction

According to LEP experience, the fully hadronic final state is limited by systematic uncertainties that are difficult to control using data. The present section therefore concentrates on the semi-leptonic final states, where one W boson decays to an electron or a muon, while the other decays hadronically. An estimate of the m_W measurement potential is presented based on $WW \to \ell\nu qq$ events ($\ell = e, \mu$), and the potential of hadronic Z boson decays to calibrate the measurement of the hadronic invariant mass is evaluated.

The W^+W^- cross section at $\sqrt{s} = 240$ GeV is about 17 pb. For an integrated luminosity of 5.6 ab^{-1}, this corresponds to a sample of about 95×10^6 W boson pairs, and 28×10^6 $WW \to \ell\nu qq$ events. For ZZ production, the cross section is about 1 pb, yielding about 5.6×10^6 Z boson pairs, and 0.53×10^6 $ZZ \to \ell\ell qq$ events. While the Z boson mass is more precisely known than m_W and the $Z \to qq$ resonance provides a useful check of the detector calibration, the sample is small compared to the $W \to qq$ one, and the presence of heavy quarks in Z boson decays has to be accounted for when deriving constraints on the hadronic response in W events.

W^+W^- event selection criteria will require the presence of one reconstructed electron or muon with energy greater than 10 GeV, and missing transverse momentum greater than 10 GeV. The invariant mass of all reconstructed final state particles should exceed 50% of the centre-of-mass energy; the hadronic system, $i.e.$ the set of all particles excluding the selected lepton, is clustered into two jets and its invariant mass distribution is used to probe the W boson mass. A b-tag veto can be applied to enrich the selected samples in light-quark decays, and reduce the systematic differences between the W and Z boson samples. In the $\mu\nu qq$ channel, the efficiency of these criteria is 71.3%, as shown in Table 9.13. Corresponding selection efficiciencies for $ZZ \to \mu\mu qq$ events are shown in Table 9.14. The corresponding hadronic invariant mass distributions are shown in Figure 9.18. After these selections, backgrounds are expected to be small and play a negligible role in the measurement.

Given the large expected statistics, the availability of the $e\nu qq$ channel and the good resolution in the invariant mass distribution, the statistical sensitivity of the m_W measurement is better than 1 MeV. Using the $ZZ \to \ell\ell qq$ sample alone, the detector calibration can be checked to about 6 MeV. Further calibration samples can be extracted from ra-

Table 9.13: Efficiency of the event selection criteria in the $WW \to \mu\nu qq$ channel.

Selection	Efficiency (%)	Nb. of events
$E_\mu > 10$ GeV, $\lvert\cos(\theta_\mu)\rvert < 0.995$	85.4	11.9×10^6
$p_{\mathrm{T}}^{\mathrm{miss}} > 10$ GeV	82.0	11.5×10^6
$m_{\mathrm{vis}} > 0.5 \times \sqrt{s}$	75.6	10.6×10^6
b-tag score < 0.5	71.3	10.0×10^6

Table 9.14: Efficiency of the event selection criteria in the $ZZ \to \mu\mu qq$ channel.

Selection	Efficiency (%)	Nb. of events
$E_\mu > 10$ GeV, $\lvert\cos(\theta_\mu)\rvert < 0.995$		
$m_{\mathrm{vis}} > 0.8 \times \sqrt{s}$		
b-tag score < 0.5		

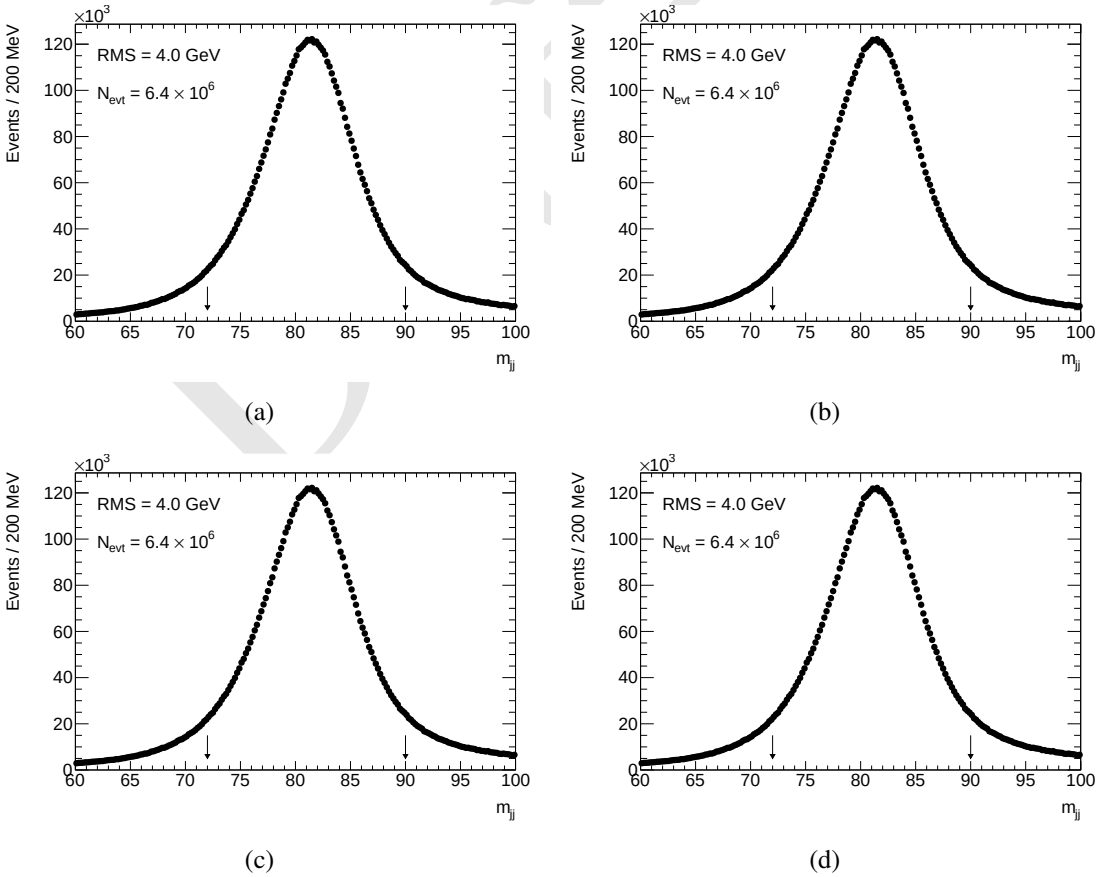

Figure 9.18: Dijet invariant mass distributions for $WW \to \mu\nu qq$ events, without (a) and with (b) a b-jet veto cut, and for $ZZ \to \mu\mu qq$ events, without (c) and with (d) a b-jet veto cut. The numbers of events and RMS of the distributions are quoted for the interval indicated by the arrows.

diative return events ($e^+e^- \to Z\gamma$). In addition, short periodic runs at $\sqrt{s} = 91.2$ GeV will be required for general detector alignment, monitoring and calibrations; these runs will provide copious samples of hadronic Z boson decays that will further constrain the hadronic calibration. Combining all information, the statistical precision of the calibration samples will match that of the W boson decays.

The statistical sensitivity can be further enhanced using kinematics fits, constraining the reconstructed lepton and jet momenta to match the known center of mass energy ($\Sigma_i E_i = \sqrt{s}$) and total event momentum ($\Sigma_i \vec{p}_i = \vec{0}$). This method was routinely used at LEP, gaining a factor of about 3 in the statistical precision, at the expense of an explicit dependence of the measurement on the beam energy. Given the expected statistical precision at CEPC, this refinement seems unnecessary here. In these conditions, the beam energy calibration, and initial state radiation are expected to contribute less than 1 MeV to the measurement uncertainty. Further significant sources of systematic uncertainty include the lepton momentum scale, which can be reduced using Z boson decays as discussed above, and the modelling of hadronization. The latter can be strongly reduced using measurements of rates and distributions of identified particles, in both Z and W boson decays.

The primary sources of uncertainty are summarized in Table 9.15, comparing LEP and CEPC. A total uncertainty at the level of 3 MeV seems reachable.

Table 9.15: Dominat sources of systematic uncertainty in the measurement of m_W using direct reconstruction, as achieved at LEP, and expected at CEPC.

Collider	LEP	CEPC
$\sqrt{s}$ (GeV)	180–203	240
$\int \mathcal{L}$	2.6 fb^{-1}	5.6 ab^{-1}
Channels	$\ell\nu qq, qqqq$	$\ell\nu qq$
Sources of uncertainty (MeV)		
Statistics	25	1.0
Beam energy	9	1.0
Hadronization	13	1.5
Radiative corrections	8	1.0
Detector effects	10	1.5
Total	33	3.0

References

[1] J. Erler, S. Heinemeyer, W. Hollik, G. Weiglein, and P. Zerwas, *Physics impact of GigaZ*, Phys.Lett. **B486** (2000) 125–133, arXiv:hep-ph/0005024 [hep-ph].

[2] ALEPH Collaboration, DELPHI Collaboration, L3 Collaboration, OPAL Collaboration, LEP Electroweak Working Group Collaboration, J. Alcaraz et al., *A Combination of preliminary electroweak measurements and constraints on the standard model*, arXiv:hep-ex/0612034 [hep-ex].

[3] L3 Collaboration, M. Acciarri et al., *Measurement of R(b) and Br($b \to$ lepton neutrino X) at LEP using double tag methods*, Eur. Phys. J. **C13** (2000) 47–61, arXiv:hep-ex/9909045 [hep-ex].

[4] OPAL Collaboration, G. Abbiendi et al., *A Measurement of R(b) using a double tagging method*, Eur. Phys. J. **C8** (1999) 217–239, arXiv:hep-ex/9810002 [hep-ex].

[5] DELPHI Collaboration Collaboration, P. Abreu et al., *A Precise measurement of the partial decay width ratio* $R_b^0 = \Gamma(b\bar{b})/\Gamma(\mathrm{had})$, Eur.Phys.J. **C10** (1999) 415–442.

[6] ALEPH Collaboration, R. Barate et al., *A Measurement of R(b) using mutually exclusive tags*, Phys. Lett. **B401** (1997) 163–175.

[7] SLD Collaboration Collaboration, K. Abe et al., *Measurement of the branching ratio of the Z0 into heavy quarks*, Phys.Rev. **D71** (2005) 112004, arXiv:hep-ex/0503005 [hep-ex].

[8] OPAL Collaboration, G. Abbiendi et al., *Precise determination of the Z resonance parameters at LEP: 'Zedometry'*, Eur. Phys. J. **C19** (2001) 587–651, arXiv:hep-ex/0012018 [hep-ex].

[9] DELPHI Collaboration, P. Abreu et al., *Cross-sections and leptonic forward backward asymmetries from the Z0 running of LEP*, Eur. Phys. J. **C16** (2000) 371–405.

[10] L3 Collaboration, M. Acciarri et al., *Measurements of cross-sections and forward backward asymmetries at the Z resonance and determination of electroweak parameters*, Eur. Phys. J. **C16** (2000) 1–40, arXiv:hep-ex/0002046 [hep-ex].

[11] ALEPH Collaboration, R. Barate et al., *Measurement of the Z resonance parameters at LEP*, Eur. Phys. J. **C14** (2000) 1–50.

[12] SLD Collaboration, K. Abe et al., *Direct measurements of A(b) and A(c) using vertex/kaon charge tags at SLD*, Phys. Rev. Lett. **94** (2005) 091801, arXiv:hep-ex/0410042 [hep-ex].

[13] ALEPH Collaboration Collaboration, A. Heister et al., *Measurement of A^b(FB) using inclusive b hadron decays*, Eur.Phys.J. **C22** (2001) 201–215, arXiv:hep-ex/0107033 [hep-ex].

[14] OPAL Collaboration Collaboration, G. Abbiendi et al., *Measurement of the b quark forward backward asymmetry around the Z0 peak using an inclusive tag*, Phys.Lett. **B546** (2002) 29–47, arXiv:hep-ex/0209076 [hep-ex].

[15] DELPHI Collaboration Collaboration, J. Abdallah et al., *Determination of A^b(FB) at the Z pole using inclusive charge reconstruction and lifetime tagging*, Eur.Phys.J. **C40** (2005) 1–25, arXiv:hep-ex/0412004 [hep-ex].

[16] L3 Collaboration Collaboration, M. Acciarri et al., *Measurement of the $e^+e^- \to Z \to b\bar{b}$ forward–backward asymmetry and the B0 anti-B0 mixing parameter using prompt leptons*, Phys.Lett. **B448** (1999) 152–162.

CHAPTER 10

FUTRUE PLANS AND R&D PROSPECTS

10.1 Tracking

10.1.1 Vertex

Enhancements of the TowerJazz 0.18 μm process or Lapis 0.2 μm process are possible by migrating to a smaller production line, 0.13 μm for example, or combining with a micro-bump 3D integration process. The latter is able to attach a second layer of pixel circuit on top of the existing layer of the sensing diode and front-end circuit. The upper tier can be fully digital part that implements data-driven readout architecture, while the lower tier can be HR CMOS or SOI pixel matrix. A promising result has been demonstrated by the successful formation of 2.5 μm Au cone bump with NpD (Nano-particle deposition) technique [**?**]. However, the throughput needs further improvement and the thinning of sensors has to be compatible with micro-bump 3D integration.

The TowerJazz process is expected to be sufficiently radiation hard for the expected TID. An N-type plain implant has recently been added to improve the charge collection efficiency [**?**], which therefore will benefit the non-ionization radiation damage. In terms of SOI process, the weak point is the BOX layer of $\mathrm{SiO_2}$. Although the TID tolerance of the SOI process has been improved dramatically by the introduction of Double-SOI and the optimization of transistor doping recipe (LDD, lightly doped drain) [**?**], SOI needs carefully study on the irradiation of large scale chip and of low power designs.

Sensor thinning and ultra-low material construction of modules are subject to the constraint of 0.15% $\mathrm{X_0}$/layer. HR CMOS wafer thinned to 50 μm is routine in semiconductor industry nowadays. SOI wafers thinned to 75 μm with backside implant have also been demonstrated by current R&D. However, low material detector modules need to in-

tegrate mechanical support, power and signal connection, and sufficient stiffness to avoid vibration.

10.1.2 Silicon tracker

- Alternative pixelated strip sensors with CMOS technologies;
- p^+-on-n silicon microstrip sensors with slim-edge structure;
- Front-end electronics with low power consumption and low noise, fabricated with CMOS technologies of small feature size;
- Efficient powering with low material budget and CO_2 cooling techniques;
- Lightweight but robust support structure and related mechanics;
- Detector layout optimization, in particular in the forward region.

10.1.3 TPC

- Continuous IBF detector module
- Laser calibration and alignment system

10.2 Calorimetry

10.2.1 HCAL

The future plans of HCAL should include prototype design and construction based on MOST funds support.

- DDHCAL based on RPC, Test beams and performance study
- MRPC with better time resolution (about 50ps)
- AHCAL based on scintillator + SiPM, prototype design and construction, performance study

10.2.2 Dual-readout calorimeter

Concerning the dual-readout calorimeter, a 3-year R&D programme is being pursued in order to address and clarifiy the following issues:

- absorber material choice, current candidates are lead, brass and iron;
- machining and assembly procedure for modules of $\sim 10 \times 10\ cm^2$ cross section;
- development of a modular, projective solution for a 4π calorimeter concerning both the construction of single modules and the design and construction of a full detector;
- identification of adequate solid-state photo-sensors in order to independently optimise both Čerenkov and scintillation light detection (with respect to PDE, linearity, dynamic range and cross-talk performance);

- readout granularity (i.e. identify the optimal fibre grouping into a single readout channel);
- identification of a tailored front-end electronics, likely composed by an ASIC and an FPGA chip, in order to extract in real time both charge and time information (in principle, a time resolution of 100 ps should allow to identify the shower starting point inside the calorimeter with a precision of about 6 cm);
- particle ID performance with Particle Flow Algorithms, with and without a longitudinal segmentation;
- development and validation of full and fast simulations of both testbeam modules and an integrated 4π detector;
- assessment of the performance for the most relevant physics channels (such as W, Z, H decays).

10.3 Magnet

About the future plan of magnet, we are going to do the following R&D work:

1. Further development of longer and higher Ic Aluminum based NbTi superconductor, the length longer than 100m, and Ic will larger than 15kA at 4 T background magnetic field. (For the reference, we have developed 10m long Aluminum based NbTi superconductor, the Ic 5kA at 4 T background magnetic field up to now.)
2. Build a prototype to study large coil winding process and cooling method by liquid helium thermal siphon.
3. Study of candidate option by using large HTS magnet and the related cooling method at 20K.

10.4 Interaction region

10.4.1 Luminosity

Prototyping, we do plan to build a small Si-W assembly to demonstrate the technology

1. SkiRoc2a is already study by USTC prof. Liu Shubin, in communication with the chip provider, Omega group. It seems that this chip fits our purpose for now.
2. there is suggestion for making CEPC silicon chips, and we certainly are looking forward for this approach.
3. The Silicon wafer shall be evaluation for read-out pitch versus precision we search for existing strip detectors for this purpose
4. Assembly precision and layout of electronics, which is basically a test-bench practice trying the best mechanical precision to a few microns

External survey and alignment system, using laser and optical devices to monitor the detector position to a few microns

10.4.2 MDI interface

to locate the position of LumiCal on magnet, the installation and limits install the detector, readout and cooling, etc and the interface with Pixel system, and possibly a tracking of very low angle electrons.

Interaction region layout re-design/optimization Background models validation with experimental data, e.g. SuperKEKB/Belle II Beampipe design together with SR photon protection, HOM absorber and cooling if needed Installation scheme that involves both LumiCal and final focusing magnets R&D on LumiCal, and demonstration of alignment of desired precision

10.5 New Colliders for a New Frontier

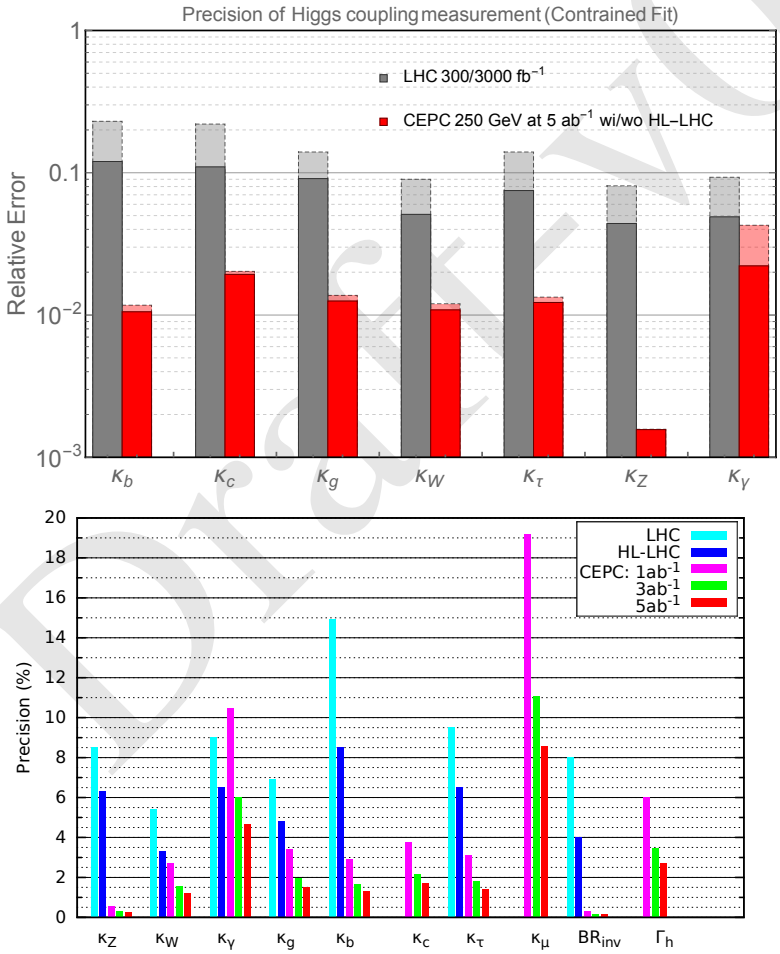

Figure 10.1: Top: The 7 parameter fit, and comparison with the HL-LHC, discussed in detail in Chapter **??**. The projections for CEPC at 250 GeV with 5 ab^{-1} integrated luminosity are shown. The CEPC results without combination with HL-LHC input are shown with dashed edges. The LHC projections for an integrated luminosity of 300 fb^{-1} are shown in dashed edges. Bottom: Comparison between the LHC and several benchmark luminosities of the CEPC.

References